2014-01-01

3D Printed Electromagnetic Transmission And Electronic Structures Fabricated On A Single Platform Using Advanced Process Integration Techniques

Paul I. Deffenbaugh
University of Texas at El Paso, pdeffenbaugh@miners.utep.edu

3D PRINTED ELECTROMAGNETIC TRANSMISSION AND ELECTRONIC STRUCTURES FABRICATED ON A SINGLE PLATFORM USING ADVANCED PROCESS INTEGRATION TECHNIQUES

PAUL ISAAC DEFFENBAUGH, M.S.E.E.
Department of Electrical and Computer Engineering

APPROVED:

Raymond C. Rumpf, Ph.D., Chair

Kenneth H. Church, Ph.D., Co-Chair

Peter Kim, Ph.D.

Thomas M. Weller, Ph.D.

Charles Ambler, Ph.D.

Dean of the Graduate School

Dedication

To my parents who have loved and educated me my entire life and
who continue to love me and support my education 100%.

3D PRINTED ELECTROMAGNETIC TRANSMISSION AND ELECTRONIC STRUCTURES FABRICATED ON A SINGLE PLATFORM USING ADVANCED PROCESS INTEGRATION TECHNIQUES

by

PAUL ISAAC DEFFENBAUGH, M.S.E.E.

DISSERTATION

Presented to the Faculty of the Graduate School of
The University of Texas at El Paso
in Partial Fulfillment
of the Requirements
for the Degree of

DOCTOR OF PHILOSOPHY

Department of Electrical and Computer Engineering
THE UNIVERSITY OF TEXAS AT EL PASO
August 2014

Acknowledgments

Thanks go to each of those who help me so much.

- Johanna Oda, my fiancée
- Xudong Chen, nScrypt, Inc.
- Kenneth Church, Ph.D., University of Texas at El Paso (UTEP), Sciperio, Inc.
- Paul Clem, Ph.D., Sandia National Laboratories
- Carlos Donado, Georgia Institute of Technologies
- David Espalin, UTEP
- Josh Goldfarb, nScrypt, Inc.
- Ibrahim Nassar, University of South Florida
- Luis Ochoa, UTEP
- Casey Perkowski, nScrypt, Inc.
- Eduardo Rojas, University of South Florida
- Ubaldo Robles, UTEP
- Ricardo Rodriguez, UTEP
- Raymond Rumpf, Ph.D., UTEP
- Mahesh Tonde, UTEP
- Harvey Tsang, UTEP
- Thomas Weller, Ph.D., University of South Florida
- Ryan Wicker, Ph.D., UTEP
- Kevin Zaras, DSM

Financial support is provided by the following sources.

- Army contract # W911NF-13-1-0109, US ARMY RDECOM ACQ CTR - W911NF, Title: HBCU/MI: 3D Formable RF Materials and Devices
- The Texas Office of the Governor, Rick Perry under the Texas Emerging Technologies Fund
- DARPA Contract # D14PC00016, Title: 3D Printed Wire Harness & Connectors for Satlets

Facilities and in-kind support is provided by the following sources.

- The W.M. Keck Center at the University of Texas at El Paso
- The EM Lab at the University of Texas at El Paso
- The WAMI Lab at the University of South Florida
- nScrypt, Inc. and Sciperio, Inc.

Executive Summary

Illustration	Project
	A 3D printed electronic circuit is fabricated on one platform.
	A printed camera circuit is printed on polyimide.
	The dielectric constant and loss tangent of many 3D printable materials in several colors and infill percentages are measured from 1 MHz to 15 GHz.
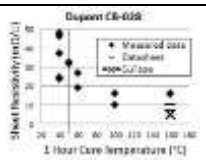	The DC loss of a printable conductive paste is measured over cure temperature and ambient temperature.
	Microstrip transmission lines are printed using stereolithography and DPAM.
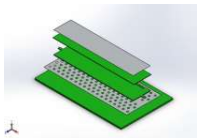	A fully 3D printed stripline is buried in a heterogeneous material on one platform. The loss is measured to be lower than microstrip.
	A novel suspended microstrip is printed using stereolithography and DPAM. The loss is measured to be lower than copper on FR4.
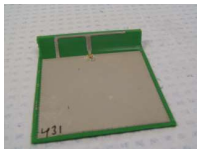	A curved inverted-F antenna is printed using FDM and DPAM.

Abstract

3D printing has garnered immense attention from many fields including in-office rapid prototyping of mechanical parts, outer-space satellite replication [18], garage functional firearm manufacture [1], and NASA rocket engine component fabrication [5]. 3D printing allows increased design flexibility in the fabrication of electronics, microwave circuits and wireless antennas and has reached a level of maturity which allows functional parts to be printed. Much more work is necessary in order to perfect the processes of 3D printed electronics especially in the area of automation. Chapter 1 shows several finished prototypes of 3D printed electronics as well as newly developed techniques in fabrication. Little is known about the RF and microwave properties and applications of the standard materials which have been developed for 3D printing. Measurement of a wide variety of materials over a broad spectrum of frequencies up to 10 GHz using a variety of well-established measurement methods is performed throughout chapter 2. Several types of high frequency RF transmission lines are fabricated and valuable model-matched data is gathered and provided in chapter 3 for future designers' use. Of particular note is a fully 3D printed stripline which was automatically fabricated in one process on one machine. Some core advantages of 3D printing RF/microwave components include rapid manufacturing of complex, dimensionally sensitive circuits (such as antennas and filters which are often iteratively tuned) and the ability to create new devices that cannot be made using standard fabrication techniques [42]-[45]. Chapter 4 describes an exemplary fully 3D printed curved inverted-F antenna [15],[16].

Table of Contents

List of Tables

List of Figures

Chapter 1: 3D Printed Devices

3D printing technologies abound and each has specific strengths and weaknesses. These technologies and others are discussed and contrasted in order to showcase what is possible in the field of 3D printing with emphasis in the area of printed electronics. A short primer is given on key technologies. The following technologies are discussed here: FDM, SL, ink jetted resin, DPAM, fused powders, fused layering of sheets, SLM, and EBM.

Fused deposition modeling (FDM) is by far the most popular 3D printing technology. This technique allows thermoplastics to be melted and layered creating strong, functional parts. FDM can be printed in air at room temperature thus lending itself to integration with other printing methods such as direct printing. Resolution and surface finish are trade-offs as compared with stereolithography (SL).

FDM begins with a 3-D computer model in the STL file format which is a collection of triangles defining the surface of the solid. The STL file is then sliced, a process which breaks the solid model into horizontal layers and then breaks down each layer into a collection of paths which the printing head will follow and save the data as a G-code file. The slicer first generates the outlines of the object then generates in-fill patterns. Significant amounts of time and material can be saved by reducing the infill percentage which also controls the dielectric constant and loss tangent. The printer constructs the object by extruding plastic while following the G-code paths that the slicer calculated.

The FDM feed system pushes the filament down a heated tube with an inner diameter (I.D.) that is only slightly larger than the filament itself. Depending on the temperature at any given position the filament will exist in one of three states: solid, liquid, or a soft/sticky state. The goal is to bring the material from solid to liquid as quickly as possible to avoid restricting

the flow through the chamber with partially-melted sticky material. The material is extruded through a small hole in the print nozzle. By adjusting the material feed rate and print speed the thickness can be controlled while also eliminating space between lines which prevents crevices from causing problems when liquid conductive paste is applied. After each layer, the nozzle is moved up by a fixed amount.

New thermoplastic materials are constantly being identified and produced in filament form for FDM. Here is a list of currently available materials. Most of these materials have lower microwave loss compared to the materials used in other printing technologies.

- Acrylonitrile butadiene styrene (ABS)
- Polycarbonate (PC)
- Polylactic acid (PLA)
- Aliphatic polyamides (nylon)
- Polyetherimide (PEI/ULTEM)
- Polyphenylsulfone (PPSF/PPSU)
- Polyvinyl acetate (PVA)
- High impact polystyrene (PS)
- Low density polyethylene (LDPE)
- Polyethylene terephthalate (PET)
- Laybrick, laywood (PET mixed with chalk or wood fibers)
- Polyhydroxyalkanoates (PHA/colorfab_xt)

Stereolithography apparatus (SLA or SL) is a close second to FDM in popularity and offers the highest level of resolution and surface finish as well as transparency. UV-curable resin is selectively hardened by a laser in a vat of liquid in machines like the 3D Systems Viper si2, the Formlabs Form 1. Materials may be separated into several basic categories: basic resins including opaque and transparent, ductile resins for resiliency, and silica- or ceramic- loaded resins for stiffness and strength. Here are several SL-compatible materials from DSM Somos which have been investigated. Other manufacturers include 3D Systems, VisiJet, Solid Concepts, Dymax, and Loctite.

- DSM Somos 9120, 9420, 14120, NeXt, (opaque white)
- DSM Somos DMX-SL 100, (resilient)
- DSM Somos 11122, 12120 ProtoTherm, (translucent)
- DSM Somos 12120 ProtoTherm, NanoForm, (high temperature)
- DSM Somos NanoTool, 15120 NanoForm (particle-filled)

Ink-jetted resin (e.g. Stratasys, Ltd. Objet) involves using inkjet technology to dispense very low viscosity UV-curable resin onto a surface followed with large UV lamp curing. Since the material deposition and curing are separate steps, slumping of the material can occur and the parts are not as detailed as SL. Due to the low-viscosity, layers must be very thin so printing time is much longer than with FDM. Since UV-cured resin used is similar to that used in SL, the electromagnetic loss tangent is likely higher than FDM. This is a liquid-deposition based method and in theory could be combined with similar methods such as DPAM.

Material patterning onto the printed substrate or object in a controlled manner can be done using a variety of approaches. Inkjet was considered; [217],[222] however, the extremely thin film would be less than the thin skin depth at high frequencies thus increasing the RF/microwave conductor loss. Thick films are thought to be a better option and several techniques exist for patterning thick film. Gravure printing [133],[134] and silk screening [1] allows thousands of patterns to be produced cheaply; however, it is not easy to change the pattern.

Micro dispensing is a good option for creating random patterns using thick film inks [223]. When micro dispensing is applied in a 3D context it is called direct print additive manufacturing (DPAM) offers the ability to pattern conductive pastes, resistive pastes, high-k and low-k dielectric inks, and adhesives in an on-demand fashion. Micro dispensing companies include nScrypt, Optomec, Nordson Asymtec, Musashi Engineering, Envision Tech, GPD Global, and Precision Valve and Automation, and Camelot. DPAM is reconfigurable and mask-

less thus saving design to manufacture cycle time compared to silk screening [1]. Micro dispensing is typically done using positive pressure on the material, which is transferred through a small orifice directly onto the desired surface. nScrypt, Inc. micro dispensing technology uses a patented valve near the dispensing orifice to control the start and stop of the material flow. Traditional dispensing, including micro dispensing, is slow and lacks resolution and accuracy. nScrypt, Inc.'s SmartPump quickly and accurately controls the material flow and allows printing at high speeds while maintaining clean starts and stops of the printing path. Figure 1 shows a cross section of the valve assembly.

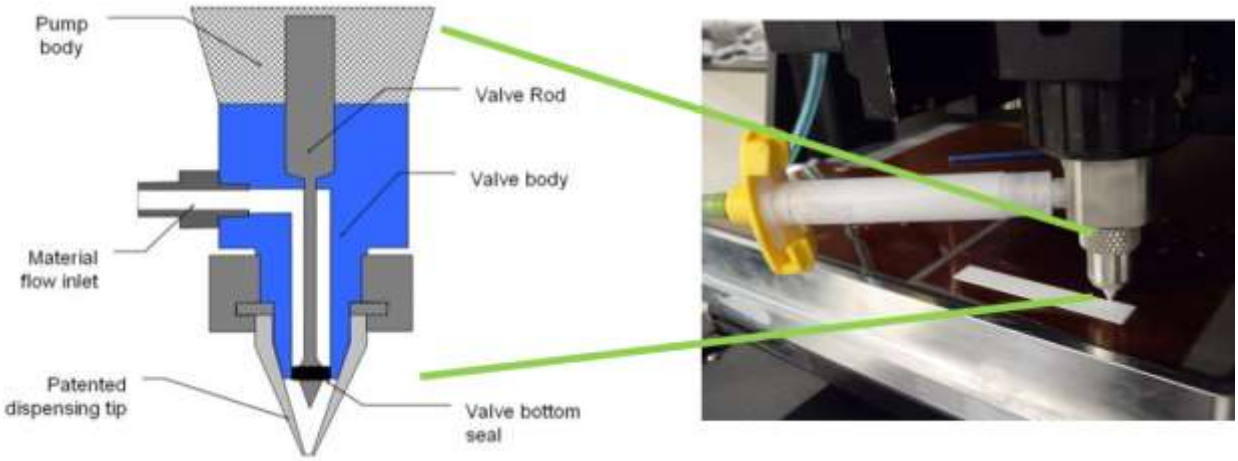

Figure 1 nScrypt, Inc. SmartPump valve assembly (diagram credit: Xudong Chen)

The material is typically transferred from a syringe by a positive pressure through the material flow inlet into the valve. The valve rod is driven by a motor and travels up and down in the channel of the valve body with a resolution of 0.1 μm. When dispensing is initialized, the valve opens, which allows the material to flow through the pen tip onto the substrate. To stop the dispensing, the valve rod moves to a closed position that not only keeps a seal to the channel, but also maintains a negative pressure in the dispensing tip chamber to induce a reverse of the material flow [214]. The shape of the pen tip is specially designed to reduce the pressure needed

to push material through the orifice compared to the commonly used tubular needle, enabling dispensing through very small holes, such as 100 µm or less. This assembly is capable of handling materials with very high viscosities. The valve will open and close in a synchronized manner with the X and Y motion control. This allows any pattern to be printed in an X, Y plane and, if necessary, conformally in the Z plane. The linear print speed of X and Y can be as fast as 500mm/second on a gantry system, and the resolution and repeatability of motion in all directions is within a few micrometers. In addition to the SmartPump and the motion platform, a high resolution vision/camera system is also integrated for substrate alignment and a real-time processing view. This aids in achieving accurate dispensing parameters on topographically-difficult materials such as FDM plastic.

The printing pattern can be generated by a number of Computer-Aided Design (CAD) software packages. The output of the CAD is transferred into a script file using nScrypt, Inc. software; this provides integrated, synchronous commands for the machine. There is no need for a screen mask or other complicated setup in the process which enables rapid prototyping in this digital manufacturing approach. This combination can reduce cost and maintenance on the production floor. In addition, the mask-less approach allows for a variety of patterns printed digitally, the precision of the XYZ motion allows for conformal printing, and the ability to dispense a wide range of materials promotes the potential to print in 3D or implement high aspect ratio features.

Fused deposition of ceramics (FDC) or powders (e.g. Z-corp zp150, Voxeljet) involves ink-jetting a binder such as cyanoacrylate into a bed of powder. Parts which are fabricated using this technique are not found to have adequate surface finish for printed electronics. Frequently

dyes are introduced with the binder in order to print in color thus the technology is well-suited for conceptual modeling. Several powders are available for this technology.

- Gypsum salt
- Plastic / PMMA
- Silica

Fused layering of sheets (e.g. Solido) involves the selective application of binder and knife-trimming between layered sheets of plastic. This technology does not allow for the integration of other printing technologies since each layer must be smooth and flat for the next layer of plastic to be applied and was thus not selected for printed electronics.

Selective laser melting (SLM) such as Renishaw and electron beam melting (EBM) such as ARCAM produces functional metal parts; however, it they require a high temperature and vacuum or inert gas environment. These technologies offer great promise in the areas of on-demand or highly complex metal components; however, do not show promise for 3D printed electronics due to the frequent necessity of a vacuum envelope, extremely high temperatures, and lack of dielectric.

1.1. Roughness Correction

The greatest drawback with FDM and other 3D printing technologies is surface finish or surface roughness. A rough surface sometimes detracts from the visual appeal of a part so it is desirable to have the smoothest finish possible. From a technical perspective, rough surfaces present two problems. The rough surfaces makes dispensing thick film pastes difficult or impossible since the peaks and valleys interfere with the printing process. Second, no matter how the material is applied, the undulating surface creates a longer path for the current to flow thus increasing the apparent resistivity of the conductor. This effect is pronounced at high frequency

due to the skin effect where high frequency currents tend to travel in the outer parts of the conductor rather than in the bulk of the material.

The difference in surface roughness is made apparent in the following materials comparison. A resonant cavity is designed using aluminum conductor and air dielectric; however, manufacturing this device is somewhat challenging due to the square edges and difficulty of machining around corners [1]. 3D printing with dissolvable support is ideally suited for a structure such as this. The resonant cavity is fabricated by the W.M. Keck Center for 3D Innovation at the University of Texas at El Paso (the Keck Center) using FDM-ABS (Figure 2) and SL-WaterShed (Figure 3) as dielectric. The devices are meant to be coated in conductive paste in order to form the cavity. A small hole for an SMA pin is provided on the top and bottom of the structure in order to couple waves into the structure. The devices were fabricated as demonstration parts for Georgia Institute of Technology. These devices showcase the difference in surface roughness between FDM and SL technologies.

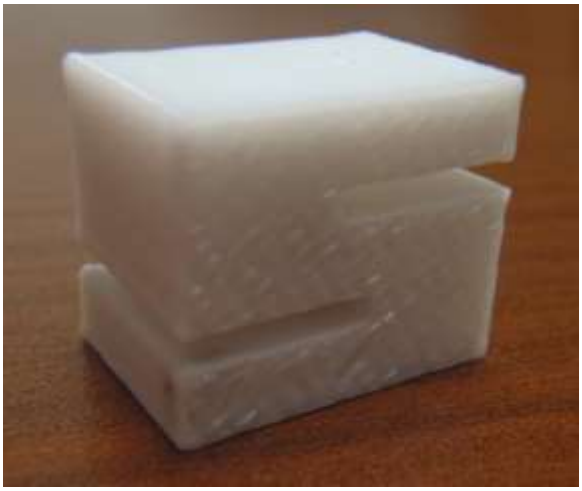

Figure 2 FDM-printed ABS resonant cavity

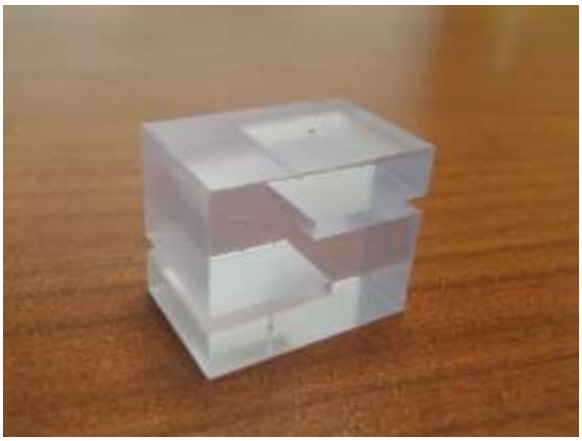

Figure 3 SL-printed WaterShed resonant cavity

It is well known that the FDM 3D printing technique produced a surface finish that is rougher than SL or DPAM. Figure 4 illustrates a bottom surface produced on a Stratasys, Ltd. machine when a raft technique is used. Rafts are a low-density infill constructed beneath parts to make part removal easy. Figure 5 shows the top surface of the same part with the less than optimal infill. Several techniques for reducing this roughness exist and different techniques may be applicable to different applications. A process involving acetone vapor is patented by Stratasys, Ltd. where the surface of ABS is chemically melted forming a smoother finish. Acetone may be applied directly to the surface; however, it is difficult to control the rate of the reaction and avoid over-melting the surface and deforming the part.

Figure 4 FDM, bottom surface

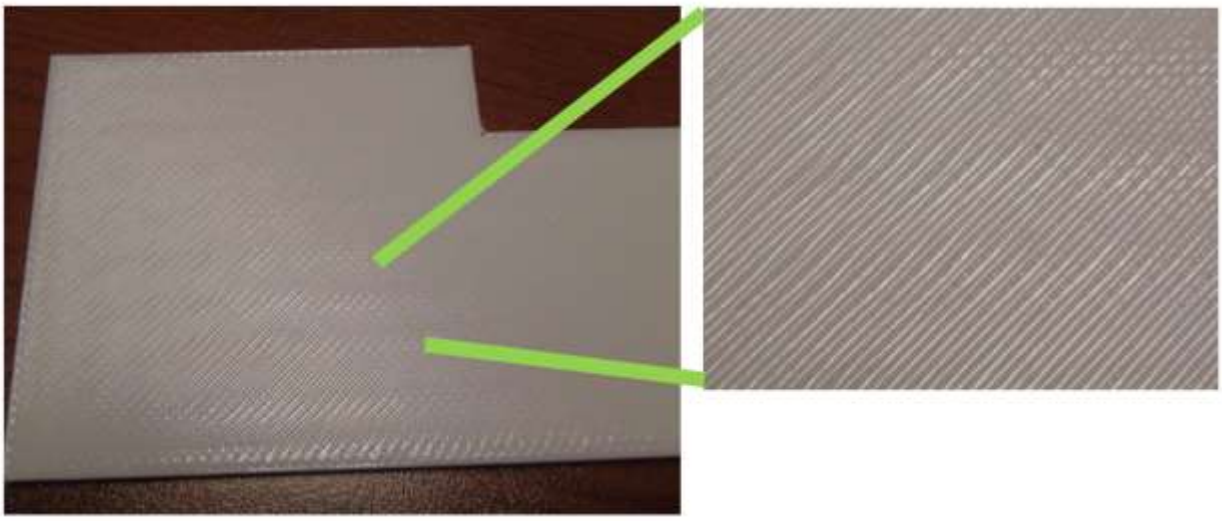

Figure 5 FDM, top surface

A smoother surface is produced and small gaps are filled by baking a 0.8 mm thick sample of FDM-ABS near its glass transition temperature, at 220 °C for 30 minutes; see Figure 6. The drawback is that since FDM almost always contains small gaps, baking the part causes it to shrink by about 5 – 10 %. Re-melting samples is not recommended for non-flat parts since the process would deform the part and manufacturing tolerances would not be maintained.

Figure 6 FDB-ABS baked at 220°C for 30 min

An obvious solution is to simply face the surface using conventional CNC milling as in Figure 7. This produces the flattest and smoothest surface of the methods that are tested. Several drawbacks exist which limit the utility of this smoothing method. Milling the surface does not fill

in gaps in FDM which can lead to top to bottom layer shorting in 3D printed circuit structures. Milling is a subtractive manufacturing process which creates waste. 3D printed electronics is moving towards a fully-integrated approach where just one machine is able to produce fully functional electronic devices. Incorporating a CNC mill into an electronics printer presents significant engineering challenges such as waste material removal and maintaining a clean work area for the application of additional layers of materials.

Figure 7 CNC milling FDM-ABS

Multiple lengths of microstrip line were printed for Georgia Institute of Technology using CNC milling for surface smoothing and 7 out of 8 of the microstrips were shorted to the bottom side ground plane. The printed conductive paste leaks through small gaps in the FDM down through the 0.8 mm thick substrate.

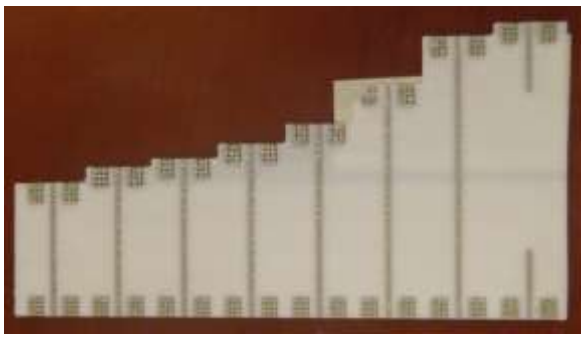

Figure 8 Printed microstrips on FDM

Figure 9 Printed microstrips on FDM

The 3D printed parts thus far are fabricated using commercial FDM machines from Stratasys, Ltd. which have limited configurability and motion repeatability. The problem of roughness in FDM has been solved using an Aerotech XYZ gantry platform which lends sufficient repeatability to allow fine tuning of the process parameters such as extrusion rate and XYZ motion speed. Additionally, the Aerotech motion control system allows binding of motion of the extruder motor with the motion of the XY motors in such a way that gaps are eliminated and over-extrusion near line ends is minimized see Figure 10. J-Head and E3D nozzles are both used to print ABS with very smooth surfaces. This FDM parameter tuning process is used successfully in the fabrication of an RF/microwave transmission line and an antenna for microwave frequencies (chapters 3 and 4).

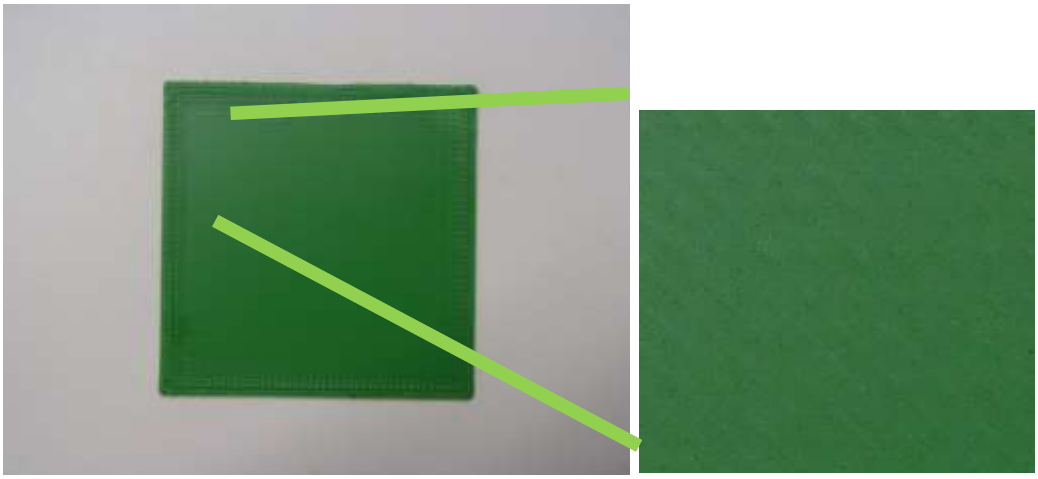

Figure 10 Smooth FDM-printed ABS

1.2. 3D Printed Electronics Flying Camera

3D printed electronics is a new and fast-growing field with the potential to allow electronic devices to become more compact and available on-demand. 3D printed electronics exists at the confluence of additive manufacturing and precision-dispensed conductors. Traditional printed electronics involves interconnects silkscreened onto a flexible substrate such as polyimide. This technique is now being used to pattern interconnects directly into 3D printed parts with no need for a printed circuit board (PCB) or mounting hardware. This concept can save weight and assembly time while also opening the door for on-demand manufacturing of objects with active functions. To showcase the latest capabilities in this process, a printed flying helicopter wireless camera is developed and manufactured by stereolithography (SL) and DPAM silver paste.

An inexpensive wireless camera is used which includes a CMOS image sensor and 2.4 GHz wireless video transmitter. The camera and transmitter are constructed on separate PCBs from the manufacturer. In order to test functionality, the circuit is first printed on polyimide substrate then onto the SL printed airframe using DuPont CB028 conductive paste. The components are harvested from the original PCB and arranged and attached to the 3D printed circuit using H20e conductive epoxy. The schematics are shown in Figure 11 and Figure 12. Three to four volt power is obtained from the helicopter's main single-cell LiPo battery and is converted to 5V by a 3D printed switching power supply for the transmitter and 2.8 V and 1.8 V by linear voltage regulators for the image sensor. The image sensor requires a crystal oscillator circuit, two startup delay RC networks, and several programming resistors in order to function. This design is shown in Figure 13.

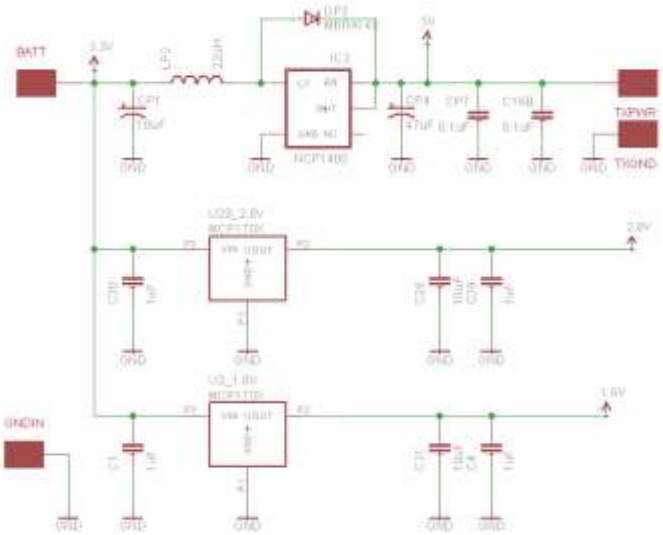

Figure 11 Camera power supply schematic

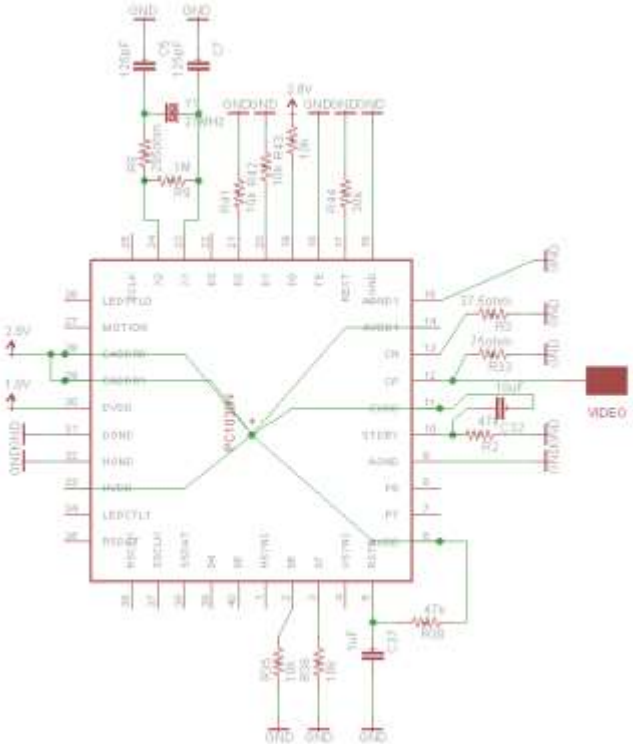

Figure 12 Image sensor schematic

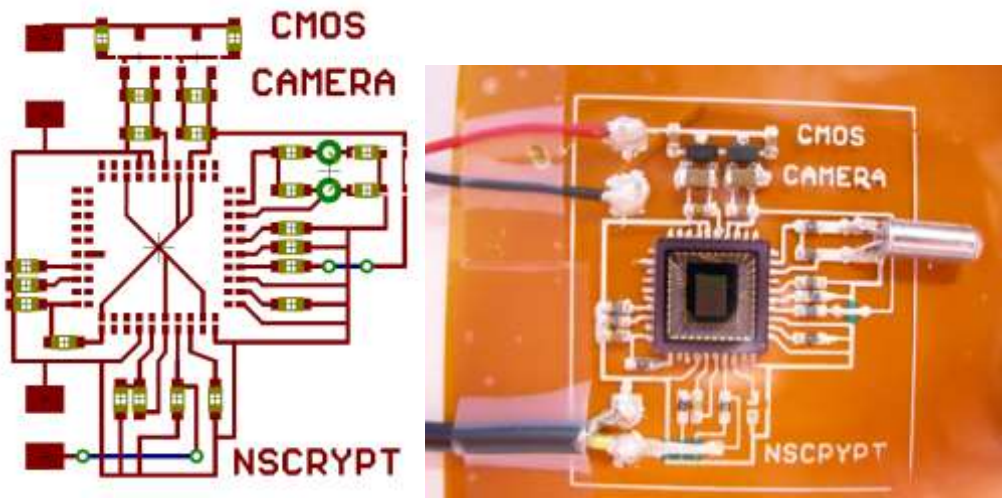

Figure 13 Printed camera test circuitry

The test camera works well and produces a clear video signal. For the 3D printed structure, the PC1030 image sensor is press-fit into the SL part as shown in Figure 14. Bridging the gap from the printed material to the press-fit camera is difficult because not using enough paste allows an open circuit to form while using too much paste shorts one pin to another. Close tolerances in forming the necessary connections to the camera mean that the camera is unreliable. This problem is effectively solved in future prototypes by modifying the design of the printed structure to allow extra space at the chip corners while eliminating as much gap as possible on the sides where the electrical connections must be made. The only flaw limiting this design is the printed trace to chip lead connections and is shown to be overcome in the last section of this chapter.


Figure 14 Image sensor press-fit into SL airframe before printing

1.3. Flatness Correction

The 3D printed SL part is loaded into a 3Dn-600 printing machine and affixed using a cradle and temporary double-stick tape. The area to be printed is scanned using a Keyence LK-G laser displacement sensor scanning system which maps the exact height (1 µm resolution, 10 µm accuracy) on a grid of 500 µm. This technique adapts the printing of silver paste by actively adjusting the height of the printing nozzle to to any imperfections in the part. The scan data is shown in Figure 15 and the process is shown in Figure 16.

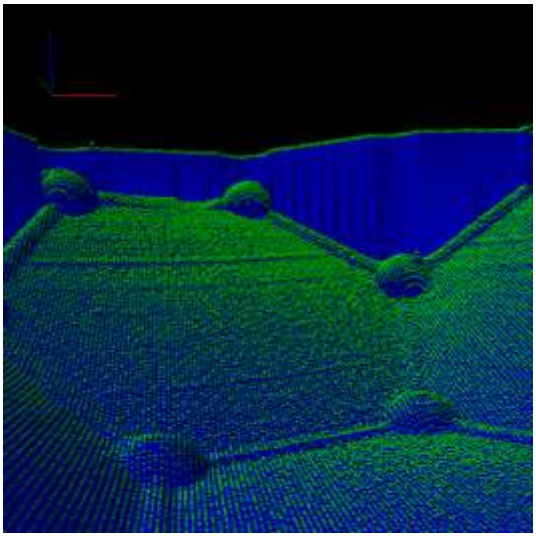

Figure 15 Pre-print laser scan data

Figure 16 nScrypt, Inc. 3D printing

1.4. Rotational Correction

Two fiducial marks are identified using cameras and machine vision techniques before the print paths are applied according to the layout shown in Figure 17. This accounts for slight rotation and translation errors and aligns the print to the 3D structure. A 125/175 tip and standard parameters are used to print DuPont CB028; see Appendix R. Components are attached using EPO-TEK H20e conductive epoxy. The power circuits in Figure 18 generate 1.8V, 2.8V, and 5V from a single 3.7V LiPo battery and are fully functional.

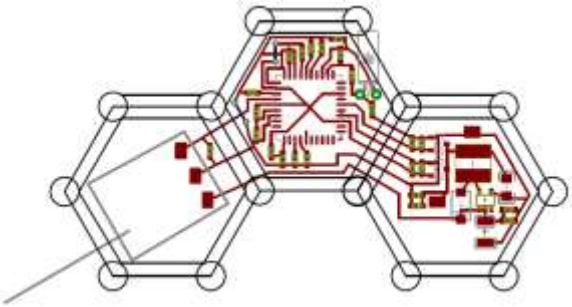

Figure 17 Flying camera circuit layout

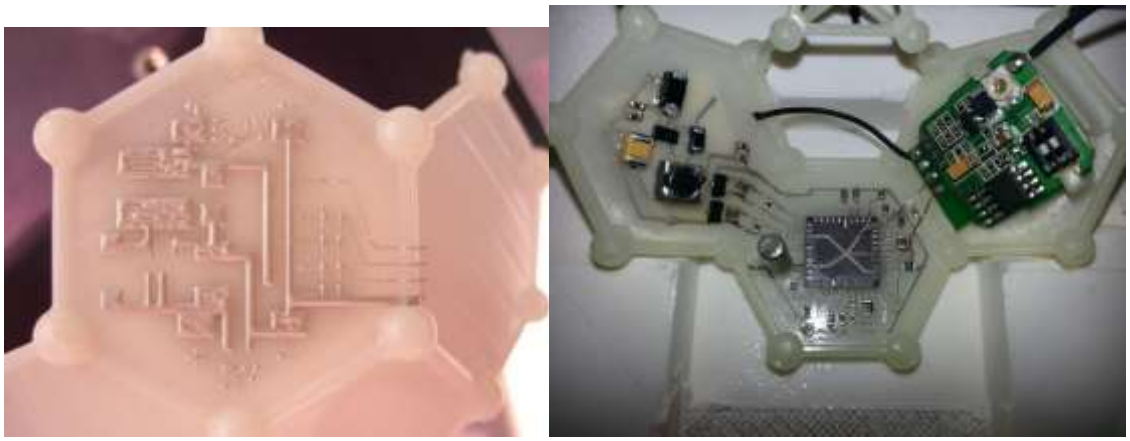

Figure 18 Flying camera printed circuitry

1.5. Leveling

FDM-printed parts are not always perfectly level once they are removed from the printing machine due to thermal warping effects. This is not a problem for 3D printers which incorporate both FDM and conductive paste deposition since parts do not need to be removed between material transitions. Currently, most of these machines perform only one of these two functions. Parts must be removed from the FDM machine and the conductive paste machine must accommodate the imperfect parts. This is typically done with laser displacement sensor scanning as described above; however, the red laser beam does not interact well with white ABS material and the grid scan data has many bad points which preclude accurate printing. This is solved in two different ways. Green colored ABS is shown to produce accurate scans when fabricating the curved antenna; see chapter 4. If white ABS is to be used, another option is shown to be successful.

When the part to be printed on is flat but un-level, a three-point correction method can be used to adjust the print file in such a way as to follow the slope of the surface. This method is used with great success. The method works as follows: first, three 3-D data points are determined from the surface describing an X-Y position and the actual surface height Z. These data points

can be taken using the laser if the measurement is performed carefully or using the actual printing tip and a process-view camera which allows the user to see accurately when the tip is touching the surface. These data points are then used to determine the normal from the surface and the angles about the cardinal axes to rotate the print file. Each data point is represented in the form shown here.

$$\langle p_n \rangle = \langle p_{n,x} \quad p_{n,y} \quad p_{n,z} \rangle \text{ where } n = \{1,2,3\} \tag{1}$$

The surface normal is represented as

$$\langle n \rangle = \langle n_x \quad n_y \quad n_z \rangle \tag{2}$$

Rotation about the Z-axis is assumed to be zero.

$$\langle n \rangle = det[(\langle p_3 \rangle - \langle p_1 \rangle) \times (\langle p_3 \rangle - \langle p_2 \rangle)] \tag{3}$$

$$\theta_x = atan\left(\frac{n_y}{n_z}\right) \tag{4}$$

$$\theta_y = atan\left(\frac{n_x}{n_z}\right) \tag{5}$$

$$\theta_z = 0 \tag{6}$$

The file representing the print consists of a set $\{L\}$ of lines and each line has two end points each described by its X,Y,Z coordinates as a vector $P = \langle p_x \quad p_y \quad p_z \rangle$. The set of all line end points is represented as $\{P\}$. In order to modify each end point in order to effectuate rotation, a rotation matrix R is defined as in equation 23 and is used as in equation 24 to modify each line's end point [3].

$$R = R_x R_y R_z \tag{7}$$

$$R_x = \begin{bmatrix} 1 & 0 & 0 \\ 0 & cos\theta_x & sin\theta_x \\ 0 & -sin\theta_x & cos\theta_x \end{bmatrix} \tag{8}$$

$$R_y = \begin{bmatrix} cos\theta_y & 0 & sin\theta_y \\ 0 & 1 & 0 \\ -sin\theta_y & 0 & cos\theta_y \end{bmatrix} \tag{9}$$

$$R_z = \begin{bmatrix} cos\theta_z & sin\theta_z & 0 \\ -sin\theta_z & cos\theta_z & 0 \\ 0 & 0 & 1 \end{bmatrix} \tag{10}$$

$$\{P_{new}\} = R\{P_{old}\} \tag{11}$$

In order to demonstrate this technique a camera circuit is printed successfully (no opens or shorts) on the first try on white FDM-ABS printed material. Substrate printing is performed on a Prusa i3. A schematic error prevents the camera from functioning properly; however, the print quality (Figure 19) exemplifies the applicability of the three-point correction technique.

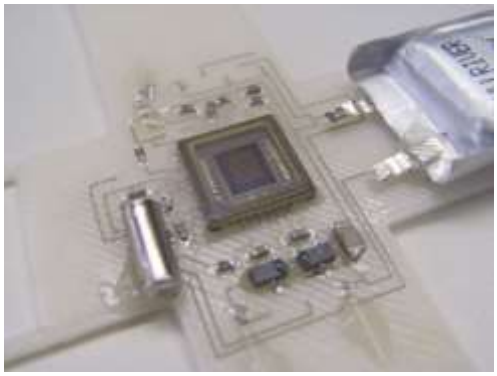

Figure 19 Printed, three-point corrected DPAM structure

1.6. Fully 3D Printed Flashing Logo

Full 3D printing is an emerging field and a few examples exist; [5],[6],[7] however, much more research is necessary in order to enable the technology. In order to demonstrate the capabilities and benefits of a fully-integrated 3D printed electronics machine, a set of sequentially flashing LEDs are designed and printed. Although the part described in this section is non-functional due to several electrical short circuits, several important printing challenges are

identified and many techniques are developed and demonstrated in a single machine [184]. The process is proven successful with the flashing heart design discussed in the next section.

Full 3D printing is the objective and involves continual development of various materials and techniques for applying these materials. Although 3D printing components such as LEDs, microcontrollers and large-value capacitors is still impractical, progress is ongoing. For instance, printed LEDs have been demonstrated [9],[10] but the process of their application to a surface involves many intricate steps such as spin coating-masking, and aluminum vapor deposition in a vacuum.

An SL-printed substrate is manufactured by Keck Center technicians. Pick and place is commonly used in the fabrication of traditional circuit boards and will continue to be useful in 3D printing systems [5], [8]. The design calls for accurate angular placement of the components and this is easily realized using the integrated rotary pick and place device. Custom pick and place tips are designed by the author and printed by technicians using WaterShed material. A special dual nozzle is invented (Figure 20) which picks larger SOIC-16 chips more easily and places them into the structure (Figure 21).

Figure 20 Printed pick and place dual nozzle

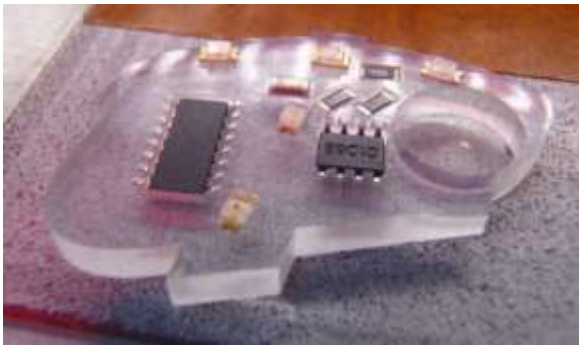

Figure 21 Pick and placed components

CB028 and a 125/175 tip are used to print traces 200 µm with a spacing of 200 µm. Care must be taken in setting the amount of material dispensed at the connection points. Laser curing of conductive pastes has been shown [12],[13]. Once the conductive traces are deposited in liquid form, a Manlight ML-30 Nd-YAG diode laser (maximum power: 30 watts, wavelength: 1080 nm) is used to cure the traces to a dry, conductive state. The laser is operated at 2 watts with a 10X focusing lens and a final spot size of 1 mm and a travel speed of 50 mm/s. The laser is normally invisible but becomes visible when the beam burns the more absorptive plastic of the SOIC chips as shown in Figure 22. A microscope slide is used to protect the dielectric-coated lens from smoke deposition which causes localized heating on the objective and cracking in the delicate glass lens.

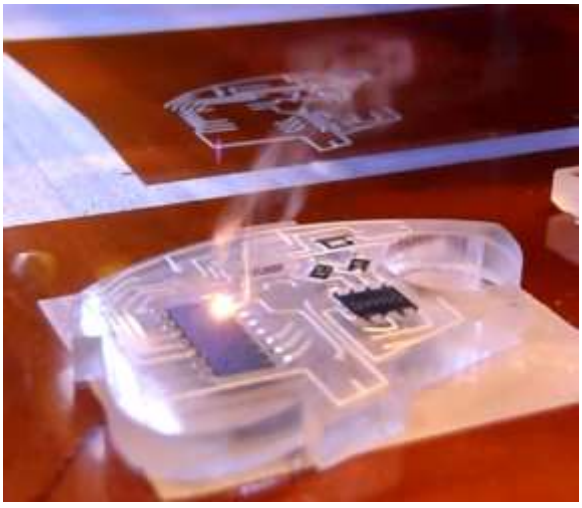

Figure 22 Laser curing CB028 paste

Ohmmeter testing reveals that all of the traces show less than 2 Ω of resistance from end to end in lengths up to 40 mm. This process enables future designs where localized heat curing is necessary.

Pin-to-pin shorting occurred on the SOIC-16 package due to excess material deposition. Making the connection from a printed trace to the lead of an integrated circuit (IC) is quite challenging and is typically addressed using solder. Solder has excellent wicking and bonding abilities which are not found in CB028 paste. Redesign of the interconnects and the use of a high-solids composition thick film silver epoxy, H20e, is shown to render the part functional in the case of the printed heart in the following section.

1.7. Fully 3D Printed Flashing Heart on One Machine

The ultimate goal for 3D printed electronics is on-demand automated fabrication of heterogeneous objects. A machine is constructed which includes provisions for printing plastic (ABS), conductive (CB028), and electro-mechanical bonding (H20e) materials in an automated fashion. This system allows the shape, size, and color to be changed at-will without retooling. An nScrypt, Inc. 3Dn-300 machine is equipped simultaneously with a SmartPump and fused deposition extruder. A heat-controlled, leveled aluminum build platform is covered with ULTEM tape (polyetherimide) with 3M acrylic adhesive. A thin layer of ABS mixed with acetone is coated onto the surface to ensure adhesion throughout the process.

The SmartPump is loaded with 3 mL of CB028 silver paste. Water cooling is used to stabilize the material rheology during printing near the hot printing surface. Without water cooling, the material heats to above 35 °C and thickens thus precluding accurate printing. 3.18 mm O.D. copper tubing is wrapped around the dispensing tip (Figure 23) and material syringe and 17 °C water from a chiller is pumped through at 0.1 L/min. By temperature feedback control

the lowest part of the dispensing tip is maintained at a constant temperature of 19 °C thus preserving the material's consistency even when near the heated bed. Using the cooling system, CB028 is dispensed onto the freshly printed 90 °C ABS material resulting in immediate automatic curing.

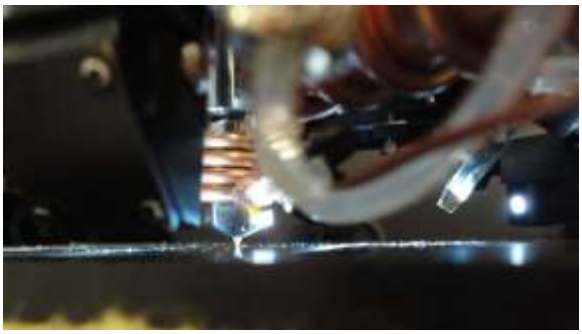

Figure 23 Water cooled SmartPump

A circuit of sequentially flashing LEDs is designed and fabricated using this automated machine. The electrical schematic is shown in Figure 24. A miniature 3.7 V 19 mAh rechargeable lithium polymer (LiPo) cell is used to power the circuit.

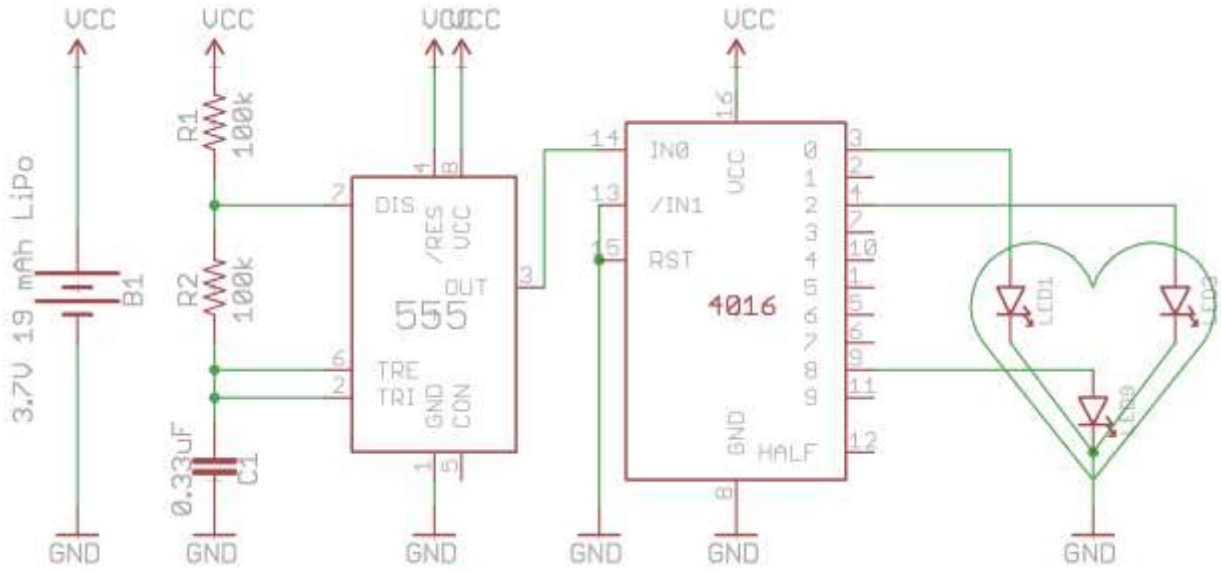

Figure 24 Flashing heart schematic

The heart is designed 50 mm wide and 42 mm long and 3.5 mm high. Two jumpers are required in the layout (Figure 25) and are realized using buried vias in ABS using H20e. Holes are provided in the top layers of ABS to provide access for charging the lithium polymer battery. The first layer of the ABS print is 200 µm thick and the following 33 layers are 100 µm each. The design is shown in Figure 26. After the first layer of CB028 has been applied, two more 200 µm layers of ABS are applied. Bridging allows these layers to cover the ICs even though they are not flush with the surface. H20e vias are formed and the structure is covered with a final two 200 µm layers of ABS.

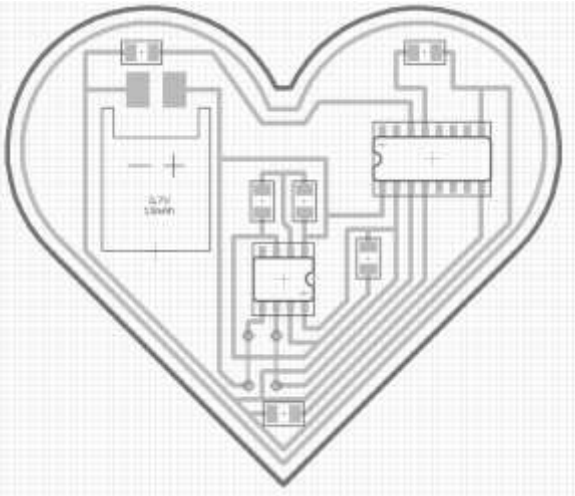

Figure 25 Flashing heart circuit layout

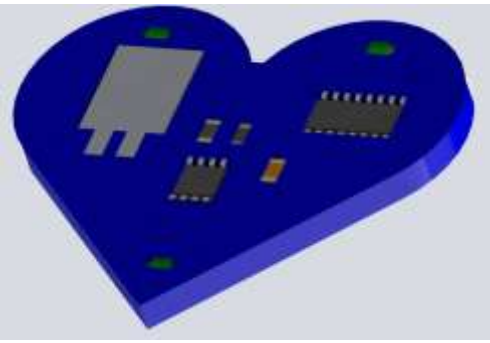

Figure 26 Flashing heart CAD model

Five machine temperatures are monitored and controlled as shown in Table 1.

Table 1 Temperature monitoring

Process	Temperature
Printing surface	90 °C ± 1 °C
Fused deposition pump	230 °C ± 3 °C
SmartPump tip	19 °C ± 2 °C
Cold water supply	17 °C ± 1 °C
Cold water return	19 °C

Once the substrate layers of ABS are printed, the components are installed manually, electrical interconnects are printed, and the entire part is buried using ABS. Figure 27 shows the process. H20e and CB028 form the two via jumpers and a third and final print of ABS seals in the part against damage. Automated component placement is shown successfully however the pick and place equipment was not available at the time that this part was fabricated.

Figure 27 Burying components

Excellent repeatability and reliability of design due to a thorough understanding of the 3D printed electronics process is demonstrated by the fabrication of two functional flashing hearts out of four attempted. Printing ABS and CB028 in the same machine on a leveled bed eliminates the need for software leveling of the print. Tight tolerances in surface finish are maintained which leads to a flat and smooth surface for applying silver paste without the need for laser scanning. Using a heat-controlled bed eliminates the need for laser curing of the CB028. Forming accurate component cutouts minimizes the gap between the IC and the printed trace

thus improving the interconnect reliability. In fact, the first heart is shown to be immediately functional in the machine and of the four hearts printed, three were functional at the time of manufacture and two show long-term reliability (Figure 28).

Figure 28 Flashing heart

Chapter 2: Microwave Frequency Characterization of 3D Printed Materials

State of the art 3D printing is not only capable of fabricating structurally functional parts but due to improvements in accuracy it can also be used to rapidly manufacture 3D RF/microwave components. The advantages of 3D printing include time saving and the ability to create new devices that cannot be made using standard fabrication techniques. High frequency characterization at several levels is important. Measurement of the raw materials involved, transmission line analysis, and microwave circuit analysis are all important to capture the performance of high frequency analog and digital signals. Recently, researchers have demonstrated the addition of electronics by combining 3D printing and printed electronics [16]-[21]. These electrically functional devices enhance the potential of 3D structures by offering greater design flexibility and tighter integration of functionality than the current process, where printed circuit boards are placed into injection-molded plastic cases. The majority of 3D electronic structures demonstrated have been DC or low frequency [16]-[21]. Some larger scale microwave devices have been demonstrated such as copper electroless-plated devices [22]-[25], electron beam melt antennas [26], ceramic SL [27]-[39], waveguide structures [40] and microwave meta-material structures [41]-[45]. It is clear that almost all high demand electronic devices must have some type of wireless capability, from the five-plus radios in cell phones down to keyless entry for automotive [46] and building access and RFID [194]-[208]. Studying RF electronic structures is important but fundamental characterization needs to be done. Microwave frequency characterization of 3D printable materials is crucial for successful design of microwave circuits that can be fabricated into structures. Loss tangent (tanδ) allows designers to balance requirements for low-loss performance with requirements for low-cost rapid fabrication and print quality. Dielectric constant is critical because it governs the characteristic

impedance of microwave transmission lines in the material which affects reflection loss, it also governs coupling between components in a circuit, and affects the bandwidth of the system. Broadband characterization captures the frequency-dependent nature of these parameters and allows this data to be used in designs at any frequency rather than just a single band of frequencies. Broadband material characterization is important for high speed digital signals whose frequency spectra are large and frequency dispersion due to varying dielectric constants can be an issue. Such data for these materials do not exist and this paper seeks to characterize materials printed using fused deposition modeling (FDM) [21] and stereo lithography (SL) [47] technologies. These two technologies are the most mature for 3D dielectrics. Future studies can determine which materials are suitable for specific applications; however, preliminary results show FDM exhibits lower microwave loss but low print resolution and a rough surface finish while SL exhibits excellent resolution and a smooth surface finish but has more loss.

2.1. Overview of Methods

Many methods exist for the characterization of materials at microwave frequencies [48]–[69]. The materials are characterized over several frequency bands using different well-established measurement techniques, I-V capacitance, RF-IV, the Nicholson-Ross-Weir (NRW) waveguide method [70]-[74], and a resonant cavity. The methods are outlined in Table 2, discussed in the following sections, and the results of these measurements are shown in Table 22 – Table 25. Many other methods exist in literature [19]; however, these methods were chosen for their applicability and availability.

Table 2 Measurement methods

Frequency	**Method**	**Error in ε_r**	**Error [b] in tanδ**
1 MHz, 2 MHz	LCR Meter	≤3.7% [a]	20 – 100% [c]
100 MHz – 1 GHz	Impedance Analyzer	≤21% [a]	25 – 300% [c]
8.2 – 11 GHz	Nicholson-Ross-Weir X-Band Waveguide	≤5.8% [b]	10 – 300% [d]
0.5 – 14 GHz	Cavity measurement	N/A	N/A

[a]Maximum estimated error.
[b]Maximum standard deviation from sample sets.
[c]Approximate range of estimated errors.
[d]Approximate range of standard deviations from samples sets.

2.2. Method 1: LCR Meter, 1 MHz, 2 MHz

An Agilent E4980A precision LCR meter [75] with an Agilent 16451B dielectric test fixture [76] is used to measure materials at 1 MHz and 2 MHz, compliant with ASTM D150 [77]. This instrument works by using the material under test (MUT) as the dielectric in a capacitor and measuring the AC current/voltage (AC I-V) relationship to determine the complex impedance which is converted to dielectric constant and loss tangent, using physical dimensions and basic equations.

$$\mathrm{Z} = R + jX \tag{12}$$

$$\varepsilon_r = \frac{t}{2\pi\varepsilon_0 f X_C A} \tag{13}$$

$$\tan\delta = \frac{R}{X_C} \tag{14}$$

The Agilent 16451B dielectric test fixture uses a 4-wire measurement in order to exclude cable impedances from the measurement. It is worth drawing a distinction between a typical 4-point probe setup and the 4-wire measurement. In the case of a 4-point probe, each probe is

positioned at a separate location on a sheet under test. In the case of a 4-wire measurement system, each pair of wires is terminated coincidentally at the devices under test so that little to no current flows over the cables used for voltage measurement (Figure 29).

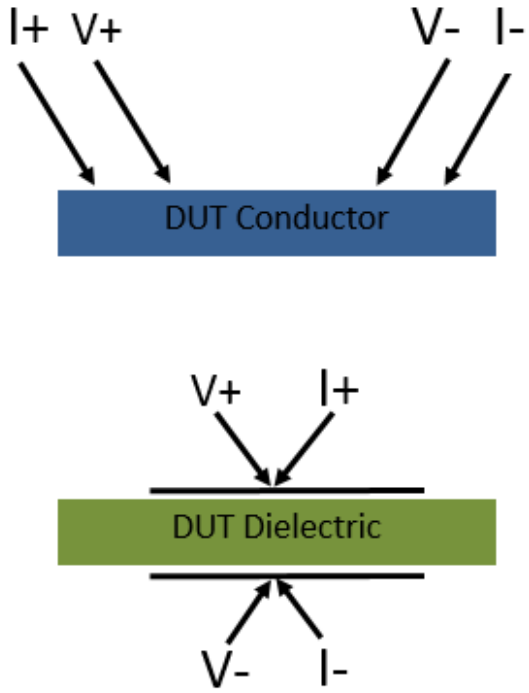

Figure 29 4-Point probe vs. 4-wire measurement

The capacitance of the disk will be slightly modified by stray capacitance around the edges of the disk and will not be accounted for in the parallel plate capacitor model. This stray capacitance is difficult to account for but, if a guarded electrode (Figure 30) is used, no stray capacitance will form but rather the newly-introduced capacitance will be accounted for during the fixture compensation step. The diameter of test materials should be much greater than the ID of the guard electrode and smaller than or equal to 56 mm. In practice, 50 mm works well.

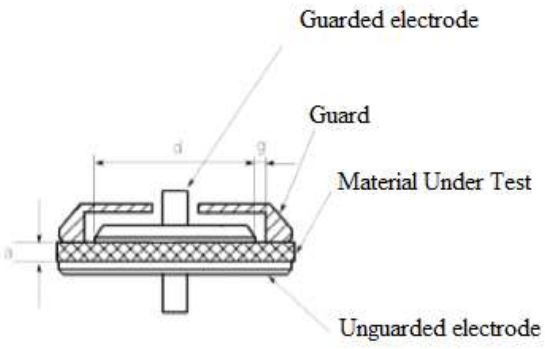

Figure 30 Dielectric test fixture with guard

Measuring the dielectric constant can be prone to error. Many factors, such as dimensional inaccuracies, air gaps, humidity, and calibration affect the measurement. Special care is taken to minimize as many of these effects as possible. Error analyses are carried out when possible in order to estimate the error present as well as to choose ideal sample dimensions which would minimize the total error. It should be noted that large standard deviations on the order of 100% exist in the measurement of the loss tangent; however, this is predicted by estimated errors of approximately the same magnitude. This is due to the high sensitivity in measuring low loss materials.

Estimated error equations are given for the Agilent E4980A Precision LCR Meter and Agilent 16451B Dielectric Test Fixture [75]. These equations are implemented in MATLAB so that the error may be estimated for any given combination of test conditions. A few interesting results of these estimated error equations are presented in plot form in the figures Figure 31 – Figure 34. Note that these plots have no relation to the measured data but illustrate the behavior of the estimated error using values close to those which are measured. Actual estimated error values for the measured data are provided in Table 23 and Table 25.

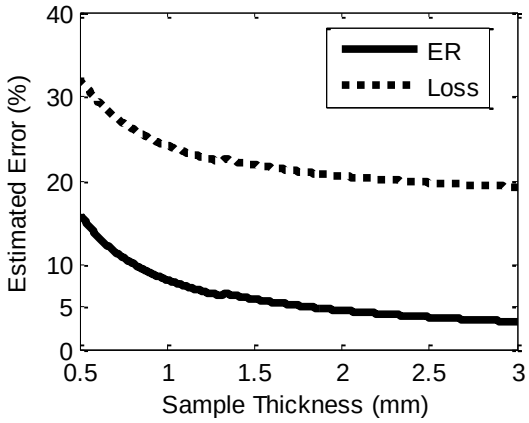

Figure 31 Estimated error in LCR meter measurement vs. sample thickness.

Solid line: estimated error in dielectric constant, er. Dashed line: estimated error in loss tangent. Condition: ε_r=3.5, tanδ=0.035, f=2 MHz, d=38 mm, Vs=1 V.

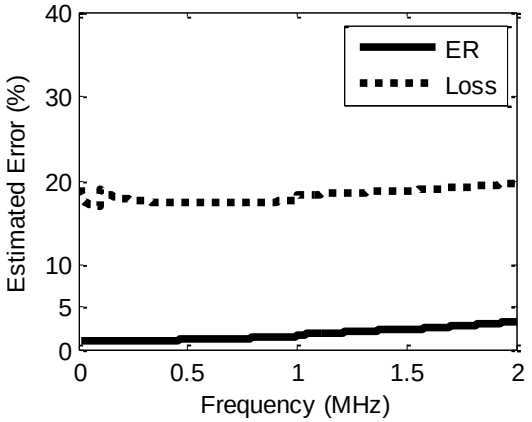

Figure 32 Estimated error in LCR meter measurement vs. frequency.

Solid line: estimated error in dielectric constant, er. Dashed line: estimated error in loss tangent. Condition: εr=3.5, tanδ=0.035, d=38 mm, t=3 mm, Vs=1 V.

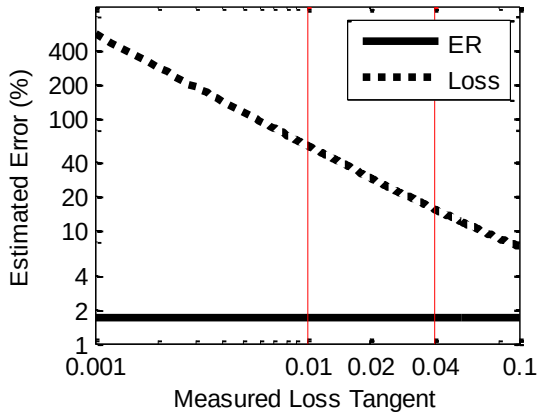

Figure 33 Estimated error in LCR meter measurement vs. loss tangent.

Solid line: estimated error in dielectric constant, ε_r. Dashed line: estimated error in loss tangent. Red lines indicate approximate measurement range. Condition: ε_r=3.5, f=1 MHz, d=38 mm, t=3 mm, Vs=1 V.

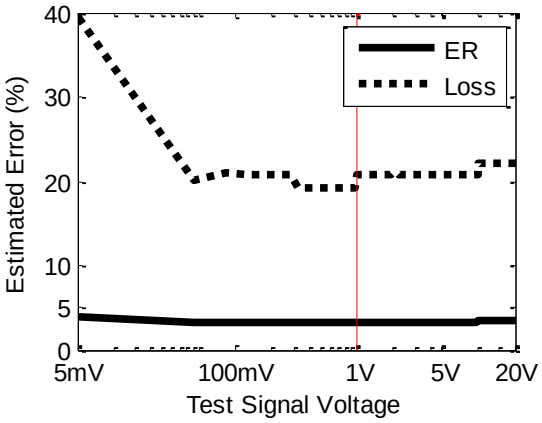

Figure 34 Estimated error in LCR meter measurement vs. test signal voltage.

Solid line: estimated error in dielectric constant, er. Dashed line: estimated error in loss tangent. Condition: ε_r=3.5, tanδ=0.035, f=2 MHz, d=38 mm, t=3 mm

Referring to Figure 31, thicker samples (t = 3 mm) allow for more accurate measurements. Referring to Figure 32, minimal variation in accuracy is expected in the

measurement range at 1 MHz and 2 MHz. Referring to Figure 33, in the range of loss tangent values from 0.01 to 0.04 the estimated error will be approximately 20% to 40%. The test signal voltage is chosen to be the maximum, 1 V, which optimizes the signal to noise ratio (SNR) of the measurement as determined from Figure 34.

Impedances on the order of 50 Ω – 50 kΩ ohms are preferred for accuracy [75] page B-1. Assuming dielectric constants on the order of 1.9 to 3.5, a sample thickness of 3 mm is selected so that the measured impedances range from 6.8 kΩ to 25 kΩ ohms from 1 – 2 MHz, thus falling within the preferred accuracy range. These values are summarized in Table 3.

Table 3 Capacitor impedances

Range	er	t	d	C	f	Z
High impedance	1.9	3 mm	38 mm	6.36 pF	1 MHz	25.03 kΩ
Low impedance	3.5	3 mm	38 mm	11.72 pF	2 MHz	6.79 kΩ

Estimated error equations are given in Agilent equipment documentation [75] and plotted against material thickness in Figure 31. Although the sample holder allows for samples up to 10 mm in thickness and error seems to reduce with increasing sample thickness, a thickness of 3 mm is selected so as to balance the error of the impedance analyzer which shows increased error with increasing sample thickness. Choosing a single sample thickness allows only one set of samples to be fabricated.

2.2.1. Air Gap Compensation in the Use of the LCR Meter, 1 MHz, 2 MHz

The given equations from the Agilent equipment documentation include inaccuracies internal to the equipment due to the cable length, and due to the sample holder geometry. There is an additional source of error, the uneven air gap between the sample and electrode. Samples cannot be manufactured with perfectly parallel faces resulting in a reduction in overall capacitance. In order to characterize this source of error the following model is used. The sample

is assumed to have non-parallel faces and the thickness is assumed to be thicker at one side than at the other (Figure 35). The effects of the fringe guard are removed via open/short compensation on the LCR meter and need not be considered.

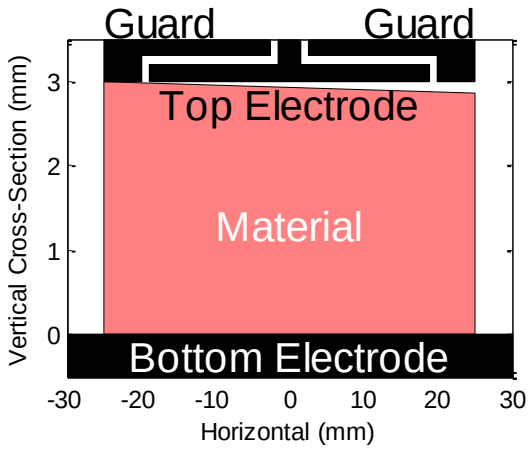

Figure 35 Diagram of air gap model for an uneven material sample.

A numerical summation is used to compute the actual capacitance of the uneven capacitor. The capacitor area is broken into N_x by N_y small squares and the capacitance of each square C_{sq} is summed to compute the total capacitance. The proper number of squares is determined by checking for convergence as shown in Figure 36 and Figure 37. N = 10,000 is used.

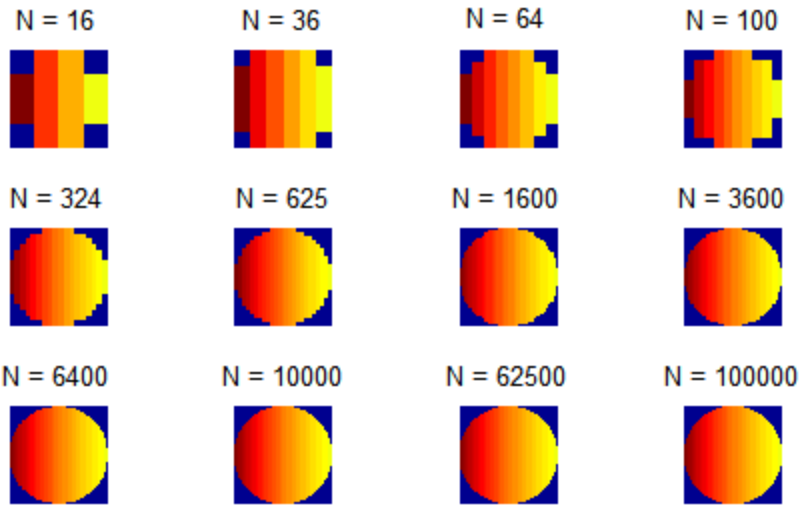

Figure 36 Variation of number of computation cells

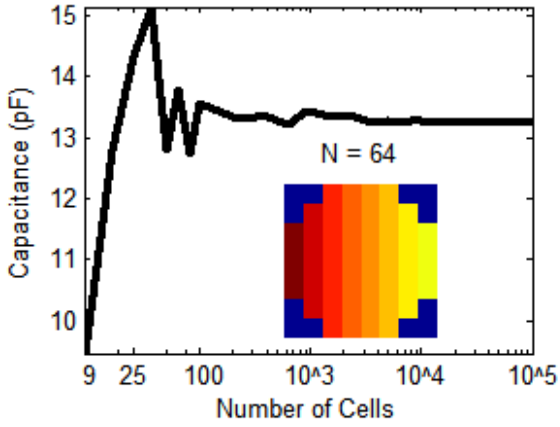

Figure 37 Convergence of number of cells

Condition: εr=3.5, t=3 mm, D=38 mm, gmax=0.15 mm. The inset is a sample model when N=64.

The capacitance contribution of each square is defined as:

$$C_{sq} = \begin{cases} \dfrac{\varepsilon_r \varepsilon_0 A}{t + \varepsilon_r g} & r < D/2 \\ 0 & r \geq D/2 \end{cases} \tag{15}$$

The area of each cell A is defined as:

$$\mathrm{A} = \frac{\mathrm{D}}{N_x}\frac{\mathrm{D}}{N_y} \tag{16}$$

T is the maximum measured sample thickness and g_{max} is the maximum gap. The air gap at each cell $g(x, y)$ and material thickness $t(x, y)$ are defined as:

$$g(x, y) = \frac{x + \frac{D}{2}}{D} g_{max} \tag{17}$$

$$t(x, y) = \mathrm{T} - g(x, y) \tag{18}$$

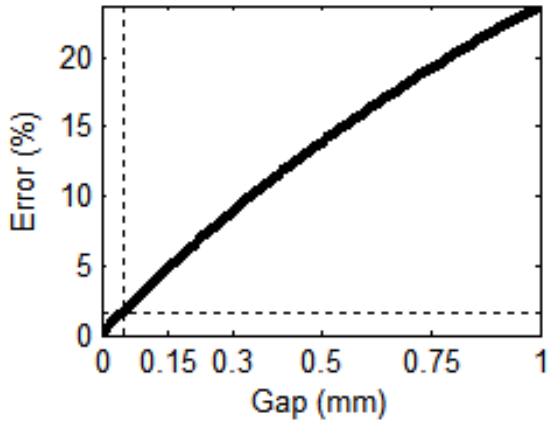

Figure 38 Estimated error in LCR meter measurement due to air gap.

Marker indicates 50 μm air gap. Condition: ε_r=3.5, t=3 mm, D=38 mm.

Referring to Figure 38, the maximum air gap of the samples fabricated is approximately 50 μm which adds about 1.68% additional error as compared against a sample without the air gap.

2.3. Method 2: Impedance Analyzer, 100 MHz – 1 GHz

An Agilent E4991A-002 impedance analyzer [78] with Agilent 16453A dielectric test fixture [79] is used to measure materials from 100 MHz to 1 GHz. This instrument works on a similar principle to the LCR meter. However, the computation of capacitance and loss tangent from the measured impedance is performed by software internal to the unit, which considers the fixture geometry automatically. Unlike the LCR meter, which uses a simple low-frequency current-voltage measurement technique, impedance measurement is performed using a radiofrequency current-voltage (RF-IV) method [49] p.2-16, [80]. The measurement setup is shown in Figure 39.

Figure 39 Dielectric test fixture

Estimated error equations are given in the Agilent equipment documentation for the Aglient E4991A RF impedance-material analyzer and Agilent 16453A dielectric test fixture [79] and are rewritten here.

$$err_{\varepsilon_r}(\%) = 5 + \left(10 + \frac{0.1}{f}\right)\frac{t}{\varepsilon_r} + 0.25\frac{\varepsilon_r}{t} + \frac{100}{\left|1 - \left(\frac{13}{f\sqrt{\varepsilon_r}}\right)^2\right|} \quad (19)$$

$$err_{\tan d}(\%) = 0.002 + \frac{0.001}{f}\frac{t}{\varepsilon_r} + 0.004f + \frac{0.1}{\left|1 - \left(\frac{13}{f\sqrt{\varepsilon_r}}\right)^2\right|} \quad (20)$$

Of particular note in Figure 40 is that the error in ε_r is 80% for frequencies around 10 MHz and is <20% on the range 100 MHz to 1 GHz. Additionally, the error in the loss tangent is so large that the values would be unusable. Thus only the values from 100 MHz to 1 GHz will be considered. The LCR meter separately provides more accurate data points at 1 MHz and 2 MHz. From Figure 41, the error in ε_r could be approximately half if the sample thicknesses are 0.4 mm vs. the 3 mm thicknesses used. Figure 42 illustrates that in the range of values of loss tangent, errors from 20% to 100% are to be expected and are intrinsic to the equipment which is used. This error would be less if either material with a larger loss tangent was being measured or a resonant method such as a split cylinder cavity was used.

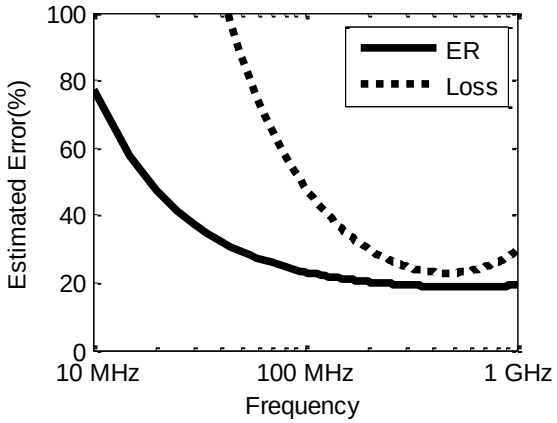

Figure 40 Estimated error in impedance analyzer measurement vs. frequency

Solid line: estimated error in dielectric constant, ε_r. Dashed line: estimated error in loss tangent. Condition: ε_r=2.5, tanδ=(arbitrary), t=3 mm.

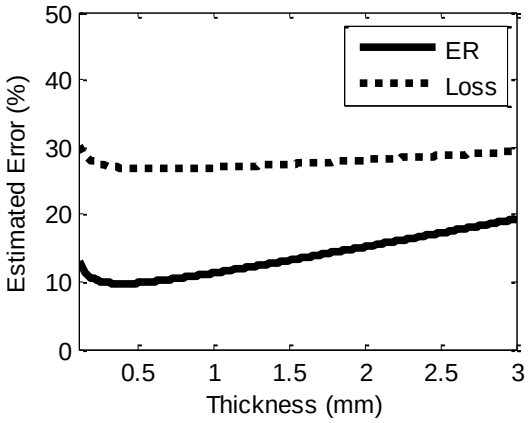

Figure 41 Estimated error in impedance analyzer measurement vs. sample thickness

Solid line: estimated error in dielectric constant, er. Dashed line: estimated error in loss tangent. Condition: ε_r=2.5, tanδ=(arbitrary) f=1 GHz.

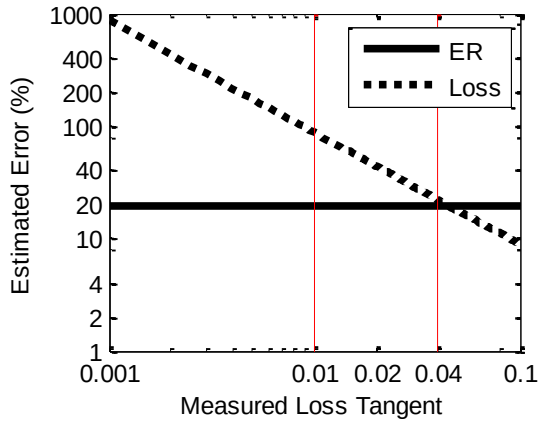

Figure 42 Estimated error in impedance analyzer measurement vs. loss tangent

Solid line: estimated error in dielectric constant, ε_r. Dashed line: estimated error in loss tangent. Thin vertical lines indicate range where actual materials fell. Condition: ε_r=2.5, f=1 GHz, t=3 mm.

2.4. Method 3: X-band Waveguide, 8.2 – 12.4 GHz

Material samples are fabricated to fit WR-90 waveguide designed for 8.2 – 12.4 GHz (Figure 43). TRL calibration is performed at the waveguide ports using a shorting plate and the ¼-wave (7.63 mm length) sample holder waveguide section. S-parameter data is taken using an Agilent N5245A PNA-X vector network analyzer and the Nicholson-Ross-Weir (NRW) method [70]-[74] is applied to extract the dielectric constant and loss tangent (Figure 44 and Figure 45). Certain waveguide sizes are readily available, their dimensions and required volume are given in Table 4. Samples in the R-band waveguide are not fabricated due to the large quantity of material that would be required. Samples in the Ku band are not fabricated due to the close dimensional tolerances that would be required.

Table 4 Waveguide dimensions

Band	Number	Frequency	Dimensions	Volume
Ku	WR 62	12.4 - 18.0 GHz	15.8x7.9x5.08	0.63 mL
X	WR 90	8.2 - 12.4 GHz	22.86x10.16x7.62	1.77 mL
R	WR 430	1.72 - 2.60 GHz	109x54.6x35.6	212 mL

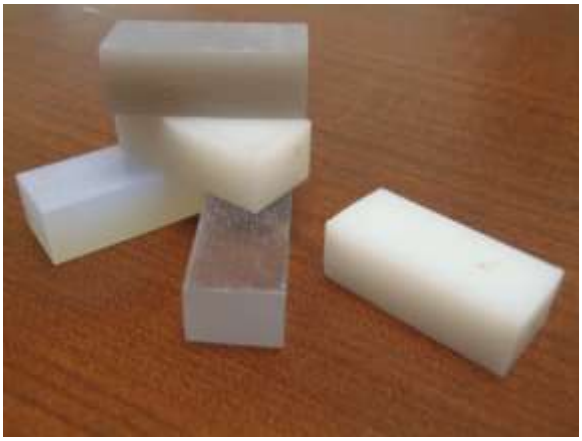

Figure 43 X-band waveguide material measurement samples

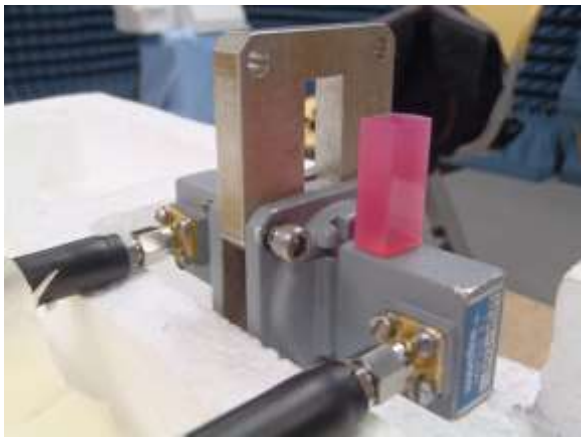

Figure 44 X-Band waveguide measurement setup

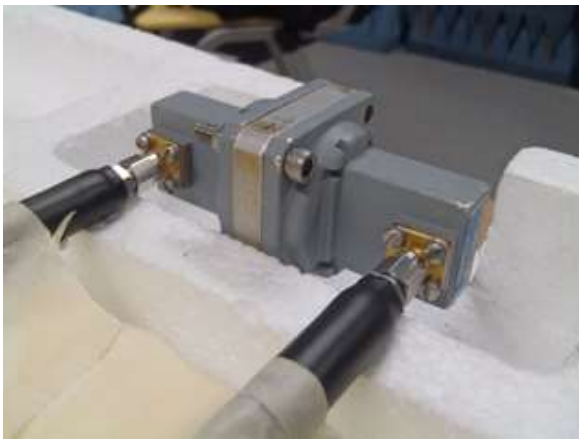

Figure 45 X-band waveguide measurement in progress

Samples tended to have an approximate dielectric constant of between 1.9 and 3.5. These materials are fabricated 7.63 mm thick to match a readily-available ¼ wavelength waveguide section. This results in an electrical length of approximately 1/2-wavelength in the frequency range from 11 – 12.4 GHz. It is known that when the sample thickness is close to ½-wavelength, the measured S-parameter data exhibits a singularity (near 100% transmission and 0% reflection) and the material parameters exhibit magnified errors [70][71]. In order to mitigate this effect, data in the range of 11-12.4 GHz is omitted from the results

A good error analysis of the Nicholson-Ross-Weir method is mentioned by Baker-Jarvis [70]; however, a simple implementation of this analysis is not available and is not implemented

here. Standard deviations of the sample sets are listed in Table 23 and Table 25 for frequencies from 8.2 – 11 GHz.

2.5. Fabrication

The W.M. Keck Center for 3D Innovation (the Keck Center) at the University of Texas at El Paso offers a broad selection of additive manufacturing technologies and materials. Materials and technologies are selected for measurement based on availability and estimated suitability for microwave device fabrication.

Fused deposition modeling (FDM) parts are fabricated by the Keck Center using a Stratasys, Ltd. FDM Titan and a T16 tip (406 μm) and 254 μm layer thickness. Three of the most common FDM-printable materials are printed in the Keck Center:

- Polycarbonate (PC) from Stratasys, Ltd.
- Acrylonitrile butadiene styrene (ABS) as Stratasys, Ltd. ABS-M30
- Stratasys, Ltd. PC-ABS blend

Stereo lithography (SL) parts are fabricated by Mahesh Tonde using a 3D Systems Viper si2, operated in high resolution mode, producing a layer thickness of 50.8 μm using a laser beam diameter of 76.2 μm. The following materials are printed at the Keck Center.

- Prototherm UV-cured
- Prototherm thermally-cured
- DSM Somos White
- Watershed 11122
- Additional SL materials are provided courtesy of DSM Somos:
- 9120
- 9420
- DMX-SL 100
- NanoForm 15120 UV-cured
- NanoTool UV-cured
- NeXT
- Prototherm UV-cured
- Watershed 11122

For capacitor-plate measurement, samples are fabricated as 50 mm × 50 mm × 3 mm plates (Figure 46 – Figure 49). Light sand papering and razor blade scraping is performed to remove only the largest FDM surface aberrations and SL support marks. For X-band waveguide measurement, samples are fabricated slightly oversized and CNC machined to 7.63 mm × 10.06 mm × 22.60 mm chunks. Each chunk is machined and sanded to fit as precisely as possible in the X-band waveguide sample holder in order to minimize air gaps near the waveguide walls.

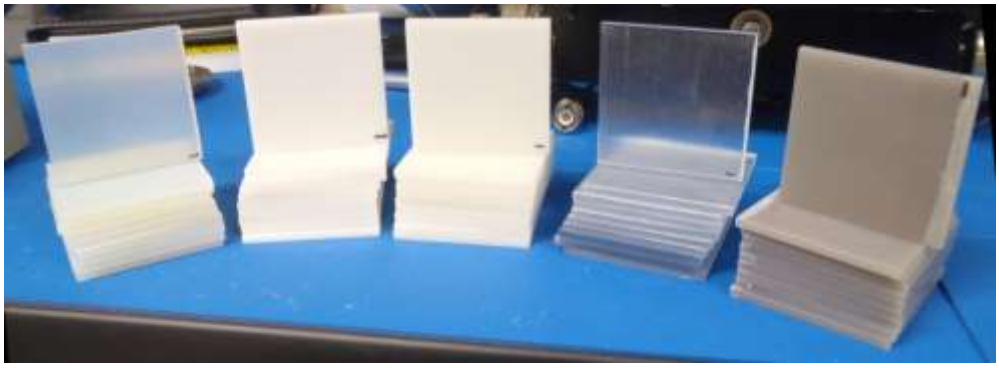

Figure 46 Low frequency material measurement samples

Figure 47 ProtoTherm, left: UV-cured, right: UV-cured and thermal post-cured

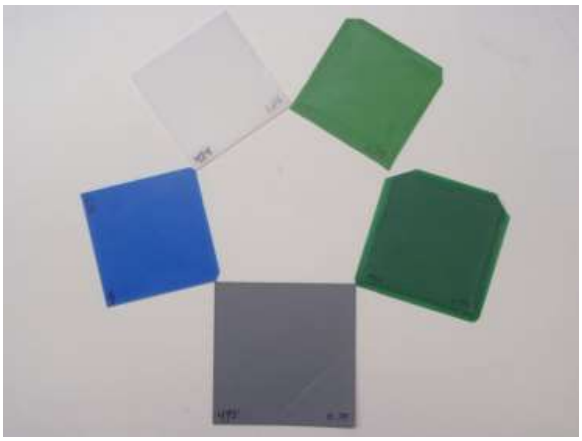

Figure 48 Variation in color

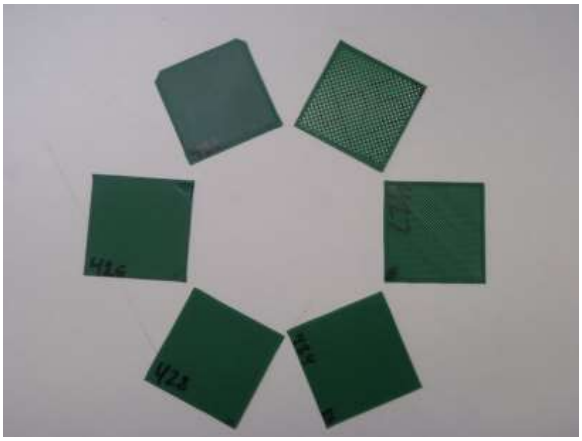

Figure 49 Variation in infill percentage

2.6. Materials Measurement Results

Measurements of the aforementioned samples is performed using the measurement methods discussed. Full data tables are provided in Appendix B and a summary is provided in Table 5. An important consideration when choosing a material for RF and microwave circuits is the amount of loss that the material introduces. It is determined that materials printed using thermoplastics and FDM technology are invariably lower-loss than photopolymer-based (resin- or epoxy-based) SL-printed materials. SL offers much higher precision and smoother surface finish than FDM which is important in fabricating microwave devices. There are, however, a few SL materials which show comparable loss to industry-standard FR-4 printed circuit board

material. Thus SL may offer an exciting alternative to FR-4 when the flexibility of 3D devices (vs. the planar nature of FR-4) is considered. FDM does offer lower loss in applications which are less concerned about resolution and smooth surface finish.

Material	Advantage	Technology	Avg. Dielectric Constant	Loss tangent
Alumina	Not printable	Raw	10.8	0.0003
PTFE	Not printable	Raw	2.1	0.0003
ABS	Easy to print	FDM	2.7	0.007
Ultem	Space-rated, high temp	FDM	2.7	0.004
PC	Avail. @ UTEP	FDM	2.8	0.007
NanoTool	High temp., higher K	SL	3.5	0.011
Watershed	High res.	SL	3.2	0.032
Prototherm	High temp. & high res.	SL	3.3	0.038

Table 5 Dielectric data summary

Certain applications demand a high dielectric constant in order to achieve miniaturization in wavelength-dependent structures. For these applications, SL materials may be the better option as shown in Table 22. NanoTool and NanoForm incorporate nanoparticles of alumina ceramic [35] which are known to have a high dielectric constant and low loss. New materials are being developed by adding higher concentrations or different types of ceramic [81][82] to the material in order to raise the final dielectric constant while at the same time substituting lossy photopolymer for ceramic nanoparticles. The concept of printed and sintered ceramic has been shown to be viable [27]-[38],[39].

Based on the measurements which are performed, 3D printed materials are viable options in future RF and microwave devices. If the dimensional properties of FDM can be tolerated or mitigated, it offers great promise. Otherwise, materials such as NanoTool actually offer lower loss than industry-standard FR-4.

2.7. Method 4: Resonant Cavity Measurement

Resonant cavity measurement allows for better accuracy than most other methods and obtains both dielectric constant and loss tangent at several discrete frequency points. The equations governing the cavity are fairly simple; however, numerical methods must be used to determine the values to a high level of accuracy. Essentially a resonant mode is set up in the cavity reflecting back and forth through the cavity and the material under test (MUT). The empty cavity resonant frequencies and cavity loss are first determined then the MUT is loaded. The shift in frequency at each resonance and material thickness leads to the dielectric constant and the delta in loss and material thickness leads to the loss tangent. Fortunately, 'Cavity' computer software from Damaskos, Inc. determines the values automatically using a VNA on a GPIB interface. Each sample measurement requires about ten minutes and returns data points as shown in Table 6 with the actual frequencies determined by the material thickness and dielectric constant as well as the cavity dimensions.

Table 6 Cavity measurement equipment

Cavity Model	**Approx. Freq. Range**	**Data Points**
Damaskos, Inc. 125HC	0.4 GHz to 5.2 GHz	0.4, 1.2, 2, 2.8, 3.6 GHz
Damaskos, Inc. 015	4 GHz to 15 GHz	4.4, 6.7, 9.9, 13.3 GHz

Samples should be 50 mm diameter discs or 50 mm x 50 mm square samples up to 1 mm in thickness with a preference towards thinner samples especially for lossy materials such as SL resins. Thickness should not be so thin that imperfections in thickness are not on the order of the average thickness, but not so thick that too much energy is dissipated in the sample which would obscure the determination of the resonant peaks. The measurement setup is shown in Figure 50 and Figure 51.

Figure 50 Cavity measurement, 0.4 to 5.2 GHz

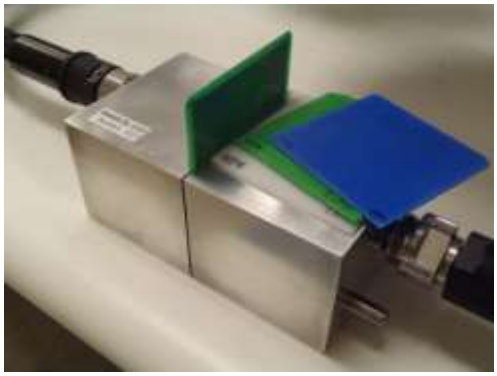

Figure 51 Cavity measurement, 4 to 15 GHz

Measurements using the resonant cavity are performed on several printed samples of ABS printed by the author using an nScrypt, Inc. 3Dn-600 machine and the dielectric constant is shown in Figure 52. The infill density is varied from 25% to 100% and several solid samples in different colors of ABS are measured. Variation occurs in the data in the transition from the 125HC cavity to the 015 cavity due to error.

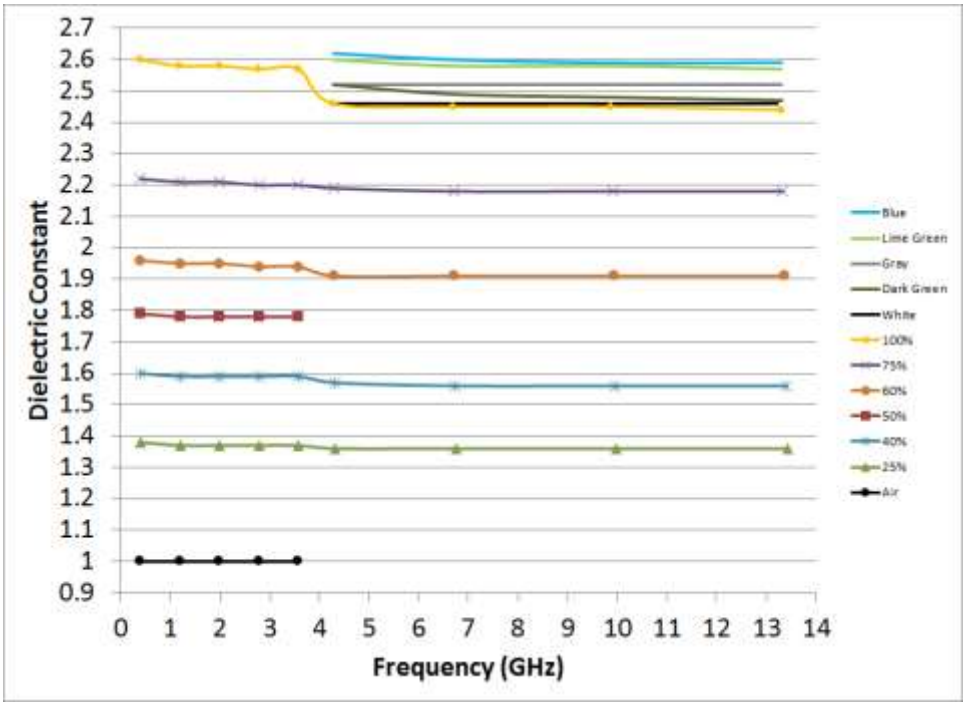

Figure 52 Dielectric constant results from cavity

Several colors of ABS are measured using the resonant cavity. Table 7 describes each sample, Figure 53 shows the dielectric constant and Figure 54 shows the loss tangent. In order to easily design successful RF and microwave devices and circuits, it is important to characterize the specific material which is to be used. Some variations between manufacturers and colors are shown here.

Table 7 ABS colored samples

Color	Source	Machine, Filament, Nozzle, Layer	Appearance
White	Stratasys, Ltd. ABS	Stratasys, Ltd. Dimension 3 layers ×254 µm = 762 µm Printed by USF CoE	Rough, porous fill
Gray	Stratasys, Ltd. ABS	Stratasys, Ltd. Dimension 3 layers ×254 µm = 762 µm Printed by USF CoE	Rough, porous fill
Dark green	MakerBot	3Dn-600 1.75 mm filament 0.4 mm J-Head nozzle 0.1 mm layers 8 layers ×100 µm = 800 µm Printed by the author	Smooth, dense
Lime green	UltiMachine	3Dn-600 1.75 mm filament 0.35 mm E3D nozzle 8 layers ×100 µm = 800 µm Printed by the author	Smooth, dense
Blue	UltiMachine	3Dn-600 1.75 mm filament 0.25 mm E3D nozzle 8 layers ×100 µm = 800 µm Printed by Sciperio, Inc	Smooth, dense

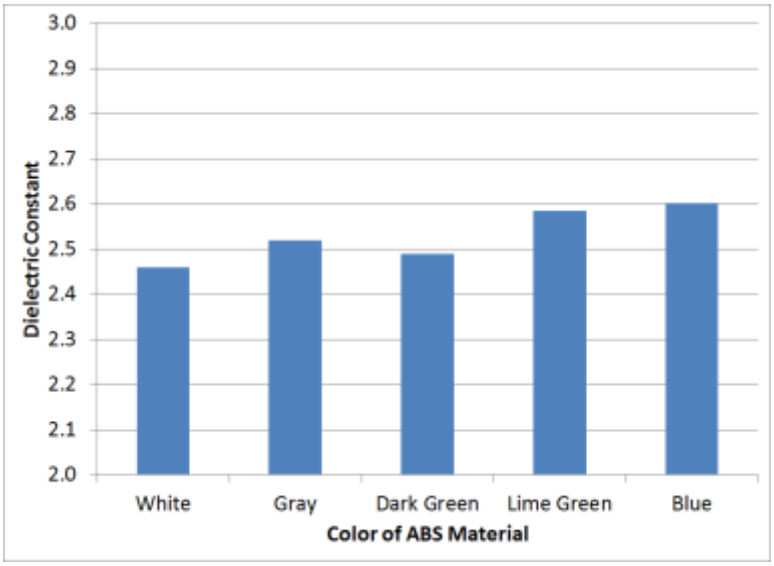

Figure 53 ABS dielectric constant vs. color

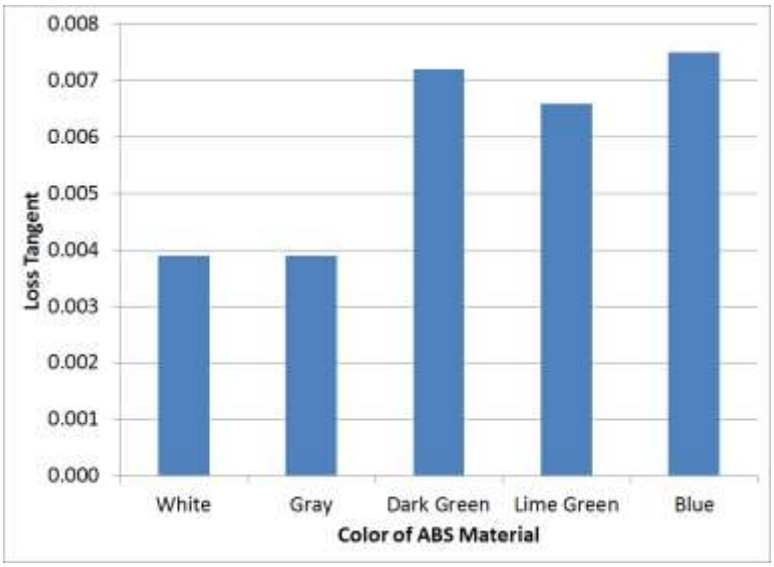

Figure 54 ABS loss tangent vs. color

As the infill density is adjusted from 0 % (air) to 100% (solid) the dielectric constant and loss tangent are seen to vary as shown in Figure 55. Variable infill density has long given mechanical designs the opportunity in 3D printing to save weight, material cost, and machine time while maintaining a configurable amount of strength. Now, it is shown that varying the infill density allows RF and microwave designers the opportunity to select a specific dielectric constant for a bulk material.

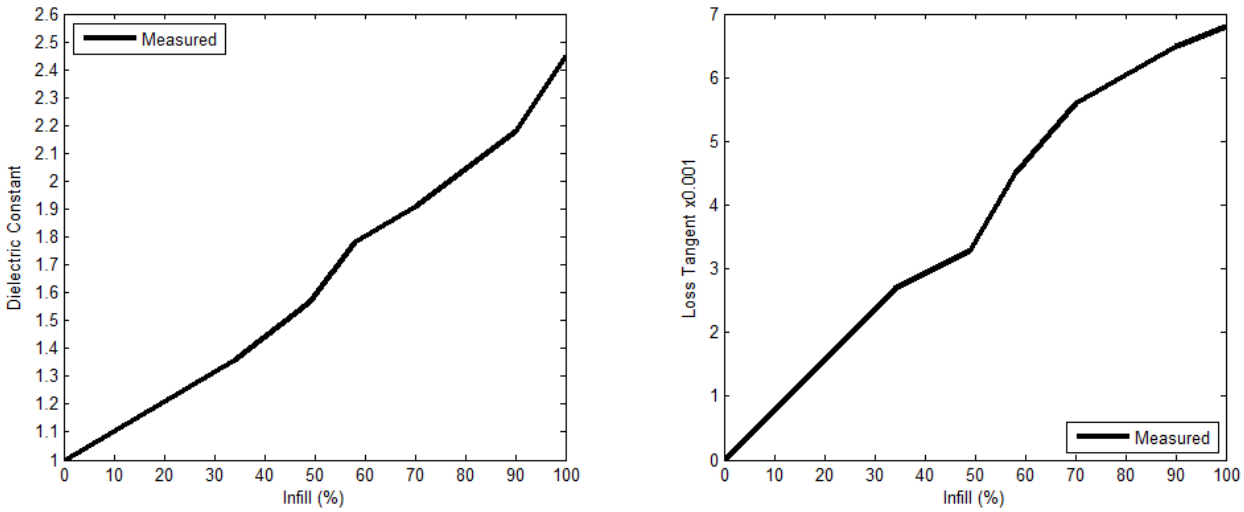

Figure 55 Measurement of 3D printed ABS with varied infill density

2.7.1. Effective Medium Theory

Effective medium theory seeks to describe the overall properties of a multi-component material based on the properties of its constituent materials. Several effective medium theory approximation equations are used to compare measured data against, see Table 8. Material '1' is considered to be the printed ABS which is not fully dense allowing air (material '2') to exist within the sample.

Table 8 Effective medium theory variables

Symbol	Material
f	Filling fraction
ε_{r1}	ABS
ε_{r2}	Air
$\varepsilon_{min}, \varepsilon_{max}$	Wiener Bounds
ε_M	Maxwell
ε_{MG}	Maxwell-Garnett / Clausius-Mossotti
ε_B	Symmetric Bruggeman
ε_{ABG}	Asymmetric Bruggeman
ε_L	Looyenga

In order to generate the machine instructions for each sample with a different infill percentage the slicing program (Slic3r) is programmed accordingly. However, due to extrusion tolerances the actual infill percentage realized varies significantly. Factors which contribute to this are extrusion temperature and speed, printing speed, liquid polymer rheology, dispensing height and width, and backpressure due to the quantity of material already deposited on the surface. Most of these are calibrated out but some variation remains. In order to accurately account for these phenomena, the samples are measured using calipers and weighed on a balance to determine the exact amount of material present in each sample. Table 9 shows the results of this process. Figure 56 shows the effective dielectric constant and loss tangent against several effective medium approximations which are individually derived later.

Table 9 Infill calculations

Design Infill Density (%)	Actual Infill Density (%)	Volume (mL)	Weight (g)	Measured dielectric constant
Air	0%	0	0	1.000
25%	34%	1.949	0.6635	1.359
40%	48%	1.955	0.9463	1.565
50%	58%	1.962	1.1387	1.782
60%	70%	1.880	1.3069	1.909
75%	90%	1.718	1.5465	2.182
100%	100%	1.969	1.9550	2.450

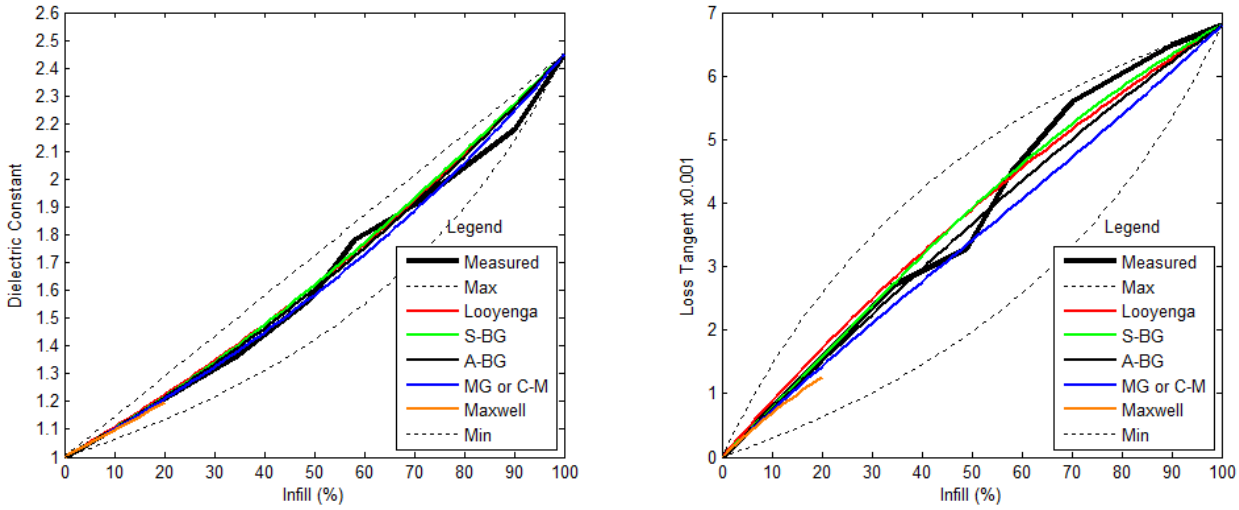

Figure 56 Effective medium theory and measured data

Chapter 3: Transmission Lines

It has been demonstrated that the loss tangent of printed materials is acceptable for their incorporation in RF/microwave designs [91],[92],[93]. In general, fused deposition modeling (FDM) can utilize materials with low microwave loss but produces poor print resolution and a rough surface finish, while stereolithography (SL) exhibits excellent resolution and a smooth surface finish but the materials have more loss. No other known work has been done to date which uses thick film silver paste and 3D printed SL material in a microwave application.

Modern electronics rely heavily on wireless technology and any new electronics fabrication technology such as 3D printing must handle microwave electronics. Transmission lines are the building blocks of microwave circuits [94]-[126]. This study [1] models and measures the performance of SL and a conductive thick film paste at DC and microwave frequencies in a microstrip structure. Basic transmission line parameters such as characteristic impedance, effective dielectric constant, dielectric loss, and conductor loss are modeled and measured for a variety of materials and techniques at frequencies up to 10 GHz. Microstrip and stripline transmission lines fabricated using 3D printing equipment are comparable in performance to similar transmission lines fabricated using traditional methods, but using less expensive materials. The SL resin ProtoTherm is seen to have a loss tangent of 0.03 and the conductive paste is seen to have an RF resistivity of 500 μΩ•cm. Although these values are higher than conventional microwave circuit materials, 3D printing brings extreme flexibility in design [127] and circuit layout which cannot be realized in a planar stack-up and it is these avenues for improvement which should bring 3D printing to microwave circuit design.

Four different microstrip transmission line samples are fabricated: printed paste on printed substrate, copper tape on printed substrate, copper foil on standard RF board material and

printed paste on a standard RF board material (Figure 59 – Figure 62) [128]. An additional set of ten printed squares are fabricated in order to measure DC resistivity.

Finally, the surface finish of FDM is improved sufficiently to allow its use in microwave transmission lines. A machine is constructed which allows deposition of both thick film silver paste and ABS plastic and a stripline structure is fabricated on this one machine resulting in a measured loss tangent of 0.012 and RF resistivity of 44 μΩ•cm.

3.1. Stereolithography

SL parts are fabricated by Keck Center technicians using a 3D Systems Viper si2, operated in high resolution mode, producing a layer thickness of 50.8 μm using a laser beam diameter of 76.2 μm. Samples are printed on top of a 125 μm sheet of polycarbonate in order to eliminate support marks and to preserve a high quality bottom surface. Sample dimensions are 50 mm long by 30 mm wide by 0.8 mm thick. A convergence model is made in the appendix which validates that the substrate width is adequate. The Viper si2 uses a 354.7 nm laser. Table 10 shows a material study of several types of SL material.

Table 10 Material study

Material	**Tg**	**tan δ @ 1 GHz**
9120 Epoxy	N/A	0.0402
9420 EP White	41 °C	0.0406
DMX-SL 100	37 °C	N/A
NeXT	43-47 °C	0.0274
Prototherm 12120 UV	74 °C	0.0205
Prototherm 12120 Th	111 °C	0.0333
NanoForm 15120 UV	39 °C	0.0225
NanoForm 15120 Th	80 °C	N/A
NanoTool	86 - 89 °C	0.0122
Watershed 11122	39 - 46 °C	0.0253
White 14120	44 °C	0.0265

DSM Somos ProtoTherm 12120 resin with thermal post-cure is used for its higher temperature capability among SL-compatible resins (111 °C glass transition temperature). The thermal post-curing process which is used is given here:

1. Clean with TPM.
2. Bake at 60 °C for 1 hour.
3. UV cure for 30 minutes per side.
4. Ramp to 160 °C at 1 °C/min.
5. Bake at 160 °C for 2 hours.
6. Ramp down to 25 °C at 1 °C/min.
7. Remove from polycarbonate sheet.

The higher glass transition temperature allows printed conductors to be cured more thoroughly thus reducing the bulk resistivity. Typical resins such as DSM Somos WaterShed have a glass transition temperature of only 41 °C and are used more commonly for their optical transparency or lower cost.

3.2. Direct Print Additive Manufacturing

Silver paste is used in microwave circuits currently and some related literature is available [195],[128]-[139]. An nScrypt, Inc. 3Dn-Tabletop direct print machine is used to apply DuPont CB028 thick film silver paste onto the printed substrates (Figure 57). On ProtoTherm,

the paste layers are 41 μm thick and the signal traces are 1.84 mm wide. On Rogers RT/Duroid 5870 the paste layers are 27 μm thick and the signal traces are 2.15 mm wide. Curing is performed at 100 °C. One sample is prepared by applying 3M 1181 HD copper tape ("1-ounce" 26 μm dead-soft annealed copper on 40 μm conductive backing) onto ProtoTherm (Figure 60) which has a final measured thickness of 68 μm including the annealed copper and the conductive adhesive. An additional set of samples of DuPont CB028 is printed using an nScrypt, Inc. 3Dn-600 HPx with dimensions 8 mm x 8 mm x 10 μm on polyamide substrates. The samples are cured at various temperatures and the DC sheet resistivity is measured.

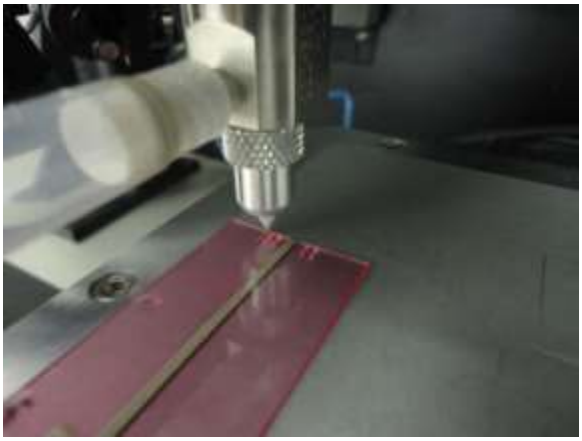

Figure 57 nScrypt, Inc. 3Dn-tabletop printing

3.3. Comparison Sample Preparation

Comparison samples are fabricated on Rogers RT/Duroid 5870 high frequency laminate that are 50 mm long by 30 mm wide by 0.762 mm thick (Figure 58). Standard "1/2-ounce" copper cladding is used which is 17 μm thick and measured to be 19 μm thick. Masking and FeCl etching is performed to pattern the signal trace and SMA pads on the top surface while retaining a solid ground plane on the bottom (Figure 61). An additional sample is prepared by etching off all of the copper cladding and printing thick film silver paste (Figure 62).

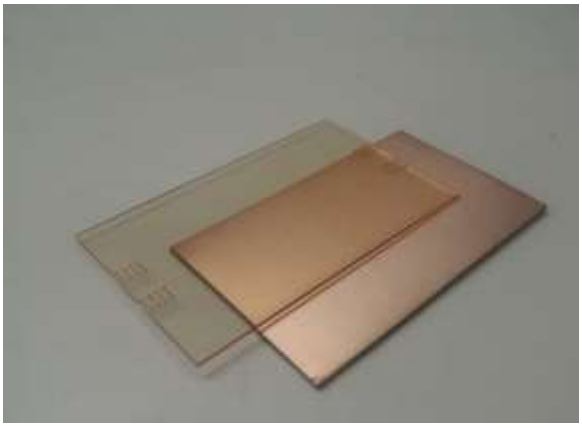

Figure 58 SL and copper-clad Rogers 5870

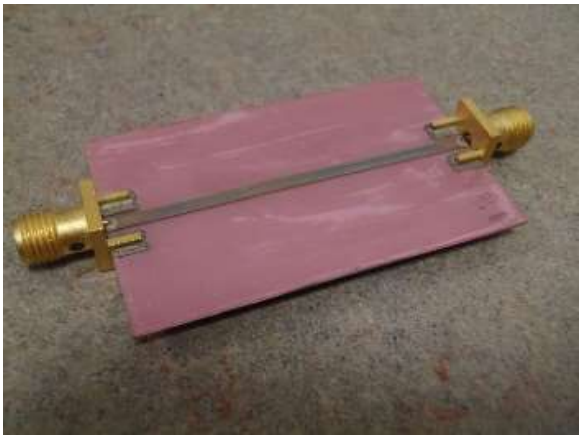

Figure 59 CB028 on ProtoTherm

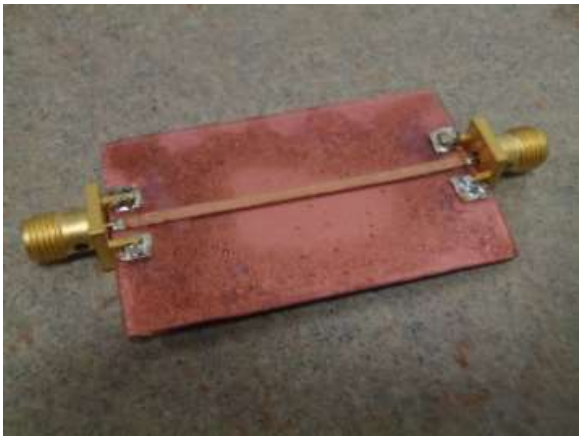

Figure 60 Copper on ProtoTherm

Figure 61 Copper on Rogers 5870

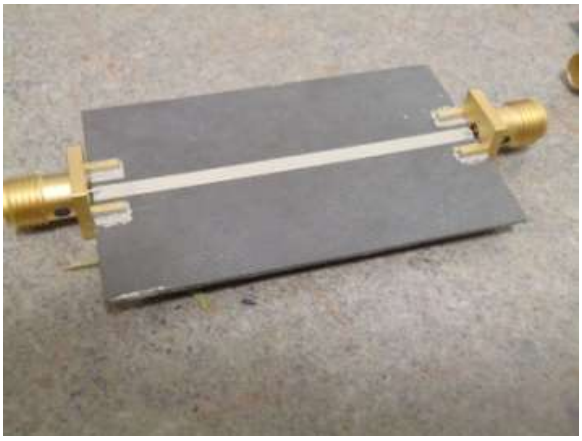

Figure 62 CB028 on Rogers 5870

GigaLane PSF-S01-008 SMA launches, specified up to 26.5 GHz, are either soldered (in the case of Cu conductors) or glued using EPO-TEK H20e conductive epoxy (in the case of printed conductors) (Figure 63). A pattern of twelve 457 μm-diameter vias beneath each arm of the SMA connector are provided.

Figure 63 SMA launch to CB028 paste

3.4. Modeling

Modeling of these microstrips proceeds in two ways, final parameter comparison and parameter back-calculation. Final parameter comparison involves modeling the entire device in a full wave simulator and adjusting the model until the S-parameters match the measured values closely. This is the easiest and most commonly-used method. Parameter back-calculation is less commonly used but offers insight into devices comprised of multiple unknown materials. See Appendix A – Appendix M for details. Connector removal is important in back-calculation [140] thus ANSYS HFSS is used to model the SMA connector to microstrip transition for the purpose of connector removal in the MATLAB analysis and to model the overall performance of the microstrip lines. Parameter extraction equations are implemented in MATLAB R2013a to process the microstrip data which are gathered by the VNA or produced by HFSS. The HFSS model of the SMA connector to microstrip transition is represented as T-parameters, and matrix division is used to effectively remove the effects of the transitions from the measured data (Figure 63 and Figure 64).

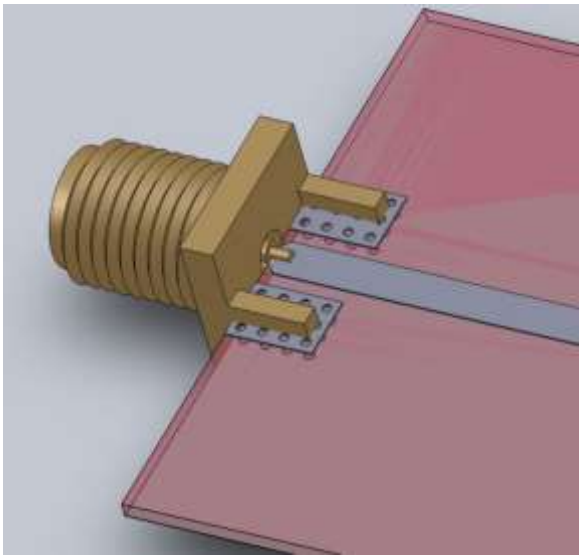

Figure 64 HFSS Model

The Nicholson-Ross-Weir method [70]-[74] is used to obtain propagation coefficient (P) from measured S-parameters. Equations 1-5 are used. Variables are described in Table 11.

$$\chi = \frac{{S_{11}}^2 - {S_{21}}^2 + 1}{2S_{11}} \tag{21}$$

$$\Gamma = \chi \pm \sqrt{\chi^2 - 1} \tag{22}$$

$$P = \frac{S_{11} + S_{21} - \Gamma}{1 - (S_{11} + S_{21})\Gamma} \tag{23}$$

$$Z_c = Z_0 \frac{1 + \Gamma}{1 - \Gamma} \tag{24}$$

$$\gamma = -\frac{1}{l}(lnP + i[\angle P - 2\pi N]) \quad N \in \mathbb{N} \tag{25}$$

Branching occurs in the solution of the propagation constant, thus the correct value of N can be observed graphically by requiring that the y-intercept of the wave number vs. frequency must be zero. According to Weir, the integer term N is understood to be the integer number of

wavelengths residing in the sample of thickness l in the rectangular waveguide. In order to determine *N*, a guess is made at the effective index of refraction, n_{guess}.

$$N = Round\left(\frac{n_{guess} f l}{c_0}\right) \tag{26}$$

$$\gamma = \alpha_T + j\frac{2\pi f\sqrt{\varepsilon_e}}{c_0} \tag{27}$$

The propagation coefficient yields both overall transmission line loss and effective permittivity. Nonlinear regression is used to determine the coefficients A and B in order to separate the dielectric loss and conductor loss. All of the variables used in this derivation are listed in Table 11.

$$\alpha_T = \alpha_d + \alpha_c = Af + B\sqrt{f} \tag{28}$$

The loss tangent follows equation 1 [141].

$$tan\delta = \frac{1}{27.3}\alpha_d\lambda_0\frac{(\varepsilon_r - 1)}{\varepsilon_r}\frac{\sqrt{\varepsilon_e}}{\varepsilon_e - 1} \tag{29}$$

Sheet resistivity is determined according [110]. Note that for compactness of notation, $r = \left(\frac{w}{h}\right)_{eff}$. th is the conductor thickness, width is the signal trace width, h is the substrate height.

$$r = \begin{cases} \frac{w}{h} + 1.25\frac{th}{\pi h}\left(1 + ln\left(\frac{4\pi w}{th}\right)\right) & \left(\frac{w}{h}\right) \leq 0 \\ \frac{w}{h} + 1.25\frac{th}{\pi h}\left(1 + ln\left(\frac{2h}{th}\right)\right) & \left(\frac{w}{h}\right) > 0 \end{cases} \tag{30}$$

$$B = \begin{cases} h & \left(\frac{w}{h}\right) \geq \frac{1}{2\pi} \\ 2\pi w & \left(\frac{w}{h}\right) < \frac{1}{2\pi} \end{cases} \tag{31}$$

$$A = 1 + \frac{1}{r}\left(1 + \frac{1}{\pi} ln\left(\frac{2B}{th}\right)\right) \tag{32}$$

$$R_s = \begin{cases} \frac{\alpha_c h Z_C}{1.38 \times A}\left(\frac{32 + r^2}{32 - r^2}\right) & \left(\frac{w}{h}\right) \leq 1 \\ \frac{\alpha_c h \varepsilon_e A}{6.1 \times 10^{-5} Zc}\left(r + \frac{0.667r}{1.444 + r}\right)^{-1} & \left(\frac{w}{h}\right) > 1 \end{cases} \tag{33}$$

Resistivity follows:

$$\rho = \frac{{R_s}^2}{\pi f \mu_0} \tag{34}$$

Table 11 Mathematical variables

Variable	Description
f	Frequency
λ_0	Free space wavelength
c_0	Speed of light
S_{11}, S_{21}	S-parameters
l	Transmission line length
w	Signal trace width
h	Substrate height
th	Signal trace metal thickness
Z_C	Characteristic impedance of transmission line
Z_0	Reference impedance
N	Integer
P	Single interface propagation coefficient
Γ	Single interface reflection coefficient
α_T	Total loss
α_d	Dielectric loss
α_c	Conductor loss
$tan\delta$	Loss tangent
ρ	Resistivity
R_s	Sheet resistivity
j	$\sqrt{-1}$
γ	Propagation coefficient
ε_e	Effective permittivity in a transmission line
ε_r	Dielectric constant or permittivity of a material

3.5. Error Mitigation

Measuring transmission lines using a VNA is prone to error. Many factors, such as dimensional inaccuracies, humidity (these materials are hygroscopic), minor connector attachment differences, and VNA calibration, affect the measurement. Special care is taken to minimize as many of these effects as possible. Measurements are performed at 25 ± 2 °C and 40 ± 10 %RH.

Errors in the computation of characteristic impedance occur when the electrical length of the line is a multiple of ½ wavelength. These errors are well-documented [71] and various methods exist to correct them. In this work the errors in characteristic impedance and loss

coefficient are minimized by using a linear interpolation to fill in the regions of high uncertainty, when the phase of the measured S21 is {0, 90, 180, 270} ± 30 °.

3.6. Resistivity Measurement

Accurate resistivity measurements are crucial in selecting and developing the best materials for 3D printing. Details are provided in Appendix N which allow easy conversion between the sometimes confusing units of resistivity and conductivity. Two primary types of resistivity measurement are available: direct linear four-point probe and four-point van der Pauw. In the first method, a simple linear four-point contact system is used where current is induced in the line through the outer two connections and the voltage drop is measured using the accurately spaced inner connections as shown in Figure 65.

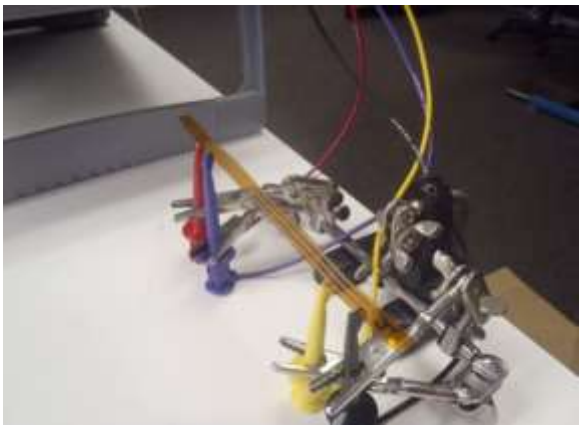

Figure 65 Resistivity measurement

3.7. Low Current Resistivity Measurement

The DC resistivity of inks has been measured previously [142]-[144]. The resistivity of the conductive paste is measured using the van der Pauw method. Samples are fabricated of a uniform thickness across an 8 mm x 8 mm square area as shown in Figure 66. Probes are attached at the corners of the sample and the current and voltage orientations are rearranged and the results averaged in order to remove additional error sources from the wiring. An Ecopia

HMS-5000 Hall Effect Measuring System is used with the SPCB-00 measurement head at a temperature of 25 °C. The hall effect [144] measurement option is not used since the samples are good conductors and not semiconductors. The current delivered is 15 mA.

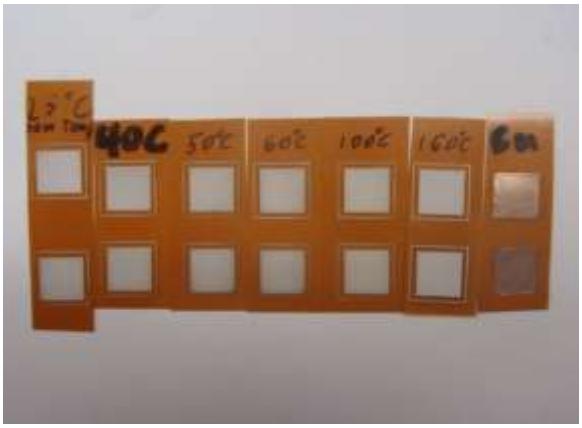

Figure 66 Van der Pauw Measurement Samples

The van der Pauw method [144]-[147] works as follows. At least two measurements are made by inducing current across terminals A and B and the voltage is measured across terminals C and D then the measurement is rotated 90 degrees and the current is induced across terminals B and C and the voltage is measured across terminals A and D. The conductor thickness 'd' must be measured and the material resistivity is computed using an iterative numerical method since the van der Pauw equation cannot be solved directly.

$$R_{AB,CD} = \frac{V_{CD}}{I_{AB}} \tag{35}$$

$$R_{BC,AD} = \frac{V_{AD}}{I_{BC}} \tag{36}$$

$$e^{-\left(\pi\frac{d+R_{AB,CD}}{\rho}\right)} + e^{-\left(\pi\frac{d+R_{BC,AD}}{\rho}\right)} = 1 \tag{37}$$

The actual thickness is measured using an AlphaStep IQ surface profiler (profilometer) and is used to compute resistivity, shown in Figure 67. Data sheet minimum and maximum

values are included in the figure along with the value for copper. It can be seen from the data that CB028 achieves a low resistivity, close it its minimum value at a cure temperature of just 100 °C. One alternative considered for use is ohmic curing of the conductor [148]. This method involves inducing a current in the conductor thus dissipating enough power sufficient to achieve a temperature for curing. The amount of current required for the width and height of the printed line precluded the use of this method.

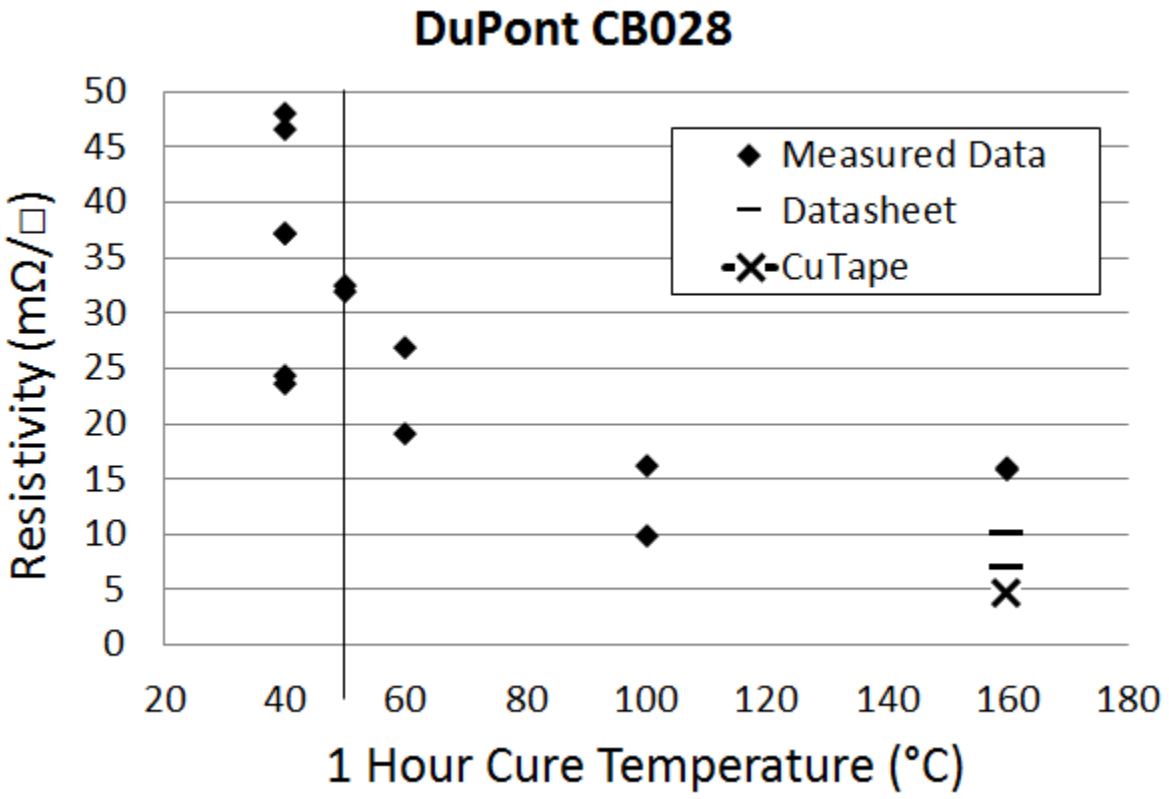

Figure 67 CB028 resistivity vs. cure temperature

An AlphaStep IQ surface profiler (profilometer) is used to measure the transmission line cross section and MATLAB is used to mathematically approximate the line width and height. The final data is shown in Table 12. The data from the profilometer have two primary shortcomings, tilt and bow. Tilt is caused by imprecisely aligned x-stage and is easily

compensated for in the AlphaStep software. Bow is caused by imprecisely aligned scan mechanisms and is compensated for using a circular arc offset applied at all points. It is desirable to determine the approximate width and height of the transmission line for modeling. A 10^6-point histogram is generated from the profile data. Two peaks stand out, one at the lower end and one at the higher end. The maximum of each peak gives the average height of the line and height of the substrate. The derivative $\frac{dh}{dw}$ (h=height, w=width) is taken at every point and processed using a 41-point moving average. The maximum and minimum of this dataset give the locations of the left and right edges of the width of the transmission line. These values are shown in Figure 68 – Figure 73 in red vertical lines.

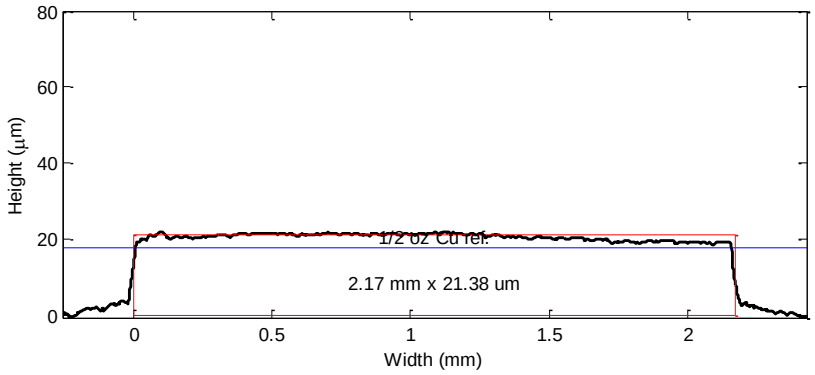

Figure 68 Profilometry data of Copper on Rogers 5870

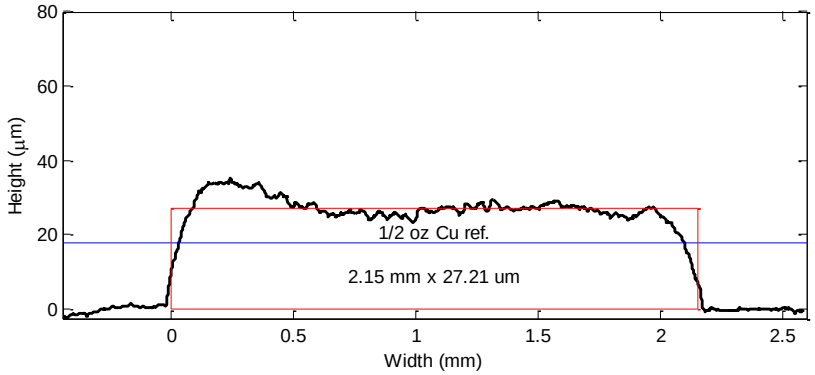

Figure 69 Profilometry data of CB028 on Rogers 5870

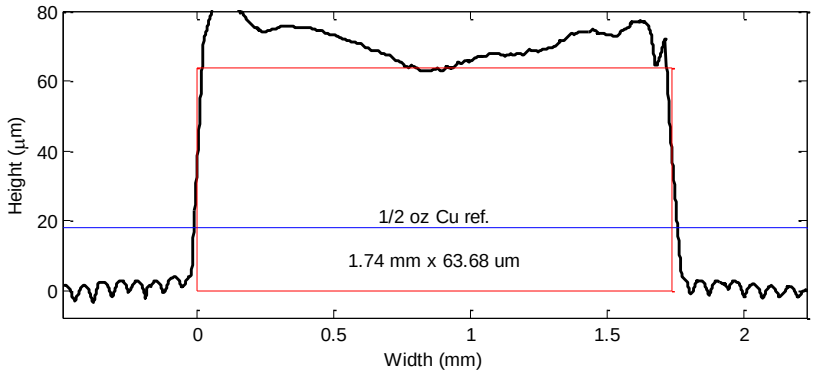

Figure 70 Profilometry data of Copper on ProtoTherm

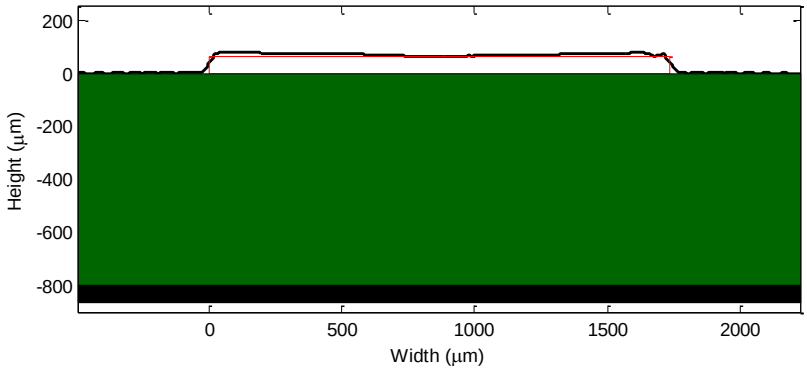

Figure 71 Profilometry data of Copper on ProtoTherm, Axis to Scale, Substrate Shown

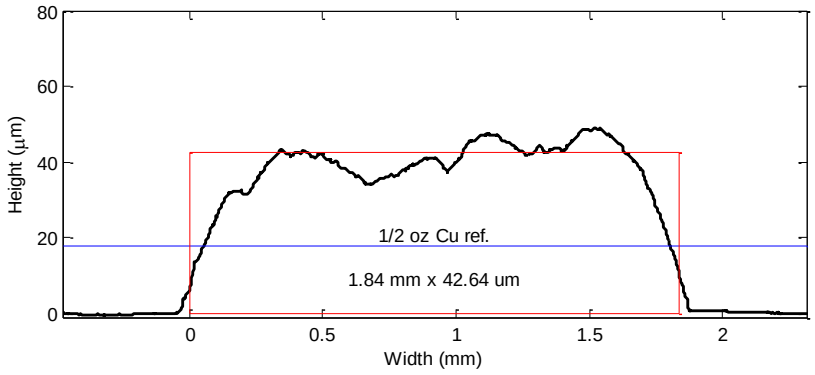

Figure 72 Profilometry data of CB028 on ProtoTherm

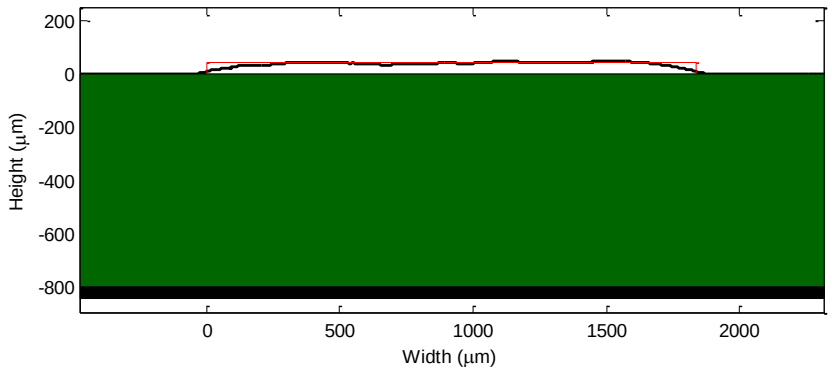

Figure 73 Profilometry data of CB028 on ProtoTherm, Axis to Scale, Substrate Shown

The copper cladding appears expectedly smooth and with sharp edges. Both CB028 samples have characteristic sloped edges and rough surfaces due to the direct print process. The copper tape appears to have a bow-top which may be explained by the compressibility of the adhesive material combined with the manner of application (compression using the back of a fingernail). The actual values which are measured and used in the models are shown in Table 12.

Table 12 Profilometer measurements

Sample	Dimensions	Design
Cu on Rogers 5870	2.17 mm x 19.66 μm	2.2 mm x 17 μm
CB028 on Rogers 5870	2.15 mm x 27.19 μm	2.2 mm x 25 μm
Cu on ProtoTherm	1.74 mm x 67.85 μm	1.75 mm x 66 μm
CB028 on ProtoTherm	1.84 mm x 40.91 μm	1.75 mm x 25 μm

3.8. High Current Resistivity Measurement

The Ecopia measurement unit is designed for low conductivity on-die measurements and uses a maximum of only 15 milliamps of current which leads to extremely low voltages across the sample which are difficult to measure accurately. In order to improve the signal to noise ratio of these high conductivity, low resistivity measurements, an Agilent E3644A 0-8V, 0-8A DC power supply and Agilent 34401A 6-1/2 digit multimeter are used in conjunction to induce 1.5 amps of current thus allowing voltages 100 times larger to be measured. Due to the good conductivity and thickness of the material under test (CB028), the power dissipated in the part is

low while offering excellent measurement values. Figure 74 shows the material probing setup. Several samples are measured in order to establish the measurement variability and the data is shown in Figure 75.

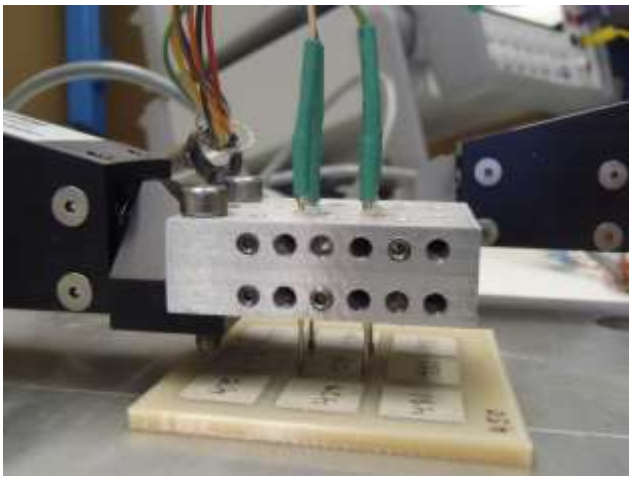

Figure 74 Measurement setup

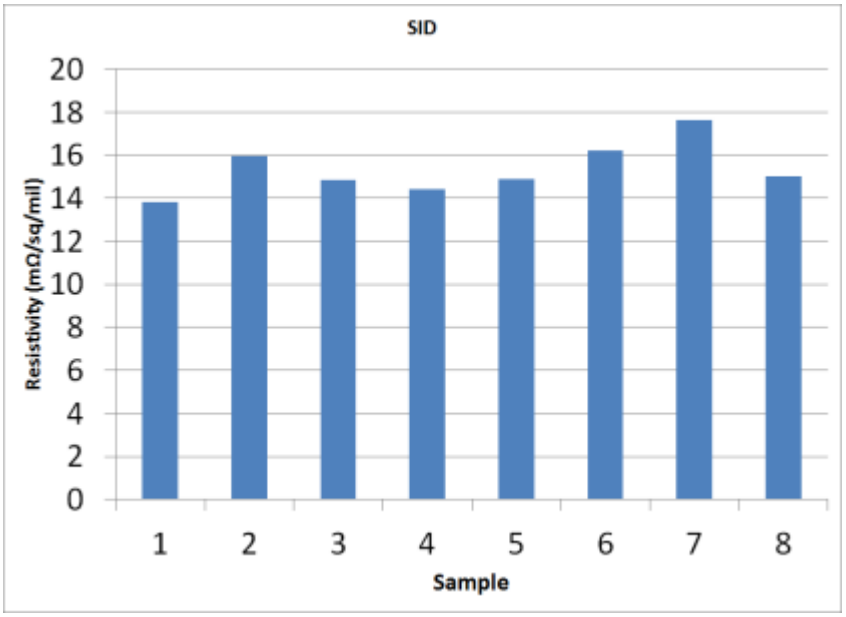

Figure 75 High current measurement results

In order to determine the actual printed conductor thickness, the Keyence brand laser scanners provided on nScrypt, Inc. printing machines are used. Several models are available on

nScrypt, Inc. equipment and their performance specifications are shown in Table 13. Due to availability limitations, the LK-082 is used and a sample data set are shown in Figure 76.

Table 13 Available Keyence laser scanners

Keyence	Spot size (um)	Range (mm)	Z Repeatability (um)	Power (mW)
LK-082	70	18	0.1	0.95
LK-G82	70	30	0.2	0.95
LK-H052	50	20	0.025	0.95
LK-V7080	48	28.5	0.5	4.8

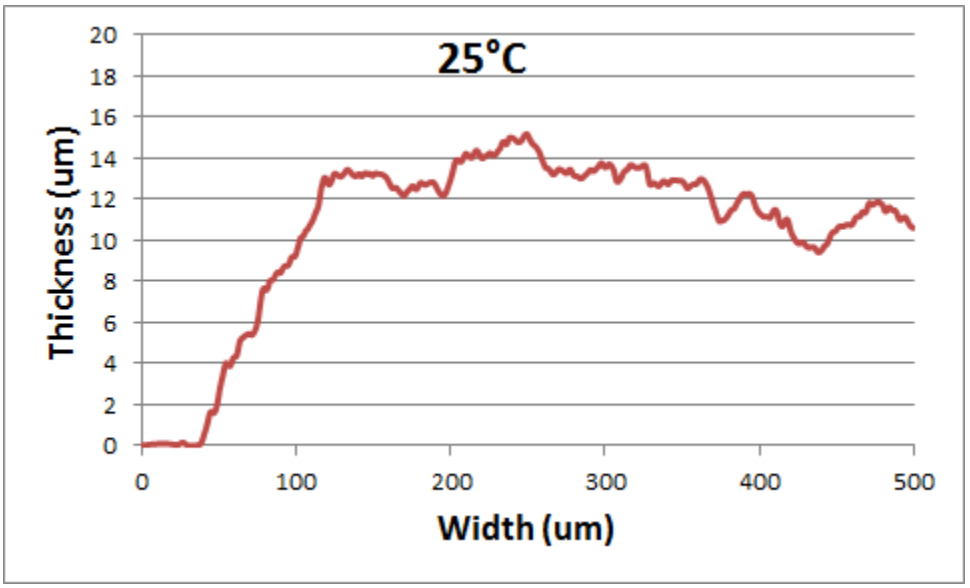

Figure 76 LK-082 Measurement of the thickness of printed CB028 material

Paste printed on rough surfaces exhibits higher effective resistivity than that printed on smooth surfaces due to the undulating surface lengthening the electrical path between electrodes. This effect is measured by printing two identical amounts of CB028 onto DuPont Kapton (smooth, 125 µm thick commercially-purchased sheet) and ULTEM (commercially 3D printed) substrates. Printing work was performed by Sam LeBlanc. Several samples are measured and the difference between substrates in material resistivity are shown in Figure 77. Also shown are the min and max datasheet values for resistivity.

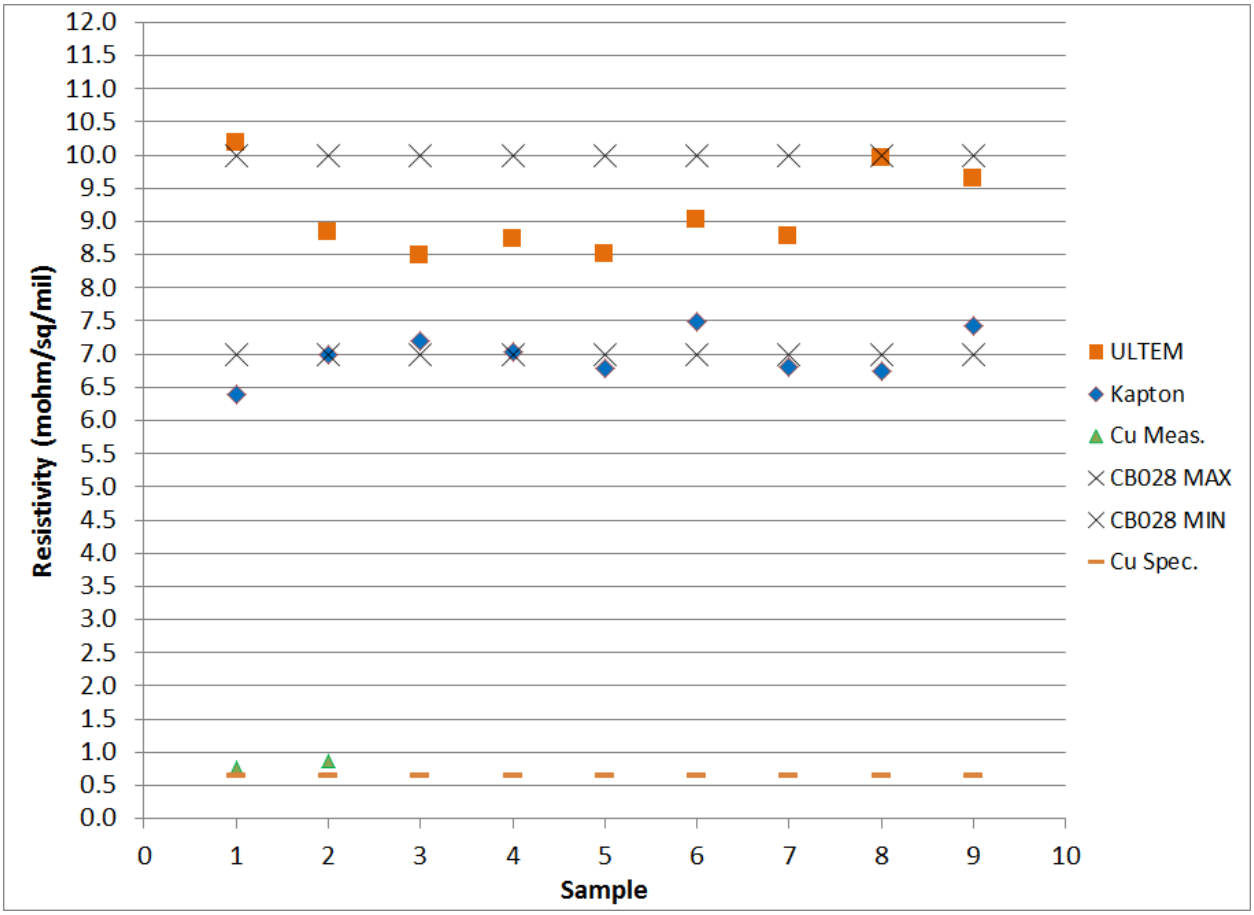

Figure 77 Resistivity measurement on smooth Kapton vs. rough ULTEM surfaces

Resistivity varies with temperature by the resistance temperature coefficient of the material (α) and the amount of thermal curing applied. Figure 78 shows these effects. The material is printed at 25 °C and cured at only 120 °C by mistake as shown in the lighter-colored traces. It is interesting to note the value of the conductivity after partial curing. Curing is completed at 160 °C which lowers the resistivity to the expected and reproducible value. As the temperature is adjusted up and down from -40 °C to 160 °C the slope of the resistivity trace gives the resistance temperature coefficient referenced to 0 °C as shown in Table 14. Also shown are approximate values for bulk copper and silver.

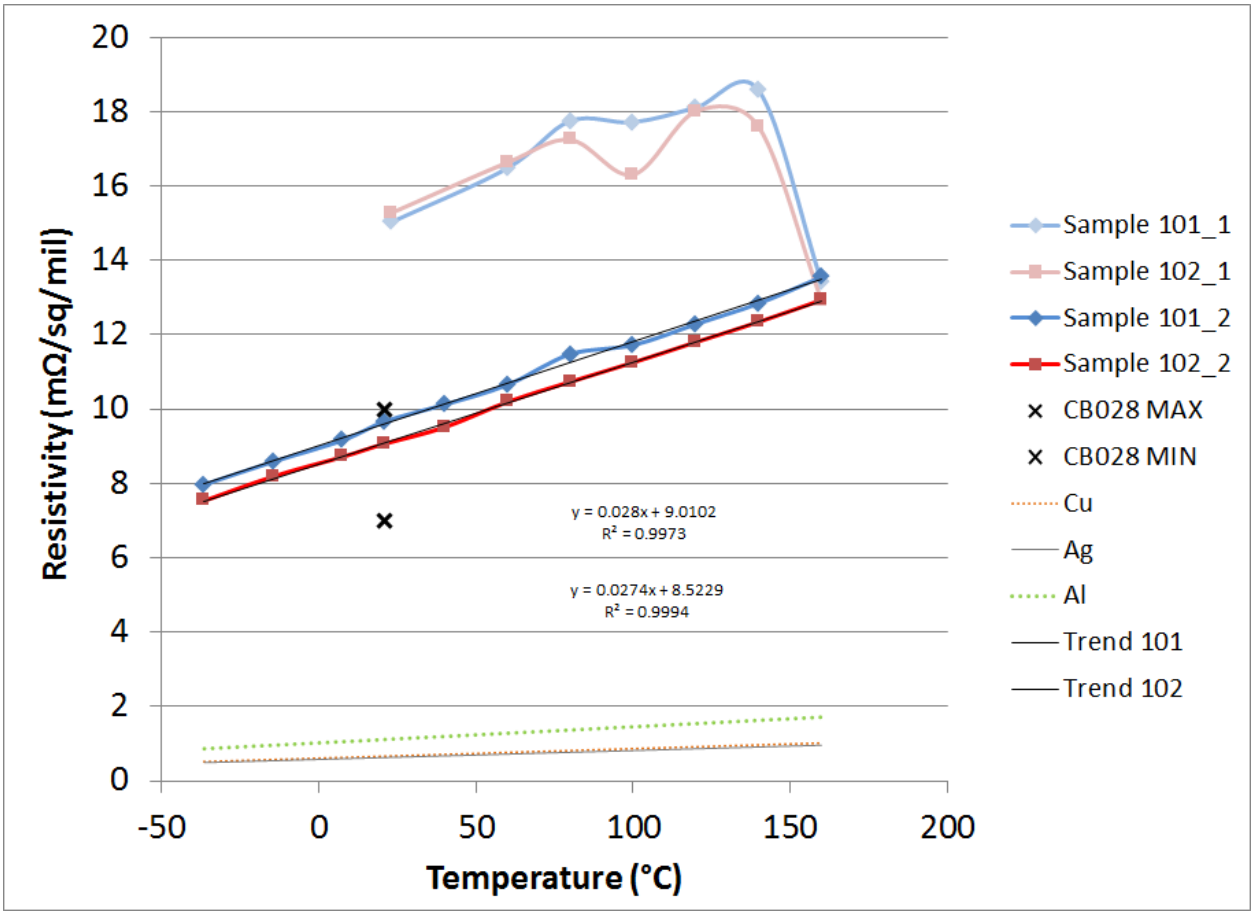

Figure 78 Resistivity of CB028 vs. ambient temperature

Table 14 Resistance coefficient of temperature

Sample	Value
Sample 101	0.003108
Sample 102	0.003215
Copper and Silver (approx.)	0.0038

3.9. Electromagnetic Measurement

An HP 8720ES 20 GHz vector network analyzer (VNA) is used with 4-point time domain averaging and a 200 ms read time for S-parameter characterization [149]. Full two-port SOLT calibration is performed using an Agilent 85033D 3.5 mm calibration kit. Cascade Microtech WinCal software is used save the data to .s2p files. Figure 79 – Figure 82 show the measured S-parameters (thick lines) and HFSS model data (thin lines).

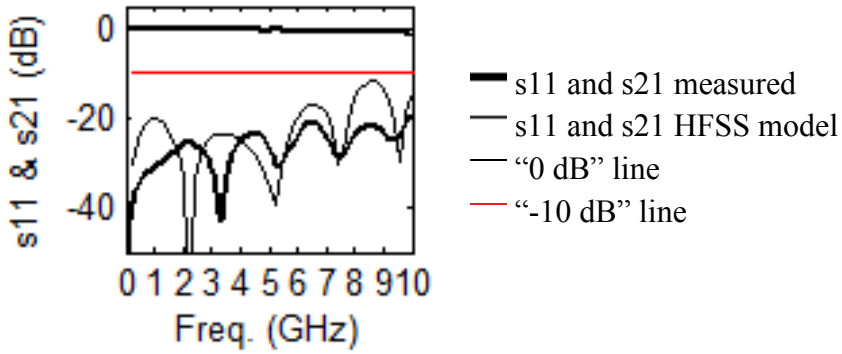

Figure 79 S-parameter data of copper on Rogers 5870

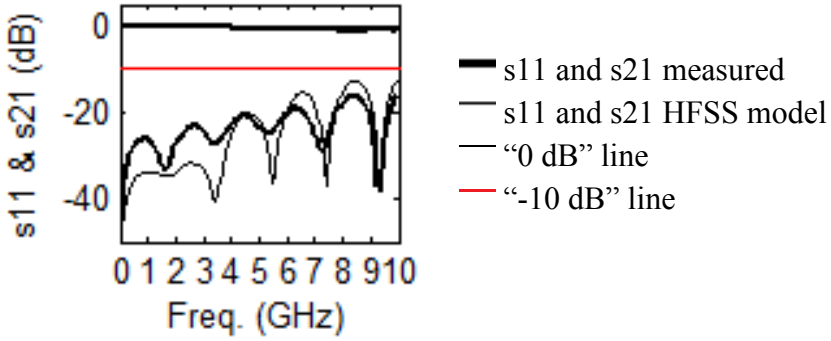

Figure 80 S-parameter data of CB028 on Rogers 5870

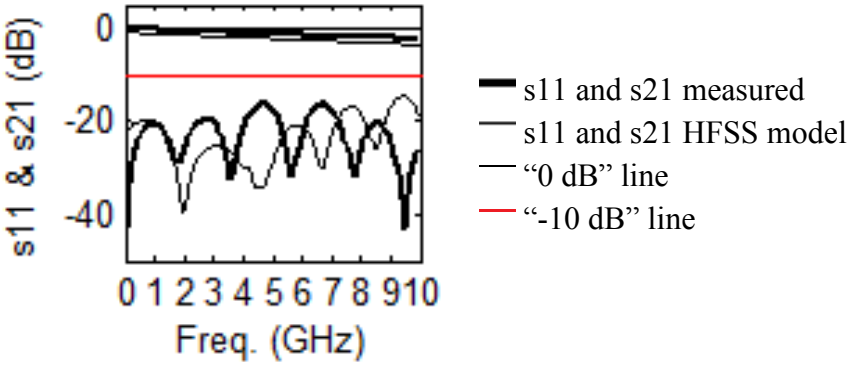

Figure 81 S-parameter data of copper on ProtoTherm

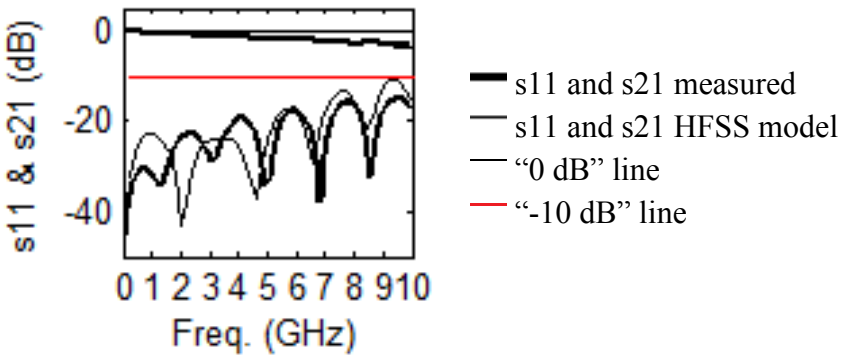

Figure 82 S-parameter data of CB028 on ProtoTherm

The results of the parameter extractions are shown in Figure 83 for the sample of CB028 on ProtoTherm and Figure 84 for the other material stack-ups. For comparison, CB028 cured at 100 °C has a resistivity of 40 μΩ•cm. At gigahertz frequencies, it is seen to be around 500 μΩ•cm. The higher resistivity of CB028 may be accounted for by considering the structure of the silver flake, surface roughness of ProtoTherm, or by the quantity of silver flake, near the surface where most of the RF current flows. DuPont CB028 paste works by deposition in a polymer carrier which is subsequently cured at a relatively low temperature to drive off solvents and cause shrinkage and tightening of the flakes to form a highly conductive material. This process may affects the RF conductivity differently than if the material is a solid metal as in the case of copper. According to [91] the properties of ProtoTherm are around $\varepsilon r = 3$ and $\tan\delta = 0.03$ which match well with the measurements of the microstrip structure.

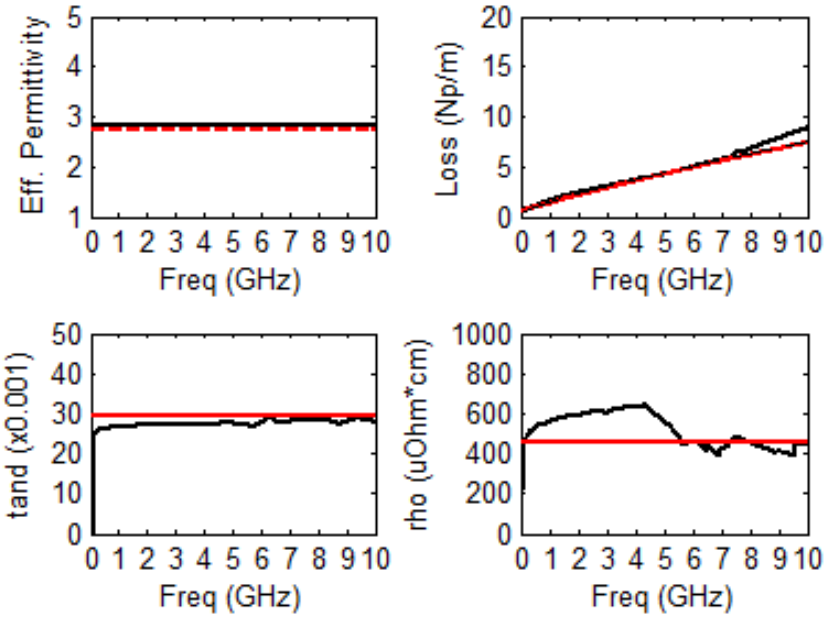

Legend: ━ Measured, ━ Model
Figure 83 Back-solved parameters of CB028 on ProtoTherm

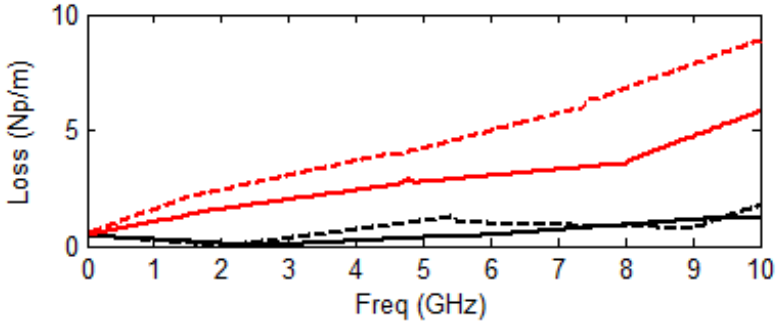

━ Cu on Rogers ┅ CB028 on Rogers ━ Cu on P.T. ┅ CB028 on P.T.
Figure 84 Loss comparison between material stack-up types

3.10. Suspended Microstrip

Transmission line design is governed as much by performance as by manufacturing technology. Waveguide allows the lowest loss possible but is bulky and difficult to manufacture. Coax is flexible but it is difficult to build a circuit containing components using coax. Coplanar waveguide keeps the field tight but requires precision manufacturing of the gap width in order to control line impedance. Stripline keeps fields tight but requires multi-layer manufacturing.

Microstrip requires less precision but since more of the field intensity is contained within the substrate, it suffers from higher loss. Also due to the air-dielectric interface, additional unwanted modes can be introduced on the line. 3D printing is revolutionizing manufacturing and allowing increased freedom of design in many areas, including microwave circuit fabrication.

Many variations on the traditional microstrip transmission line are available. One idea that is explored here is suspended microstrip [150]-[179] . The device is fabricated using stereolithography for its high resolution capabilities as well as the ability to create overhangs. It may be possible to fabricate this type of structure using FDM if the system is tuned specially for overhangs. Figure 85 shows a typical microstrip structure. Part of the field is contained in the substrate between the signal trace and the ground on the bottom, and part is allowed to exist in the air above the signal trace. The signal propagates in a quasi-TEM mode under ideal conditions but the wave can propagate at different phase velocities. Higher-order modes can be induced on the line by manufacturing imperfections at the launches which compromise performance. Figure 85 shows a standard microstrip structure as modeled in Ansoft Q2D extractor with these parameters: h=0.8 mm, w=1.75 mm, tanδ=0.04, att=5.48 Np/m @ 10GHz.

Table 15 Color key for following figures

Color	Material
Red or Green	Dielectric
Gold / Yellow	Signal Trace
Silver / Gray	Ground / Return Path
White	Air
Blue line	Vertical axis

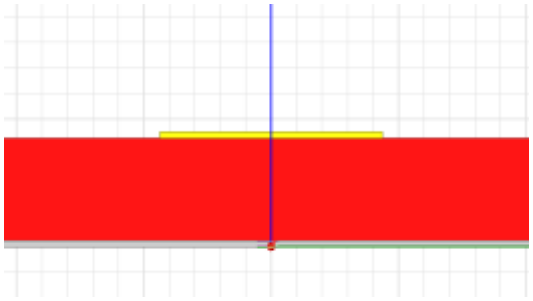

Figure 85 Standard microstrip

A hypothetical (non-manufactural) microstrip with uniform dielectric which is also lossless is one formed only in air since dielectric losses are near zero. Since only one dielectric constant is involved and the phase velocity on the line is fixed, the maximum frequency is determined only by the height and width of the microstrip. Field containment and managing impedance are drawbacks. Figure 86 shows the model with parameters h=3 mm, w=1.75 mm, tanδ=0, att=0.

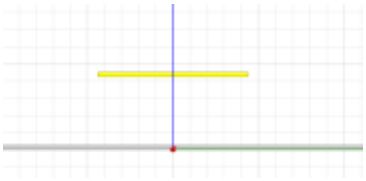

Figure 86 Microstrip in air

Supporting the signal trace allows the structure to be fabricated; this is called suspended microstrip. It is proposed to hold up the signal trace by rows of support columns. These support columns can be omitted for 2D simulations; see the appendix for a verification of this assumption. Figure 87 shows a suspended microstrip with dielectric parameters h=0.15 mm, w=1.75 mm, tanδ=0.04, air gap h=0.5 mm, and substrate width=10 mm. The characteristic impedance is found to be 75.3 Ω and the loss is 0.6 Np/m @ 10 GHz. A microstrip with similar dimensions would have an impedance of 50 Ω and loss of 5.48 Np/m @ 10 GHz. It is clear from these models that a savings of 9 times in dielectric loss is possible with suspended microstrip.

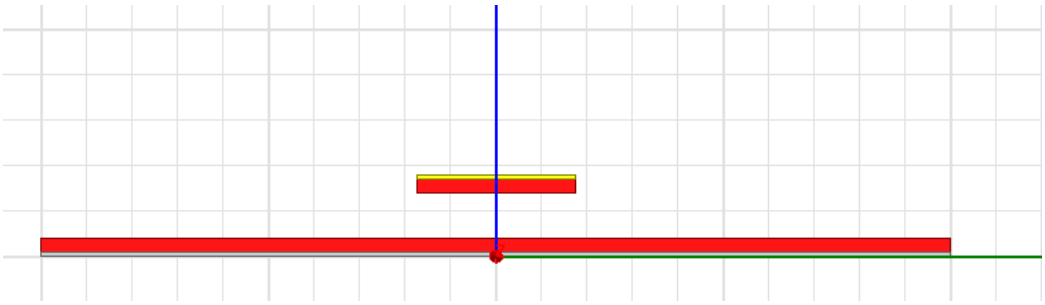

Figure 87 Suspended microstrip model

The suspended microstrip is modeled using MATLAB, ANSYS Designer, ANSYS Q2D, and ANSYS HFSS (see the appendix). An improvement of more than 3 Np/m is observed by adding 1 mm of air within a 1.6 mm microstrip. According to the HFSS model, the loss increases by 0.05 Np/m when the poles are introduced. To ease the manufacturing tolerances, the poles can be made larger without increasing the dielectric loss significantly. This will benefit future manufacturing using less accurate technologies such as FDM. Additionally, it is evident that the poles may be omitted allowing the use of Q2D to model the device. The use of Q2D speeds up the simulation time from many minutes to a few seconds.

Modeling a longer substrate in HFSS improves the loss measurement significantly; see Appendix O. The S-parameter data for the same measurement setup are shown in Figure 88 (50 mm length) and Figure 89 (100 mm length).

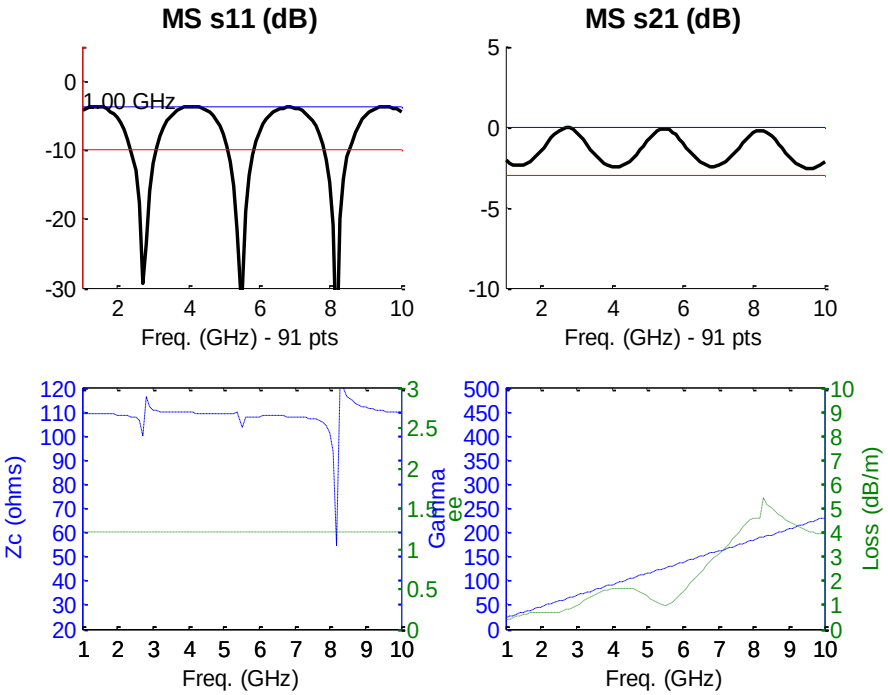

Figure 88 Suspended microstrip, 50 mm length, 13 poles

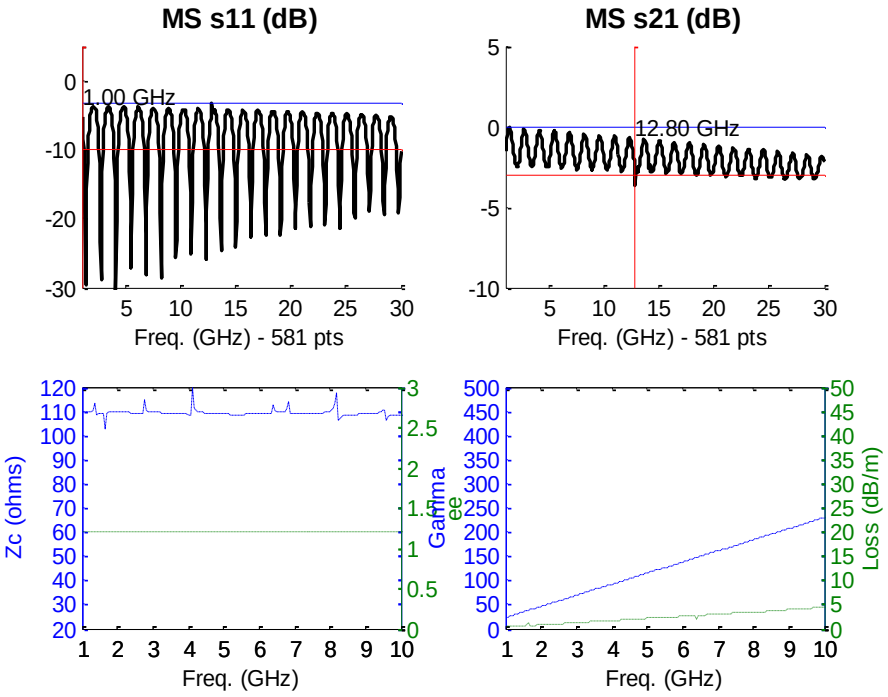

Figure 89 Suspended microstrip, 100 mm length, 27 poles

The solid microstrip h=1.6, w=1.75 has a characteristic impedance around 80 ohms and with 1 mm of air within the substrate, the impedance rises to around 110 ohms. In order to bring

the impedance back down to 50 ohms, the height must be reduced so the width must be increased. Due to current manufacturing tolerances (0.3 mm on top and bottom) the height cannot be reduced and the width must be increased. Unfortunately, to achieve 50 ohms, the width must be around 6.25 mm and these dimensions lead to a mode-free maximum frequency less than 1 GHz. It is proposed that once the manufacturing tolerances of 3D printing improve (i.e. smaller structures can be fabricated), this method will be more useful at high frequencies.

The design is realized using stereolithography. Parts are fabricated by Keck Center technicians using a 3D Systems Viper si2 operated in high resolution mode producing a layer thickness of 50.8 μm using a laser beam diameter of 76.2 μm. Samples are printed on top of a 125 μm sheet of polycarbonate in order to eliminate support marks and preserve a high quality bottom surface. DSM Somos WaterShed XC 11122 is used for its higher resolution capability in the manufacture of the suspended microstrips; however, this comes at the cost of a lower glass transition temperature (41 °C) than other SL resins. A series of four design iterations are conducted and the minimum manufacturing limitations are determined to be those shown in Table 16. The printed parts are shown in Figure 91 - Figure 93.

Table 16 DSM Somos watershed manufacturing minimums

Dimension	Value
Beam diameter	76.2 μm
Layer height	50.8 μm
Round vertical pole diameter	200 μm
Vertical pole height, max	> 1 mm
Vertical pole height, min	200 μm
Bottom horizontal layer thickness, min	300 μm
Suspended horizontal layer thickness, min	250 μm

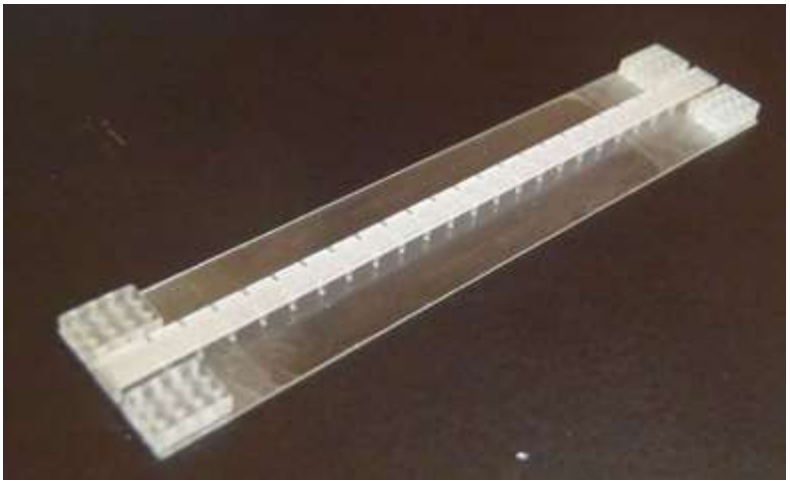

Figure 90 3D printed suspended microstrip before metalization

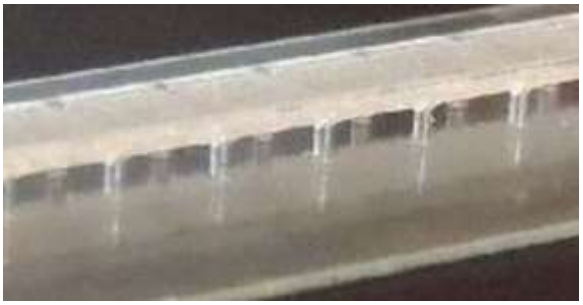

Figure 91 3D printed suspended microstrip, close-up

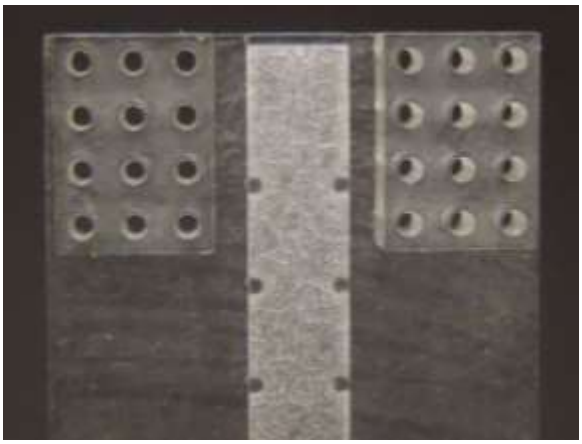

Figure 92 3D printed suspended microstrip termination

Figure 93 3D printed suspended microstrip, completed

The suspended microstrip is modeled using Ansoft Q2D and the S-parameter data matches well as shown in Figure 94. The black trace indicates measured data and the red trace indicates model data. Performance is good up to about 8 GHz which is higher than predicted using microstrip mode estimation calculations.

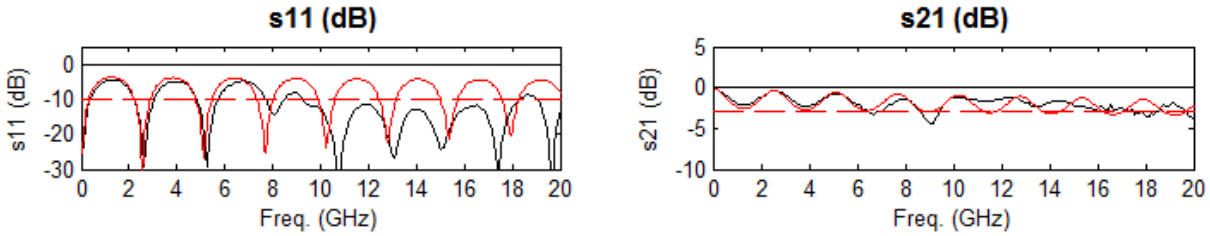

Figure 94 Suspended microstrip S-parameter data

Extremely low losses are demonstrated. The loss of the 3D printed suspended microstrip is actually lower than that of a copper on FR4 comparison sample even considering the use of printed silver paste vs. bulk copper. This is due to the extremely low dielectric loss of the

suspended structure outweighing the lossy CB028. Figure 95 shows the measured loss data in black and model data in red. It is hypothesized that the oscillations in the loss measurement are due to mismatch losses at the connectors.

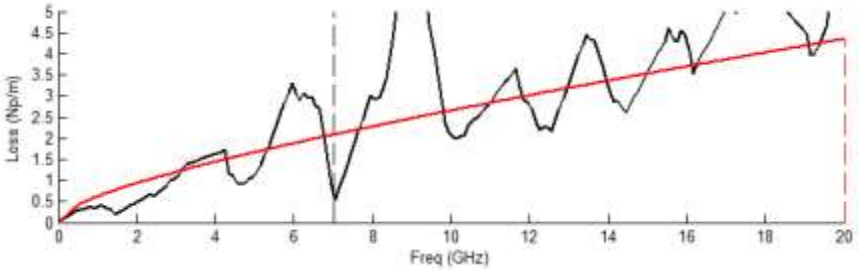

Figure 95 Suspended microstrip loss data

3.11. Stripline

Improvements by the author in fused deposition parameter tuning now allow smoother surfaces and greater infill density than were previously possible. Commercially fabricated (eg. Stratasys, Ltd. Dimension) machines tend to have rough top surfaces making conductive paste printing difficult and tend to exhibit less than 100% infill which introduces porosity and top-to-bottom shorts. These improvements are first used in the curved inverted-F antenna described in chapter 4 but the dispensing of conductive paste and printing of ABS are performed on two different machines and although printing is performed on a curved surface, only a two-layer print is realized. Here a six-layer print (Figure 96) is realized on one machine while also showcasing the RF/microwave abilities of 3D printing by fabricating a stripline [150].

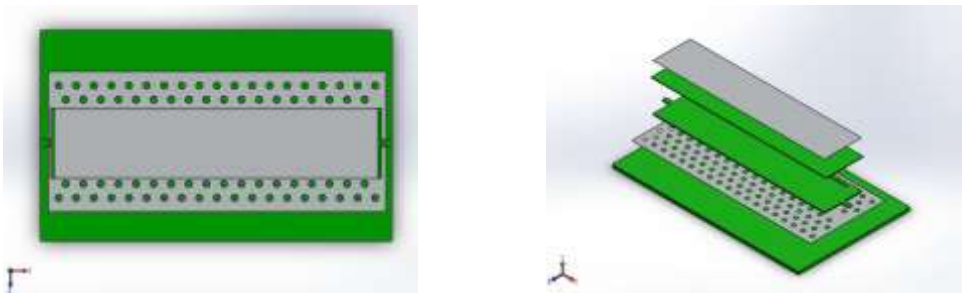

Figure 96 Stripline model

First, the dielectric constant and loss tangent (approx. 2.6 and 0.007) are measured (Figure 97) using the cavity measurement systems described in chapter 2 on a 50 x 50 x 0.8 mm lime green colored ABS measurement sample which is printed using the same parameters as the actual stripline samples.

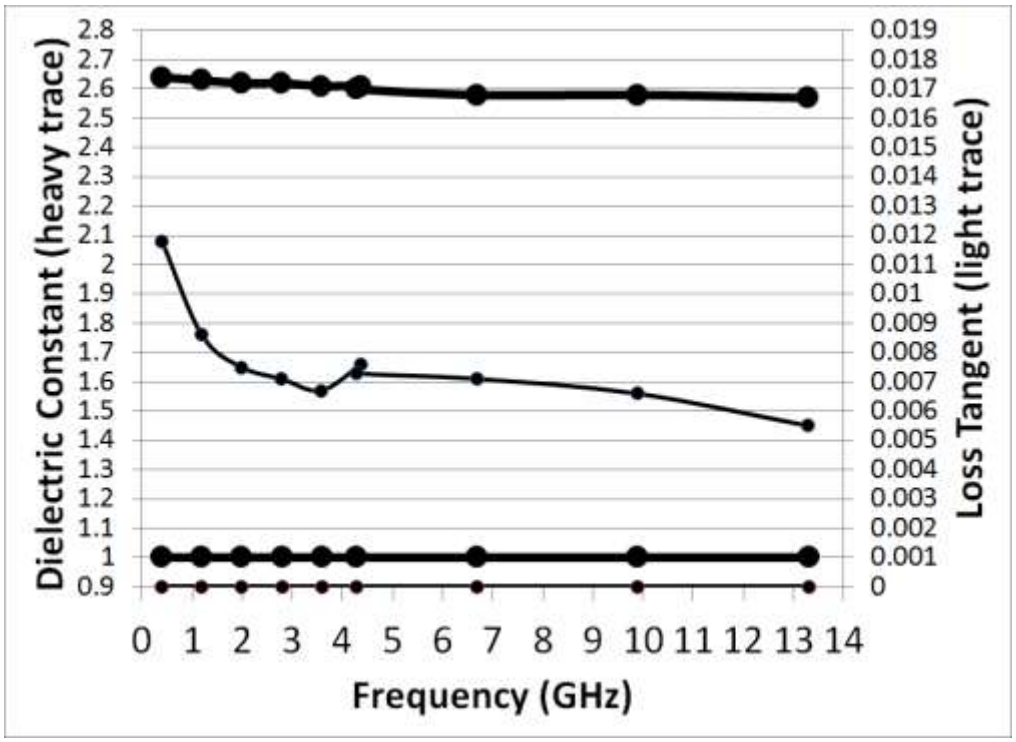

Figure 97 Dielectric measurement results of ABS used in stripline

The printing process begins with a heat-controlled aluminum surface set to 90 °C. Adhesive polyethylene terephthalate (PET tape) is adhered to the surface. A SmartPump loaded

with CB028 is manually switched with the fused deposition pump in order to form each layer of the part. The CB028 was allowed to instantly and automatically cure on the hot bed but a one hour post cure in the oven at 90 °C is also used to ensure maximum silver conductivity. Significant clogging and thickening of the CB028 is observed even though the SmartPump and material are unloaded between conductive layers. This problem is solved when printing the flashing heart design with the water cooled SmartPump described in chapter 1. Twelve samples are fabricated. Six were accidentally baked in the oven at 120 °C which warped the ABS substrate. Of the remaining six, three are of excellent quality and produce smooth S-parameter data. The data shown here is from the best sample. The printing steps are shown in Table 17.

Table 17 Fully 3D printed stripline on one machine

Substrate		
Bottom ground		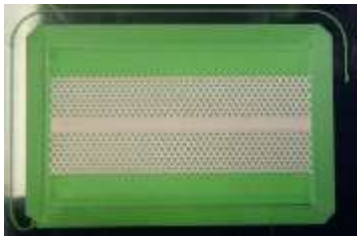
Bottom dielectric	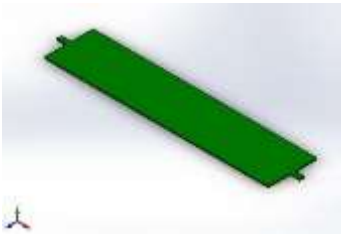	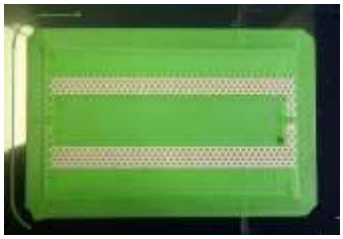
Strip		
Top dielectric	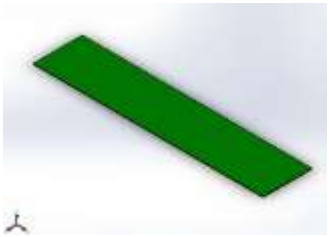	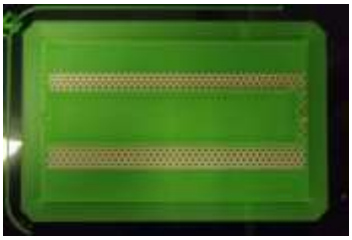
Top ground	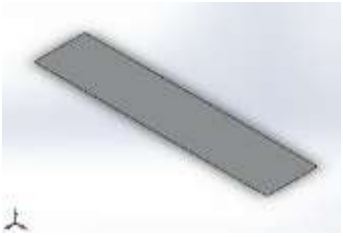	

The printing process is completed by adding grounding “straps” formed using H20e conductive epoxy on the sides connecting the top ground to the bottom ground. The device is

probed using Pico probes with a pitch of 1850 µm. The measurement setup CAD design and actual setup are shown in Figure 98 and Figure 99.

Figure 98 Measurement setup (modeled and photographed)

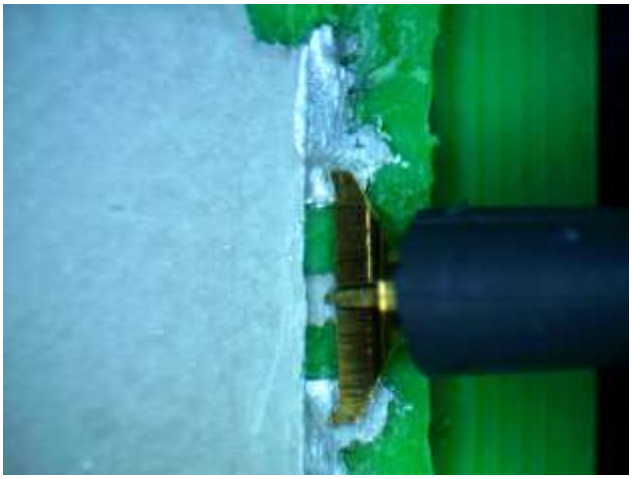

Figure 99 Measurement using pico probes

The width of the printed stripline is verified using a camera-equipped microscope. The actual width of the strip is found to be 0.85 mm. The thickness of the stripline is observed by slicing the stripline and scanning the cross section using an SEM; however, it is difficult to observe the stripline when sputter-coated with gold and charge-up magnifies the appearance of the strip. Laser scan measurements are more trusted and read the thickness of the printed stripline to be approx. 25 µm but the SEM photos (Figure 100) show a lighter area about 90 µm thick.

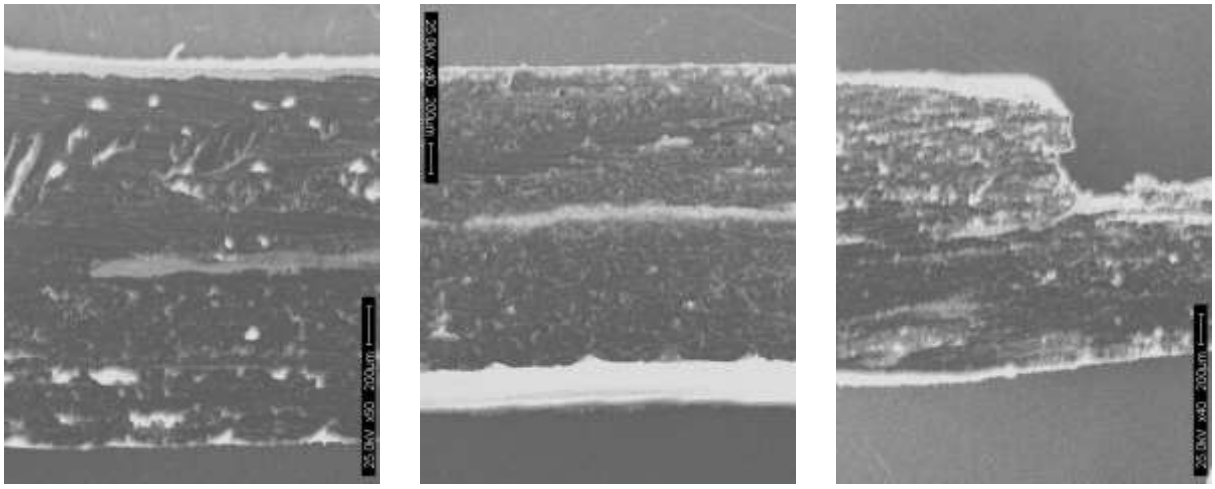

Figure 100 SEM photos of the cross-section of fully 3D printed stripline

Measurements are made using an Agilent 8720 ES network analyzer (Figure 101) and parameters are back-calculated as described previously. Based on the measured strip width and dielectric height, the stripline impedance is calculated to be 39 Ω which matches well to the back-solved value (Figure 102). The resonant cavity measurement of dielectric constant 2.7 matches well as shown in Figure 103.

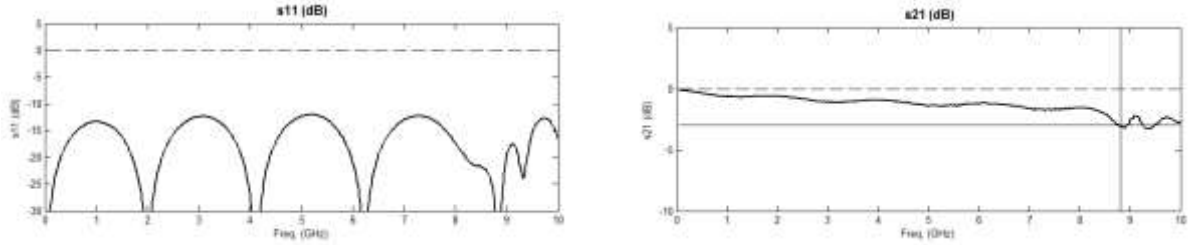

Figure 101 S-parameter measurement

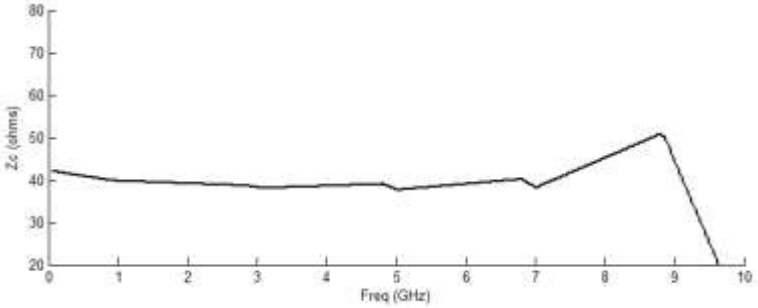

Figure 102 Measured/back-solved characteristic impedance

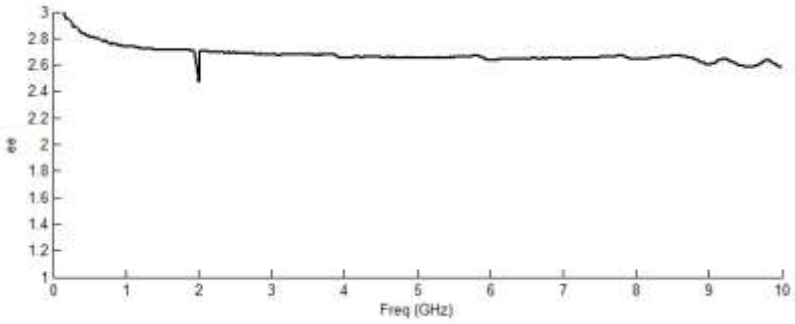

Figure 103 Measured/back-solved dielectric constant

Referring to Figure 104, the total loss is shown in black and a curve-fit is made as the blue dash line. From the curve-fit, the conductor loss (red dash) and dielectric loss (black dash) are determined.

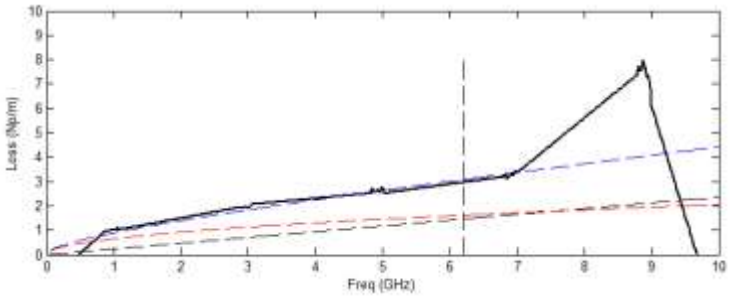

Figure 104 Loss measurement

The loss tangent as measured in the resonant cavity is 0.007 and matches closely to the back-solved measurements shown in Figure 105.

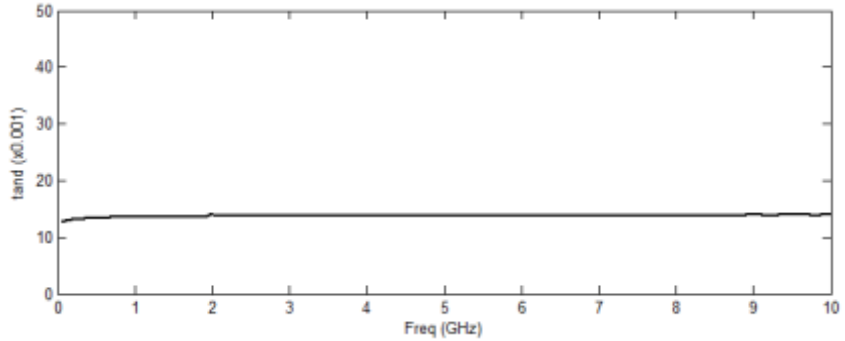

Figure 105 Loss tangent measurement/back-solve

Resistivity measurements are performed using a four-point probe and the resistivity is found to be 23 $\mu\Omega$·cm. Additional unaccounted-for loss is and has been observed in RF/microwave structures made of CB028 paste but the value determined here of 44 $\mu\Omega$·cm (Figure 106) matches more closely than previous work.

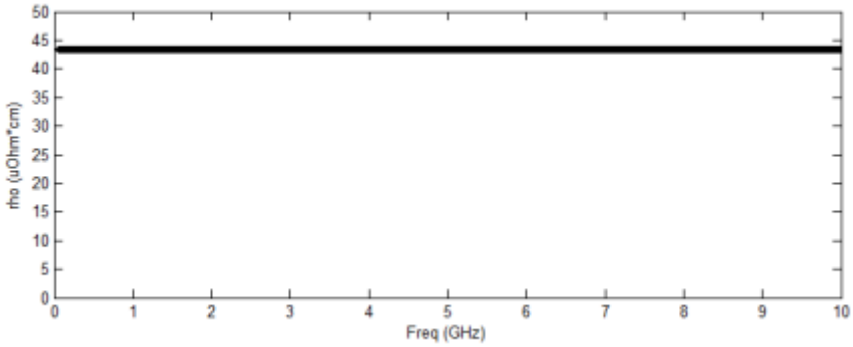

Figure 106 Conductor resistivity

Maximum frequency is observed to be around 7 GHz with a sharp discontinuity around 9 GHz. Ideal stripline is expected to perform far beyond this cutoff; however, the dielectric width surrounding the stripline is 10 mm. Theory reveals that this width corresponds to one-half wavelength at 9.7 GHz thus allowing a dielectric waveguide mode to propagate. Reductions in the dielectric width will increase the cutoff frequency.

3.12. Transmission Line Loss

The losses and breakdown over frequency of different types of transmission lines are compared in Figure 107. Black: CPW by Rojas [93], blue: microstrip, green: stripline, red: FR-4 microstrip, pink: suspended microstrip. The 3D printed stripline has a clear advantage over the microstrip line, maintaining low loss even up to 12 GHz and smooth performance to 9 GHz. The performance is close to that of a comparison sample of microstrip FR-4 which was measured using an Agilent 8753 6 GHz VNA.

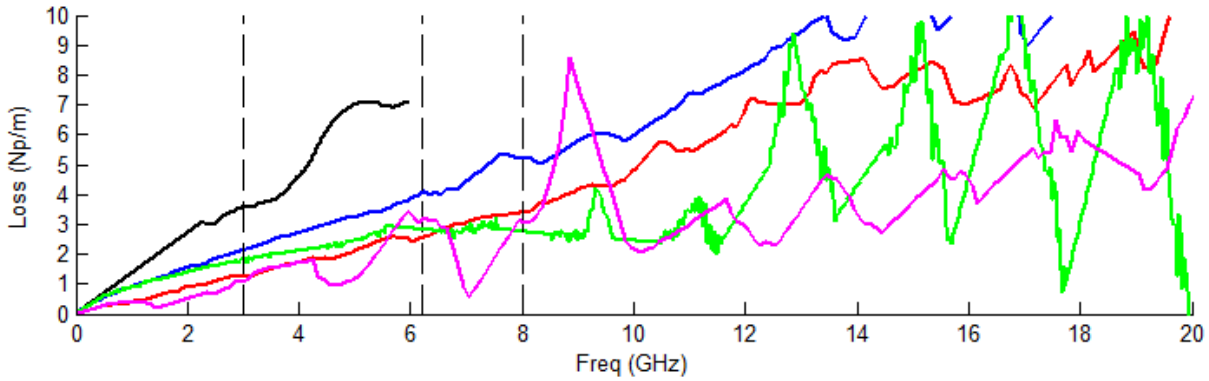

Figure 107 Frequency breakdown of transmission lines

Table 18 Design guide for 3D printed stack-ups

Material	$tan\delta$	ρ	α_d	α_c	α_T	α_T
CB028 as CPW (Rojas)	0.054	314.7	4.10	2.19	6.29	(7.04)
Copper on Rogers	0.0012	1.68	0.08	0.11	0.19	(0.36)
CB028 on Rogers	0.0012	500	0.08	1.91	1.99	(1.08)
Copper on ProtoTherm	0.030	1.68	2.11	0.11	2.22	(2.76)
CB028 on ProtoTherm	0.030	500	2.11	1.91	4.02	(4.22)
CB028 as Stripline	0.012	44	1.25	1.40	2.66	(2.62)
FR-4	0.023	1.68	1.74	0.18	1.82	(2.15)
Suspended Microstrip	0.030	100	0.51	0.51	1.03	(1.20)

Table notes: The loss data given here are from models which are fitted to measured data. Values in parentheses are measured data. The data are given at 5 GHz. Units are resistivity ρ (μΩ·cm) and loss α (Np/m). CPW by Eduardo Rojas [93].

Table 18 shows a summary of the material data and the models which best fit the measured data. An improvement is observed in the losses of the stripline vs. the microstrip. The conductor loss improvement is probably due to improvements in measuring technique using probes as opposed to SMA connectors. The dielectric loss improvement is due to using FDM printed ABS as opposed to stereolithography-compatible ProtoTherm but does not quite compete with the suspended microstrip. The stripline is good to higher frequencies and is much more mechanically rugged than the suspended microstrip.

The loss in CB028 as measured at DC using a four point probe measurement system and van der Pauw equations gives resistivity values close to the data sheet specification of 7-10 mΩ/□/mil at room temperature when cured at 160 °C. In the case of the printed transmission lines which are discussed here, the resistivity values have been back-solved from the measured S-parameters. Also, models are generated and the S-parameters are matched. The RF effective resistivity is found to be in the range of 100 to 500 mΩ/□/mil depending on the type of transmission line. Each transmission line type has a different current transport profile across the cross-section. Models are available for better understanding of RF loss mechanisms such as skin

effect or its interaction with surface roughness in bulk materials. State of the art RF materials such as rolled or electrodeposited copper as is conventionally used in RF circuits can still have a roughness value, but these are smooth as compared to printed substrates and conductive patterns. The low temperature silver paste is composed of silver flakes suspended in a polymer and therefore other RF loss mechanisms must be considered. 3D printed substrates are naturally rough given the nature of the printing process as compared to flat and pressed ceramic, LCP or Kapton sheets. In addition, the sides of the printed silver flake lines will also have a roughness factor which is especially important in transmission lines such as CPW where currents primarily flow along the edges of the line. Loss due to rough surfaces and edges are well understood and do impact the loss that has been measured in the printed devices shown. Further study is merited to quantify the losses in printed materials which. The insights gained will lead to better RF transmission lines in the future.

Although the conductor loss mechanisms in 3D printable silver ink are not fully understood, the loss is accurately measured and it is possible to design a transmission line with predictable loss using the information given here. A fundamental understanding of fused deposition allows the author to tune the process to create smooth substrates compatible with conductive paste printing. This realizes improvements in overall transmission line loss by allowing low loss ABS material to be used. The construction of a multi-material capable machine allows fast switching between materials and automatic curing of the silver paste. The ability to make multilayer stripline structures opens the door to higher frequency operation as opposed to microstrip since all of the fields exist within the dielectric. Using the multi-material machine, several functional samples are produced with ease due to a thorough understanding of the entire process and a properly adjusted machine. In conclusion, lower loss, high frequency

RF/microwave transmission lines are demonstrated which match well with model data and are produced in an easy, reproducible fashion. Model data is now available for future designers to use in the fabrication of more complex RF/microwave circuits.

Chapter 4: Fully 3D Printed 2.4 GHz Bluetooth/Wi-Fi Antenna

3D printing is mature for fabricating complex 3D structures and this is currently done using various materials such as polymers and metals. Heterogeneous 3D printing [189],[190] is more challenging given the issues of adhesion and thermal mismatch. Melding diverse materials for enhanced mechanical properties is common and exploited in the area of composites. Electronics are made with diverse materials but are not typically made with structure as the focus, but instead electrical function. FR4 is a standard composite used for Printed Circuit Boards (PCB). PCBs have the advantage of combining a number of diverse electronic components including antennas. Another approach for antenna fabrication is to print on flexible but flat substrates and place the antenna within a structure.

Currently wireless smart objects are simply objects which have electronic circuit modules and antennas placed inside them. Much work has been done in the area of thin film RFID antennas and circuits [180],[191]-[208]; however, these devices are still placed into objects. Thin film antennas are flexible and may be easily adhered to objects but this requires extra processing steps to fabricate the antenna and apply it to the target object. Work has been done in larger printed antennas; however, the extra processing step of electro-less plating is used to metallize all surfaces [25]. Little work has been done in the area of 3D printed antennas in 3D printed objects, an opportunity that eliminates the need to separately fabricate and install electronics in objects, thus reducing processing steps.

Combining mechanical and electrical properties and forming a unique 3D electrically structural device has merit but conventional fabrication methods are not conducive for this. One approach to do this is to combine 3D printing and printed electronic processes. Researchers have done a variety of demonstrative 3D printed electrical functional devices but the majority of these

have been for DC applications [213]. A study and demonstration that integrates both mechanical structure and wireless functionality directly into an object is shown.

Here is presented [15],[16] a simple 2.4 GHz antenna in a 3D printed object. Full-wave models are generated using Ansoft HFSS. In order to demonstrate functionality, real-world tests using a Class 1 “100 m” Bluetooth module are conducted and compared against the performance of an industry-standard quarter-wave antenna. Printed antennas, conformal direct printing, and printed electronics are not new but it is emphasized that this is the first occasion that a printed antenna is patterned directly onto a 3D printed FDM part. The anticipated issues regarding extreme surface roughness and lower conductivity do not appear to significantly affect the final part.

Radiation pattern, resistive loss efficiency, effective aperture, and matching are modeled, measured and compared. Antenna size is not considered since 3D printed antennas are able to use a large part of the object in which they are functioning as a substrate and are not confined to a PCB (such as with typical PCB trace or chip antennas) and do not protrude from the device as monopoles do.

4.1. 3D Printing and Printed Electronics

The original term for 3D printing is additive manufacturing (AM). AM is a layer by layer approach to fabricating 3D objects. This is a direct digital approach and therefore it is possible to fabricate complex structures that are not possible using other fabrication processes [42],[43],[44]. Some AM processes use a two-print process which implies a sacrificial material that is soluble in a specified solution. A 3D object is designed using CAD software and this 3D image is then sliced into many layers that range from 100 microns in thickness to hundreds of microns in thickness. Each of these layers are then printed and layered. Experts over the years have

optimized the union of layers to create a process that is repeatable and reliable. Printed electronics has a variety of processes used to obtain electronic function on thin substrates such as paper or plastic. These thin substrates are electrically compatible and are very similar in nature to standard paper used in magazines or newspapers which are processed using a roll-to-roll process. A significant portion of the printed electronics processes is done using the roll-to-roll approach. For non-roll-to-roll printed devices, these are sometimes referred to as Direct Writing (DW) [7]. DW is an implied slow process and therefore another term of Direct Print (DP) is used to express digital printing patterns and including DW processes but done so using multiple nozzles or increased speeds [214].

The combination of 3D printing and printed electronics is not a difficult concept to grasp since both of these are CAD processes. In addition to being CAD processes, there are also some closely related specific processes within these two broader areas. FDM and direct printing are both extrusion technologies and therefore it is feasible to put these on a common platform. For example, stereolithography might be an ideal choice for its smooth surface finish; however, integrating a liquid-vat based printing system with other technologies proves difficult [190]. nScrypt, Inc. is capable of combining FDM and direct printing on their 3Dn series machines. nScrypt, Inc. has patented technology in micro-dispensing for high viscosity applications such as silver paste and in addition also has technology in fused deposition that is similar to FDM which allows for finer features to be achieved.; These share the same platform thus promoting the integration of 3D building and electronic integration.

Epoxy materials, also called thermosets, are two-part liquid components which when mixed thermally set to form a strong, rigid plastic material. Cure times at room temperature range from 5 minutes to 24 hours depending on the formulation. Typical “5-minute” epoxy

comes in a clear to yellowish form and is useful for coating electronic components in a tough shell; however, curing in only 5-10 minutes means that the material is difficult or impossible to print. EPO-TEK H20e is a silver epoxy used frequently for component attachment. The material has a pot life greater than 24 hours and is easily printed; however, it must be baked at greater than 90 °C or setting does not occur. The material is heavily loaded with silver and has good conductivity; however, it does not provide a strong mechanical bond and thus is commonly used in conjunction with a clear epoxy overcoating in order to hold components in place. SEM photographs are taken of the H20e material and are shown in Figure 108 and Figure 109.

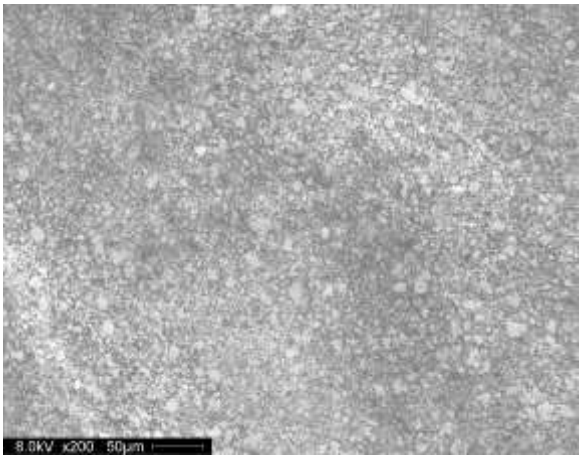

Figure 108 EPO-TEK H20e silver epoxy, 200X

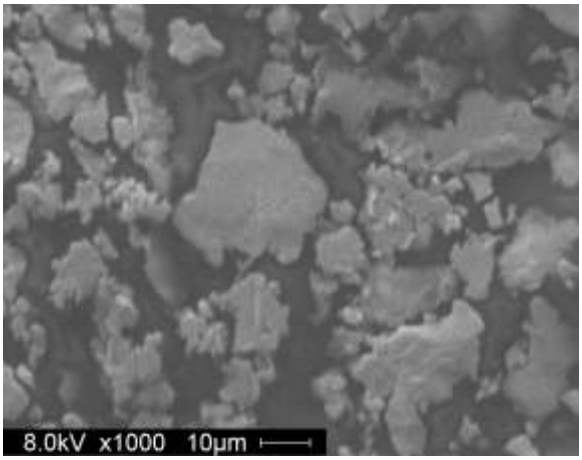

Figure 109 EPO-TEK H20e silver epoxy, 1000X

4.2. Antenna Design for Bluetooth

Several antenna designs are considered. Patch antennas (Figure 110) may benefit greatly from 3D printing because of the flexibility over thickness that is offered when a structure is printed as opposed to etched into copper-clad circuit board material. Patch antenna properties are improved with increased dielectric height but feed lines require thin boards. 3D printing frees the designer to vary the dielectric thickness as needed; however, patch antennas are highly directional and narrow-band, properties not desirable for objects which are typically used in random orientations and with frequency-hopping spread-spectrum (FHSS). Planar inverted-F antennas (PIFAs) (Figure 111) will benefit from 3D printing and it is recommended that future designs take advantage of bridging (printing with air underneath) to form the PIFA. Meander-line antennas are commonly used for their compactness. 3D printing offers the chance to take the antenna off the PCB and integrate the antenna into the case or structure thus freeing the antenna designer from cramped circuit board areas while allowing increased antenna efficiency with larger designs. Monopole and dipole antennas (such as the quarter-wave monopole antenna in Figure 112) may be excellent choices; however, these types typically require a lumped-element balun and may have unacceptably-large nulls.

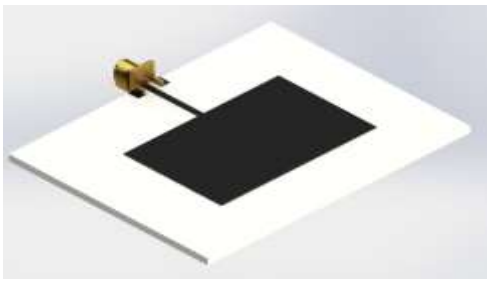

Figure 110 Patch antenna

Figure 111 Planar inverted-F antenna (PIFA)

Figure 112 Quarter-wave monopole

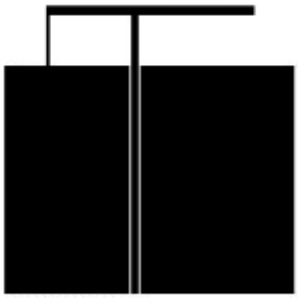

Figure 113 Inverted-F antenna (IFA)

An inverted "F" antenna (IFA) design is chosen for its ease of matching, omni-directionality, and efficiency. These antennas are used commonly in cell phones for GSM, 3G, Wi-Fi, Bluetooth, and GPS. IFAs have four main components. 1) A radiating element, 2) an L-shaped inductor, 3) a short feed line, and 4) a ground plane split by a coplanar waveguide. Figure 114 illustrates the antenna structure, basic dimensions, chosen axis orientation, and the four main components by number.

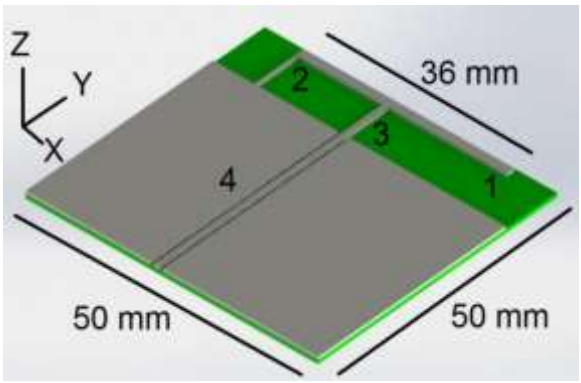

Figure 114 IFA design

Complete antenna dimensions are shown in Figure 115 and are chosen as follows. The length of the radiating element is one quarter-wavelength at 2.45 GHz and tuned to 36 mm. An inductor (the "top" of the "F") is formed by a 7 mm length of 0.5 mm width line and aids in matching. The radiating element is fed at a position which is calculated as the length divided by 3.5 [191]. The 50 ohm coplanar waveguide feed has a width of 1 mm and spacing of 0.5 mm on a 0.8 mm board. The substrate is reasonably-sized considering the size of the antenna while making the ground area as large as possible, 50 x 50 mm. The ground plane measures 50 mm x 39.1 mm.

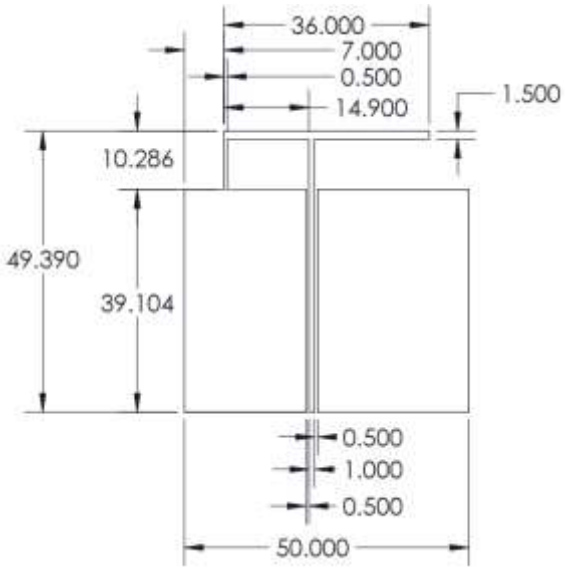

Figure 115 IFA dimensions (mm)

In the case of the curved IFA, the dimensions are reduced slightly to maintain proper tuning with the inclusion of additional dielectric beneath the antenna. In order to better isolate the antenna for measurement, the coaxial feed location is moved to the base of the antenna and the coplanar waveguide is removed. The structure is printed using a 3Dn-600 machine. The dimensions are shown in Figure 116.

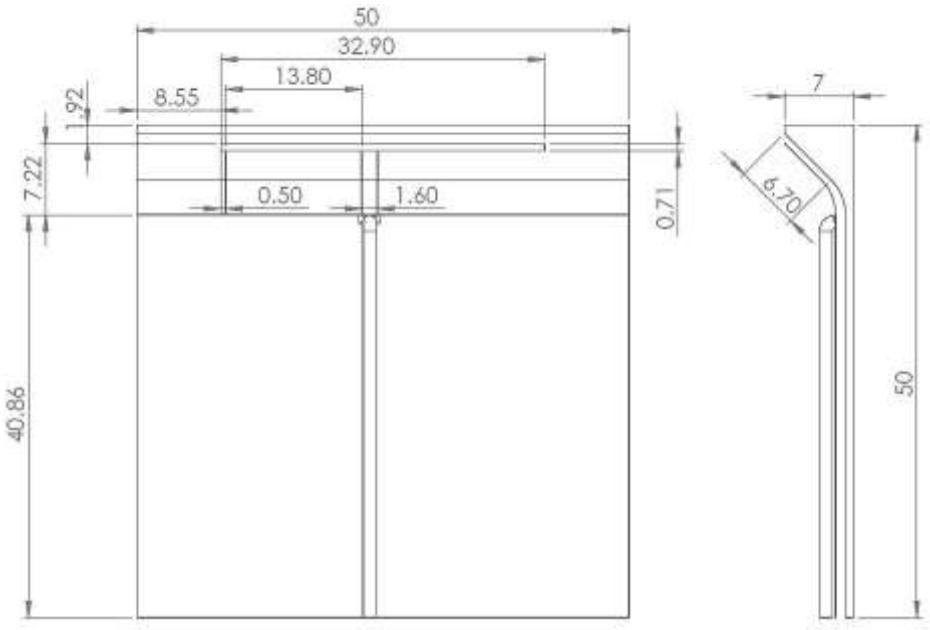

Figure 116 Curved IFA dimensions (mm)

4.3. Dielectric Fabrication

ABS is chosen because it is low-cost, easy to print, readily-available in almost all 3D printing systems, and most importantly, has one of the lowest loss tangents of all 3D printable materials. It has a dielectric constant ε_r = 2.6 to 2.8 and loss tangent D=0.003 [91]. The white ABS substrate is printed using a Stratasys, Ltd. Dimension 1200es 3D printer by technicians at the University of South Florida.

In the case of the curved IFA, the structure is printed using a 3Dn-600 machine and the hardware listed in Table 19. By adjusting the feed rate and print speed the space between lines is

eliminated which prevents crevices from causing problems when conductive paste is applied. No manual surface modification is necessary after printing as is commonly performed on FDM-printed parts since the machine is well-tuned for a smooth surface finish. The layer thickness of 100 µm creates a smooth slope for printing conductive paste. The curved IFA is printed using the equipment and material outlined in below. Temperatures are 230 °C and 90 °C for the nozzle and bed and print speeds are 30 mm/s. The tip is 350 µm, layers are 100 µm, and widths are 500 µm. PET tape is used as a printing surface. A separate flat dielectric constant measurement coupon is fabricated with dimensions 50 mm x 50 mm x 0.8 mm.

Table 19 Curved IFA printing equipment

Item	**Model**	**Supplier/Manufacturer**
Motion	3Dn-600	nScrypt, Inc.
Filament	Lime green ABS	Ultimachines
Extruder	Greg's Wade Reloaded with Herring Bone Gear	Ultibots
Hot end	J-Head	Reifsnyder Precision Works

4.4. Conductor Fabrication

In the case of the flat IFA, CB028 conductive paste is deposited onto the surface of the FDM substrate using an nScrypt, Inc. SmartPump and 3Dn-450 direct printing machine. Designs are loaded in the DXF file format and the printing parameters are shown in Table 20.

Table 20 nScrypt, Inc. printing parameters

Parameter	**Value**
Tip	125/175 i.d./o.d. (μm)
Line width	200 μm
Dispense gap	100 μm
Speed	30 mm/s
Valving	0.5 mm at 8 mm/s
Pressure	8 psi

Drying is performed near the glass transition (maximum) temperature of ABS at 90 ºC for 60 minutes in order to maximize the silver paste conductivity without damaging the substrate. The final part is shown in Figure 117. The resulting cured material is photographed using an SEM in Figure 121.

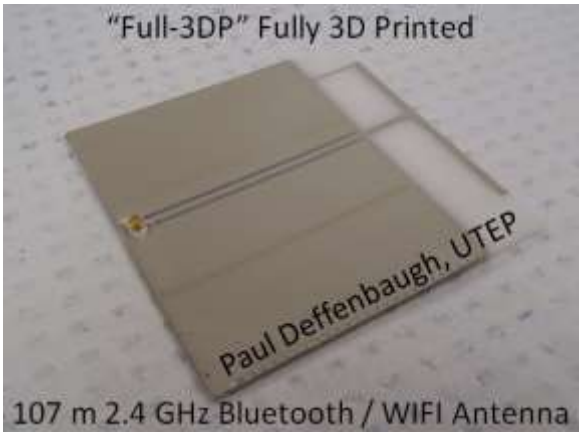

Figure 117 3D printed 2.4 GHz antenna

Metallization in the case of the curved IFA is much more difficult due to the curved surface. CB028 and a 3Dn-Tabletop are used with similar printing parameters to those in Table 20. A Keyence LK-082 laser scanner is used to scan the surface and correct the height of the dispensing tip while the antenna is printed conformal to the surface. 90 ºC post-curing is used. The final part is shown in Figure 118.

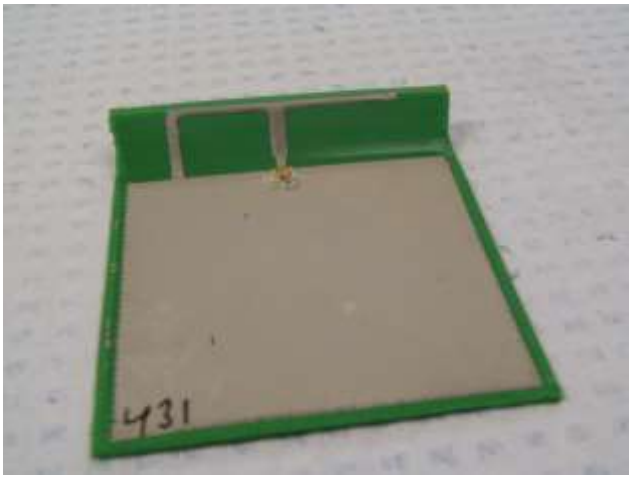

Figure 118 Completed fully 3D printed curved inverted-F antenna

4.5. Coaxial Connection

Surface-mount Hirose U.FL (UMCC) microwave connectors (Figure 119) are used because of their small size and prevalence of use in both laptop and cell phone Wi-Fi and Bluetooth modules including the Bluetooth modules used during testing. Two-part conductive epoxy (Epotek H20E) is deposited in the area of the connector and the connector is installed. The epoxy is cured at 90 ºC for 60 minutes. Several separate test samples of the material are placed in the oven at various temperatures and it is determined that this type of epoxy does not cure below 90 ºC. The epoxy is photographed using an SEM in Figure 120.


Figure 119 Affixed U.FL connector

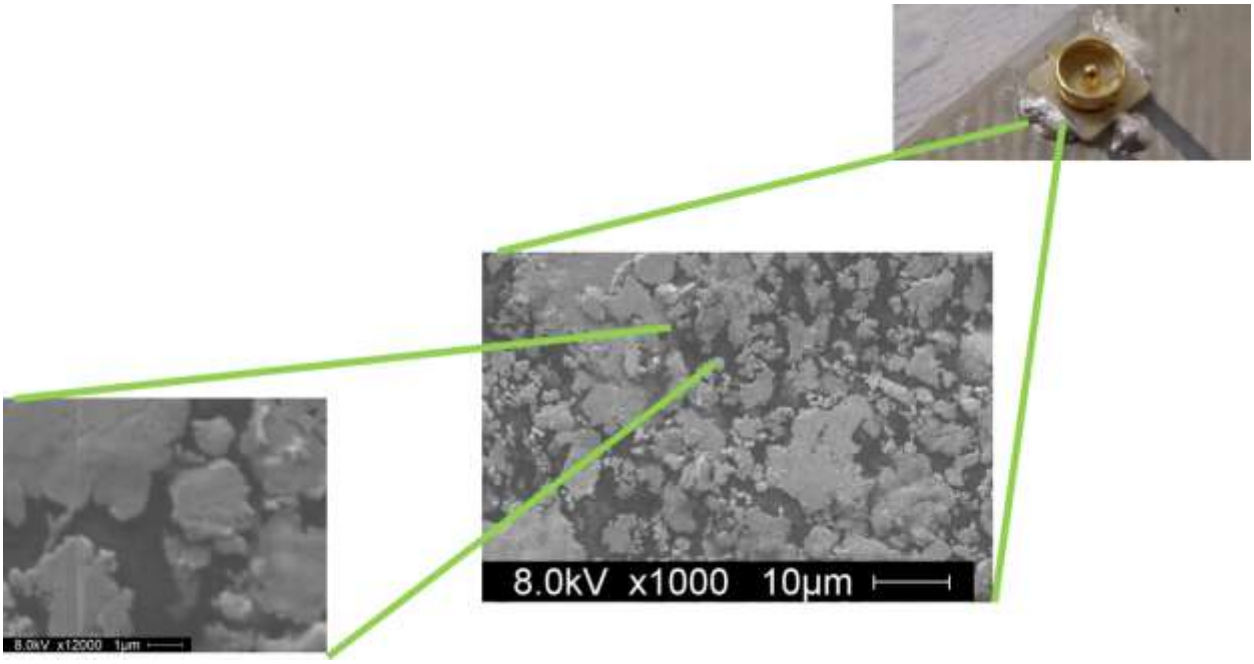

Figure 120 EPO-TEK H20e conductive epoxy

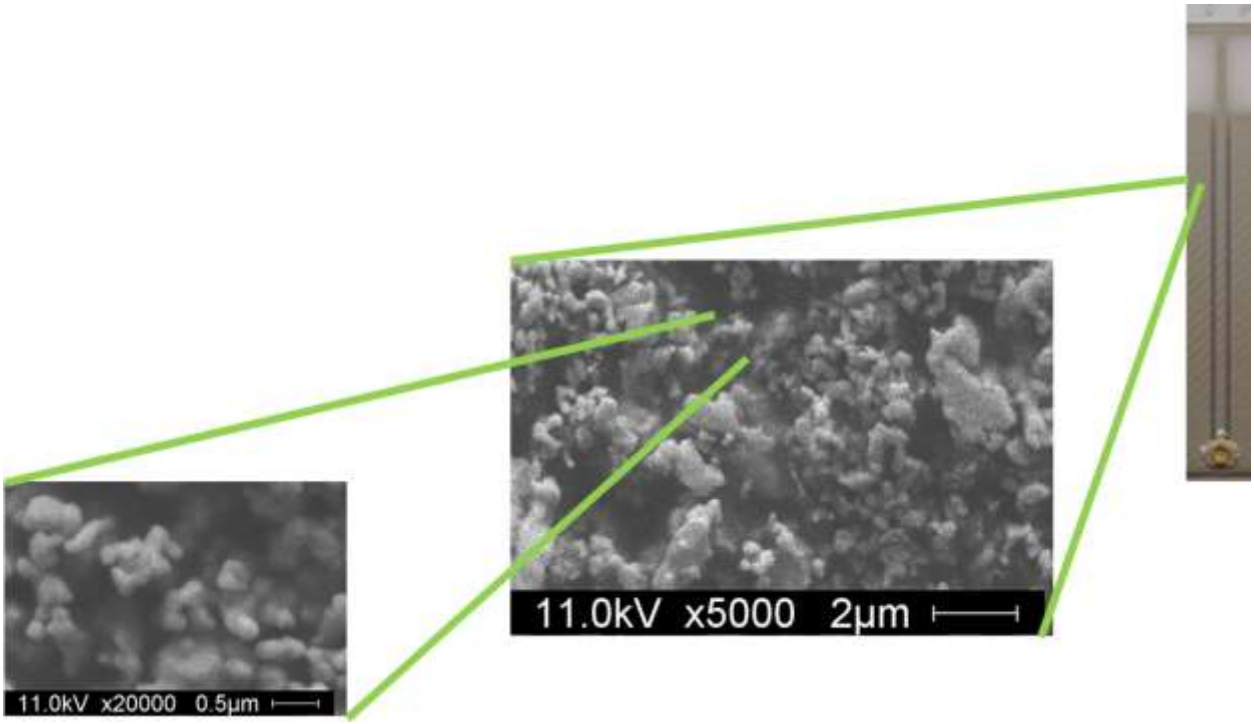

Figure 121 DuPont CB028 thick film silver paste

On top of the conductive epoxy, two-part adhesive epoxy is applied (Figure 119 and Figure 120) to strengthen the connector attachment. The entire connector application process is designed for automation which will result in a completely automated build process.

4.6. Modeling and Measurement

Basic return loss measurements are conducted and are shown as the solid blue lines in Figure 122 – Figure 124. A 100 mm SMA to U.FL adapter cable is used to connect the antenna to an Agilent 8720 VNA. SMA SOLT calibration is used. Cascade Microtech WinCAL software is used to save the S-parameter data to a computer. ANSYS HFSS v15.0.3 is used to model the structure and simulate the antennas expected performance and the data are plotted side-by-side. Appendix Q shows the HFSS model parameters which are used.

4.6.1. Flat IFA

Figure 122 – Figure 124 show data from the flat antenna. The solid blue line shows measured data, the dashed green line shows HFSS data based on printed dimensions, and the red dotted line shows HFSS data based on design dimensions. Certain dimensions such as the CPW feed width and spacing as well as radiating arm width and length are slightly different from the design and these differences are accounted for and modeled.

The difference between the measured and HFSS model data (solid blue/dashed green, 1-2 dB) can be accounted for in the SMA to U.FL cable and U.FL surface-mount connector and conductive epoxy connection.

The ideal design shows better than 1.4:1 SWR from 2.4 – 2.5 GHz and a better than 2:1 SWR is achieved from 2.32 – 2.58 GHz. Referring to Figure 123, the -10 dB bandwidth is 14.4 %.

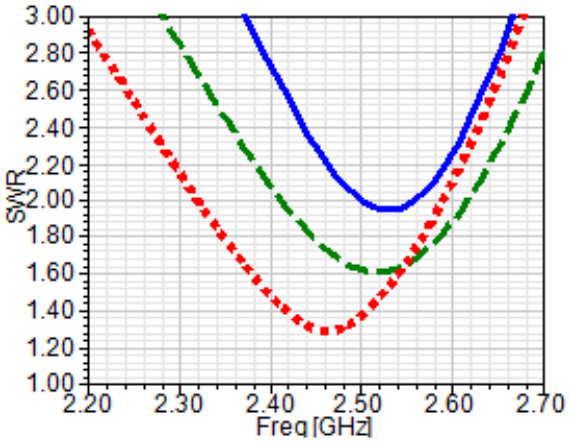

Figure 122 SWR

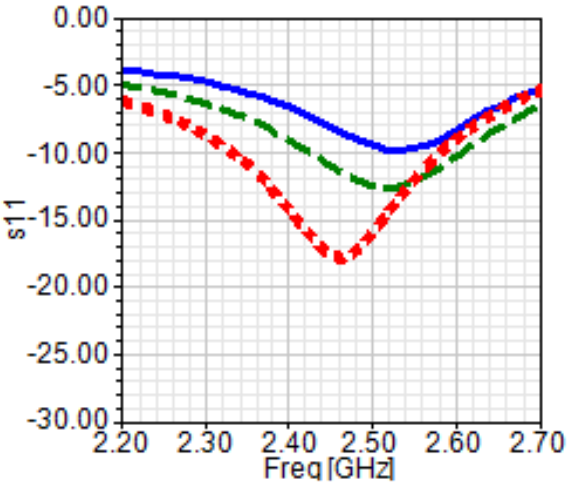

Figure 123 Return loss

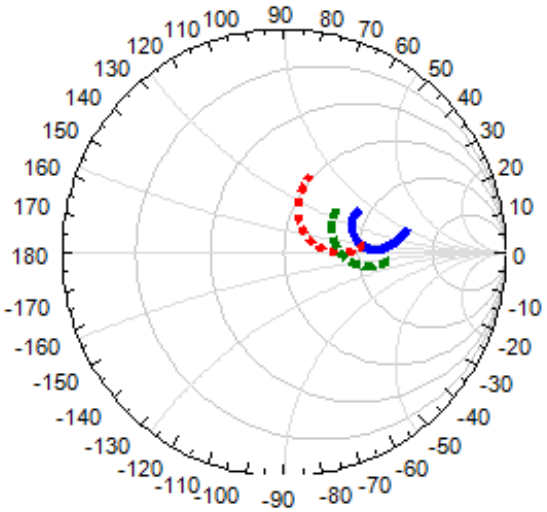

Figure 124 Reflection

Figure 125 shows modeled radiation patterns for the flat antenna. The maximum gain is 5.6 dB in the direction of the Z-axis up from the substrate plane. The gain is better than -10 dB in most directions with an expected null in the direction of the inductor (-X direction) and the ground plane (-Y direction). An IFA is a type of slot antenna and thus radiates mostly in a direction orthogonal to the arm and feed line, across the gap between the arm and ground plane. The E-field polarization is across this gap as well.

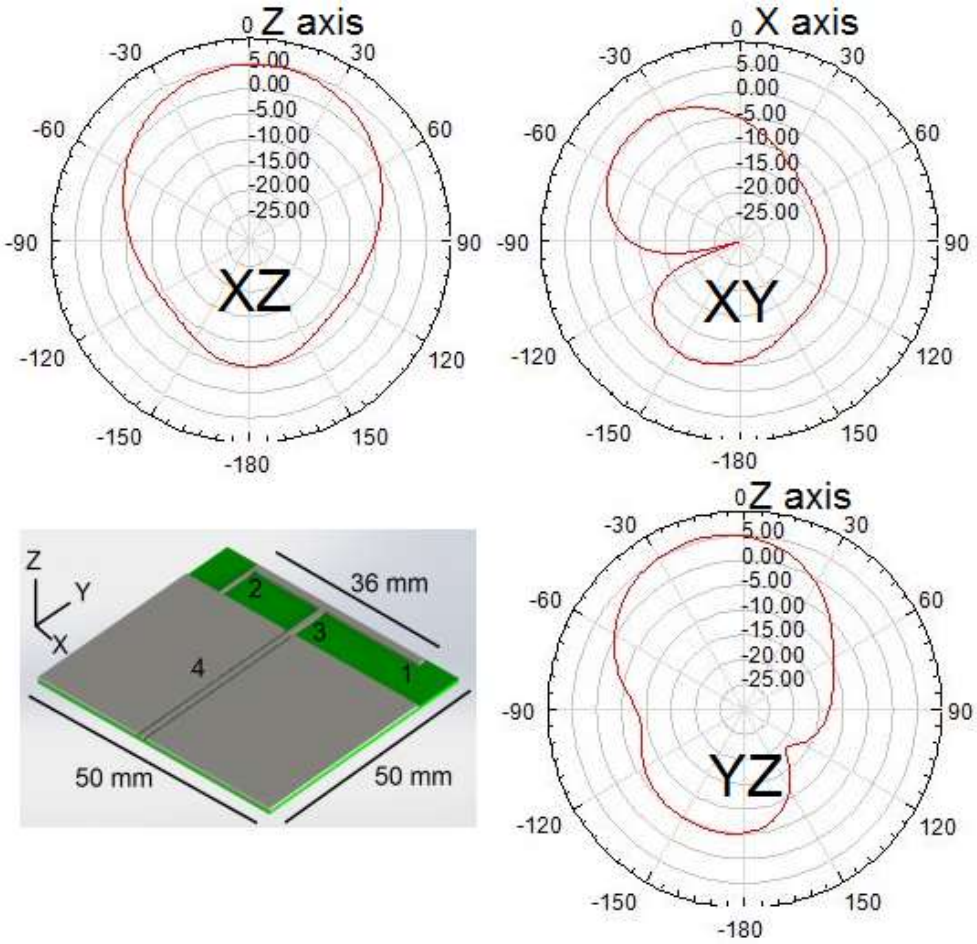

Figure 125 Modeled radiation patterns

4.6.2. Curved IFA

Figure 126 shows the curved IFA as modeled in HFSS. The antennas are measured using the USF antenna measurement chamber. An SAS 570 standard gain horn is used and the raw

data is calibrated to a virtual isotropic radiator to determine realized gain which is plotted with the modeled data in Figure 127. The black trace indicates the measured curved IFA, red: measured data from the flat IFA, green: modeled data from the curved IFA, pink: modeled data from the flat IFA, blue: measured data from the quarter-wave monopole. Performance between the flat and curved antennas is similar and expectedly lower than the quarter-wave antenna which is used for comparison. A slightly lower than expected gain is seen at -90° in the 'minus-Y' direction, the direction of the inductive grounded stub indicating that this maybe interrupting radiation in that direction.

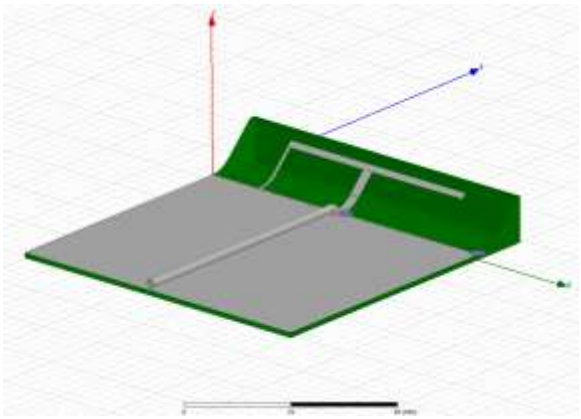

Figure 126 Curved IFA HFSS Model

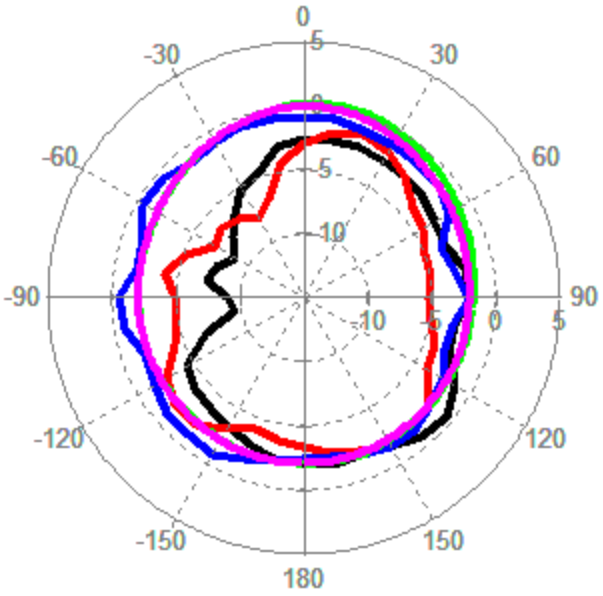

Figure 127 Measured vs. modeled data in the XZ plane

Field testing is conducted using a standard Bluetooth module from Roving Networks (model number RN41XVU-IRM). The module outputs +16 dBm during transmit and receives down to –80 dBm. Bluetooth uses FHSS/GFSK in the band 2.402 – 2.480 GHz. The module is connected to a laptop computer and constitutes the base station. A mobile laptop computer is paired via Bluetooth and the outdoor range is checked. Performance is compared against an SMA quarter-wave monopole antenna which is similar to those used in many laptop computers. The antennas used are Pulse part number W1010 having 2 dBi gain and SWR $\leq$ 2.0 in the range 2.4 – 2.5 GHz. The antennas are connected to the Bluetooth modules using 100 mm long SMA to U.FL cables. Three tests are conducted with different laptops and in different areas at an altitude of 1.5 m above ground. The results are summarized in Table 21. The curved antenna is seen to perform better than the flat antenna, probably due to the lack of printed CPW feed line in the flat antenna. Performance is comparable to but slightly lower than when using the quarter-wave antenna.

Table 21 Test results

Antenna	Test 1	Test 2	Test 3
Base Station Location	N28.5880 W81.2003	N28.5880 W81.2003	N28.5907 W81.1966
Laptop (integrated antennas)	XPS M1330	Q400A	Q400A
Wireless Chipset	Dell BT 355	Intel Wireless-N 2230	Intel Wireless-N 2230
		Useful range in meters	
Conventional Quarter-Wave Antenna	114	240	331
Fully 3D Printed IFA	107	209	275
Fully 3D Printed Curved IFA	N/A	223	292

Conclusion and Recommendations

It is shown here that it is possible to 3D print complex electronic systems directly into the structure of a device with repeatable, reliable results. It is hoped that the techniques discovered and demonstrated here pave the way for the rapid, on-demand, custom manufacture of high-functioning 3D printed objects in a single automated multi-material machine. In the future, it is hoped that software will be made available which allows an easy CAD to print interface for full 3D printing. From a hardware perspective, automated component feed systems will be important additions to 3D printing machines. FDM has characteristically been a low-resolution technology. It is hoped that high resolution FDM will allow miniaturization.

Based on the measurements which are performed, 3D printed materials are viable options for future electronic, RF, and microwave devices. It is suggested that more elaborate RF/microwave components should be made which take advantage of the flexibility, compactness, and rapidity of design to manufacture which 3D printing offers. In light of the unexpectedly high losses which are observed and recorded at high frequencies, characterization of the RF conductor loss mechanism in printable materials is urgently needed.

Rapid manufacture of custom microwave transmission lines of various types is demonstrated. 3D printing allows microwave designers greater flexibility of design in terms of the 3rd dimension while also allowing designers to rapidly tune structures outside of computer based models. The model-verified data which is collected is ready for use in designing more complex structure such as filters, mixers, power dividers and amplifiers, and other microwave devices which rely on fundamental knowledge of the high frequency performance of materials and structures. This allows future work in the area of rapid design to manufacture of

electromagnetic devices which should speed along RF designers in the engineering and tuning process.

Antennas for wireless devices such as cell phones, tablets, and laptop computers have been 3D printed which are shown to perform comparably to typical wire antennas. These antennas are fabricated in an automated fashion with minimal operator interaction. This opens another door for highly complex wireless devices such as the coveted 3D printed cell phone, biometric devices, pacemakers, and others. In particular, it is suggested that in-situ printing and testing will allow rapid test and increased creativity in antenna design.

To summarize, automated multi-layer multi-material printing on one machine is realized, the loss in 3D printed transmission lines is improved, and a fully 3D printed antenna is fabricated using advanced process integration. A process is given here for the fabrication of low loss, high frequency, and dimensionally accurate electronics on one machine. These advancements bring the state of the art closer to providing widespread access to "click-to-print" electronics. It is hoped that not only manufacturers but designers and even consumers will have on-site access to this technology for the rapid fabrication of arbitrary objects.

References

[1] Rashid O. Kadara, Norman Jenkinson, Bo Li, Kenneth H. Church, Craig E. Banks, "Manufacturing electrochemical platforms: Direct-write dispensing versus screen printing, Electrochemistry Communications," vol.10, iss.10, pp.1517-1519, Oct. 2008.

[2] Carlos A. Donado, Dissertation, Doctor of Philosophy, Georgia Institute of Technology, Dec. 2012, available: https://smartech.gatech.edu/bitstream/handle/1853/47532/donado_carlos_a_201305_phd.pdf

[3] D. Jacobs, "Linear Algebra SVD," available: www.cs.umd.edu/~djacobs/CMSC426/LinearAlgebraSVD.pdf or available: www.cs.umd.edu/~djacobs/CMSC426/LinearAlgebraSVD.ppt

[4] A. C. Estes. "Cody Wilson's Fully 3D-Printed Gun Works Alarmingly Well," Retrieved Dec. 5, 2013, available: http://motherboard.vice.com/blog/cody-wilsons-fully-3d-printed-gun-works-alarmingly-well

[5] Ed Sells, Adrian Bowyer, "Directly incorporating electronics into conventional rapid prototypes," 7th National Conference on Rapid Design, Prototyping and Manufacturing, Jun. 1, 2006, available: http://www.reprap.org/mediawiki/images/e/ee/DocumentationMain-sells-bowyer.doc

[6] Edward A. Sells, "Towards a Self-Manufacturing Rapid Prototyping Machine," Ph.D./M.S. thesis, University of Bath, Bath, United Kingdom, Jan. 2009, available: http://opus.bath.ac.uk/20452/2/UnivBath_PhD_2009_E_A_Sells.pdf

[7] Ricardo X. Rodriguez and K. Church, "Process Development for Micro-Electronics Packaging with Direct Printed Additive Manufacturing," W.M. Keck Center for 3D Innovation, University of Texas at El Paso, El Paso, TX.

[8] Tim, "Pick 'n Place Head," Retrieved Jul. 26, 2010, available: http://tim.cexx.org/?p=728

[9] Gul Amin, "ZnO and CuO Nanostructures: Low Temperature Growth, Characterization, their Optoelectronic and Sensing Applications," dissertation, Linköping Studies in Science and Technology, Norrköping Sweden, 2012.

[10] NTH Degree Technologies, retrieved Jun. 6, 2014, available: http://www.nthdegreetech.com/printed-lights.php

[11] C. Morales, J. Dewdney, S. Pal, S. Skidmore, K. Stojak, H. Srikanth, Tom Weller, Wang Jing, "Tunable Magneto-Dielectric Polymer Nanocomposites for Microwave Applications," IEEE Trans. on MTT, vol.59, no.2, pp.302-310, Feb. 2011.

[12] K. Myong-Ki, et al., "Laser Sintering of Inkjet-Printed Silver Nanoparticles on Glass and PET Substrates," 10th IEEE Conference on Nanotechnology, pp.520-524, Aug. 17-20, 2010.

[13] K. Myong-Ki, et al., "Laser Sintering of the Printed Silver paste," IEEE International Symposium on Assembly and Manufacturing, pp.155-158, Nov. 17-20, 2009.

[14] M. Gannon, "3D-Printed Rocket Part Passes Biggest NASA Test Yet," Retrieved Dec. 5, 2013, available: http://www.space.com/22568-3d-printed-rocket-engine-test-video.html

[15] P. I. Deffenbaugh, Josh Goldfarb, Xudong Chen, Kenneth Church, "Fully 3D Printed 2.4 GHz Bluetooth/Wi-Fi Antenna," IMAPS, 46th International Symposium on Microelectronics, Orlando, Florida, Sep. 30 – Oct. 3, 2013, available: http://utminers.utep.edu/pdeffenbaugh

[16] Paul I. Deffenbaugh, "Fully 3D Printed 2.4 GHz Bluetooth/Wi-Fi Antenna," presentation, IMAPS 2013 - Orlando, 46th International Symposium on Microelectronics, Orlando, Florida, Oct. 1, 2013, available: http://utminers.utep.edu/pdeffenbaugh

[17] Cassie. D. Gutierrez, "Three-Dimensional Structural Electronic Integration for Small Satellite Fabrication," M.S. thesis, Elect. Eng., Univ. of Texas at El Paso, El Paso, TX, 2012, available: http://digitalcommons.utep.edu/dissertations/AAI1512575

[18] Cassie. D. Gutierrez, R. Salas, G. Hernandez, D. Muse, R. Olivas, E. MacDonald, M. Irwin, M. Newton, Kenneth H. Church, B. Zufelt, "CubeSat Fabrication Through Additive Manufacturing and Micro-Dispensing," IMAPS 2011.

[19] Amit J. Lopes, Eric MacDonald, Ryan B. Wicker, "Integrating Stereolithography and Direct Print Technologies for 3D Structural Electronics Fabrication," Rapid Prototyping Journal, vol.18, iss.2, 2012.

[20] Frank R. Medina, et al., "Hybrid Manufacturing Integrating Direct Write and Stereolithography," Aug. 23, 2005, available: http://utwired.engr.utexas.edu/lff/symposium/proceedingsArchive/pubs/Manuscripts/2005/2005-05-Medina.pdf

[21] R. I. Olivas, "Conformal Electronics Packaging Through Additive Manufacturing and Micro-Dispensing," Thesis, University of Texas, El Paso, ProQuest Dissertations and Theses, paper number AAI1494367, pp.71, Jan. 1 ,2011, available: http://search.proquest.com/docview/874289503?accountid=14745.

[22] Bosui Liu; Xun Gong; Chappell, W.J., "Applications of layer-by-layer polymer stereolithography for three-dimensional high-frequency components," IEEE Trans. on MTT, vol.52, no.11, pp.2567-2575, Nov. 2004

[23] B. Liu, et al., "Layer-by-layer polymer stereolithography fabrication for three-dimensional RF components," Microwave Symposium Digest, IEEE MTT-S International, vol.2, pp.481–484, Jun. 2004.

[24] Bosui Liu, et al., "Applications of layer-by-layer polymer stereolithography for three-dimensional high-frequency components," IEEE Trans. on MTT, vol.52, no.11, pp.2567–2575, Nov. 2004.

[25] Y. Huang, et al., "Layer-by-layer stereolithography of three-dimensional antennas," 2005 IEEE IEEE Trans. on Ant. and Prop. Society International Symposium, vol.1A, pp.276–279 vol. 1A, Jul. 3, 2005.

[26] Cesar R. Garcia, et al., "Effects of extreme surface roughness on 3D printed antenna horn," Electronics Letters, vol. 49, no. 12, Jun. 6, 2013.

[27] K.F. Brakora, et al., "Design of 3-D Monolithic MMW Antennas Using Ceramic Stereolithography," IEEE Trans. on Ant. and Prop., vol.55, no.3, pp.790–797, Mar. 2007.

[28] Brakora, K.F; Halloran, J; Sarabandi, K., "Design of 3-D Monolithic MMW Antennas Using Ceramic Stereolithography," IEEE Trans. on Ant. and Prop., IEEE Transactions on , vol.55, no.3, pp.790,797, Mar. 2007

[29] N. Delhote, et al., "Ceramic Layer-By-Layer Stereolithography for the Manufacturing of 3-D Millimeter-Wave Filters," IEEE Trans. on MTT, vol.55, no.3, pp.548-554, Mar. 2007.

[30] N. Delhote, Baillargeat, D; Verdeyme, S; Delage, C; Chaput, C., "Ceramic Layer-By-Layer Stereolithography for the Manufacturing of 3-D Millimeter-Wave Filters," IEEE Trans. on MTT, vol.55, no.3, pp.548-554, Mar. 2007.

[31] N. Delhote, D. Baillargeat, S. Verdeyme, C. Delage, C. Chaput, C. Duterte, Y. Abouliatim, T. Chartier, "Electromagnetic band gap millimeter and sub-millimeter 3D resonators manufactured by ceramic stereolithography," Asia-Pacific Microwave Conference, 2007, pp.1,4, Dec. 11-14, 2007.

[32] N. Delhote, et al., "Innovative Shielded High Dielectric Resonator Made of Alumina by Layer-by-Layer Stereolithography," IEEE Microwave and Wireless Components Letters, vol.17, no.6, pp.433-435, Jun. 2007.

[33] N. Delhote, et al., "Large Experimental Bandpass Waveguide in 3D EBG Woodpile Manufactured by Layer-by-Layer Ceramic Stereolithography," Microwave Symposium 2007, IEEE/MTT-S International, pp.1431-1434, Jun. 3, 2007.

[34] N. Delhote, et al., "Narrow Ka Bandpass Filters Made Of High Permittivity Ceramic By Layer-By-Layer Polymer Stereolithography," 36th European Microwave Conference, pp.510-513, Sep. 10, 2006.

[35] DSM Somos, NanoTool datasheet, available: http://www.mfg.uky.edu/tech/ts/nanotool_datasheet.pdf

[36] M. L. Griffith, J. W. Halloran, "Freeform fabrication of ceramics via stereolithography," J. Amer. Ceram. Soc., vol. 79, no. 10, pp.2601–608, 1996.

[37] N. T. Nguyen, et al., "Design and Characterization of 60-GHz Integrated Lens Antennas Fabricated Through Ceramic Stereolithography," IEEE Trans. on Ant. and Prop., vol.58, no.8, pp.2757–2762, Aug. 2010.

[38] Ngoc Tinh Nguyen, N. Delhote, M. Ettorre, D. Baillargeat, L. Le Coq, R. Sauleau, "Design and Characterization of 60-GHz Integrated Lens Antennas Fabricated Through Ceramic Stereolithography," IEEE Trans. on Ant. and Prop., vol.58, no.8, pp.2757-2762, Aug. 2010

[39] M.K. Agarwala, R. van Weeren, R. Vaidyanathan, A. Bandyopadhyay, G. Carrasquillo, V. Jamalabad*, N. Langrana*, A. Safari, S.H. Garofalini, and S.C. Danforth, "Structural Ceramics by Fused Deposition of Ceramics,"

[40] F. Klocke and C. Ader, “Direct laser sintering of ceramics”, Proceedings of Solid Freeform Fabrication Symposium, Austin, TX, USA, pp.447-55, 2003.

[41] Cesar R. Garcia, et al., “3D printing of anisotropic metamaterials,” Progress in Electromagnetics Research Letters, vol.34, pp.75-82, 2012.

[42] Raymond C. Rumpf, et al., “3D Printed Spatially Variant All-Dielectric Metameterials,” unpublished, Jan. 2013.

[43] Raymond C. Rumpf and Javier Pazos, “Synthesis of spatially variant lattices,” Optics Express, vol. 20, no.14, 15263-15274, 2012.

[44] Raymond C. Rumpf, et al., “3D Printed Lattices with Spatially Variant Self-Collimation,” Progress in Electromagnetics Research, vol. 139, pp.1-14, 2013.

[45] Raymond C. Rumpf, et al., “Electromagnetic Isolation of a Microstrip by Embedding in a Spatially Variant Anisotropic Metamaterial,” Progress in Electromagnetics Research, vol. 142, pp.243-260, Sep. 2, 2013.

[46] User name MakerBlock, MakerBot Blog, online, Jan. 14, 2012, accessed 1/15/2014, available: http://www.makerbot.com/blog/tag/key-fob/

[47] M. P. Tonde, “Retrofitting a Stereolithography System Within a Laminar Flow Hood,” M.S. thesis, Mech. Eng., Univ. of Texas at El Paso, El Paso, TX, 2009, available: http://digitalcommons.utep.edu/dissertations/AAI1473894

[48] M.N. Afsar, J.R. Birch, R.N. Clarke, G.W. Chantry, “The measurement of the properties of materials,” Proceedings of the IEEE, vol.74, no.1, pp.183,199, Jan. 1986.

[49] Agilent Technologies, “Agilent Technologies Impedance Measurement Handbook, 4th ed.,” Agilent Technologies, Santa Clara, CA, available: http://cp.literature.agilent.com/litweb/pdf/5950-3000.pdf

[50] D.I. Amey, S. Horowitz, “Materials Performance At Frequencies Up To 20 GHz,” 1st Joint International Electronic Manufacturing Symposium and the International Microelectronics Conference, pp.331,336, Apr. 16-18, 1997.

[51] J. Baker-Jarvis, et al., “High-Frequency Dielectric Measurements,” Instrumentation & Measurement Magazine, IEEE, vol.13, no.2, pp.24-31, Apr. 2010.

[52] J. Baker-Jarvis, E.J. vanzura, W. A. Kissick, “Improved technique for determining complex permittivity with the transmission/reflection method,” IEEE Transactions on, Microwave Theory and Techniques, vol.38, no.8, pp.1096,1103, Aug. 1990.

[53] J. Baker-Jarvis, M. Janezic, D.C. DeGroot, “High-frequency dielectric measurements,” IEEE Instrumentation & Measurement Magazine, vol.13, no.2, pp.24,31, Apr. 2010.

[54] J. Coonrod, “Understanding the variables of dielectric constant for PCB materials used at microwave frequencies,” 41st European Microwave Conference (EuMC), pp.938,-944, Oct. 10-13, 2011.

[55] N.K. Das, S. Voda, David M. Pozar, “Two Methods for the Measurement of Substrate Dielectric Constant,” IEEE Trans. on MTT, vol.35, no.7, pp.636-642, Jul 1987.

[56] DuPont Microcircuit Materials, “DuPont Green Tape Material System Design and Layout Guidelines,” Product Usage Guidelines.

[57] Ferro Electronic Materials, "LTCC PROCESSING INSTRUCTIONS for ferro a6 and L8 Tape," Product Usage Guidelines, available: http://www.ferro.com/non-cms/ems/EPM/content/docs/Ferro%20LTCC%20Design%20Guide.pdf

[58] Hewelett Packard, "Basics of measuring the dielectric properties of materials," application note 1217-1, 1997.

[59] Holzman, E.L., "Wideband measurement of the dielectric constant of an FR4 substrate using a parallel-coupled microstrip resonator," IEEE Trans. on MTT, vol.54, no.7, pp.3127-3130, Jul. 2006.

[60] Hussein Kassem, Valerie Vigneras, Guillaume Lunet, "Characterization techniques for materials properties measurement," Microwave and Millimeter Wave Technologies: from Photonic Bandgap Devices to Antenna and Applications, InTech, Mar. 1, 2010.

[61] K.P. Latti, J.M. Heinola, M. Kettunen, J.P. Strom, P. Silventoinen, "A Review of Microstrip T-resonator Method in Determination of Dielectric Properties of Printed Circuit Board Materials," Proceedings of the 2005 IEEE Instrumentation and Measurement Technology Conference (IMTC), vol.1, pp.62-66, May 16-19, 2005.

[62] A.L. de paula, J.J. Barroso, M.C. Rezende, "Modified Nicolson-Ross-Weir (NRW) method to retrieve the constitutive parameters of low-loss materials," 2011 SBMO/IEEE MTT-S International Microwave & Optoelectronics Conference (IMOC), pp.488-492, Oct. 29 - Nov. 1, 2011.

[63] ABHILASH RAJAGOPAL, "PRINTED CIRCUIT BOARD (PCB) LOSS CHARACTERIZATION UP-TO 20 GHz AND MODELING, ANALYSIS AND VALIDATION," Masters' Thesis, University of Missouri-Rolla, 2007.

[64] B. Riddle, J. Baker-Jarvis, J. Krupka, "Complex permittivity measurements of common plastics over variable temperatures," IEEE Trans. on MTT, vol.51, no.3, pp.727-733, Mar 2003.

[65] Rogers Corporation, "Width and Effective Dielectric Constant Equations for Design of Microstrip Transmission Lines," Application Note, 1982.

[66] Rogers Corporation, "General Design Dielectric Constant Values for Rogers Corporation's High Frequency Materials," available: https://globalcommhost.com/rogers/semiprivate_dev2/docs/General_%20Design_Dielectric_Constant_rev6.pdf

[67] Rogers Corporation, "General Information of Dielectric Constants for Circuit Design using Rogers High Frequency Materials," available: https://globalcommhost.com/rogers/semiprivate_test/docs/General_information_of_design_dk_rev4.pdf

[68] M. V. Schneider, "Dielectric losses in integrated microwave circuits," Bell System Technical Journal, vol.48, no.7, pp.2325-2332, Sept 1969.

[69] J.D. Welch and H.J. Pratt, "Losses in Microstrip Transmission Systems for Integrated Microwave Circuits," NEREM Rec., vol. 8, pp.100-101, 1966.

[70] J. Baker-Jarvis, "Transmission/Reflection and Short-Circuit Line Permittivity Measurements," Technical Note 1341, NIST, Boulder, CO, 2001, available:

http://www.eeel.nist.gov/advanced_materials_publications/Baker-Jarvis%20TN%2090.pdf

[71] T. L. Blakney, W. B. Weir, "Comments on "Automatic measurement of complex dielectric constant and permeability at microwave frequencies," Proceedings of the IEEE, vol.63, no.1, pp.203-205, Jan. 1975.

[72] A. M. Nicolson, G. F. Ross, "Measurement of the Intrinsic Properties of Materials by Time-Domain Techniques," IEEE Transactions on Instrumentation and Measurement, vol.19, no.4, pp.377-382, Nov. 1970.

[73] A. N. Vicente, et al., "The Step by Step Development of NRW Method," Microwave & Optoelectronics Conference (IMOC), 2011 SBMO/IEEE MTT-S International, pp.738-742, Oct. 29, 2011.

[74] W. B. Weir, "Automatic measurement of complex dielectric constant and permeability at microwave frequencies," Proceedings of the IEEE, vol.62, no.1, pp.33-36, Jan. 1974.

[75] Agilent Technologies, "Agilent E4980A Precision LCR Meter 20 Hz to 2 MHz Data Sheet," Agilent Technologies, Santa Clara, CA, available: http://cp.literature.agilent.com/litweb/pdf/5989-4435EN.pdf

[76] Agilent Technologies, "Agilent 16451B Dielectric Test Fixture Operation Manual," Agilent Technologies, Santa Clara, CA, available: http://cp.literature.agilent.com/litweb/pdf/16451-90020.pdf

[77] ASTM Standard D150-11, 2011, "Standard Test Methods for AC Loss Characteristics and Permittivity (Dielectric Constant) of Solid Electrical Insulation," ASTM International, West Conshohocken, PA, 2003, DOI: 10.1520/D0150-11.

[78] Agilent Technologies, "Agilent E4991A RF Impedance/Material Analyzer Data Sheet," Agilent Technologies, Santa Clara, CA, available: http://cp.literature.agilent.com/litweb/pdf/5980-1233E.pdf

[79] Agilent Technologies, "Agilent 16453A Dielectric Material Test Fixture Specification and Service Manual," Agilent Technologies, Santa Clara, CA, available: http://cp.literature.agilent.com/litweb/pdf/16453-90010.pdf

[80] Agilent Technologies, Application Note 1369-2, "Advanced Impedance Measurement Capability of the RF I-V Method Compared to the Network Analysis Method," Agilent Technologies, Santa Clara, CA, available: http://cp.literature.agilent.com/litweb/pdf/5988-0728EN.pdf

[81] David Cure, "Reconfigurable Low Profile Antennas Using Unable High Impedance Surfaces," Dissertation, University of South Florida, Jan. 1, 2013.

[82] David Cure, et al., "Development of a Flexible Electrically-Thick PDMS/LCP Microstrip Antenna", under review at for IEEE Trans. on Ant. and Prop.

[83] William M. Merrill, R.E. Diaz, M.M. LoRe, M.C. Squires, N.G. Alexopoulos, "Effective medium theories for artificial materials composed of multiple sizes of spherical inclusions in a host continuum," IEEE Trans. on Ant. and Prop., vol.47, no.1, pp.142-148, Jan 1999.

[84] O. Wiener, Abh. Math. Phys. K1 Königl. Sächs. Issue 32, p. 509, 1912.

[85] J. C. M. Garnett, “Colors in metal glasses and in metallic films,” Philosoph. Trans. Royal Soc. London, vol.203, pp.385, 1904.

[86] J. C. M. Garnett, “Colors in metal glasses, in metallic films, and in metallic solutions—II,” Philosoph. Trans. Royal Soc. London, vol.205, pp.237–288, 1906.

[87] O. F. Mossotti, “Mem. di mathem. e fisica in Modena,” no.24, issue II, pg.49, 1850.

[88] Rudolf Clausius, “Die mechanische U’grmetheorie 2,” book, pg.62, 1879.

[89] V. D. A. G. Bruggeman, “Betechnung vershiedener physikalischer konstanten von heterogenen substanzen,” Annalen der Physik, vol. 24, ser.5, pp.636–664, 1935.

[90] H. Looyenga, “Dielectric constants of heterogeneous mixtures,” Physica, vol.31, pp.401–406, 1965.

[91] P. I. Deffenbaugh, R. C. Rumpf, K. H. Church, “Broadband Microwave Frequency Characterization of 3-D Printed Materials,” IEEE Transactions on Components, Packaging and Manufacturing Technology (CPMT), accepted for publication, available for early-access: http://ieeexplore.ieee.org/stamp/stamp.jsp?tp=&arnumber=6574280&isnumber=5673025

[92] Jonathan M. O’Brien, Eduardo Rojas, Thomas M. Weller, “A Switched-Line Phase Shifter Fabricated with Additive Manufacturing”. IMAPS 2013.

[93] Eduardo A. Rojas-Nastrucci, T. Weller, Vera Lopez Aida, Fan Cai, John Papapolymerou, “A Study on 3D-Printed Coplanar Waveguide with Meshed and Finite Ground Planes,” WAMICON 2014, Jun. 2014.

[94] Agilent Technologies, “Applying the 8510 TRL Calibration for Non-Coaxial Measurements,” Product Note 8510-8A, May 4, 2001.

[95] Inder J. Bahl, D.K. Trivedi, “A Designer’s Guide to Microstrip Line,” Microwaves, 1977.

[96] P. Barnwell, M.P. O'Neill, C. Free, “Integrated microwave structures using an advanced thick-film technology,” 1999 IEEE Radio and Wireless Conference (RAWCON), pp.259-262, 1999

[97] M.C. Bailey, and M.D. Despande, “Characteristic Impedance of Microstrip Lines,” Nov. 1989.

[98] T. Björninen, “Performance Comparison of Silver paste and Copper Conductors for Microwave Applications,” Microwaves, Antennas & Propagation (IET), vol.4, no.9, pp.1224-1231, Sep. 2010.

[99] S. Cantaragiu, “Analysis of shielded microstrip lines by finite-difference method,” Proceedings of the 6th IEEE International Conference on Electronics, Circuits and Systems (ICECS), vol.1, pp.565-567, 1999.

[100] E. J. Denlinger, “Losses of Microstrip Lines,” IEEE Trans. on MTT, vol. 28, no 6, Jun. 1980.

[101] M.J. Degerstrom, B.K. Gilbert, E.S. Daniel, “Accurate Resistance, Inductance, Capacitance, and Conductance (RLCG) from Uniform Transmission Line Measurements,” Electrical Performance of Electronic Packaging, pp.77,80, Oct. 27-29, 2008.

[102] W.J. Getsinger, “Measurement and Modeling of the Apparent Characteristic Impedance of Microstrip,” Microwave Theory and Techniques, IEEE Transactions on, vol.31, no.8, pp.624-632, Aug. 1983.

[103] E.O. Hammerstad, “Equations for Microstrip Circuit Design,” 5th European Microwave Conference, pp.268-272, Sep. 1-4, 1975.

[104] Schneider, M.V., "Microstrip lines for microwave integrated circuits," The Bell System Technical Journal, vol.48, no.5, pp.1421-1444, May-Jun. 1969.

[105] Dave Kirkby, “Finding the Characteristics of Arbitrary Transmission Lines,” Dec. 1996.

[106] Ivo Locher, Gerhard Troster, “Screen-printed Textile Transmission Lines,” Textile Research Journal, vol.77, no.11, pp.837-842, Nov. 2007.

[107] R. Makinen, “Wide-band Electrical Characterization of Printable Nano-Particle Copper Conductors,” Microwave Conference, Asia Pacific, pp.2455,2458, Dec. 7-10, 2009.

[108] Sophocles J. Orfanidis, Electromagnetic Waves and Antennas, online book, 2004.

[109] Chen Peng, Fang Shao-jun, Wang En-cheng, “Analysis of characteristic impedance of asymmetric coplanar waveguide using finite-difference time-domain method,” IEEE International Symposium on Microwave, Antenna, Propagation and EMC Technologies for Wireless Communications, (MAPE), vol.1, pp.91,94, Aug. 8-12, 2005.

[110] R. A. Pucel, et al., “Losses in Microstrip,” IEEE Trans. on MTT, vol.16, no.6, pp.342-350, Jun. 1968, available: http://ieeexplore.ieee.org/stamp/stamp.jsp?tp=&arnumber=1126691

[111] V. Pynttari, et al., “High-Frequency Characterization and Simulation of Conductor Loss in Printable Electronics Technology,” IEEE Electrical Performance of Electronic Packaging, pp.219-222, Oct. 29-31, 2007.

[112] V. Pynttari, et al., “Significance of Conductivity and Thickness of Thin Inkjet Printed Microstrip Lines,” 12th IEEE Workshop on Signal Propagation on Interconnects, pp.1-4, May 12-15, 2008

[113] J. C. Rautio, “An Investigation of Microstrip Conductor Loss,” Microwave Magazine, pp.60-67, Dec. 2000.

[114] C. Reig, E. A. Navarro, V. Such, “Calculation of the characteristic impedance of microstrips using a full-wave 2-D FDTD scheme,” Microwave Optical Technology. Letters, no.16, pp.58–60, 1997.

[115] Rogers Corp., “Width and Effective Dielectric Constant Equations for Design of Microstrip Transmission Lines,” Application Note.

[116] O.S. Rosales, D. Suster, “Finite-difference computation of the characteristic impedance of unbounded striplines and microstrip lines,” Proceedings of the First IEEE

International Caracas Conference on Devices, Circuits and Systems, pp.323-327, Dec. 12-14, 1995.

[117] M.N.O. Sadiku, C.N. Obiozor, “Finite element computation of the characteristic impedance of transmission lines,” Proceedings of Southeastcon '97, Engineering the New Century, pp.166-168, Apr. 12-14, 1997.

[118] M. K. Sampath, “On Addressing the Practical Issues in the Extraction of RLGC Parameters for Lossy Multiconductor Transmission Lines using S-parameter Models,” Electrical Performance of Electronic Packaging, pp.259-262, Oct. 27-29, 2008

[119] M.V. Schneider, “Computation of Impedance and Attenuation of TEM-Lines by Finite Difference Methods,” IEEE Transactions on MTT, vol.13, no.6, pp.793-800, Nov 1965.

[120] B. Shao, “Electrical Characterization of Inkjet Printed Interconnections on Flexible Substrates,” Online, available: http://www.ecgepro.eu/pub/pubdok/botao.pdf

[121] UltraCAD Design, Inc., “Microstrip Propagation Times, Slower Than We Think,” available: www.ultracad.com/mentor/microstrip%20propagation.pdf

[122] Welch and Pratt, “Losses in microstrip Transmission systems for integrated microwave circuits,” NEREM rec. col 8, pp 100-101, 1966.

[123] Harold A. Wheeler, "Transmission-Line Properties of Parallel Strips Separated by a Dielectric Sheet," IEEE Transactions on MTT, vol.13, no.2, pp.172-185, Mar 1965.

[124] Harold A. Wheeler, “Transmission-Line Properties of a Strip on a Dielectric Sheet on a Plane,” IEEE Transactions on MTT, vol.25, no.8, pp.631-647, Aug 1977.

[125] J. M. Wilson, et al., “High-Frequency Characterization of Printed CPW Lines on Textiles using a Custom Test Fixture,” IEEE Workshop on Signal Propagation on Interconnects, pp.279-280, May 9-12, 2006.

[126] Heping Yue, K.L. Virga, J. Prince, “Dielectric constant and loss tangent measurement using a stripline fixture,” 48th IEEE Electronic Components & Technology Conference, pp.1077-1082, May 25-28, 1998.

[127] A. Artemenko, A. Maltsev, R. Maslennikov, A. Sevastyanov, V. Ssorin, “Design of Wideband Waveguide to Microstrip Transition for 60 GHz Frequency Band,” Proceedings of the 41st European Microwave Conference, Oct. 10-13, 2011.

[128] Paul I. Deffenbaugh, Thomas M. Weller, Kenneth H. Church, “Fabrication and Microwave Characterization of 3D-Printed Microstrip Transmission Lines,” submitted for publication, IEEE Transactions on Components and Manufacturing Technologies, Feb. 2014.

[129] P.S.A. Evans, P.M. Harrey, B.J. Ramsey, D.J. Harrison, “Lithographic film circuits – a review”, Circuit World, vol. 27, iss.3, pp.31–35, 2001.

[130] P. S. A. Evans, B. J. Ramsey, D. J. Harrison, P. R. Shepherd, “Further Developments of Microwave CLFs,” Automated R.F. and Microwave Measurement Society Conf. 7th - 8th, 2001.

[131] Lilja, J; Makinen, R; Pynttari, V; Mansikkamaki, P; Kivikoski, M., “Application of Thin-Film RCLG Model for the Modeling of Inkjet Printed Microstrip Lines,” 12th

IEEE Workshop on Signal Propagation on Interconnects (SPI), pp.1,4, May 12-15, 2008.

[132] S. Merilampi, T. Laine-Ma, P. Ruuskanen, "The characterization of electrically conductive silver paste patterns on flexible substrates," Microelectronics Reliability, vol.49, iss.7, Jul. 2009, pp.782-790.

[133] E. Hrehorova, et al., "Gravure Printing of Conductive pastes on Glass Substrates for Applications in Printed Electronics," Journal of Display Technology, vol.7, no.6, pp.318-324, Jun. 2011.

[134] Marko Pudas, Niina Halonen, Päivi Granat, Jouko Vähäkangas, "Gravure printing of conductive particulate polymer inks on flexible substrates," Progress in Organic Coatings, vol.54, iss.4, pp.310-316, Dec. 1, 2005.

[135] Pynttari, V; Makinen, R; Lilja, J; Pekkanen, V; Mantysalo, M; Mansikkamaki, P; Kivikoski, M., "High-frequency characterization and simulation of conductor loss in printable electronics technology," IEEE Electrical Performance of Electronic Packaging, pp.219-222, Oct. 29-31, 2007.

[136] Pynttari, V; Makinen, R; Lilja, J; Pekkanen, V; Mansikkamaki, P; Kivikoski, M., "Significance of Conductivity and Thickness of Thin Inkjet Printed Microstrip Lines," 12th IEEE Workshop on Signal Propagation on Interconnects (SPI), pp.1-4, May 12-15, 2008.

[137] Botao Shao, Roshan Weerasekera, Abraham Tareke Woldegiorgis, Li-Rong Zheng, Ran Liu, Werner Zapka, Peter Lindberg, "Electrical Characterization of Inkjet Printed Interconnections on Flexible Substrates," available: http://www.ecgepro.eu/pub/pubdok/botao.pdf

[138] Shepherd, P.R; Taylor, C; Evans, P. S A; Harrison, D.J., "Measurement and Modeling of MIC Components Using Conductive Lithographic Films," 31st European Microwave Conference, pp.1-4, Sep. 24-26, 2001.

[139] Z. Radivojevic1, K. Andersson1, K. Hashizume, M. Heino1, M. Mantysalo, P. Mansikkamaki, Y. Matsuba, N. Terada, "OPTIMISED CURING OF SILVER PASTE JET BASED PRINTED TRACES," TIMA Editions/THERMINIC 2006, Nice, Côte d'Azur, France, Sep. 27-29, 2006.

[140] G. Antonini, et al., "Equivalent circuit extraction for an SMA connector," Progress in Electromagnetic Research Symposium, Pisa, Italy, Mar. 28-31, 2004.

[141] D. M. Pozar, "Microwave Engineering," 4th edition, Wiley, Nov. 22, 2011.

[142] P. C. Joshi, et al., "Direct Digital Additive Manufacturing Technologies: Path Towards Hybrid Integration," Materials Science and Technology Division, Oak Ridge National Laboratory, Oak Ridge, TN.

[143] Andrzej Dziedzic, "Polymer/conductive filler composites - chosen properties and application," Proceedings of SPIE, vol.2780, pp.18-24.

[144] T. Björninen, S. Merilampi, L. Ukkonen, P. Ruuskanen, L. Sydänheimo, "Performance comparison of silver paste and copper conductors for microwave applications," IET Microwaves, Antennas & Propagation, vol.4, no.9, pp.1224-1231, Sep. 2010.

[145] Keithly Corp., "Performing van der Pauw Sheet Resistance Measurements Using the Keithley S530 Parametric Tester," Application Note Number 3180, available: http://www.keithley.com/data?asset=57003

[146] NIST, "Hall effect measurement," website, available: http://www.nist.gov/pml/div683/hall_effect.cfm#vanderpauw

[147] Van der Pauw, L. J. "A Method of Measuring Specific Resistivity and Hall Effect of Discs of Arbitrary Shape" Philips Research Reports, 12.1, vol. 13, no. 1, Feb. 1958, pp1-9, available: http://socrates.berkeley.edu/~phylabs/adv/ReprintsPDF/SHE%20Reprints/01-Measuring%20Discs.pdf

[148] David A. Roberson, R.B. Wicker, E. MacDonald, "Ohmic Curing of Printed Silver Conductive Traces," Journal of Electronic Materials, vol. 41, no.9, 2012.

[149] Agilent Technologies, Application Note 1287-1, "Understanding the Fundamental Principles of Vector Network Analysis," Agilent Technologies, Santa Clara, CA, available: http://cp.literature.agilent.com/litweb/pdf/5988-0728EN.pdf

[150] Leung Chiu; Quan Xue; Chi-Hou Chan, "Performance enhancement of microwave circuits using parallel-strip line," IEEE Potentials Magazine, vol.29, no.5, pp.16-21, Sep.-Oct. 2010.

[151] Dib, N. I; Harokopus, W. P., Jr; Katehi, P.B; Ling, C.C; Rebeiz, G.M., "Study of a novel planar transmission line," IEEE MTT-S International Microwave Symposium Digest, pp.623-626 vol.2, Jul. 10-14, 1991

[152] Drach, W.C; Koscica, T.E., "Transitioning between microstrip and inverted microstrip," IEEE Microwave and Guided Wave Letters, vol.1, no.3, pp.49-50, Mar. 1991

[153] L. Harle, L.P.B. Katehi, "A Vertically Integrated Micromachined Filter," IEEE Trans. on MTT, vol.50, no.9, pp.2063-2068, Sep. 2002.

[154] K. Hettak, M.G. Stubbs, K. Elgaid, I.G.Thayne, "Design and Characterization of Elevated CPW and Thin Film Microstrip Structures for Millimeter-Wave Applications," European Microwave Conference, vol.2, pp.4, Oct. 4-6, 2005.

[155] Park, K. Y; Park, J.Y; Choi, H. K; Lee, J.C; Lee, B; Kim, J.H; Kim, N.Y; Park, J.Y; Kim, G.H; Kim, D.W; Bu, J.U; Chung, K.W., "A novel Ka-band bandpass filter using LIGA micromachined process," Asia-Pacific Microwave Conference, pp.1306-1309, 2000

[156] K.C. Gupta, Ramesh Garg, Inder J. Bahl, Prakash Bhartia, "Microstrip Lines and Slotlines," Second Edition, Artech House, Norwood, MA, 02062, 1996.

[157] Gi-Hyon Ryu; Dae-Hyun Kim; Lee, Jae-Hak; Kwang-Seok Seo, "A Novel 3-dB Coupler for MMIC using Air-Gap Stacked Microstrip Lines," IEEE Microwave and Guided Wave Letters, vol.10, no.1, pp.1-3, Jan 2000.

[158] Inho Jeong; Seong-Ho Shin; Ju-Hyun Go; Joong-Soo Lee; Choong-Mo Nam; Dong-Wook Kim; Young-Se Kwon, "High-Performance Air-Gap Transmission Lines and Inductors for Millimeter-Wave Applications," IEEE Trans. on MTT, vol.50, no.12, pp.2850-2855, Dec. 2002.

[159] Koul, S.K; Bhat, B; Krishnaswamy, M. C., "Passive Components in Inverted Microstrip and Suspended Microstrip Configurations," 1983 IEEE MTT-S International Microwave Symposium Digest, , pp.412-414, May 31-Jun. 3, 1983

[160] Koul, S.K; Bhat, B., "Inverted microstrip and suspended microstrip with anisotropic substrates," Proceedings of the IEEE, vol.70, no.10, pp.1230-1231, Oct. 1982

[161] Lucyszyn, S; Miyaguchi, K; Jiang, H.W; Robertson, Ian D; Fisher, G; Lord, A; Joo-Young Choi, "Micromachined RF-Coupled Cantilever Inverted-Microstrip Millimeter-Wave Filters," Journal of Microelectromechanical Systems, vol.17, no.3, pp.767-776, Jun. 2008.

[162] Musa, S.M; Sadiku, M.N.O., "Modeling of shielded, suspended and inverted, microstrip lines," IEEE Southeastcon, 2008, pp.309,313, Apr. 3-6, 2008.

[163] Musa, S.M; Sadiku, M.N.O., "Modeling of Unshielded Suspended and Inverted Substrate Microstrip Lines," 2008 IEEE Region 5 Conference, pp.1-5, Apr. 17-20, 2008.

[164] C.B. Mulenga, J.A. Flint, R. Vaja, A. Chauraya, "Measurement Techniques for Polar Electromagnetic Bandgap Structures using an Air Spaced Microstrip Line," IEEE Trans. on Ant. and Prop. Conference, Loughborough, pp.341-344, Mar. 17-18, 2008.

[165] Schellenberg, J.M., "CAD models for suspended and inverted microstrip," IEEE Trans. on MTT, vol.43, no.6, pp.1247-1252, Jun 1995.

[166] M.V. Schneider, "Dielectric Loss in Integrated Microwave Circuits," Bell Labs Technical Journal, vol.48, iss.7, pp.2325-2332, Sep. 1969.

[167] S. Seong-Ho, et al., "Ka-Band Branch Line Coupler Using High-Performance Air-Buried Microstrip Lines," 33rd European Microwave Conference, pp.951-954, Oct. 2003.

[168] S. Seong-Ho, et al., "Monolithic Implementation of Air-Buried Microstrip Lines for High-Density Microwave and Millimeter Wave ICs," Proceedings 52nd Electronic Components and Technology Conference, pp.1018-1020, 2002.

[169] S. Shin et al., "Ka-Band Branch Line Coupler Using High-Performance Air-Buried Microstrip Lines," 33rd European Microwave Conference, pp.951-954, Oct. 2003.

[170] T.J. Spencer, R. Saha, Jikai Chen, R. Bashirullah, Kohl, A. Paul, "Air Cavity Transmission Lines for Off-Chip Interconnects Characterized to 40 GHz," IEEE Transactions on Components, Packaging and Manufacturing Technology, vol.2, no.3, pp.367-374, Mar. 2012.

[171] Thomas McCrea Weller, "Micromachined High Frequency Transmission Lines on Thin Dielectric Membranes," Ph.D. dissertation, The University of Michigan, May 1995.

[172] Thomas McCrea Weller, Katehi, L.P.B; Rebeiz, G.M., "High performance microshield line components," IEEE Trans. on MTT, vol.43, no.3, pp.534-543, Mar 1995.

[173] Thomas McCrea Weller, Rebeiz, G.M; Katehi, L.P., "Experimental results on microshield transmission line circuits," 1993 IEEE MTT-S International Microwave Symposium Digest, pp.827-830 vol.2, Jun. 14-18, 1993.

[174] Thomas McCrea Weller, Katehi, L. P; Rebeiz, G. M., "Fabrication and characterization of microshield circuits," National Radio Astronomy Observatory, Apr. 1993.

[175] Willke, T.L; Gearhart, S.S., "LIGA micromachined planar transmission lines and filters," IEEE Trans. on MTT, vol.45, no.10, pp.1681-1688, Oct 1997.

[176] Willke, T.L; Gearhart, S.S., "Novel micromachined LIGA microstrip transmission lines and filters," 1996 IEEE MTT-S International Microwave Symposium Digest, vol.2, pp.1189-1192, Jun. 17-21, 1996.

[177] Yu, J.I; Kwon, Y.S., "Low Insertion Loss K-band BPF using Parallel-Coupled Air-Suspended Microstrip Lines on Anodised Aluminium Substrate," Electronics Letters, vol.48, no.8, pp.437-438, Apr. 12, 2012.

[178] Hualiang Zhang; Jinwen Zhang; L.L.W.Leung, K.J. Chen, "Bandpass and Bandstop Filters using CMOS-Compatible Micromachined Edge-Suspended Coplanar Waveguides," Asia-Pacific Microwave Conference Proceedings, vol.1, pp.4, Dec. 4-7, 2005.

[179] Jianmin Zhang; Drewniak, J.L; Pommerenke, D.J; DuBroff, R.E; Zhiping Yang; Wheling Cheng; Fisher, J; Camerlo, S., "Signal link-path characterization up to 20 GHz based on a stripline structure," 2006 IEEE International Symposium on Electromagnetic Compatibility (EMC), vol.2, pp.356-361, Aug. 14-18, 2006.

[180] K. Kirschenmann, K.W. Whites, S.M. Woessner, "Inkjet-Printed Microwave Frequency Multilayer Antennas," IEEE Trans. on Ant. and Prop. Society International Symposium, pp.924-927, Jun. 9-15, 2007.

[181] T. Blecha, A. Hamacek, J. Reboun, "High Frequency Behavior of Microstrip Lines on Composite Photopolymer Substrate," 30th International Spring Seminar on Electronics Technology, pp.208-212, May 9-13, 2007.

[182] G. Selli, et al., "3D Modeling and Circuit Model Extraction of Vias in Multilayer Printed Circuit Boards," Progress in Electromagnetic Research Symposium, Pisa, Italy, Mar. 28-31, 2004.

[183] Tian, Zhengrong; Free, C; Barnwell, Peter; Wood, James; Aitchison, Colin, "Design of Novel Multilayer Microwave Coupled-Line Structures using Thick- Film Technology," 31st European Microwave Conference, pp.1-4, Sep. 24-26, 2001.

[184] Kenneth H, Church, Harvey Tsang, Ricardo Rodriguez, Paul Deffenbaugh, Raymond Rumpf, "Printed Circuit Structures, the Evolution of Printed Circuit Boards," ICP APEX EXPO Conference, available: http://www.ipcoutlook.org/pdf/printed_circuit_structures_ipc.pdf

[185] Kenneth H. Church, Eric MacDonald, Patrick Clark, Robert Taylor, D. Paul, K. Stone, M. Wilhelm, Frank Medina, J. Lyke, Ryan Wicker, "Printed electronic processes for flexible hybrid circuits and antennas," 2009 Flexible Electronics & Displays Conference and Exhibition, pp.1-7, Feb. 2-5, 2009.

[186] Paul M. Harrey, Peter S. A. Evans, Member, and David J. Harrison, Member, "Integrated Capacitors for Conductive Lithographic Film Circuits," IEEE Transactions on Electronics Packaging Manufacturing, vol.24, no.4, Oct. 2001.

[187] Ubaldo Robles, Paul Deffenbaugh, Harvey Tsang, Raymond Rumpf, "3D Printed Impedance Elements by Micro-Dispensing," Jun. 2013, available: http://digitalcommons.utep.edu/elec_comp_papers/72/ Abstract: http://www.imaps.org/abstracts/system/new/abstract_preview.asp?abstract=2013imaps235

[188] Paul I. Deffenbaugh, "A Printed-Electronics Flying Camera," presentation, IMAPS Florida Chapters Microelectronics, Manufacturing, Materials and Application Symposium & Exhibition, Orlando, Florida, Feb. 24, 2011, available: http://utminers.utep.edu/pdeffenbaugh

[189] Paul I. Deffenbaugh, "Microwaves in 3D Printed Electronics," presentation, IMAPS Advanced Technology Workshop on 3D and Conformable Printed Electronic Packaging Materials, Manufacturing & Applications, El Paso, TX, Feb. 22-23, 2012, available: http://utminers.utep.edu/pdeffenbaugh

[190] Ryan B. Wicker, Francisco Medina, and Chris J. Elkins, "MULTIPLE MATERIAL MICRO-FABRICATION: EXTENDING STEREOLITHOGRAPHY TO TISSUE ENGINEERING AND OTHER NOVEL APPLICATIONS," Proceedings of 15th Annual Solid Freeform Fabrication Symposium, Austin, TX, Aug. 4, 2004.

[191] I. Rosu, "Small Antennas for High Frequencies," [Online], available: http://www.qsl.net/va3iul/Antenna/Small_Antennas_for_High_Frequencies/Small_Antennas_for_High_Frequencies.pdf

[192] J. Siden, M.K. Fein, A. Koptyug, H.E. Nilsson, "Printed antennas with variable conductive paste layer thickness," Microwaves, Antennas & Propagation (IET), vol.1, no.2, pp.401-407, Apr. 2007.

[193] J. Siden, T. Olsson, A. Koptioug, Hans-Erik Nilsson, "Reduced Amount of Conductive paste with Gridded Printed Antennas," 5th International Conference on Polymers and Adhesives in Microelectronics and Photonics, Polytronic, pp.86-89, Oct. 23-26, 2005.

[194] R. A. Li Yang, et al., "RFID Tag and RF Structures on a Paper Substrate using Inkjet-Printing Technology," IEEE Trans. on MTT, vol.55, no.12, pp.2894-2901, Dec. 2007.

[195] Toni Björninen, Sari Merilampi, Leena Ukkonen, Lauri Sydänheimo, Pekka Ruuskanen, "The Effect of Fabrication Method on Passive UHF RFID Tag Performance," International Journal of IEEE Trans. on Ant. and Prop., Jan. 2009.

[196] John Costenoble, "Rotary Screen Printing: The Productive Solution for HF/UHF RFID Labels," SGIA Journal Fourth Quarter, 2005.

[197] A. Dziedzic, P. Slobodzian. "Modern Microelectronic Technologies in Fabrication of RFID Tags," Radio engineering Proceedings of Czech and Slovak Technical Universities, vol.20, no.1, Apr. 2011 available: http://www.radioeng.cz/fulltexts/2011/11_01_187_193.pdf

[198] K. Janeczek, G. Koziol, T. Serzysko, M. Jakubowska, "Investigation of RFID tag antennas printed on flexible substrates using two types of conductive pastes," 3rd Electronic System-Integration Technology Conference (ESTC), pp.1,5, Sep. 13-16 2010.

[199] Botao Shao; R. Weerasekera, A.T. Woldegiorgis, Li-Rong Zheng; Ran Liu; W. Zapka, "High frequency characterization and modeling of inkjet printed interconnects on flexible substrate for low-cost RFID applications," 2nd Electronics System-Integration Technology Conference (ESTC), pp.695-700, Sep. 1-4, 2008.

[200] B. Shao, "High Frequency Characterization and Modeling of Inkjet-Printed Interconnects on Flexible Substrate for Low-Cost RFID Applications," 2nd Electronics System-Integration Technology Conference, pp.695-700, Sep. 1-4, 2008.

[201] DuPont, "Processing Guide for Printing RFID Antennae," DuPont Microcircuit Materials, available: http://www2.DuPont.com/MCM/en_US/assets/downloads/prodinfo/RFID_ProcessingGuide.pdf

[202] A. Dziedzic, P. Slobodzian. "Modern Microelectronic Technologies in Fabrication of RFID Tags," Radioengineering Proceedings of Czech and Slovak Technical Universities, vol.20, no.1, Apr. 2011, available: http://www.radioeng.cz/fulltexts/2011/11_01_187_193.pdf

[203] Anne Blayo, Bernard Pineaux, "Printing Processes and their Potential for RFID Printing," sOc-EUSAI '05 Proceedings of the 2005 joint conference on Smart objects and ambient intelligence: innovative context-aware services: usages and technologies, ACM, pp.27-30, New York, NY, USA, 2005.

[204] Matti Mäntysalo, Pauliina Mansikkamäki, An inkjet-deposited antenna for 2.4 GHz applications, AEU - International Journal of Electronics and Communications, vol.63, iss.1, no.17, pp.31-35, Jan. 2009.

[205] Sari Linnea Merilampi, Toni Björninen, Leena Ukkonen, Pekka Ruuskanen, Lauri Sydänheimo, "Characterization of UHF RFID tags fabricated directly on convex surfaces by pad printing," International Journal of Advanced Manufacturing Technologies, iss.53, pp.577–591, Jul. 28, 2010.

[206] Sari Merilampi, Leena Ukkonen, Lauri Sydänheimo, Pekka Ruuskanen, and Markku Kivikoski, "Analysis of Silver paste Bow-Tie RFID Tag Antennas Printed on Paper Substrates," International Journal of IEEE Trans. on Ant. and Prop., 2007.

[207] Steven Edward Molesa, "Ultra-Low-Cost Printed Electronics," Technical Report, May 15, 2006.

[208] Amin H. Rida, "Conductive pastejet Printed Antennas on Flexible Low-Cost Paper-Based Substrates for RFID and WSN Applications", Master's Thesis, Georgia Institute of Technology, May 2009.

[209] Ibrahim T. Nassar, Thomas M. Weller, and Jeffrey L. Frolik, "A Compact 3-D Harmonic Repeater for Passive Wireless Sensing," Microwave Theory and Techniques, IEEE Transactions on, vol.60, no.10, pp.3309-3316, Oct. 2012.

[210] Ibrahim T. Nassar and T. Weller, "Development of Novel 3-D cube Antennas for Compact Wireless Sensor Nodes," IEEE Trans. on Ant. and Prop., vol.60, pp.1059-1065, Feb. 2012.

[211] Ibrahim T. Nassar, J. Wang and T. Weller, "A High-Efficiency, Miniaturized Sensor Node with Machined-Substrate Antennas for Embedded Wireless Monitoring," submitted to the 2013 International Microwave Symposium, Dec. 2012.

[212] Ibrahim T. Nassar and T. Weller, "An Electrically-Small, 3-D Cube Antenna Fabricated with Additive Manufacturing," accepted to 2013 Radio and Wireless Symposium, Sep. 2012.

[213] S. Castillo et al., "Electronics Integration in Conformal Substrates Fabricated with Additive Layered Manufacturing", Proceedings of the 20th Annual Solid Freeform Fabrication Symposium, University of Texas at Austin, Austin, TX, pp.730-737, 2009.

[214] Xudong Chen, et al., "High Speed Non-Contact Printing for Solar Cell Front Side Metallization," 36st IEEE PVSC, 2010.

[215] Bo Li, Patrick A. Clark, Kenneth H. Church, "Robust Printing and Dispensing Solutions with Three Sigma Volumetric Control for 21st Century Manufacturing and Packaging", MRS Spring 2007 Meeting, Symposium N: Printing Methods for Electronics, Photonics and Biomaterials, Apr. 2007.

[216] Y. Huang, et al., "Layer-by-Layer Stereolithography of Three-Dimensional Antennas," IEEE IEEE Trans. on Ant. and Prop. Society International Symposium, vol.1A, pp.276–279 vol. 1A, Jul. 3, 2005.

[217] Paul Calvert, "Inkjet Printing for Materials and Devices," Chem. Mater., vol.13, iss.10, pp.3299-3305, Sep. 12, 2001.

[218] J. Mirales, et al., "Fused Deposition Modeling of Metals," Proceedings of the Solid Freeform Fabrication Symposium, Austin, Texas, Jan. 2013, available: http://utwired.engr.utexas.edu/lff/symposium/proceedingsArchive/pubs/Manuscripts/2012/2012-64-Mireles.pdf

[219] M.D. Janezic, J.A. Jargon, "Complex permittivity determination from propagation constant measurements," IEEE Microwave and Guided Wave Letters, vol.9, no.2, pp.76-78, Feb 1999.

[220] Kenneth H. Church, Xudong Chen, Joshua M. Goldfarb, Casey W. Perkowski, Samuel LeBlanc, "Advanced Printing for Microelectronic Packaging," submitted for publication in IPC APEX Expo 2014, Las Vegas, Nevada, Dec. 12, 2013.

[221] Ballato, J; van Weeren, R; Agarwala, M; Riman, R.E; Danforth, S.C., "Patterning for planar waveguides," Electronics Letters , vol.33, no.1, pp.83,84, Jan 2, 1997.

[222] John B. Szczech, Constantine M. Megaridis, Daniel R. Gamota, Senior Member, and Jie Zhang, Member, "Fine-Line Conductor Manufacturing Using Drop-On-Demand PZT Printing Technology," IEEE Transactions on Electronics Packaging Manufacturing, vol.25, no.1, Jan. 2002.

[223] Bo Li, Patrick A. Clark, "Robust Direct-Write Dispensing Tool and Solutions for Micro/Meso-Scale Manufacturing and Packaging," MSEC 2007, Proceedings of the 2007 International Manufacturing Science and Engineering Conference, Oct. 15-17, 2007.

[224] D. A. Frickey, “Conversions Between S, Z, Y, H, ABCD, and T Parameters which are Valid for Complex Source and Load Impedances,” IEEE Trans. on MTT, vol.42, no.2, pp.205-211, Feb 1994.

[225] END

Appendix A Basic Equations

Constants related to electromagnetics are provided here.

$$c_0 = 2.99792458 \times 10^8 \left[\frac{m}{s}\right] \tag{38}$$

$$\varepsilon_0 = 8.854187817 \times 10^{-12} \left[\frac{F}{m}\right] \tag{39}$$

$$\mu_0 = 1.25663706 \times 10^{-6} \left[\frac{H}{m}\right] \tag{40}$$

$$Z_0 = 120\pi[\Omega] \tag{41}$$

Maxwell's equations are provided here.

$$\nabla \cdot D = \rho_v \tag{42}$$

$$\nabla \cdot B = 0 \tag{43}$$

$$\nabla \times E = -\frac{\partial B}{\partial t} \tag{44}$$

$$\nabla \times H = \frac{\partial D}{\partial t} + J \tag{45}$$

Some background conversion equations are provided here.

$$c_0 = \frac{1}{\sqrt{\mu_0 \varepsilon_0}} \tag{46}$$

$$Z_0 = \sqrt{\frac{\mu_0}{\varepsilon_0}} \tag{47}$$

$$\beta = k = \omega\sqrt{\mu\varepsilon} = \omega\sqrt{\mu_0\varepsilon_0}\sqrt{\mu_r\varepsilon_r}$$

$$k = \omega \frac{1}{c_0}\sqrt{\mu_r\varepsilon_r} \tag{48}$$

$$\beta = \frac{2\pi f\sqrt{\varepsilon_e}}{c_0} \tag{49}$$

$$k_0 = \frac{2\pi f}{c_0} \tag{50}$$

$$\beta = imag(\gamma) \tag{51}$$

$$\varepsilon_e = \left(\frac{c_0 \beta}{2\pi f}\right)^2 \tag{52}$$

$$\omega = 2\pi f \tag{53}$$

$$n = \sqrt{\mu_r \varepsilon_r} \tag{54}$$

$$\lambda = \frac{1}{f} \tag{55}$$

$$\varepsilon_r = \varepsilon_r{}' + j\varepsilon_r{}'' \tag{56}$$

$$D = tan\delta = \frac{\varepsilon_r{}''}{\varepsilon_r{}'} \tag{57}$$

$$\Gamma = \frac{Z_c - Z_0}{Z_c + Z_0} \tag{58}$$

$$Z_c = Z_0 \frac{1 + \Gamma}{1 - \Gamma} \tag{59}$$

Appendix B Dielectric Data

Table 22 Dielectric constant

Manuf-acturer	Material	Data Sheet	1 MHz	2 MHz	100 MHz	500 MHz	1 GHz	8.2 GHz	9 GHz	10 GHz	11 GHz
Somos	9120	NA	3.83	3.94	3.85	3.58	3.45	2.86	2.83	2.82	2.83
Somos	9420	3.94	3.83	3.97	3.84	3.56	3.44	2.8	2.78	2.68	2.63
Keck FDM	ABS-M30 Lay	2.8	2.63	2.59	2.81	2.79	2.77	2.53	2.54	2.56	2.6
Keck FDM	ABS-M30 St	2.8	NA	NA	NA	NA	NA	2.53	2.56	2.54	2.55
Pure	ABS	2.8	2.79	2.76	2.83	2.81	2.8	2.6	2.62	2.54	2.54
Keck SL	DMX-SL 100	3.7	NA	NA	NA	NA	NA	2.97	2.94	2.98	3.09
Somos	NeXT	3.62	3.65	3.72	3.57	3.38	3.29	2.76	2.8	2.67	2.65
Keck FDM	PC Lay	2.9	2.74	2.7	2.92	2.89	2.86	2.56	2.54	2.57	2.59
Keck FDM	PC St	2.9	NA	NA	NA	NA	NA	2.51	2.5	2.51	2.47
Pure	PC	2.9	2.91	2.87	2.93	2.9	2.89	2.67	2.7	2.59	2.61
Keck FDM	PC-ABS	2.8	2.74	2.7	2.82	2.8	2.77	NA	NA	NA	NA
Keck SL	Prototherm 12120 Th	3.53	3.44	3.38	3.49	3.35	3.28	NA	NA	NA	NA
Keck SL	Prototherm 12120 UV	3.81	3.8	3.78	3.82	3.6	3.49	2.8	2.76	2.75	2.77
Somos	Prototherm 12120 Th	3.53	3.45	3.48	3.3	3.19	3.13	2.84	2.83	2.74	2.71
Somos	Prototherm 12120 UV	3.81	3.68	3.6	3.6	3.42	3.33	2.94	2.96	2.88	2.93
Pure	PTFE	2.1	2.12	2.1	2.07	2.08	2.07	1.96	1.98	1.95	1.97
Keck FDM	NanoForm 15120	3.73	NA	NA	NA	NA	NA	3.17	3.14	3.07	2.97
Somos	NanoForm 15120	3.73	3.75	3.84	3.81	3.66	3.58	3.05	3.05	2.93	2.88
Somos	NanoTool	3.6	3.57	3.52	3.7	3.61	3.56	3.28	3.33	3.2	3.29
Somos	Watershed 11122	3.45	3.44	3.49	3.35	3.19	3.11	2.68	2.71	2.62	2.62
Keck SL	Watershed 11122	3.45	3.57	3.57	3.55	3.36	3.27	NA	NA	NA	NA
Keck SL	White 14120	3.5	3.47	3.35	3.46	3.29	3.2	2.77	2.74	2.75	2.78

Entries marked “NA” indicate that samples of this type are not fabricated.
“Th” = Thermally post-cured, “UV” = UV post-cured only, “Lay” = laying down orientation, “St” = standing up orientation.
Sample dimensions: 1 MHz – 1 GHz: 3 mm thick × 50 mm dia., 8.2-11 GHz: 7.63 mm × 10.06 mm × 22.60 mm

Table 23 Percent std. dev. and estimated percentage error in dielectric constant

Mfgr.	Material	1 MHz	2 MHz	100 MHz	500 MHz	1 GHz	8.2 GHz	9 GHz	10 GHz	11 GHz
Somos	9120	1.9/1.9	2.0/3.7	0.9/17	0.8/15	0.8/17	1.5	1.8	1.9	2.6
Somos	9420	1.4/1.8	0.8/3.7	1.7/17	1.5/15	1.5/17	1.7	1.7	2.3	2.7
KeckFDM	ABS-M30 Lay	0.5/1.3	0.5/2.6	0.8/21	0.7/18	0.7/18	1.1	0.9	1.0	1.4
KeckFDM	ABS-M30 St	NA	NA	NA	NA	NA	1.3	1.6	2.1	2.5
Pure	ABS	0/1.3	0/3.5	0/21	0/17	0/18	0.5	0.8	0.3	0.8
KeckSL	DMX-SL 100	NA	NA	NA	NA	NA	2.1	1.6	2.5	3.1
Somos	NeXT	0.8/1.8	1.0/3.5	0.9/18	0.8/16	0.8/17	0.9	0.9	0.9	1.3
KeckFDM	PC Lay	3.1/1.3	2.1/2.6	2.9/21	3.0/17	2.9/18	2.1	2.0	1.8	1.3
KeckFDM	PC St	NA	NA	NA	NA	NA	0.8	1.4	1.1	1.0
Pure	PC	0/1.4	0/2.7	0/21	0/17	0/18	0.5	0.3	0.8	0.5
KeckFDM	PC-ABS	3.1/1.3	2.1/2.6	0.8/21	0.9/18	0.9/18	NA	NA	NA	NA
Keck SL	Prototherm Th	0.9/1.7	1.2/3.2	0.6/18	0.5/16	0.5/17	NA	NA	NA	NA
Keck SL	Prototherm UV	2.9/1.8	1.4/3.5	1.1/17	1.0/15	1.0/16	2.3	2.5	2.4	3.3
Somos	Prototherm Th	0.4/1.6	1.7/3.2	0.6/19	0.2/16	0.5/17	1.2	1.8	2.8	4.2
Somos	Prototherm UV	0.9/1.8	0.7/3.4	0.8/18	0.8/15	0.7/17	0.8	0.9	1.0	1.9
Pure	PTFE	0/1.0	0/2.2	0/26	2.0/21	0/21	0	0	0	0
KeckFDM	NanoForm 15120	NA	NA	NA	NA	NA	1.5	1.1	3.9	5.8
Somos	NanoForm 15120	0.9/1.8	1.4/3.5	2.6/17	2.5/15	2.4/16	1.8	1.9	2.1	3.1
Somos	NanoTool	1.0/1.6	0.9/3.1	1.7/18	1.6/15	1.6/16	0.6	0.8	0.5	1.7
Somos	Watershed 11122	0.3/1.6	0.6/3.2	1.1/19	0.9/16	1.0/17	2.2	2.1	2.3	2.2
Keck SL	Watershed 11122	0.9/1.8	1.3/3.4	0.6/18	0.5/16	0.5/17	NA	NA	NA	NA
Keck SL	White 14120	1.3/1.7	1.6/3.2	1.1/18	0.9/16	1.0/17	2.2	1.7	3.2	3.0

Entries marked "NA" indicate that samples of this type are not fabricated.
"Th" = Thermally post-cured, "UV" = UV post-cured only, "Lay" = laying down orientation, "St" = standing up orientation.
Notation is "%std. dev. / %est. err". Estimated error is not available for X-band measurements.
Sample dimensions: 1 MHz – 1 GHz: 3 mm thick × 50 mm dia., 8.2-11 GHz: 7.63 mm × 10.06 mm × 22.60 mm

Table 24 Loss tangent

Manuf-acturer	Material	1 MHz	2 MHz	100 MHz	500 MHz	1 GHz	8.2 GHz	9 GHz	10 GHz	11 GHz
Somos	9120	0.0196	0.0226	0.0413	0.0426	0.0402	0.0313	0.0348	0.0379	0.0347
Somos	9420	0.0201	0.0234	0.0410	0.0428	0.0406	0.0288	0.0312	0.0384	0.0319
KeckFDM	ABS-M30Lay	0.0069	0.0053	0.0037	0.0033	0.0033	0.0108	0.0138	0.0181	0.0098
KeckFDM	ABS-M30St	NA	NA	NA	NA	NA	0.0075	0.0090	0.0207	0.0130
Pure	ABS	0.0067	0.0049	0.0044	0.0038	0.0031	0.0169	0.0114	0.0151	0.0106
KeckSL	DMX-SL100	NA	NA	NA	NA	NA	0.0115	0.0135	0.0162	0.0130
Somos	NeXT	0.0311	0.0357	0.0344	0.0302	0.0274	0.0253	0.0288	0.0502	0.0305
KeckFDM	PCLay	0.0076	0.0072	0.0050	0.0044	0.0037	0.0073	0.0096	0.0018	0.0066
KeckFDM	PCSt	NA	NA	NA	NA	NA	0.0036	0.0038	0.0059	0.0050
Pure	PC	0.0075	0.0073	0.0052	0.0050	0.0040	0.0020	0.0024	0.0052	0.0049
KeckFDM	PC-ABS	0.0076	0.0072	0.0049	0.0038	0.0038	NA	NA	NA	0.0055
KeckSL	Prototherm12120Th	0.0224	0.0238	0.0244	0.0219	0.0205	NA	NA	NA	0.0226
KeckSL	Prototherm12120UV	0.0171	0.0193	0.0333	0.0346	0.0333	0.0122	0.0130	0.0115	0.0170
Somos	Prototherm12120Th	0.0224	0.0243	0.0223	0.0191	0.0176	0.0074	0.0102	0.0149	0.0196
Somos	Prototherm12120UV	0.0148	0.0161	0.0285	0.0303	0.0293	0.0513	0.0434	0.0437	0.0368
Pure	PTFE	0	0	0.0008	0.0002	0.0001	0.0027	0.0009	0	0.0016
KeckFDM	NanoForm15120	NA	NA	NA	NA	NA	0.0286	0.0257	0.0256	0.0286
Somos	NanoForm15120	0.0131	0.0148	0.0222	0.0229	0.0225	0.0275	0.0221	0.0245	0.0286
Somos	NanoTool	0.0097	0.0096	0.0130	0.0127	0.0122	0.0329	0.0252	0.0255	0.0176
Somos	Watershed11122	0.0236	0.0263	0.0292	0.0271	0.0253	0.0212	0.0235	0.0424	0.0273
KeckSL	Watershed11122	0.0123	0.0312	0.0341	0.0305	0.0282	NA	NA	NA	0.0254
KeckSL	White14120	0.0296	0.0031	0.0321	0.0291	0.0265	0.0214	0.0266	0.0277	0.0246

Entries marked “NA” indicate that samples of this type are not fabricated.
“Th” = Thermally post-cured, “UV” = UV post-cured only, “Lay” = laying down orientation, “St” = standing up orientation.
Values of “0” indicate that the value is so small that it is measured as a negative number due to normal measurement error.
Sample dimensions: 1 MHz – 1 GHz: 3 mm thick × 50 mm dia., 8.2-11 GHz: 7.63 mm × 10.06 mm × 22.60 mm

Table 25 Percent standard deviation and estimated percentage error in loss tangent

Manuf-acturer	Material	1 MHz	2 MHz	100 MHz	500 MHz	1 GHz	8.2 GHz	9 GHz	10 GHz	11 GHz
Somos	9120	2.4/31	2.6/29	2.3/25	1.1/15	0.8/23	108	98	73	69
Somos	9420	1.3/30	0.8/28	2.1/25	1.9/15	1.8/22	120	112	118	54
KeckFDM	ABS-M30 Lay	0.5/83	0.8/108	39/442	19/203	3.0/267	74	80	63	96
KeckFDM	ABS-M30 St	NA	NA	NA	NA	NA	63	64	87	71
Pure	ABS	0.0/86	0.0/116	0.0/295	0.0/175	0.0/285	1	4	64	5
KeckSL	DMX-SL 100	NA	NA	NA	NA	NA	106	109	140	353
Somos	NeXT	1.2/20	1.3/19	1.9/32	1.6/21	1.0/33	106	106	105	316
KeckFDM	PC Lay	2.1/76	2.7/80	23/263	9.9/149	3.7/236	90	98	349	209
KeckFDM	PC St	NA	NA	NA	NA	NA	185	241	220	272
Pure	PC	0.0/77	0.0/80	0.0/309	0.0/149	0.0/236	939	352	61	649
KeckFDM	PC-ABS	2.1/76	2.7/80	28/45	14/177	4.8/233	NA	NA	NA	NA
Keck SL	Prototherm Th	1.7/27	1.5/27	2.5/31	1.9/29	1.4/44	NA	NA	NA	NA
Keck SL	Prototherm UV	2.1/35	1.9/33	3.3/52	1.4/18	1.0/27	74	78	126	558
Somos	Prototherm Th	0.9/27	2.2/26	0.7/38	0.9/34	1.9/51	648	332	231	368
Somos	Prototherm UV	0.7/40	0.6/38	1.9/38	1.9/21	1.2/31	15	23	30	18
Pure	PTFE	0.0/HIGH	0.0/ HIGH	0.0/ HIGH	135/ HIGH	0/HIGH	0	0	0	0
KeckFDM	NanoForm 15120	NA	NA	NA	NA	NA	96	87	85	109
Somos	NanoForm 15120	0.9/45	0.9/41	2.8/46	3.2/27	3.1/41	99	100	112	125
Somos	NanoTool	0.9/60	1.0/62	4.6/81	3.2/49	2.5/74	28	60	87	71
Somos	Watershed 11122	0.8/25	0.5/25	2.9/39	1.6/24	1.4/35	79	73	62	269
Keck SL	Watershed 11122	5.3/47	2.7/21	4.3/32	1.5/21	1.8/32	NA	NA	NA	NA
Keck SL	White 14120	1.6/21	2.0/185	3.0/35	2.5/22	1.1/34	105	99	97	139

Entries marked “NA” indicate that samples of this type are not fabricated.
“Th” = Thermally post-cured, “UV” = UV post-cured only, “Lay” = laying down orientation, “St” = standing up orientation.
Notation is “std. dev. / est. err”. Estimated error is not available for X-band measurements.
Sample dimensions: 1 MHz – 1 GHz: 3 mm thick × 50 mm dia., 8.2-11 GHz: 7.63 mm × 10.06 mm × 22.60 mm

Appendix C Effective Medium Theory Derivations

Effective medium theory seeks to describe the overall properties of a multi-component material based on the properties of its constituent materials. Many theories exist and several are reviewed here. Referring to Table 8, printed ABS is considered material '1' which is not fully dense allowing air (considered material '2') to exist within the sample.

Table 26 Effective medium theory variables

Symbol	Material
f	Filling fraction
ε_{r1}	ABS
ε_{r2}	Air
$\varepsilon_{min}, \varepsilon_{max}$	Wiener Bounds
ε_M	Maxwell
ε_{MG}	Maxwell-Garnett / Clausius-Mossotti
ε_B	Symmetric Bruggeman
ε_{ABG}	Asymmetric Bruggeman
ε_L	Looyenga

Boundaries are given by Wiener [83][84] which limit the minimum and maximum values the average dielectric constant may be based on the fill fraction and

$$\varepsilon_{min} = \frac{1}{f\frac{1}{\varepsilon_{r1}} + (1-f)\frac{1}{\varepsilon_{r2}}} \tag{60}$$

$$\varepsilon_{max} = f\varepsilon_{r1} + (1-f)\varepsilon_{r2} \tag{61}$$

The formula of Maxwell offers the simplest computation of effective material properties. A straightforward derivation is offered here.

$$\frac{\varepsilon_{MG}-\varepsilon_{r2}}{\varepsilon_{MG}+2\varepsilon_{r2}}=f\frac{\varepsilon_{r1}-\varepsilon_{r2}}{\varepsilon_{r1}+2\varepsilon_{r2}} \tag{62}$$

$$(\varepsilon_{MG}-\varepsilon_{r2})(\varepsilon_{r1}+2\varepsilon_{r2})=f(\varepsilon_{r1}-\varepsilon_{r2})(\varepsilon_{MG}+2\varepsilon_{r2}) \tag{63}$$

$$\begin{aligned}\varepsilon_{MG}\varepsilon_{r1}-\varepsilon_{r1}\varepsilon_{r2}+2\varepsilon_{MG}\varepsilon_{r2}-2\varepsilon_{r2}\varepsilon_{r2}\\ =f\varepsilon_{MG}\varepsilon_{r1}-f\varepsilon_{MG}\varepsilon_{r2}+2f\varepsilon_{r1}\varepsilon_{r2}-2f\varepsilon_{r2}\varepsilon_{r2}\end{aligned} \tag{64}$$

$$\begin{aligned}\varepsilon_{MG}\varepsilon_{r1}+2\varepsilon_{MG}\varepsilon_{r2}-f\varepsilon_{MG}\varepsilon_{r1}+f\varepsilon_{MG}\varepsilon_{r2}\\ =+2f\varepsilon_{r1}\varepsilon_{r2}-2f\varepsilon_{r2}\varepsilon_{r2}+2\varepsilon_{r2}\varepsilon_{r2}+\varepsilon_{r1}\varepsilon_{r2}\end{aligned} \tag{65}$$

$$\varepsilon_{MG}=\frac{2f\varepsilon_{r1}\varepsilon_{r2}+\varepsilon_{r1}\varepsilon_{r2}+2\varepsilon_{r2}\varepsilon_{r2}-2f\varepsilon_{r2}\varepsilon_{r2}}{\varepsilon_{r1}+2\varepsilon_{r2}-f\varepsilon_{r1}+f\varepsilon_{r2}} \tag{66}$$

$$\varepsilon_{MG}=\varepsilon_{r2}+\varepsilon_{r2}\frac{3f(\varepsilon_{r1}-\varepsilon_{r2})}{\varepsilon_{r1}+2\varepsilon_{r2}} \tag{67}$$

The formula named for Maxwell-Garnett [85][86][87] and Clausius-Mossotti [88] (MG or C-M) is a very common approximation and follows equation 26.

$$\varepsilon_{MGCM}=\frac{\varepsilon_{r2}\left(1+\frac{2f(\varepsilon_{r1}-\varepsilon_{r2})}{\varepsilon_{r1}+2\varepsilon_{r2}}\right)}{1-\frac{f(\varepsilon_{r1}-\varepsilon_{r2})}{(\varepsilon_{r1}+2\varepsilon_{r2})}} \tag{68}$$

Bruggemann [89] offers two equations, a symmetric and asymmetric model of effective medium computation. Here is given a derivation of the symmetric model.

$$f\frac{\varepsilon_{r1}-\varepsilon_B}{\varepsilon_{r1}+2\varepsilon_B}+(1-f)\frac{\varepsilon_{r2}-\varepsilon_B}{\varepsilon_{r2}+2\varepsilon_B}=0 \tag{69}$$

$$f(\varepsilon_{r1}-\varepsilon_B)(\varepsilon_{r2}+2\varepsilon_B)+(1-f)(\varepsilon_{r2}-\varepsilon_B)(\varepsilon_{r1}+2\varepsilon_B)=0 \tag{70}$$

$$\begin{aligned} f(\varepsilon_{r1}\varepsilon_{r2}-\varepsilon_B\varepsilon_{r2}+2\varepsilon_B\varepsilon_{r1}-2\varepsilon_B\varepsilon_B) \\ +(1-f)(\varepsilon_{r1}\varepsilon_{r2}-\varepsilon_B\varepsilon_{r1}+2\varepsilon_B\varepsilon_{r2}-2\varepsilon_B\varepsilon_B)=0 \end{aligned} \tag{71}$$

$$\begin{aligned} \varepsilon_{r1}\varepsilon_{r2}f-\varepsilon_B\varepsilon_{r2}f+2\varepsilon_B\varepsilon_{r1}f-2\varepsilon_B\varepsilon_Bf+\varepsilon_{r1}\varepsilon_{r2}-\varepsilon_B\varepsilon_{r1}+2\varepsilon_B\varepsilon_{r2}-2\varepsilon_B\varepsilon_B \\ -\varepsilon_{r1}\varepsilon_{r2}f+\varepsilon_B\varepsilon_{r1}f-2\varepsilon_B\varepsilon_{r2}f+2\varepsilon_B\varepsilon_Bf=0 \end{aligned} \tag{72}$$

$$\begin{aligned} +\varepsilon_{r1}\varepsilon_{r2}f-\varepsilon_B\varepsilon_{r2}f+2\varepsilon_B\varepsilon_{r1}f-2\varepsilon_B\varepsilon_Bf \\ +(\varepsilon_{r1}\varepsilon_{r2}-\varepsilon_B\varepsilon_{r1}+2\varepsilon_B\varepsilon_{r2}-2\varepsilon_B\varepsilon_B)-\varepsilon_{r1}\varepsilon_{r2}f+\varepsilon_B\varepsilon_{r1}f \\ -2\varepsilon_B\varepsilon_{r2}f+2\varepsilon_B\varepsilon_Bf=0 \end{aligned} \tag{73}$$

$$+3\varepsilon_B\varepsilon_{r1}f-3\varepsilon_B\varepsilon_{r2}f+(\varepsilon_{r1}\varepsilon_{r2}-\varepsilon_B\varepsilon_{r1}+2\varepsilon_B\varepsilon_{r2}-2\varepsilon_B\varepsilon_B)=0 \tag{74}$$

$$\varepsilon_B{}^2(-2)+\varepsilon_B(3\varepsilon_{r1}f-3\varepsilon_{r2}f-\varepsilon_{r1}+2\varepsilon_{r2})+(\varepsilon_{r1}\varepsilon_{r2})=0 \tag{75}$$

$$a=-2 \tag{76}$$

$$b=3\varepsilon_{r1}f-3\varepsilon_{r2}f-\varepsilon_{r1}+2\varepsilon_{r2} \tag{77}$$

$$c=\varepsilon_{r1}\varepsilon_{r2} \tag{78}$$

$$\varepsilon_B=\frac{-b\pm\sqrt{b^2-4ac}}{2a} \tag{79}$$

$$\varepsilon_B=\frac{-b\pm\sqrt{b^2-4ac}}{2a} \tag{80}$$

$$\begin{aligned} &\varepsilon_B \\ &=\frac{1}{4}\Big(3f(\varepsilon_{r1}-\varepsilon_{r2})+2\varepsilon_{r2}-\varepsilon_{r1} \\ &+\sqrt{(1-3f)^2\varepsilon_{r1}{}^2+2(2+9f-9f^2)\varepsilon_{r1}\varepsilon_{r2}+(1-3f)^2\varepsilon_{r2}{}^2}\Big) \end{aligned} \tag{81}$$

The asymmetric Bruggemann model [89] assumes spherical particles in a host material and may or may not offer a good representation of effective medium for dielectric constant in partial infill printed material. The solution is computed numerically according to the following derivation using the modified secant method.

$$\frac{\varepsilon_i - \varepsilon_{eff}}{\varepsilon_i - \varepsilon_h} = (1-f)\left(\frac{\varepsilon_{eff}}{\varepsilon_h}\right)^{\frac{1}{3}} \tag{82}$$

$$\varepsilon_i - \varepsilon_{eff} = (1-f)(\varepsilon_i - \varepsilon_h)\left(\frac{\varepsilon_{eff}}{\varepsilon_h}\right)^{\frac{1}{3}} \tag{83}$$

$$\varepsilon_i - \varepsilon_{eff} = (1-f)(\varepsilon_i - \varepsilon_h)\varepsilon_h{}^{-\frac{1}{3}}\varepsilon_{eff}{}^{\frac{1}{3}} \tag{84}$$

$$\varepsilon_{eff} + (1-f)(\varepsilon_i - \varepsilon_h)\varepsilon_h{}^{-\frac{1}{3}}\varepsilon_{eff}{}^{\frac{1}{3}} - \varepsilon_i = 0 \tag{85}$$

$$\varepsilon_{eff} + B\varepsilon_{eff}{}^{\frac{1}{3}} + C = 0 \tag{86}$$

$$B = (1-f)(\varepsilon_i - \varepsilon_h)\varepsilon_h{}^{-\frac{1}{3}} \tag{87}$$

$$C = -\varepsilon_i \tag{88}$$

Looyenga [90] offers another simple method for effective medium approximation based on cube roots.

$$\varepsilon_L = \left(\left(\sqrt[3]{\varepsilon_{r1}} - \sqrt[3]{\varepsilon_{r2}}\right)f + \sqrt[3]{\varepsilon_{r2}}\right)^3 \tag{89}$$

Appendix D Propagation Constant from Coefficient

In the back-calculation of transmission lines, it is frequently necessary to determine the propagation constant from the propagation coefficient. This computation produces infinitely many values depending on the number of wavelengths which exist on the line. In order to determine the correct value, a guess ($\varepsilon_{e,guess}$) is made at the effective permittivity (ε_e) based on the material dielectric and the type of transmission line. The value *n* is chosen such that ε_e most closely matches $\varepsilon_{e,guess}$.

$$n \in [0,20] \tag{90}$$

$$\gamma(n) = -\frac{1}{l}[ln(|P|) + j(ang(P) - 2\pi n)] \tag{91}$$

$$\beta = imag(\gamma) \tag{92}$$

$$\varepsilon_e = \left(\frac{c_0\beta}{2\pi f}\right)^2 \tag{93}$$

Appendix E TRL Calibration

TRL calibration relies on three calibration standards to extract microstrip line parameters; through, reflect, and line. The method works by assuming that the length of transmission line of interest is embedded between two symmetrical error boxes which introduce additional reflections and transmission loss to the combined system. The through standard is a very short connection of just these two error boxes. The reflect standard is just one of these error boxes open circuited or short circuited. The line standard is a length of transmission line connected between two error boxes. The line length can be any length other than a multiple of one half wavelength.

$$T = \begin{bmatrix} T_{11} & T_{12} \\ T_{21} & T_{22} \end{bmatrix} \qquad (94)$$

$$T_{11}, T_{12}$$

$$R = \begin{bmatrix} R_{11} & R_{12} \\ R_{21} & R_{22} \end{bmatrix} \qquad (95)$$

$$R_{11}$$

$$L = \begin{bmatrix} L_{11} & L_{12} \\ L_{21} & L_{22} \end{bmatrix} \qquad (96)$$

$$L_{11}, L_{12}$$

Each standard measurement is shown here followed by its signal flow graph and derived equations in order to determine the unknown error box parameters.

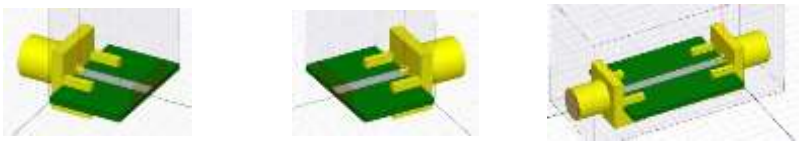

Figure 128 Through standard

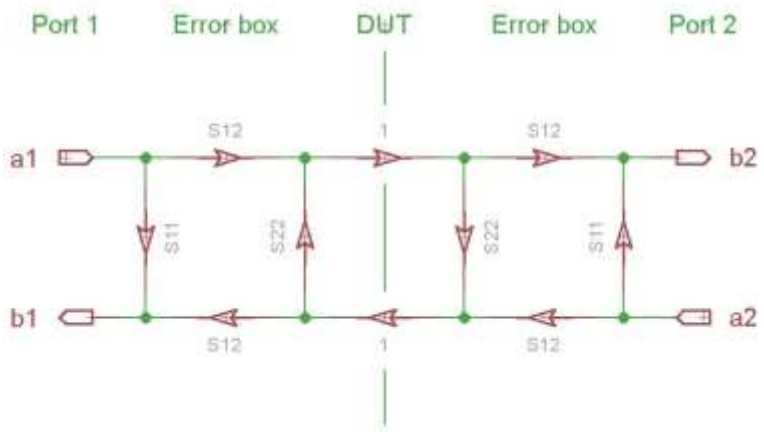

Figure 129 Thru signal flow graph

$$T_{11} = T_{22} = \frac{b_1}{a_1}\Big|_{a_2=0} = S_{11} + \frac{S_{22}{S_{12}}^2}{1 - {S_{22}}^2} \tag{97}$$

$$T_{12} = T_{21} = \frac{b_1}{a_2}\Big|_{a_1=0} = \frac{{S_{12}}^2}{1 - {S_{22}}^2} \tag{98}$$

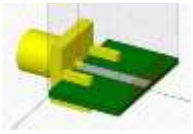

Figure 130 Reflect standard

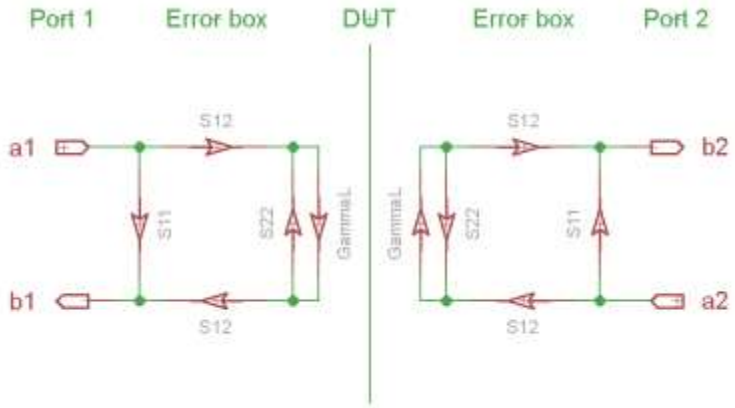

Figure 131 Reflect signal flow graph

$$R_{11} = R_{22} = \frac{b_1}{a_1}\Big|_{a_2=0} = S_{11} + \frac{{S_{12}}^2 \Gamma_L}{1 - S_{22}\Gamma_L} \tag{99}$$

$$R_{12} = R_{21} = 0$$

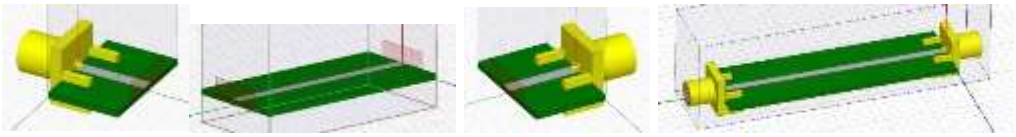

Figure 132 Line standard

$$L_{11} = L_{22} = \frac{b_1}{a_1}\Big|_{a_2=0} = S_{11} + \frac{S_{22}{S_{12}}^2 e^{-2\gamma l}}{1 - {S_{22}}^2 e^{-2\gamma l}} \tag{100}$$

$$L_{12} = L_{21} = \frac{b_1}{a_2}\Big|_{a_1=0} = \frac{{S_{12}}^2 e^{-\gamma l}}{1 - {S_{22}}^2 e^{-2\gamma l}} \tag{101}$$

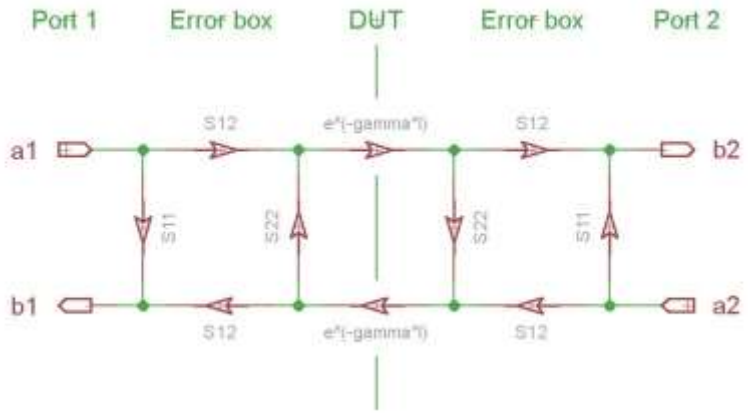

Figure 133 Line signal flow graph

There are five complex parameters which consist of ten numbers and five complex equations so a solution may be found.

$$T_{11} = S_{11} + \frac{S_{22}{S_{12}}^2}{1 - {S_{22}}^2} \tag{102}$$

$$T_{12} = \frac{{S_{12}}^2}{1 - {S_{22}}^2} \tag{103}$$

$$R_{11} = S_{11} + \frac{{S_{12}}^2 \Gamma_L}{1 - S_{22}\Gamma_L} \tag{104}$$

$$L_{11} = S_{11} + \frac{S_{22}{S_{12}}^2 e^{-2\gamma l}}{1 - {S_{22}}^2 e^{-2\gamma l}} \tag{105}$$

$$L_{12} = \frac{{S_{12}}^2 e^{-\gamma l}}{1 - {S_{22}}^2 e^{-2\gamma l}} \tag{106}$$

Table 27 Simpler variable names

Outputs	Inputs
$A = T_{11}$	$v = S_{11}$
$B = T_{12}$	$w = {S_{12}}^2$
$C = L_{11}$	$x = S_{22}$
$D = L_{12}$	$y = e^{-\gamma l}$
$R_{11} = R_{11}$	$z = \Gamma_L$

Equations from signal flow graphs:

$$A = v + \frac{xw}{1 - x^2} \tag{107}$$

$$B = \frac{w}{1 - x^2} \tag{108}$$

$$R_{11} = v + \frac{wz}{1 - xz} \tag{109}$$

$$C = v + \frac{xwy^2}{1 - x^2y^2} \tag{110}$$

$$D = \frac{wy}{1 - x^2y^2} \tag{111}$$

There are now five equations for the five unknowns, v, w, x, y, and z; the solution is straightforward but lengthy. Only one equation contains z, the other four equations are solved for the other four unknown. *w* can also be eliminated from the system of equations.

$$A = v + Bx \tag{112}$$

$$C = v + Dxy \tag{113}$$

$$C = v + \frac{B(1+x)(1-x)xy^2}{(1+xy)(1-xy)} \tag{114}$$

$$D = \frac{B(1+x)(1-x)y}{(1+xy)(1-xy)} \tag{115}$$

v can be eliminated as follows:

$$A - Bx = v = C - Dxy \tag{116}$$

$$D = \frac{B(1+x)(1-x)y}{(1+xy)(1-xy)} \tag{117}$$

$$D(y^2 - x^2) = B(y - x^2y) \tag{118}$$

This leaves two equations for x and y:

$$Dy^2 - Dx^2 = By - Bx^2y \tag{119}$$

$$y^2(A - Bx) - Ax^2 = C(y^2 - x^2) - Bx \tag{120}$$

A solution is found for x.

$$x^2 = \frac{By - Dy^2}{B - D} = y\frac{B - Dy}{B - D} \tag{121}$$

A substitution is made using x to give a quadratic equation for y.

$$Ay^2 - Bxy^2 - Ax^2 - Cy^2 + Cx^2 + Bx = 0 \tag{122}$$

$$DBy^2 - D^2y - B^2y + A^2y + C^2y - 2ACy + DB = 0 \tag{123}$$

Application of the quadratic formula then gives the solution for y in terms of the measured TRL S-parameters as:

$$DBy^2 + (-D^2 - B^2 + (A - C)^2)y + DB = 0 \tag{124}$$

$$a = DB \tag{125}$$

$$b = -D^2 - B^2 + (A - C)^2 \tag{126}$$

$$c = DB \tag{127}$$

$$y = \frac{-b \pm \sqrt{b^2 - 4ac}}{2a} \tag{128}$$

$$y = \frac{D^2 + B^2 - (A - C)^2 \pm \sqrt{(D^2 + B^2 - (A - C)^2)^2 - 4D^2B^2}}{2DB} \tag{129}$$

The choice of sign can be determined by the requirement that the real and imaginary parts of γ be positive, or by knowing the phase of z as determined from the last final equation to within 180 degrees.

Next x is multiplied in and subtracted from the first equation to giving the following.

$$Bx = \frac{xw}{1 - x^2} \tag{130}$$

$$A = v + \frac{xw}{1 - x^2} \tag{131}$$

$$A = v + Bx \tag{132}$$

Further manipulations give:

$$Dx = \frac{xwy}{1 - x^2y^2} \tag{133}$$

$$C = v + \frac{xwy^2}{1 - x^2y^2} \tag{134}$$

$$C = v + Dy \tag{135}$$

Eliminating v from these two equations gives x in terms of y as:

$$C - Dy = v = A - Bx \tag{136}$$

$$x = \frac{A - C}{B - Dy} \tag{137}$$

Solving for *v* gives:

$$v = Bx - A \tag{138}$$

Solving for *w* gives:

$$w = B(1 - x^2) \tag{139}$$

Solving for *z* to gives:

$$R_{11} = v + \frac{wz}{1 - xz} \tag{140}$$

$$R_{11} - R_{11}xz = v - vxz + wz \tag{141}$$

$$-R_{11}xz - wz + vxz = v - R_{11} \tag{142}$$

$$wz + R_{11}xz - vxz = R_{11} - v \tag{143}$$

$$(w + R_{11}x - vx)z = R_{11} - v \tag{144}$$

$$z = \frac{R_{11} - v}{w + x(R_{11} - v)} \tag{145}$$

Here the equations are summarized.

$$a = DB \tag{146}$$

$$b = (D^2 + B^2 - (C - A)^2) \tag{147}$$

$$c = DB \tag{148}$$

$$y = \frac{-b \pm \sqrt{b^2 - 4ac}}{2a} \tag{149}$$

$$x = \frac{A - C}{B - Dy} \tag{150}$$

$$v = Bx - A \tag{151}$$

$$w = B(1 - x^2) \tag{152}$$

$$z = \frac{R_{11} - v}{w + x(R_{11} - v)} \tag{153}$$

Revert to original variables.

$$a = L_{12}T_{12} \tag{154}$$

$$b = {L_{12}}^2 + {T_{12}}^2 - (L_{11} - T_{11})^2 \tag{155}$$

$$c = L_{12}T_{12} \tag{156}$$

$$P = e^{-\gamma l} = \frac{-b \pm \sqrt{b^2 - 4ac}}{2a} \tag{157}$$

$$e^{-\gamma l} = \frac{{L_{12}}^2 + {T_{12}}^2 - (L_{11} - T_{11})^2 \pm \sqrt{\left[{L_{12}}^2 + {T_{12}}^2 - (T_{11} - L_{11})^2\right]^2 - 4{L_{12}}^2{T_{12}}^2}}{2L_{12}T_{12}} \tag{158}$$

$$P_p = -\frac{b}{2a} + \frac{\sqrt{b^2 - 4ac}}{2a} \tag{159}$$

$$P_m = -\frac{b}{2a} - \frac{\sqrt{b^2 - 4ac}}{2a} \tag{160}$$

$$\gamma_p = \text{propP2g}(P_p) \tag{161}$$

$$\gamma_m = \text{propP2g}(P_m) \tag{162}$$

$$P = \begin{cases} P_p & sign(re(\gamma)) = sign(im(\gamma)) = +1 \\ P_m & sign(re(\gamma)) = sign(im(\gamma)) = +1 \end{cases} \tag{163}$$

$$\gamma = \begin{cases} \gamma_p & sign(re(\gamma)) = sign(im(\gamma)) = +1 \\ \gamma_m & sign(re(\gamma)) = sign(im(\gamma)) = +1 \end{cases} \tag{164}$$

$$S_{22} = \frac{T_{11} - L_{11}}{T_{12} - L_{12}e^{-\gamma l}} \tag{165}$$

$$S_{11} = T_{11} - S_{22}T_{12} \tag{166}$$

$${S_{12}}^2 = T_{12}\left(1 - {S_{22}}^2\right) \tag{167}$$

$$S_{12} = S_{21} = \begin{cases} +\sqrt{{S_{12}}^2} & sign(?) = +1 \\ -\sqrt{{S_{12}}^2} & sign(?) = +1 \end{cases} \tag{168}$$

$$C_x = \begin{bmatrix} S_{11} & S_{12} \\ S_{21} & S_{22} \end{bmatrix} \tag{169}$$

$$\Gamma_L = \frac{R_{11} - S_{11}}{{S_{12}}^2 + S_{22}(R_{11} - S_{11})} \tag{170}$$

The error box S-parameters are represented as $\tilde{S} = \begin{bmatrix} S_{11} & S_{12} \\ S_{21} & S_{22} \end{bmatrix}$. The measured S-parameters of the device are represented as $\widetilde{D} = \begin{bmatrix} D_{11} & D_{12} \\ D_{21} & D_{22} \end{bmatrix}$. Both of these matrices must be converted to T-parameters. $\tilde{S} \rightarrow \widetilde{T_A}$ and $\widetilde{D} \rightarrow \widetilde{T_D}$.

$$T_{11} = -\frac{|S|}{S_{21}} \tag{171}$$

$$T_{12} = \frac{S_{11}}{S_{21}} \tag{172}$$

$$T_{21} = -\frac{S_{22}}{S_{21}} \tag{173}$$

$$T_{22} = \frac{1}{S_{21}} \tag{174}$$

Once the effects of the error boxes $\widetilde{T_A}$ are removed, the resulting line parameters are found as $\widetilde{T_L}$.

$$\widetilde{T_L} = \widetilde{T_A}^{-1}\widetilde{T_D}\widetilde{T_A}^{-1} \tag{175}$$

These device T-parameters are converted back to S-parameters.

$$S_{11} = \frac{T_{12}}{T_{22}} \tag{176}$$

$$S_{12} = \frac{|T|}{T_{22}} \tag{177}$$

$$S_{21} = \frac{1}{T_{22}} \tag{178}$$

$$S_{22} = -\frac{T_{21}}{T_{22}} \tag{179}$$

The resulting S-parameters represent just the device as though it were connected directly to two ports of exactly the reference impedance, without the effects of the connectors which were represented by the error box. The resulting S-parameters are now ready for further processing.

Appendix F Nicholson-Ross-Weir Method

Recognizing that solving the Nicholson-Ross-Weir [71]-[74] problem involves a two-interface air-dielectric-air system, the Fabry–Pérot cavity (with its infinite internal reflections) problem is solved for the overall reflection and transmission coefficients S_{11} and S_{21}. Ray tracing is used where the slab is seen as a box in which rays bounce back and forth infinitely many times and each time a portion of the energy leaks out and a portion reflects. Phase is accumulated as the imaginary single-transmission propagation constant, $P = e^{-jkl}$. Each reflection is described by the single-interface reflection coefficient, Γ. The single interface reflection coefficient is not directly measurable; however, the overall reflection and transmission coefficients are measurable and the single interface reflection coefficient may be determined from them by solving analytical equations for the Fabry–Pérot cavity.

The overall reflection and transmission coefficients, S_{11} and S_{21} are solved in terms of the single-interface reflection coefficient, Γ and the single-transmission propagation constant, $P = e^{-jkl}$. Note that the reflection coefficient from air to dielectric is Γ while the reflection coefficient from inside the dielectric to air is – Γ. Phase is always accumulated as e^{-jkl}.

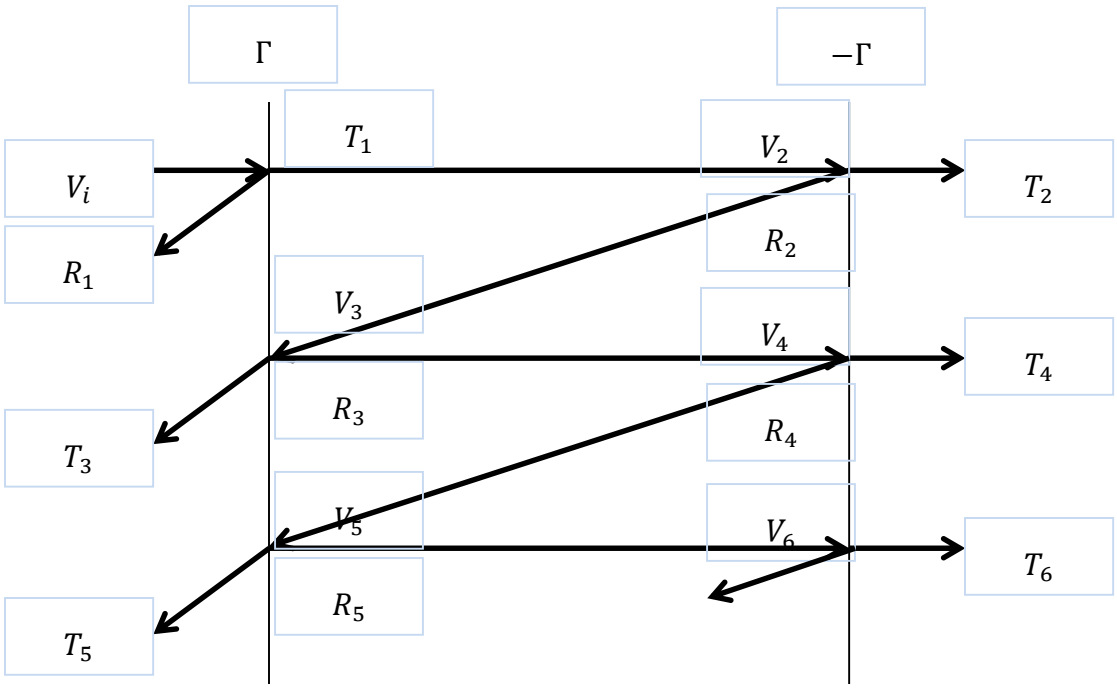

Figure 134 Ray tracing of Fabry–Pérot cavity

Table 28 First Fabry–Pérot cavity reflections

Voltage at point 'n'	**Transmission parameter**	**Reflection parameter**
$V_1 = V_{inc} = 1$	$T_1 = (1-\Gamma)$	$R_1 = \Gamma$
$V_2 = (1-\Gamma)e^{-jkl}$	$T_2 = (1+\Gamma)(1-\Gamma)e^{-jkl}$	$R_2 = -\Gamma(1-\Gamma)e^{-jkl}$
$V_3 = -\Gamma(1-\Gamma)e^{-2jkl}$	$T_3 = -\Gamma(1+\Gamma)(1-\Gamma)e^{-2jkl}$	$R_3 = \Gamma^2(1-\Gamma)e^{-2jkl}$
$V_4 = \Gamma^2(1-\Gamma)e^{-3jkl}$	$T_4 = \Gamma^2(1+\Gamma)(1-\Gamma)e^{-3jkl}$	$R_4 = -\Gamma^3(1-\Gamma)e^{-3jkl}$
$V_5 = -\Gamma^3(1-\Gamma)e^{-4jkl}$	$T_5 = -\Gamma^3(1+\Gamma)(1-\Gamma)e^{-4jkl}$	$R_5 = \Gamma^4(1-\Gamma)e^{-4jkl}$
$V_6 = \Gamma^4(1-\Gamma)e^{-5jkl}$	$T_6 = \Gamma^4(1+\Gamma)(1-\Gamma)e^{-4jkl}$	Not computed

First the infinite summations are solved.

$$S_{11} = R_1 + T_3 + T_5 + \cdots T_\infty \tag{180}$$

$$S_{11} = \Gamma - \Gamma(1+\Gamma)(1-\Gamma)e^{-2jkl} - \Gamma^3(1+\Gamma)(1-\Gamma)e^{-4jkl} + \cdots T_\infty \tag{181}$$

$$S_{11} = \Gamma - \sum_{n=0}^{\infty}\left\{\Gamma^{2n+1}(1+\Gamma)(1-\Gamma)e^{-(2n+2)jkl}\right\} \tag{182}$$

$$S_{21} = T_2 + T_4 + T_6 + \cdots T_\infty \tag{183}$$

$$\begin{aligned} S_{21} = {} & (1+\Gamma)(1-\Gamma)e^{-jkl} + \Gamma^2(1+\Gamma)(1-\Gamma)e^{-3jkl} \\ & + \Gamma^4(1+\Gamma)(1-\Gamma)e^{-4jkl} + \cdots T_\infty \end{aligned} \tag{184}$$

$$S_{21} = \sum_{n=0}^{\infty}\left\{\Gamma^{2n}(1+\Gamma)(1-\Gamma)e^{-(2n+1)jkl}\right\} \tag{185}$$

In order to solve these infinite sums, the geometric series in the following form is used

$$\sum_{n=0}^{\infty}\{a\mathrm{r}^n\} = \frac{a}{1-r} \tag{186}$$

Here is the simplification of S_{11}

$$S_{11} = \Gamma - \sum_{n=0}^{\infty}\left\{\Gamma^{2n+1}(1+\Gamma)(1-\Gamma)e^{-(2n+2)jkl}\right\} \tag{187}$$

$$S_{11} = \Gamma - \sum_{n=0}^{\infty}\left\{\left(\Gamma^2 e^{-2jkl}\right)^n \Gamma(1+\Gamma)(1-\Gamma)e^{-2jkl}\right\} \tag{188}$$

$$a = \Gamma(1+\Gamma)(1-\Gamma)e^{-2jkl} \tag{189}$$

$$\mathrm{r} = \Gamma^2 e^{-2jkl} \tag{190}$$

$$S_{11} = \Gamma - \frac{\Gamma(1+\Gamma)(1-\Gamma)e^{-2jkl}}{(1-\Gamma^2 e^{-2jkl})} \tag{191}$$

$$S_{11} = \frac{\Gamma\left(1 - \Gamma^2 e^{-2jkl}\right) - \Gamma(1+\Gamma)(1-\Gamma)e^{-2jkl}}{(1 - \Gamma^2 e^{-2jkl})} \tag{192}$$

$$S_{11} = \Gamma - \frac{\Gamma(1+\Gamma)(1-\Gamma)e^{-2jkl}}{(1 - \Gamma^2 e^{-2jkl})} \tag{193}$$

$$S_{11} = \frac{\Gamma\left(1 - \Gamma^2 e^{-2jkl}\right) - \Gamma(1+\Gamma)(1-\Gamma)e^{-2jkl}}{(1 - \Gamma^2 e^{-2jkl})} \tag{194}$$

$$S_{11} = \frac{\Gamma\left(1 - \Gamma^2 e^{-2jkl}\right) - \Gamma(1+\Gamma)(1-\Gamma)e^{-2jkl}}{(1 - \Gamma^2 e^{-2jkl})} \tag{195}$$

$$S_{11} = \frac{\Gamma - \Gamma^3 e^{-2jkl} - (\Gamma - \Gamma^2 + \Gamma^2 - \Gamma^3)e^{-2jkl}}{(1 - \Gamma^2 e^{-2jkl})} \tag{196}$$

$$S_{11} = \frac{\Gamma - (\Gamma^3 + \Gamma - \Gamma^2 + \Gamma^2 - \Gamma^3)e^{-2jkl}}{(1 - \Gamma^2 e^{-2jkl})} \tag{197}$$

$$S_{11} = \frac{\Gamma - (\Gamma)e^{-2jkl}}{(1 - \Gamma^2 e^{-2jkl})} \tag{198}$$

$$S_{11} = \frac{\left(1 - e^{-2jkl}\right)\Gamma}{(1 - \Gamma^2 e^{-2jkl})} \tag{199}$$

$$P = e^{-jkl} \tag{200}$$

$$S_{11} = \frac{(1 - P^2)\Gamma}{1 - \Gamma^2 P^2} \tag{201}$$

Here is the simplification of S_{21}

$$S_{21} = \sum_{n=0}^{\infty} \left\{\Gamma^{2n}(1+\Gamma)(1-\Gamma)e^{-(2n+1)jkl}\right\} \tag{202}$$

$$S_{21} = \sum_{n=0}^{\infty} \left\{ \left(\Gamma^2 e^{-2jkl} \right)^n (1+\Gamma)(1-\Gamma) e^{-jkl} \right\} \tag{203}$$

$$a = (1+\Gamma)(1-\Gamma)e^{-jkl} \tag{204}$$

$$\mathrm{r} = \Gamma^2 e^{-2jkl} \tag{205}$$

$$S_{21} = \frac{(1+\Gamma)(1-\Gamma)e^{-jkl}}{(1-\Gamma^2 e^{-2jkl})} \tag{206}$$

$$S_{21} = \frac{(1-\Gamma)^2 e^{-jkl}}{(1-\Gamma^2 e^{-2jkl})} \tag{207}$$

$$P = e^{-jkl} \tag{208}$$

$$S_{21} = \frac{(1-\Gamma^2)P}{1-\Gamma^2 P^2} \tag{209}$$

These equations relate the measured S-parameters to the single-interface reflection coefficient Γ and the single-transmission propagation constant, $P = e^{-jkl}$. These equations must be solved for Γ and P in terms of S_{11} and S_{21}

$$S_{11} = \frac{(1-P^2)\Gamma}{1-\Gamma^2 P^2} \tag{210}$$

$$S_{21} = \frac{(1-\Gamma^2)P}{1-\Gamma^2 P^2} \tag{211}$$

Solution in S_{11}

$$S_{11}(1-\Gamma^2 P^2) = (1-P^2)\Gamma \tag{212}$$

$$\Gamma P^2 - S_{11}\Gamma^2 P^2 = \Gamma - S_{11} \tag{213}$$

$$(\Gamma - S_{11}\Gamma^2)P^2 = \Gamma - S_{11} \tag{214}$$

$$P^2 = \frac{\Gamma - S_{11}}{\Gamma - S_{11}\Gamma^2} \tag{215}$$

$$P = \pm\sqrt{\frac{\Gamma - S_{11}}{\Gamma - S_{11}\Gamma^2}} \tag{216}$$

Solution in S_{21}

$$S_{21} = \frac{(1 - \Gamma^2)P}{1 - \Gamma^2 P^2} \tag{217}$$

$$P\Gamma^2 - S_{21}\Gamma^2 P^2 = P - S_{21} \tag{218}$$

$$(P - S_{21}P^2)\Gamma^2 = P - S_{21} \tag{219}$$

$$\Gamma^2 = \frac{P - S_{21}}{P - S_{21}P^2} \tag{220}$$

Combining equations

$$\Gamma^2 = \frac{\pm\sqrt{\frac{\Gamma - S_{11}}{\Gamma - S_{11}\Gamma^2}} - S_{21}}{\pm\sqrt{\frac{\Gamma - S_{11}}{\Gamma - S_{11}\Gamma^2}} - \frac{S_{21}\Gamma - S_{21}S_{11}}{\Gamma - S_{11}\Gamma^2}} \tag{221}$$

$$\Gamma^2 = \frac{\pm\sqrt{\frac{(\Gamma - S_{11})(\Gamma - S_{11}\Gamma^2)}{(\Gamma - S_{11}\Gamma^2)(\Gamma - S_{11}\Gamma^2)}} - \frac{S_{21}(\Gamma - S_{11}\Gamma^2)}{(\Gamma - S_{11}\Gamma^2)}}{\pm\sqrt{\frac{(\Gamma - S_{11})(\Gamma - S_{11}\Gamma^2)}{(\Gamma - S_{11}\Gamma^2)(\Gamma - S_{11}\Gamma^2)}} - \frac{S_{21}\Gamma - S_{21}S_{11}}{\Gamma - S_{11}\Gamma^2}} \tag{222}$$

$$\Gamma^2 = \frac{\frac{\pm\sqrt{(\Gamma - S_{11})(\Gamma - S_{11}\Gamma^2)} - S_{21}\Gamma + S_{21}S_{11}\Gamma^2}{\Gamma - S_{11}\Gamma^2}}{\frac{\pm\sqrt{(\Gamma - S_{11})(\Gamma - S_{11}\Gamma^2)} - S_{21}\Gamma + S_{21}S_{11}}{\Gamma - S_{11}\Gamma^2}} \tag{223}$$

$$\Gamma^2 = \frac{\pm\sqrt{(\Gamma - S_{11})(\Gamma - S_{11}\Gamma^2)} - S_{21}\Gamma + S_{21}S_{11}\Gamma^2}{\pm\sqrt{(\Gamma - S_{11})(\Gamma - S_{11}\Gamma^2)} - S_{21}\Gamma + S_{21}S_{11}} \tag{224}$$

Γ^2

$$= \frac{\left(\pm\sqrt{(\Gamma - S_{11})(\Gamma - S_{11}\Gamma^2)} - S_{21}\Gamma + S_{21}S_{11}\Gamma^2\right)\left(\pm\sqrt{(\Gamma - S_{11})(\Gamma - S_{11}\Gamma^2)} - S_{21}\Gamma + S_{21}S_{11}\right)}{\left(\pm\sqrt{(\Gamma - S_{11})(\Gamma - S_{11}\Gamma^2)} - S_{21}\Gamma + S_{21}S_{11}\right)^2}$$

Γ

$$= \frac{\sqrt{\left(\pm\sqrt{(\Gamma - S_{11})(\Gamma - S_{11}\Gamma^2)} - S_{21}\Gamma + S_{21}S_{11}\Gamma^2\right)\left(\pm\sqrt{(\Gamma - S_{11})(\Gamma - S_{11}\Gamma^2)} - S_{21}\Gamma + S_{21}S_{11}\right)}}{\pm\sqrt{(\Gamma - S_{11})(\Gamma - S_{11}\Gamma^2)} - S_{21}\Gamma + S_{21}S_{11}}$$

Γ

$$= \frac{\sqrt{\left(\pm\sqrt{\Gamma^2 - \Gamma S_{11} + S_{11}S_{11}\Gamma^2 + S_{11}\Gamma^3} - S_{21}\Gamma + S_{21}S_{11}\Gamma^2\right)\left(\pm\sqrt{(\Gamma - S_{11})(\Gamma - S_{11}\Gamma^2)} - S_{21}\Gamma + S_{21}S_{11}\right)}}{\pm\sqrt{(\Gamma - S_{11})(\Gamma - S_{11}\Gamma^2)} - S_{21}\Gamma + S_{21}S_{11}}$$

$$(a + b)(a + c) = a^2 + ab + ac + bc$$

$$\chi = \frac{{S_{11}}^2 - {S_{21}}^2 + 1}{2S_{11}} \tag{225}$$

$$\Gamma = \chi \pm \sqrt{\chi^2 - 1} \tag{226}$$

$$P = \frac{S_{11} + S_{21} - \Gamma}{1 - (S_{11} + S_{21})\Gamma} \tag{227}$$

In reverse

$$\chi = \frac{{S_{11}}^2 - {S_{21}}^2 + 1}{2S_{11}} \tag{228}$$

$$\Gamma = \chi \pm \sqrt{\chi^2 - 1} \tag{229}$$

$$P = \frac{S_{11} + S_{21} - \Gamma}{1 - (S_{11} + S_{21})\Gamma} \tag{230}$$

Reflection coefficient

$$\Gamma = \frac{{S_{11}}^2 - {S_{21}}^2 + 1}{2S_{11}} \pm \sqrt{\left(\frac{{S_{11}}^2 - {S_{21}}^2 + 1}{2S_{11}}\right)^2 - 1} \tag{231}$$

$$\Gamma = \frac{{S_{11}}^2 - {S_{21}}^2 + 1}{2S_{11}} \pm \sqrt{\frac{\left({S_{11}}^2 - {S_{21}}^2 + 1\right)^2 - (2S_{11})^2}{(2S_{11})^2}} \tag{232}$$

$$\Gamma = \frac{{S_{11}}^2 - {S_{21}}^2 + 1}{2S_{11}} \pm \frac{\sqrt{\left({S_{11}}^2 - {S_{21}}^2 + 1\right)^2 - 4{S_{11}}^2}}{2S_{11}} \tag{233}$$

$$\Gamma = \frac{{S_{11}}^2 - {S_{21}}^2 + 1 \pm \sqrt{\left({S_{11}}^2 - {S_{21}}^2 + 1\right)^2 - 4{S_{11}}^2}}{2S_{11}} \tag{234}$$

Propagation Constant

$$P = \frac{-{S_{11}}^2 + {S_{21}}^2 + 1 \pm \sqrt{\left({S_{11}}^2 - {S_{21}}^2 + 1\right)^2 - 4{S_{11}}^2}}{2S_{11}} \tag{235}$$

Solve these equations for S_{11} and S_{21} in terms of Γ and P

$$\Gamma = \frac{{S_{11}}^2 - {S_{21}}^2 + 1 \pm \sqrt{\left({S_{11}}^2 - {S_{21}}^2 + 1\right)^2 - 4{S_{11}}^2}}{2S_{11}} \tag{236}$$

$$P = \frac{-{S_{11}}^2 + {S_{21}}^2 + 1 \pm \sqrt{\left({S_{11}}^2 - {S_{21}}^2 + 1\right)^2 - 4{S_{11}}^2}}{2S_{11}} \tag{237}$$

Solutions

$$\chi = \frac{{S_{11}}^2 - {S_{21}}^2 + 1}{2S_{11}} \tag{238}$$

$$\Gamma = \chi \pm \sqrt{\chi^2 - 1} \tag{239}$$

$$P = \frac{S_{11} + S_{21} - \Gamma}{1 - (S_{11} + S_{21})\Gamma} \tag{240}$$

In order to resolve the sign ambiguity in Γ, the sign is chosen so that the magnitude of the reflection coefficient is less than one. Essentially, for implementation, a sign is chosen and if the resulting magnitude of the reflection coefficient is greater than one, the opposite sign is chosen.

$$\Gamma = \begin{matrix} \chi + \sqrt{\chi^2 - 1} \\ \chi - \sqrt{\chi^2 - 1} \end{matrix} \Big| \; (|\Gamma| \leq 1) \tag{241}$$

Having discovered equations for the single interface reflection coefficient Γ and the single-transmission propagation coefficient, P, material parameters are sought from these quantities.

The definition of impedance states that

$$Z = \sqrt{\frac{\mu}{\varepsilon}} = \sqrt{\frac{\mu_0 \mu_r}{\varepsilon_0 \varepsilon_r}} = \sqrt{\frac{\mu_0}{\varepsilon_0}} \sqrt{\frac{\mu_r}{\varepsilon_r}} = Z_0 \sqrt{\frac{\mu_r}{\varepsilon_r}} \tag{242}$$

The definition of the single-interface reflection coefficient Γ states that

$$\Gamma = \frac{Z - Z_0}{Z - Z_0} = \frac{Z_0\sqrt{\frac{\mu_r}{\varepsilon_r}} - Z_0}{Z_0\sqrt{\frac{\mu_r}{\varepsilon_r}} + Z_0} = \frac{\sqrt{\frac{\mu_r}{\varepsilon_r}} - 1}{\sqrt{\frac{\mu_r}{\varepsilon_r}} + 1} \tag{243}$$

Nicholson, Ross and Weir define the single-transmission propagation constant *P* differently so both definitions will be derived here; however, for rectangular waveguide, the Weir method is appropriate.

The definition of the single-transmission propagation constant *P* according to Nicholson-Ross states that

$$P = e^{-jkl} = e^{-j\omega\sqrt{\mu\varepsilon}l} = e^{-j2\pi f\sqrt{\mu_0\mu_r\varepsilon_0\varepsilon_r}l} = e^{-j2\pi f\sqrt{\mu_0\varepsilon_0}\sqrt{\mu_r\varepsilon_r}l} = e^{-j\frac{2\pi f}{c_0}\sqrt{\mu_r\varepsilon_r}l} \tag{244}$$

Weir defines a different single-transmission propagation constant P. Because the waveguide is not a TEM transmission line, the maximum cutoff wavelength of the guide must be considered, λ_c. Thus Weir defines a slightly different single-transmission propagation constant which takes this cutoff wavelength into account. $\lambda_0 = \frac{1}{f_0}$ and f_0 is the actual measured frequency.

$$f = \sqrt{\frac{1}{{\lambda_0}^2} - \frac{1}{{\lambda_c}^2}} \tag{245}$$

The guide cutoff wavelength for rectangular waveguide may be solved using this simple relation.

$$\lambda_c = \frac{c_0}{2a} \tag{246}$$

$$P = e^{-jkl} = e^{-j\omega\sqrt{\mu\varepsilon}l} = e^{-j2\pi f\sqrt{\mu_0\mu_r\varepsilon_0\varepsilon_r}l} = e^{-j2\pi f\sqrt{\mu_0\varepsilon_0}\sqrt{\mu_r\varepsilon_r}l} \tag{247}$$

$$P = e^{-j2\pi\sqrt{\frac{1}{{\lambda_0}^2}-\frac{1}{{\lambda_c}^2}}\sqrt{\mu_r\varepsilon_r}l} \tag{248}$$

The Nicholson-Ross method as described by the original authors solves for material parameters, permittivity and permeability. The derivations of ε_r and μ_r are started using the Nicholson-Ross method and solve the following two equations for ε_r and μ_r in terms of P, Γ

$$\Gamma = \frac{\sqrt{\frac{\mu_r}{\varepsilon_r}} - 1}{\sqrt{\frac{\mu_r}{\varepsilon_r}} + 1} \tag{249}$$

$$P = e^{-j\frac{2\pi f}{c_0}\sqrt{\mu_r\varepsilon_r}l} \tag{250}$$

Solution from Γ

$$\Gamma = \frac{\sqrt{\frac{\mu_r}{\varepsilon_r}} - 1}{\sqrt{\frac{\mu_r}{\varepsilon_r}} + 1} \tag{251}$$

$$\Gamma\sqrt{\frac{\mu_r}{\varepsilon_r}} + \Gamma = \sqrt{\frac{\mu_r}{\varepsilon_r}} - 1 \tag{252}$$

$$\sqrt{\frac{\mu_r}{\varepsilon_r}} - \Gamma\sqrt{\frac{\mu_r}{\varepsilon_r}} = 1 + \Gamma \tag{253}$$

$$\sqrt{\frac{\mu_r}{\varepsilon_r}}(1 - \Gamma) = 1 + \Gamma \tag{254}$$

$$\frac{\mu_r}{\varepsilon_r} = \left(\frac{1+\Gamma}{1-\Gamma}\right)^2 \tag{255}$$

$$\frac{1}{\varepsilon_r} = \left(\frac{1+\Gamma}{1-\Gamma}\right)^2 \frac{1}{\mu_r} \tag{256}$$

Solution from *P*

$$P = e^{-j\frac{2\pi f}{c_0}\sqrt{\mu_r\varepsilon_r}l} \tag{257}$$

$$\frac{1}{P} = e^{j\frac{2\pi f}{c_0}\sqrt{\mu_r\varepsilon_r}l} \tag{258}$$

$$ln\left(\frac{1}{P}\right) = j\frac{2\pi f}{c_0}\sqrt{\mu_r\varepsilon_r}l \tag{259}$$

$$\sqrt{\mu_r\varepsilon_r} = \frac{c_0}{j2\pi fl} ln\left(\frac{1}{P}\right) \tag{260}$$

$$\mu_r\varepsilon_r = \left(\frac{c_0}{j2\pi fl} ln\left(\frac{1}{P}\right)\right)^2 \tag{261}$$

$$\mu_r\varepsilon_r = \left(\frac{1}{j}\right)^2 \left(\frac{c_0}{j2\pi fl} ln\left(\frac{1}{P}\right)\right)^2 \tag{262}$$

$$\mu_r = -\frac{1}{\varepsilon_r}\left(\frac{c_0}{2\pi fl} ln\left(\frac{1}{P}\right)\right)^2 \tag{263}$$

Here is the solution for μ_r by the Nicholson-Ross method. Note that a special solution exists to solve the ambiguity of $ln\left(\frac{1}{P}\right)$ because the logarithm of a complex number produces infinitely many possible solutions. This solution will be discussed once the equations at hand are solved.

$$\mu_r = \left(\frac{1+\Gamma}{1-\Gamma}\right)^2 \frac{1}{\mu_r}\left(\frac{c_0}{j2\pi fl} ln\left(\frac{1}{P}\right)\right)^2 \tag{264}$$

$$\mu_r{}^2 = \left(\frac{1+\Gamma}{1-\Gamma}\right)^2 \left(\frac{c_0}{j2\pi f l} ln\left(\frac{1}{P}\right)\right)^2 \tag{265}$$

$$\mu_r = \left(\frac{1+\Gamma}{1-\Gamma}\right) \frac{c_0}{j2\pi f l} ln\left(\frac{1}{P}\right) \tag{266}$$

Here is the solution for ε_r by the Nicholson-Ross method. Note that a special solution exists to solve the ambiguity of $ln\left(\frac{1}{P}\right)$ because the logarithm of a complex number produces infinitely many possible solutions. This solution will be discussed once the equations at hand are solved.

$$\varepsilon_r = \left(\frac{1+\Gamma}{1-\Gamma}\right)^2 \mu_r \tag{267}$$

$$\varepsilon_r = \left(\frac{1+\Gamma}{1-\Gamma}\right)^2 \frac{1}{\varepsilon_r} \left(\frac{c_0}{2\pi f l} ln\left(\frac{1}{P}\right)\right)^2 \tag{268}$$

$$\varepsilon_r{}^2 = \left(\frac{1+\Gamma}{1-\Gamma}\right)^2 \left(\frac{c_0}{2\pi f l} ln\left(\frac{1}{P}\right)\right)^2 \tag{269}$$

$$\varepsilon_r = \left(\frac{1-\Gamma}{1+\Gamma}\right) \frac{c_0}{2\pi f l} ln\left(\frac{1}{P}\right) \tag{270}$$

The Nicolson-Ross method was modified by Weir in order to solve for material properties when the material is in a waveguide. Recall that these solutions for ε_r and μ_r using the Nicholson-Ross method do not consider the cutoff wavelength of rectangular waveguide due to its non-TEM nature. Alternate equations are derived from the method of Weir. The two equations for ε_r and μ_r are solved in terms of P, Γ

$$\Gamma = \frac{\sqrt{\frac{\mu_r}{\varepsilon_r}} - 1}{\sqrt{\frac{\mu_r}{\varepsilon_r}} + 1} \tag{271}$$

$$P = e^{-j\frac{2\pi\sqrt{\mu_r\varepsilon_r}l}{\sqrt{\frac{1}{\lambda_0{}^2} - \frac{1}{\lambda_c{}^2}}}} \tag{272}$$

Solution from Γ

$$\Gamma = \frac{\sqrt{\frac{\mu_r}{\varepsilon_r}} - 1}{\sqrt{\frac{\mu_r}{\varepsilon_r}} + 1} \tag{273}$$

$$\Gamma\sqrt{\frac{\mu_r}{\varepsilon_r}} + \Gamma = \sqrt{\frac{\mu_r}{\varepsilon_r}} - 1 \tag{274}$$

$$\sqrt{\frac{\mu_r}{\varepsilon_r}} - \Gamma\sqrt{\frac{\mu_r}{\varepsilon_r}} = 1 + \Gamma \tag{275}$$

$$\sqrt{\frac{\mu_r}{\varepsilon_r}}(1 - \Gamma) = 1 + \Gamma \tag{276}$$

$$\frac{\mu_r}{\varepsilon_r} = \left(\frac{1 + \Gamma}{1 - \Gamma}\right)^2 \tag{277}$$

$$\frac{1}{\varepsilon_r} = \left(\frac{1 + \Gamma}{1 - \Gamma}\right)^2 \frac{1}{\mu_r} \tag{278}$$

Solution from *P*

$$P = e^{-j2\pi\sqrt{\frac{1}{\lambda_0{}^2} - \frac{1}{\lambda_c{}^2}}\sqrt{\mu_r\varepsilon_r}l} \tag{279}$$

$$\frac{1}{P} = e^{j2\pi\sqrt{\frac{1}{{\lambda_0}^2}-\frac{1}{{\lambda_c}^2}}\sqrt{\mu_r\varepsilon_r}l} \tag{280}$$

$$ln\left(\frac{1}{P}\right) = j2\pi\sqrt{\frac{1}{{\lambda_0}^2}-\frac{1}{{\lambda_c}^2}}\sqrt{\mu_r\varepsilon_r}l \tag{281}$$

$$\sqrt{\mu_r\varepsilon_r} = \frac{1}{j2\pi l\sqrt{\frac{1}{{\lambda_0}^2}-\frac{1}{{\lambda_c}^2}}}ln\left(\frac{1}{P}\right) \tag{282}$$

$$\mu_r\varepsilon_r = \left(\frac{1}{j}\right)^2\frac{1}{\sqrt{\frac{1}{{\lambda_0}^2}-\frac{1}{{\lambda_c}^2}}}\left(\frac{1}{j2\pi l}ln\left(\frac{1}{P}\right)\right)^2 \tag{283}$$

$$\mu_r = -\frac{1}{\varepsilon_r}\frac{1}{\sqrt{\frac{1}{{\lambda_0}^2}-\frac{1}{{\lambda_c}^2}}}\left(\frac{1}{2\pi l}ln\left(\frac{1}{P}\right)\right)^2 \tag{284}$$

Here is the solution for μ_r by the Weir method. Note that a special solution exists to solve the ambiguity of $ln\left(\frac{1}{P}\right)$ because the logarithm of a complex number produces infinitely many possible solutions. This solution will be discussed once the equations at hand are solved.

$$\mu_r = -\left\{\left(\frac{1+\Gamma}{1-\Gamma}\right)^2\frac{1}{\mu_r}\right\}\frac{1}{\sqrt{\frac{1}{{\lambda_0}^2}-\frac{1}{{\lambda_c}^2}}}\left(\frac{1}{2\pi l}ln\left(\frac{1}{P}\right)\right)^2 \tag{285}$$

$${\mu_r}^2 = -\left(\frac{1+\Gamma}{1-\Gamma}\right)^2\frac{1}{\sqrt{\frac{1}{{\lambda_0}^2}-\frac{1}{{\lambda_c}^2}}}\left(\frac{1}{2\pi l}ln\left(\frac{1}{P}\right)\right)^2 \tag{286}$$

$$\mu_r = -\left(\frac{1+\Gamma}{1-\Gamma}\right)\frac{1}{\sqrt{\frac{1}{\lambda_0{}^2}-\frac{1}{\lambda_c{}^2}}}\left(\frac{1}{2\pi f l}ln\left(\frac{1}{P}\right)\right) \tag{287}$$

Define intermediate parameter

$$\frac{1}{\Lambda^2} = -\left(\frac{1}{2\pi l}ln\left(\frac{1}{P}\right)\right)^2 \tag{288}$$

$$\mu_r = \left(\frac{1+\Gamma}{1-\Gamma}\right)\frac{1}{\Lambda}\frac{1}{\sqrt{\frac{1}{\lambda_0{}^2}-\frac{1}{\lambda_c{}^2}}} = \frac{1+\Gamma}{\Lambda(1-\Gamma)\sqrt{\frac{1}{\lambda_0{}^2}-\frac{1}{\lambda_c{}^2}}} \tag{289}$$

Here is the solution for ε_r by the Weir method. Note that a special solution exists to solve the ambiguity of $ln\left(\frac{1}{P}\right)$ because the logarithm of a complex number produces infinitely many possible solutions. This solution will be discussed once the equations at hand are solved.

From Weir

$$\left(\frac{\varepsilon_r\mu_r}{\lambda_0{}^2}-\frac{1}{\lambda_c{}^2}\right) = -\left(\frac{1}{2\pi l}ln\left(\frac{1}{P}\right)\right)^2 \tag{290}$$

$$\left(\frac{\varepsilon_r\mu_r\lambda_c{}^2-\lambda_0{}^2}{\lambda_0{}^2\lambda_c{}^2}\right) = -\left(\frac{1}{2\pi l}ln\left(\frac{1}{P}\right)\right)^2 \tag{291}$$

$$\left(\frac{\varepsilon_r\mu_r}{\lambda_0{}^2}-\frac{1}{\lambda_c{}^2}\right) = -\left(\frac{1}{2\pi l}ln\left(\frac{1}{P}\right)\right)^2 \tag{292}$$

$$\frac{\varepsilon_r\mu_r}{\lambda_0{}^2} = -\left(\frac{1}{2\pi l}ln\left(\frac{1}{P}\right)\right)^2 + \frac{1}{\lambda_c{}^2} \tag{293}$$

$$\frac{\varepsilon_r \mu_r}{{\lambda_0}^2} = \frac{1}{\mu_r}\left[\left(\frac{1}{2\pi l} ln\left(\frac{1}{P}\right)\right)^2 - \frac{1}{{\lambda_c}^2}\right] \tag{294}$$

$$\varepsilon_r = \frac{1}{\mu_r}\left(\left(\frac{1}{2\pi l} ln\left(\frac{1}{P}\right)\right)^2 {\lambda_0}^2 + \frac{{\lambda_0}^2}{{\lambda_c}^2}\right) \tag{295}$$

Define intermediate parameter

$$\frac{1}{\Lambda^2} = -\left(\frac{1}{2\pi l} ln\left(\frac{1}{P}\right)\right)^2 \tag{296}$$

$$\varepsilon_r = \frac{1}{\mu_r}\left(\frac{{\lambda_0}^2}{\Lambda^2} + \frac{{\lambda_0}^2}{{\lambda_c}^2}\right) \tag{297}$$

Solution of logarithm of a complex number

$$ln\left(\frac{1}{P}\right) = ln\left(Mag\left(\frac{1}{P}\right)\right) + i \times Phase\left(\frac{1}{P}\right) + 2\pi n = ln\left|\frac{1}{P}\right| + i\left[\angle\left(\frac{1}{P}\right) + 2\pi n\right] \tag{298}$$

According to Weir, the integer term is understood to be the integer number of wavelengths residing in the sample of thickness l in the rectangular waveguide.

$$n = Integer\left(\frac{l}{\lambda_g}\right) \tag{299}$$

Maximum cutoff wavelength in terms of the narrow dimension of the waveguide

$$\lambda_c = \frac{c_0}{2a} \tag{300}$$

Actual measured frequency

$$\lambda_0 = \frac{1}{f_0} \tag{301}$$

Wavelength in the rectangular waveguide

$$\lambda_g = \frac{\lambda_0}{\sqrt{1 - \left(\frac{\lambda_0}{\lambda_c}\right)^2}} \tag{302}$$

Assume quarter-wave sample length

$$l = \frac{1}{4}\lambda_g \tag{303}$$

$$n = Integer\left(\frac{l}{\lambda_g}\right) = Integer\left(\frac{1}{4}\right) = 0 \tag{304}$$

Appendix G Characteristic Impedance from S-parameters

In the Nicolson-Ross-Weir method and after solving the single-interface reflection and transmission coefficients, the characteristic impedance of the line must be solved using transmission line equations.

$$\chi = \frac{{S_{11}}^2 - {S_{21}}^2 + 1}{2S_{11}} \tag{305}$$

$$\Gamma = \chi \pm \sqrt{\chi^2 - 1} \tag{306}$$

$$P = \frac{S_{11} + S_{21} - \Gamma}{1 - (S_{11} + S_{21})\Gamma} \tag{307}$$

$$\Gamma = \frac{\frac{Z_c}{Z_0} - 1}{\frac{Z_c}{Z_0} + 1} \tag{308}$$

$$P = e^{-j\frac{2fnl}{c_0}} \tag{309}$$

Solution from Γ

$$\Gamma = \frac{\frac{Z_c}{Z_0} - 1}{\frac{Z_c}{Z_0} + 1} \tag{310}$$

$$\Gamma\frac{Z_c}{Z_0} + \Gamma = \frac{Z_c}{Z_0} - 1 \tag{311}$$

$$\frac{Z_c}{Z_0} - \Gamma\frac{Z_c}{Z_0} = 1 + \Gamma \tag{312}$$

$$Z_c = Z_0\frac{1 + \Gamma}{1 - \Gamma} \tag{313}$$

Solution from *P*

$$P = e^{-j\frac{2\pi fnl}{c_0}} \tag{314}$$

$$\frac{1}{P} = e^{j\frac{2\pi fnl}{c_0}} \tag{315}$$

$$ln\left(\frac{1}{P}\right) = j\frac{2\pi fnl}{c_0} \tag{316}$$

$$n = \frac{c_0}{j2\pi fl} ln\left(\frac{1}{P}\right) \tag{317}$$

Note that a special solution exists to solve the ambiguity of $ln\left(\frac{1}{P}\right)$ because the logarithm of a complex number produces infinitely many possible solutions.

Solution of logarithm of a complex number

$$ln\left(\frac{1}{P}\right) = ln\left(Mag\left(\frac{1}{P}\right)\right) + i \times Phase\left(\frac{1}{P}\right) + 2\pi n \tag{318}$$

$$ln\left(\frac{1}{P}\right) = ln\left|\frac{1}{P}\right| + i\left[\angle\left(\frac{1}{P}\right) + 2\pi N\right] \tag{319}$$

According to Weir, the integer term N is understood to be the integer number of wavelengths residing in the sample of thickness l in the rectangular waveguide. In order to determine N a guess is made at the effective index of refraction, n_{guess}.

$$N = Round\left(\frac{n_{guess} fl}{c_0}\right) \tag{320}$$

$$n = \frac{c_0}{j2\pi fl}\left(ln\left|\frac{1}{P}\right| + i\left[\angle\left(\frac{1}{P}\right) + 2\pi N\right]\right) \tag{321}$$

Final Two Equations

$$\gamma = -\frac{1}{l}(lnP + i[\angle P - 2\pi N]) \tag{322}$$

$$Z_c = Z_0 \frac{1+\Gamma}{1-\Gamma} \tag{323}$$

Single Equation

$$\gamma = -\frac{1}{l}\left(ln\left|\frac{S_{11}+S_{21}-\Gamma}{1-(S_{11}+S_{21})\Gamma}\right| + i\left[angle\left[\frac{S_{11}+S_{21}-\Gamma}{1-(S_{11}+S_{21})\Gamma}\right] - 2\pi N\right]\right) \tag{324}$$

$$\alpha = -\frac{1}{l} ln\left|\frac{S_{11}+S_{21}-\Gamma}{1-(S_{11}+S_{21})\Gamma}\right| \tag{325}$$

$$\beta = -\frac{1}{l} angle\left[\frac{S_{11}+S_{21}-\Gamma}{1-(S_{11}+S_{21})\Gamma}\right] + \frac{2\pi N}{l} \tag{326}$$

$$Z_c = Z_0 \frac{1 + \frac{{S_{11}}^2 - {S_{21}}^2 + 1}{2S_{11}} \pm \sqrt{\left(\frac{{S_{11}}^2 - {S_{21}}^2 + 1}{2S_{11}}\right)^2 - 1}}{1 - \left(\frac{{S_{11}}^2 - {S_{21}}^2 + 1}{2S_{11}} \pm \sqrt{\left(\frac{{S_{11}}^2 - {S_{21}}^2 + 1}{2S_{11}}\right)^2 - 1}\right)} \tag{327}$$

Appendix H S-parameters from Single-Interface T and R constants

Usual transmission line solutions produce the characteristic impedance and effective dielectric constant and it is frequently useful to determine from these parameters, the frequency, and the line length, the S-parameters which would be seen if the system were connected to a VNA. These equations produce the characteristic humps in an S-parameter plot over frequency of a length of transmission line.

$$\Gamma = \frac{\frac{Z_c}{Z_0} - 1}{\frac{Z_c}{Z_0} + 1} \tag{328}$$

$$n = \sqrt{\varepsilon_e} \tag{329}$$

$$\lambda = \frac{c_0}{fn} \tag{330}$$

$$\beta = \frac{2\pi}{\lambda} \tag{331}$$

$$\gamma = \alpha + j\beta \tag{332}$$

$$P = e^{-\gamma l} \tag{333}$$

$$S_{11} = \frac{(1 - P^2)\Gamma}{1 - \Gamma^2 P^2} \tag{334}$$

$$S_{21} = \frac{(1 - \Gamma^2)P}{1 - \Gamma^2 P^2} \tag{335}$$

Appendix I Microstrip Modeling

Several closed-form approximations of microstrip transmission line are available. The first derivation here is of the method of Bahl and Trivedi [95]. For most practical transmission lines and all of those discussed here, the assumption $\frac{w}{h} \geq 1$ is valid.

$$Z_c = \frac{120\pi}{\sqrt{\varepsilon_e}} \frac{1}{\frac{w}{h} + 1.393 + \frac{2}{3} ln\left(\frac{w}{h} + 1.444\right)} \tag{336}$$

$$\varepsilon_e = \frac{\varepsilon_r + 1}{2} + \frac{\varepsilon_r - 1}{2}\left(1 + 12\frac{h}{w}\right)^{-1/2} \tag{337}$$

The more complex method which is used here is the Hammerstad method [103]. First several fill fraction factors are computed. For the work here, two separate computations are used in order to separate cases and yet still operate on entire vectors of data at once. It is more computationally efficient to compute both cases in parallel as arrays and then select the correct solution between them.

$$\mathrm{F}_2 = \left(1 + 12\frac{h}{w}\right)^{-1/2} \tag{338}$$

$$\mathrm{F}_1 = \mathrm{F}_2 + 0.04\left(1 - \frac{w}{h}\right)^2 \tag{339}$$

$$\varepsilon_{e,1} = \frac{1}{2}(\varepsilon_r + 1 + (\varepsilon_r - 1)\mathrm{F}_1) \tag{340}$$

$$\varepsilon_{e,2} = \frac{1}{2}(\varepsilon_r + 1 + (\varepsilon_r - 1)\mathrm{F}_2) \tag{341}$$

$$\varepsilon_e = \begin{cases} \varepsilon_{e,1} & \frac{w}{h} < 1 \\ \varepsilon_{e,2} & \frac{w}{h} \geq 1 \end{cases} \tag{342}$$

Effective width considering metallization thickness.

$$w_{eff} = \mathrm{w} + \mathrm{t}\left(1 + \frac{1}{\varepsilon_r}\right)\frac{1}{2\pi} ln\left(\frac{4e}{\sqrt{\left(\frac{t}{h}\right)^2 + \left(\frac{1}{\pi}\frac{1}{\frac{w}{t} + \frac{11}{10}}\right)^2}}\right) \tag{343}$$

Compute transmission line characteristic impedance

$$Z_c = \frac{\mathrm{Z}_0}{2\pi\sqrt{2(1+er)}} \times ln\left(1 + \frac{4h}{w_{eff}} \times \left(\left(14 + \frac{8}{\varepsilon_r}\right)\frac{4h}{11w_{eff}} + \sqrt{\left(\left(14 + \frac{8}{\varepsilon_r}\right)\frac{4h}{11w_{eff}}\right)^2 + \frac{\pi^2}{2}\left(1 + \frac{1}{\varepsilon_r}\right)}\right)\right) \tag{344}$$

Effective dielectric constant considering metallization thickness.

$$\varepsilon_e = \varepsilon_e - \frac{(\varepsilon_r - 1)t}{4.6h\sqrt{\frac{w}{h}}} \tag{345}$$

Transmission line loss can be modeled as four separate loss mechanisms: dielectric loss, conductor loss, radiation loss, and reflection loss. Reflection loss is taken into consideration in

modeling the line's characteristic impedance and reflection coefficient. There is no way to account for radiation loss in an equation-based model. Radiation loss is assumed to be zero at the frequencies of interest. Rigorous modeling of the radiation loss is reserved for full wave 3-D simulations. Here are presented approximate equations for the dielectric and conductor losses in microstrip lines. All losses which are computed here are given in units of Np/m.

$$\alpha_{Total} = \alpha_d + \alpha_c + \alpha_r + \alpha_{refl.} \tag{346}$$

Given here is the wavelength and wave number which will be used in following equations.

$$k_0 = \frac{2\pi f}{c_0} \tag{347}$$

$$\lambda_0 = \frac{c_0}{f} \tag{348}$$

Conductor loss is due to the resistance in the conductive material and is quantified as the material resistivity at DC. At high frequencies, the current flows only in a thin layer near the surface of the conductor within a few skin depths. This effectively reduces the conductivity of the material and is quantified by the sheet resistivity. Dielectric loss is proportional to frequency. Conductor loss is proportional to the square root of frequency.

Only one dielectric loss equation is presented by three authors; however, the equation is arranged differently. Each form is given here. It is easily seen that dielectric loss varies linearly with wave number, inversely with wavelength, and linearly with frequency.

Dielectric loss, from Orfanidis [108]

$$\alpha_d = \frac{1}{2}\beta tan\delta = \frac{1}{2}\frac{\omega}{c_0} tan\delta \tag{349}$$

$$\alpha_d = q\frac{\omega}{2c_0} tan\delta = \frac{f}{c_0}\pi q\sqrt{\varepsilon_e} tan\delta = \frac{1}{\lambda}\pi q\sqrt{\varepsilon_e} tan\delta = \tag{350}$$

$$\alpha_d = \frac{1}{\lambda}\pi\left(\frac{1-\sqrt{\varepsilon_e}}{1-\sqrt{\varepsilon_r}}\right)\sqrt{\varepsilon_e}tan\delta \tag{351}$$

$$\alpha_d = \frac{k_0\varepsilon_r(\varepsilon_e - 1)tan\delta}{2\sqrt{\varepsilon_e}(\varepsilon_r - 1)} \tag{352}$$

Dielectric loss, from Pozar pg. 149 [141]

$$\gamma = \alpha_d + j = \sqrt{{k_c}^2 - \omega^2\mu_0\varepsilon_0\varepsilon_r(1 - jtan\delta)} \tag{353}$$

Lossless wave number

$$k = \sqrt{\omega^2\mu_0\varepsilon_0\varepsilon_r} \tag{354}$$

Taylor series simplification

$$\gamma = \sqrt{{k_c}^2 - k^2 + jk^2tan\delta} \tag{355}$$

$$\gamma \cong \sqrt{{k_c}^2 - k^2} + \frac{jk^2tan\delta}{2\sqrt{{k_c}^2 - k^2}} \tag{356}$$

$$j\beta = \sqrt{{k_c}^2 - k^2} \tag{357}$$

$$\gamma \cong \frac{k^2tan\delta}{2\beta} + j\beta \tag{358}$$

For TE or TM

$$\alpha_d = \frac{k^2tan\delta}{2\beta} \tag{359}$$

For TEM

$$k_c = 0 \tag{360}$$

$$\beta = k \tag{361}$$

$$\alpha_d = \frac{k\ tan\delta}{2}[Np/m] \tag{362}$$

$$k_0 = k\sqrt{\varepsilon_e} \tag{363}$$

Microwave Engineering 4th ed Pozar, Pg 149 [141]

$$f = \frac{\varepsilon_r(\varepsilon_e - 1)}{\varepsilon_e(\varepsilon_r - 1)} \tag{364}$$

$$\alpha_d = \frac{k_0 tan\delta}{2\sqrt{\varepsilon_e}} f = \frac{k_0\varepsilon_r(\varepsilon_e - 1)tan\delta}{2\sqrt{\varepsilon_e}(\varepsilon_r - 1)} \tag{365}$$

$$\alpha_d = \frac{k_0\varepsilon_r(\varepsilon_e - 1)tan\delta}{2\sqrt{\varepsilon_e}(\varepsilon_r - 1)} \tag{366}$$

Dielectric loss, from Pucel et al., 1968 [110]

$$\alpha_d = \pi\frac{\varepsilon_r}{\sqrt{\varepsilon_e}}\frac{\varepsilon_e - 1}{\varepsilon_r - 1}\frac{tan\delta}{\lambda_0} \tag{367}$$

Dielectric loss, from Bahl and Trivedi, 1977 [95]

$$\mathrm{q} = \frac{\varepsilon_e - 1}{\varepsilon_r - 1} \tag{368}$$

$$\lambda_g = \lambda_0\sqrt{\varepsilon_e} \tag{369}$$

$$\alpha_d = \pi\mathrm{q}\varepsilon_r\frac{tan\delta}{\lambda_g} \tag{370}$$

DC resistance is easily calculated as follows.

$$R_{DC} = \rho t$$

RF resistance, however, is effected by the frequency-dependent skin depth [124]

$$\delta_s = \sqrt{\frac{\rho}{\pi f \mu_0}} \tag{371}$$

RF sheet resistivity is given as follows.

$$R_s = \sqrt{\pi f \mu_0 \rho} \tag{372}$$

Three different approximation equations are given for conductor loss by three different authors. In each case, it is easily seen that conductor loss varies linearly with RF sheet resistivity and RF sheet resistivity varies with the square root of frequency.

Conductor loss, from Pozar, 2012, pg. 149 [141], and Orfanidis 2004 [108] is computed as follows. This simple approximation is based on the exact solution of parallel plate lines modified slightly for microstrip.

$$\alpha_c = \frac{R_s}{re(Z)w} \tag{373}$$

Although the textbooks of Pozar and Orfanidis give a simple approximation, a more accurate approximation of conductor loss is given by Pucel et al., 1968 [110].

$$w_h = \frac{w}{h} \tag{374}$$

$$w_{h,eff} = \begin{cases} w_h + 1.25\frac{t}{\pi h}\left(1 + ln\left(\frac{4\pi w}{t}\right)\right) & w_h \leq \frac{1}{2\pi} \\ w_h + 1.25\frac{t}{\pi h}\left(1 + ln\left(\frac{2h}{t}\right)\right) & w_h > \frac{1}{2\pi} \end{cases} \tag{375}$$

$$B = \begin{cases} h & w_h \geq \frac{1}{2\pi} \\ 2\pi w & w_h < \frac{1}{2\pi} \end{cases} \tag{376}$$

$$A = 1 + \frac{1}{w_{h,eff}}\left(1 + \frac{1}{\pi} ln\left(\frac{2B}{t}\right)\right) \tag{377}$$

$$\alpha_c = \begin{cases} \frac{1}{2\pi}\frac{AR_s}{h\left(re(Z)\right)}\frac{32 - {w_{h,eff}}^2}{32 + {w_{h,eff}}^2} & w_h \leq 1 \\ 7 \times 10^{-6} AR_s re(Z)\frac{\varepsilon_e}{h}\left(w_{h,eff} + \frac{0.667 w_{h,eff}}{1.444 + w_{h,eff}}\right) & w_h > 1 \end{cases} \tag{378}$$

An even more advanced approximation is given by Bahl and Trivedi, 1977 [95]. This is the approximation used in this work.

$$w_{h,eff} = \mathrm{w} + \begin{cases} \frac{t}{\pi} ln\left(4\pi\frac{w}{t} + 1\right) & w_h \leq \frac{1}{2\pi} \\ \frac{t}{\pi} ln\left(2\frac{w}{t} + 1\right) & w_h > \frac{1}{2\pi} \end{cases} \tag{379}$$

$$A = R_s \frac{1 - \left(\frac{w_{h,eff}}{4h}\right)^2}{2\pi\left(re(Z)\right)h} \tag{380}$$

$$B = 1 + \frac{h}{w_{h,eff}} + \frac{h}{\pi w_{h,eff}}\left(ln\left(4\pi\frac{w}{t} + 1\right) - \frac{1 - \frac{t}{w}}{1 + \frac{t}{4\pi w}}\right) \tag{381}$$

$$C = 1 + \frac{h}{w_{h,eff}} + \frac{h}{\pi w_{h,eff}}\left(ln\left(2\frac{h}{t} + 1\right) - \frac{1 + \frac{t}{w}}{1 + \frac{t}{2h}}\right) \tag{382}$$

$$D = \left(\frac{w_{h,eff}}{h} + \frac{2}{\pi}\, ln\left(2ln(1)\left(\frac{w_{h,eff}}{2h} + 0.94\right)\right)\right)^2 \tag{383}$$

$$E = \frac{w_{h,eff}}{h} + \frac{w_{h,eff}}{\pi h} \frac{1}{\frac{w_{h,eff}}{2h} + 0.94} \tag{384}$$

$$\alpha_c = \begin{cases} AB & w_h \leq \frac{1}{2\pi} \\ AC & \frac{1}{2\pi} < w_h \leq 2 \\ \frac{ACE}{D} & w_h > 2 \end{cases} \tag{385}$$

Appendix J Splitting Microstrip Loss Contributions

As discussed previously, loss in transmission lines results from four separate sources, two of which are assumed to be zero. When S-parameter data is taken of a transmission line using a VNA only the total loss is determined. In order to thoroughly understand loss contributions, it is desirable to separate from this one total loss parameter the conductor and dielectric losses. This is done using nonlinear regression and the fact that dielectric loss varies directly with frequency and conductor loss varies with the square root of frequency.

$$\alpha_T = \alpha_d + \alpha_c \tag{386}$$

$$\alpha_d = \frac{k_0 tan\delta}{2\sqrt{\varepsilon_e}} f = a_1 f \tag{387}$$

$$\alpha_c = \frac{\sqrt{\frac{2\pi\mu_0}{2\sigma}}}{re(Z_0) \times w} \sqrt{f} = a_2\sqrt{f} \tag{388}$$

$$\alpha_T = a_1 f + a_2\sqrt{f} \tag{389}$$

In order to solve this two-variable equation, nonlinear regression curve fitting is used. The initial condition is $a_1 = \begin{bmatrix} 1 \cdot 10^{-12} \\ 1 \cdot 10^{-6} \end{bmatrix}_{2\times1}$.

$$f_i = \begin{bmatrix} a_{i-1,1} f \\ a_{i-1,2}\sqrt{f} \end{bmatrix}_{2\times1} \tag{390}$$

$$d_{n\times1} = \alpha_{T_{n\times1}} - f_{i_{2\times1}} \tag{391}$$

$$Z_{n\times2} = [f_{n\times1} \quad d_{n\times1}]_{n\times2} \tag{392}$$

$$da = Z' \times Z \setminus (Z' \times d) \tag{393}$$

$$a_i = a_{i-1} + da \tag{394}$$

$$err = max\left(\frac{da}{a}\right) \tag{395}$$

Appendix K Solving Microstrip Dimensions from Impedance

In the back-calculation of impedance from S-parameter data it is sometimes desirable to compute what microstrip dimensions led to the returned values of characteristic impedance and effective permittivity. This is done by using the equations for microstrip of Bahl and Trivedi [95] in reverse. This is not easily done since the equations are non-separable so a numerical method is used.

Assume $\frac{w}{h} \geq 1$

$$Z_c = \frac{120\pi}{\sqrt{\varepsilon_e}} \frac{1}{\frac{w}{h} + 1.393 + \frac{2}{3} ln\left(\frac{w}{h} + 1.44\right)} \tag{396}$$

$$\varepsilon_e = \frac{\varepsilon_r + 1}{2} + \frac{\varepsilon_r - 1}{2}\left(1 + 12\frac{h}{w}\right)^{-1/2} \tag{397}$$

Adjust ε_r to minimize $err(Z_c)$:

$$\varepsilon_e = \frac{\varepsilon_r + 1}{2} + \frac{\varepsilon_r - 1}{2}\left(1 + 12\frac{h}{w}\right)^{-1/2} \tag{398}$$

$$Z_c = \frac{120\pi}{\sqrt{\varepsilon_e}} \frac{1}{\frac{w}{h} + 1.393 + \frac{2}{3} ln\left(\frac{w}{h} + 1.44\right)} \tag{399}$$

$$\frac{dZ_c}{d\varepsilon_r} = \frac{120\pi}{\frac{w}{h} + 1.393 + \frac{2}{3} ln\left(\frac{w}{h} + 1.44\right)} \left\{ -\left[\left(\sqrt{\frac{\frac{w}{h}}{\frac{w}{h} + 12}} + 1 \right) \frac{1}{\sqrt{2}} \left(\sqrt{\frac{\frac{w}{h}}{\frac{w}{h} + 12}} (\varepsilon_r - 1) + \varepsilon_r + 1 \right) \right]^{-3/2} \right\} \tag{400}$$

$$\Delta\varepsilon_r = \frac{Z_{c,X} - Z_c}{\frac{dZ_c}{d\varepsilon_r}} \tag{401}$$

$$\varepsilon_{r,i} = \varepsilon_{r,(i-1)} + \Delta\varepsilon_r \tag{402}$$

$$err = \left| \frac{Z_{c,X} - Z_c}{Z_{c,X}} \right| \tag{403}$$

Adjust $\frac{w}{h}$ to minimize $err(Z_c)$

$$\varepsilon_e = \frac{\varepsilon_r + 1}{2} + \frac{\varepsilon_r - 1}{2}\left(1 + 12\frac{h}{w}\right)^{-1/2} \tag{404}$$

$$Z_c = \frac{120\pi}{\sqrt{\varepsilon_e}} \frac{1}{\frac{w}{h} + 1.393 + \frac{2}{3} ln\left(\frac{w}{h} + 1.44\right)} \tag{405}$$

$$\frac{dZ_c}{d\frac{w}{h}} = \frac{120\pi}{\sqrt{\varepsilon_e}}\left(1 + \frac{\frac{2}{3}}{1.414 + \frac{w}{h}}\right) \frac{1}{\left(\frac{1}{1.393} + \frac{w}{h} + \frac{2}{3} ln\left(1.414 + \frac{w}{h}\right)\right)^2} \tag{406}$$

$$\Delta\frac{w}{h} = \frac{Z_{c,X} - Z_c}{\frac{dZ_c}{d\frac{w}{h}}} \tag{407}$$

$$\left(\frac{w}{h}\right)_i = \left(\frac{w}{h}\right)_{(i-1)} + \Delta\frac{w}{h} \tag{408}$$

$$err = \left|\frac{\left(\frac{w}{h}\right)_X - \frac{w}{h}}{\left(\frac{w}{h}\right)_X}\right| \tag{409}$$

Adjust ε_r to minimize $(err\varepsilon_e)$

$$\varepsilon_e = \frac{\varepsilon_r + 1}{2} + \frac{\varepsilon_r - 1}{2}\left(1 + 12\frac{h}{w}\right)^{-1/2} \tag{410}$$

$$\frac{d\varepsilon_e}{d\varepsilon_r} = \frac{1}{2} + \frac{1}{2}\left(1 + 12\frac{h}{w}\right)^{-1/2} \tag{411}$$

$$\Delta\varepsilon_r = \frac{\varepsilon_{e_X} - \varepsilon_e}{\frac{d\varepsilon_e}{d\varepsilon_r}} \tag{412}$$

$$\left(\frac{w}{h}\right)_i = \left(\frac{w}{h}\right)_{(i-1)} + \Delta\frac{w}{h} \tag{413}$$

$$err = \left|\frac{\left(\frac{w}{h}\right)_X - \frac{w}{h}}{\left(\frac{w}{h}\right)_X}\right| \tag{414}$$

Appendix L Stripline Modeling

The equations for stripline are derived from Pozar.

$$\varepsilon_{eff} = \varepsilon_r \tag{415}$$

$$\frac{w_e}{b} = \frac{w}{b} - \begin{cases} 0 & \frac{w}{b} > 0.35 \\ \left(0.35 - \frac{w}{b}\right)^2 & \frac{w}{b} \leq 0.35 \end{cases} \tag{416}$$

$$w_e = \left(\frac{w_e}{b}\right) b \tag{417}$$

$$Z_c = \frac{30\pi b}{\sqrt{\varepsilon_r}(w_e + 0.441b)} \tag{418}$$

$$\alpha_d = \frac{\pi\sqrt{\varepsilon_r} Df}{c_0} \quad \left[\frac{Np}{m}\right] \tag{419}$$

$$\lambda_0 = \frac{c_0}{f} \tag{420}$$

$$R_s = \sqrt{\pi f \mu_0 \rho} \tag{421}$$

$$A = 1 + \frac{2w}{b-t} + \frac{1}{\pi}\frac{b+t}{b-t} ln\left(\frac{2b-t}{t}\right) \tag{422}$$

$$B = 1 + \frac{b}{(0.5w + 0.7)}\left(0.5 + \frac{0.414t}{w} + \frac{1}{2\pi} ln\frac{4\pi w}{t}\right) \tag{423}$$

$$\alpha_c = \begin{cases} \frac{2.7 \times 10^{-3} R_S \varepsilon_r Z_c}{30\pi(b-t)} A & \sqrt{\varepsilon_r} Z_c < 120 \\ \frac{0.16 R_S}{Z_c b} B & \sqrt{\varepsilon_r} Z_c \geq 120 \end{cases} \quad \left[\frac{Np}{m}\right] \tag{424}$$

Stripline parameters from impedance and dielectric constant

$$x = \frac{30\pi}{\sqrt{\varepsilon_r} Z_c} - 0.441 \tag{425}$$

$$\frac{w}{b} = \begin{cases} x & \sqrt{\varepsilon_r} Z_c < 120 \\ 0.85 - \sqrt{0.6 - x} & \sqrt{\varepsilon_r} Z_c \geq 120 \end{cases} \tag{426}$$

$$A = 1 + \frac{2w}{b-t} + \frac{1}{\pi}\frac{b+t}{b-t} ln\left(\frac{2b-t}{t}\right) \tag{427}$$

$$B = 1 + \frac{b}{(0.5w + 0.7)}\left(0.5 + \frac{0.414t}{w} + \frac{1}{2\pi} ln\frac{4\pi w}{t}\right) \tag{428}$$

$$R_S = \begin{cases} \alpha_c \dfrac{30\pi(b-t)}{2.7 \times 10^{-3} \varepsilon_r Z_c A} & \sqrt{\varepsilon_r} Z_c < 120 \\ \alpha_c \dfrac{Z_c b}{0.16B} & \sqrt{\varepsilon_r} Z_c \geq 120 \end{cases} \left[\frac{Np}{m}\right] \tag{429}$$

$$\rho = \frac{{R_s}^2}{\pi f \mu_0} \tag{430}$$

$$D = \frac{1}{\pi} \alpha_d \lambda_0 \frac{(\varepsilon_r - 1)}{\varepsilon_r} \frac{\sqrt{\varepsilon_e}}{\varepsilon_e - 1} \; [Np/m] \tag{431}$$

Appendix M Transmission Line Parameter Conversions

The following equations are used to convert RLGC parameters to impedance, propagation constant, and loss [224].

$$\omega = 2\pi f \tag{432}$$

$$Z = R + j\omega L \tag{433}$$

$$Y = G + j\omega C \tag{434}$$

$$Z_c = \sqrt{\frac{Z}{Y}} \tag{435}$$

$$\gamma = \sqrt{ZY} \tag{436}$$

$$\gamma = \alpha + j\beta \tag{437}$$

$$v = \frac{\omega}{\beta} \tag{438}$$

$$\varepsilon_e = n^2 \tag{439}$$

$$\alpha_d = \frac{G \times real(Z_c)}{2} \tag{440}$$

$$\alpha_c = \frac{R}{2 \times real(Z_c)} \tag{441}$$

Impedance and propagation constant to RLGC. This may be used for any amount of loss.

$$Z = \gamma Z_c \tag{442}$$

$$Y = \frac{\gamma}{Z_c} \tag{443}$$

$$R = real(Z) \tag{444}$$

$$L = \frac{imag(Z)}{2\pi f} \tag{445}$$

$$G = real(Y) \tag{446}$$

$$C = \frac{imag(Y)}{2\pi f} \tag{447}$$

The following equations are used to convert characteristic impedance and propagation constant to RLGC parameters. The low loss assumption $\frac{imag(Z_c)}{real(Z_c)} < 0.05$ is taken to be true.

$$R = 2\alpha_c Z_c \tag{448}$$

$$L = \sqrt{\varepsilon_e}\frac{Z_c}{c_0} \tag{449}$$

$$G = \frac{2\alpha_d}{Z_c} \tag{450}$$

$$C = \frac{\sqrt{\varepsilon_e}}{Z_c c_0} \tag{451}$$

The following equation is used to convert S-parameters to T-Parameters

$$T = \begin{bmatrix} -\frac{d}{s_{21}} & \frac{s_{11}}{s_{21}} \\ -\frac{s_{22}}{s_{21}} & \frac{1}{s_{21}} \end{bmatrix} \tag{452}$$

The following equation is used to convert T-Parameters to S-parameters

$$S = \begin{bmatrix} \frac{t_{12}}{t_{22}} & \frac{1}{t_{22}} \\ \frac{d}{s_{22}} & -\frac{t_{21}}{t_{22}} \end{bmatrix} \tag{453}$$

The following equation is used to convert S-parameters to Z-Parameters

$$Z_0 = 50 \tag{454}$$

$$d_s = (1 - s_{11})(1 - s_{22}) - s_{12}s_{21} \tag{455}$$

$$Z = \begin{bmatrix} [(1+s_{11})(1-s_{22}) + s_{12}s_{21}]\frac{Z_0}{d_s} & 2s_{12}\frac{Z_0}{d_s} \\ 2s_{21}\frac{Z_0}{d_s} & [(1-s_{11})(1+s_{22}) + s_{12}s_{21}]\frac{Z_0}{d_s} \end{bmatrix} \quad (456)$$

The following equation is used to convert Z-Parameters to S-parameters

$$Z_0 = 50 \quad (457)$$

$$d_s = (z_{11} + Z_0)(z_{22} - Z_0) - z_{12}z_{21} \quad (458)$$

$$S = \begin{bmatrix} [(1-z_{11})(z_{22}+Z_0) - z_{12}z_{21}]\frac{1}{d_s} & 2z_{12}\frac{Z_0}{d_s} \\ 2z_{21}\frac{Z_0}{d_s} & [(1+z_{11})(z_{22}-Z_0) - z_{12}z_{21}]\frac{1}{d_s} \end{bmatrix} \quad (459)$$

The following equation is used to convert Z-Parameters to Y-Parameters

[y11,y21,y12,y22] = z2y(z11,z21,z12,z22)

$$d = z_{11}z_{22} - z_{12}z_{21} \quad (460)$$

$$Y = \begin{bmatrix} \frac{z_{22}}{d} & -\frac{z_{12}}{d} \\ -\frac{z_{21}}{d} & \frac{z_{11}}{d} \end{bmatrix} \quad (461)$$

The following equation is used to convert Y-Parameters to Z-Parameters

[z11,z21,z12,z22] = y2z(y11,y21,y12,y22)

$$d = y_{11}y_{22} - y_{12}y_{21} \quad (462)$$

$$Y = \begin{bmatrix} \frac{y_{22}}{d} & -\frac{y_{12}}{d} \\ -\frac{y_{21}}{d} & \frac{y_{11}}{d} \end{bmatrix} \quad (463)$$

The following equations are used to convert S-parameters to ABCD-Parameters

[A,B,C,D] = s2abcd(s11,s21,s12,s22)

$$Z_{01} = 50 \tag{464}$$

$$Z_{02} = 50 \tag{465}$$

$$R_{01} = real(Z_{01}) \tag{466}$$

$$R_{02} = real(Z_{02}) \tag{467}$$

$$d = 2s_{21}\sqrt{R_{01}R_{02}} \tag{468}$$

$$A = \frac{({Z_{01}}^{*} + s_{11}Z_{01})(1 - s_{22}) + s_{12}s_{21}Z_{01}}{d} \tag{469}$$

$$B = \frac{({Z_{01}}^{*} + s_{11}Z_{01})({Z_{02}}^{*} + s_{22}Z_{01}) - s_{12}s_{21}Z_{01}Z_{02}}{d} \tag{470}$$

$$C = \frac{(1 - s_{11})(1 - s_{22}) - s_{12}s_{21}}{d} \tag{471}$$

$$D = \frac{(1 - s_{11})({Z_{02}}^{*} + s_{22}Z_{02}) + s_{12}s_{21}Z_{02}}{d} \tag{472}$$

$$ABCD = \begin{bmatrix} A & B \\ C & D \end{bmatrix} \tag{473}$$

The following equation is used to convert ABCD-Parameters to S-parameters

$$Z_0 = 50 \tag{474}$$

$$d = A + \frac{B}{Z_0} + CZ_0 + D \tag{475}$$

$$S = \begin{bmatrix} \frac{A + \frac{B}{Z_0} - CZ_0 - D}{d} & \frac{2(AD - BC)}{d} \\ \frac{2}{d} & \frac{-A + \frac{B}{Z_0} - CZ_0 + D}{d} \end{bmatrix} \tag{476}$$

Appendix N Resistivity Conversions

Several units are commonly used in specifying a resistivity or conductivity. In particular, a differentiation must be made between bulk resistivity and sheet resistivity. Sheet resistivity is commonly given when the thickness of the conductor on a surface is not known but the resistance, length, and width are known. If the conductor is printed twice as thick, the sheet resistivity would indicate a lower resistance. Units of sheet resistivity are commonly $\Omega/\square$ or "ohms per square". Bulk resistivity takes into consideration thickness and is a constant unit of measure versus dimensions and may be used to compare one material against another. If the thickness of the conductor can be determined, sheet resistivity can be converted to the more general bulk resistivity by multiplication.

$$\rho = R_S t \tag{477}$$

Table 29 Loss conversions

Variable	Unit	Formula
Resistivity ρ	$\Omega \cdot m$	$1e8[\mu\Omega \cdot cm] = [\Omega \cdot m]$ $100[\Omega \cdot cm] = [\Omega \cdot m]$ $\frac{1}{[\mathrm{S/m}]} = [\Omega \cdot m]$
Resistivity ρ	$\mu\Omega \cdot cm$	$2.54[\mathrm{m\Omega/\square/mil}] = [\mu\Omega \cdot cm]$ $1\mathrm{e}8\frac{1}{[\mathrm{S/m}]} = [\mu\Omega \cdot cm]$
Resistivity ρ	$\mathrm{m\Omega/\square/mil}$	$0.3937[\mu\Omega \cdot cm] = [\mathrm{m\Omega/\square/mil}]$ $3.937\mathrm{e}7\frac{1}{[\mathrm{S/m}]} = [\mathrm{m\Omega/\square/mil}]$
Conductivity σ	$[\mathrm{S/m}]$	$3.937\mathrm{e}7\frac{1}{[\mathrm{m\Omega/\square/mil}]} = [\mathrm{S/m}]$ $1\mathrm{e}8\frac{1}{[\mu\Omega \cdot cm]} = [\mathrm{S/m}]$

Table 30 Example Conductor Loss Values

Unit	Silver (Solid)	Copper (Solid)	ESL 9912-F (800ºC)	DuPont CB028 (160ºC)	EPO-TEK H20e (100ºC)
$\Omega \cdot m$	1.59e-8	1.72e-8	2.249e7	2.54e-7	4e-6
$\mu\Omega \cdot cm$	1.59	1.72	4.45	25.4	400
$\mathrm{m\Omega/\square/mil}$	0.63	0.68	1.750	10	157
$[\mathrm{S/m}]$	6.29e7	5.80e7	2.249e7	3.94e6	2.50e5
Relative	105%	100%		7.75%	0.42%

Table 31 Example loss tangent values

Material	Advantage	Technology	Loss tangent
Alumina		Raw	0.0003
PTFE		Raw	0.0003
ABS	Cheap, avail. @ USF	FDM	0.003
Ultem	Space-rated, high temp	FDM	0.004
PC	Cheap, easy to print	FDM	0.005
NanoTool	High temp.	SL	0.022
Watershed	High res.	SL	0.032
Prototherm	High temp. & high res.	SL	0.038

When loss is discussed in relation to a transmission line the natural units Nepers (Np) or decibels (dB) are used. If the line is to be compared to other lines of different lengths, the units Np/m or dB/m are commonly used. The following equations allow conversion between Nepers and decibels.

$$[dB] = \frac{20}{ln(10)}[Np] \tag{478}$$

$$8.6859 = \frac{[dB]}{[Np]} \tag{479}$$

Appendix O Modeling Verification

Five modeling methods are used in analyzing the performance characteristics of microstrip transmission line. The methods are as follows.

- Designers' equations (MATLAB)
- Ansoft Designer
- Agilent ADS
- Ansoft Q2D
- Ansys HFSS

Each method produces results in a different format and typically comparisons between microwave components are made using overlaid S-parameters. In order to more clearly distinguish the characteristics of each component, the analysis which is presented here will use the Nicholson-Ross-Weir approach modified for conversion from S-parameters to impedance. The following parameters are solved for: characteristic impedance (Zc), effective permittivity (ee), and the propagation constant (gamma) which is composed of the loss coefficient (alpha) and the phase constant (beta). These frequency-dependent parameters are plotted and compared.

The designers' equations are simple algebraic approximations of microstrip transmission line and produce characteristic impedance and effective dielectric constant.

Ansoft Designer models microwave networks as lumped blocks connected together and produces as output S-parameters. This method uses the same underlying designers' equations but provides an easy-to-use GUI.

Agilent ADS (advanced design studio) models microwave networks as lumped blocks connected together and produces as output S-parameters. This method uses the same underlying designers' equations but provides an easy-to-use GUI.

Ansoft Q2D models 2D cross-sections of arbitrary transmission lines and typically outputs RLGC parameters. An option is available in the software to export S-parameters. The

conversion from RLGC parameters to S-parameters is elementary. RLGC parameters offer one additional advantage over S-parameters in that they offer the ability to separate dielectric and conductor losses directly.

Ansys HFSS models 3D devices and produces only S-parameters for the device as a whole. For the 2D cross-section at the ports, characteristic impedance, effective permittivity, and propagation constant are also available; however, these parameters do not necessarily reflect the device as a whole.

The following basic parameters will be used in all cases except as specified otherwise.

Table 32 Basic parameters

Parameter	**Variable**	**Value**
Width	w	1.75
Height	h	0.8 mm
Permittivity	er	3
Thickness	th	25 μm
Loss tangent	tand	0.03
Length	l	50 mm
Resistivity	rho	21.59 μΩcm @ DC
Conductivity	sigma	4631774 S/m @ DC
Frequency	f	10 GHz
Substrate width	sub_w	30 mm

In order to validate each modeling method, the methods are compared. Two data sets are compiled, the first with the basic parameters and the second with the same parameters but 200 mm long. Data marked with an asterisk (*) are given directly from the software and are not derived from the NRW S-parameter back-solve. Matches between data marked with an asterisk and unmarked data validate the NRW back-solve algorithms.

Table 33 Comparison, 50 mm length

	MATLAB	Designer	ADS	Q2D	Q2D*	HFSS	HFSS*
Zc @ 1 GHz	53.73	53.94	54.04	53.87	54.27	66.49	N/A
Zc @ 10 GHz	53.73	54.34	55.47	54.74	55.07	69.33	N/A
ee @ 1 GHz	2.383	2.39	2.4	2.45	2.42	2.45	2.40
ee @ 10 GHz	2.383	2.44	2.35	2.34	2.31	2.38	2.36
alpha @ 1 GHz	0.73	0.61	0.54	0.60	0.59	0.69	0.58
alpha @ 10 GHz	5.21	4.95	4.84	4.56	4.53	4.94	4.88
tand @ 1 GHz	0.030	0.031	0.032	0.031	N/A	0.028	N/A
tand @ 10 GHz	0.030	0.031	0.033	0.031	N/A	0.028	N/A
rho @ 1 GHz	65.11	18	4.33	28.76	N/A	73.59	N/A
rho @ 10 GHz	65.11	17.34	4.38	30.35	N/A	73.90	N/A

Table 34 Comparison, 200 mm length

	MATLAB	Designer	ADS	Q2D	Q2D*	HFSS	HFSS*
Zc @ 1 GHz	53.73	53.94	54.04	53.87	54.27		N/A
Zc @ 10 GHz	53.73	54.34	55.47	54.74	55.07		N/A
ee @ 1 GHz	2.383	2.39	2.40	2.45	2.42		
ee @ 10 GHz	2.383	2.44	2.35	2.34	2.31		
alpha @ 1 GHz	0.83	0.61	0.54	0.60	0.59		
alpha @ 10 GHz	7.09	4.95	4.84	4.56	4.53		
tand @ 1 GHz	0.030	0.031	0.032	0.031	N/A		N/A
tand @ 10 GHz	0.030	0.031	0.033	0.031	N/A		N/A
rho @ 1 GHz	65.11	18	4.33	28.76	N/A		N/A
rho @ 10 GHz	65.11	17.34	4.38	30.35	N/A		N/A

The suspended microstrip is modeled using MATLAB, ANSYS Designer, ANSYS Q2D, and ANSYS HFSS. Each method is benchmarked against one another for three structures (as available), a solid substrate (standard microstrip), an air-filled substrate (fully-suspended), and a pole-supported substrate (realistic suspended). It can be seen that the methods are in agreement.

Table 35 Suspended microstrip modeling results

Method	Structure	Freq (GHz)	Z (ohms)	beta	alpha	ee
MATLAB	Solid	10	80.13	316.64	N/A	2.28
Designer	Solid	10	82.44	323.89	4.24	2.39
Q2D	Solid	10	79.88	310.24	3.89	2.19
HFSS	Solid	10	86.32	319.66	4.29	2.33
Q2D	Air-Filled	10	106.02	235.22	0.63	1.26
HFSS	Air-Filled	10	110.12	227.87	0.40	1.18
HFSS	Poles	10	109.28	229.30	0.45	1.20

Appendix P Microstrip Width Convergence

The necessary substrate width to accurately determine microstrip parameters is important and a convergence of impedance with increasing substrate width is performed here. The characteristic impedance at 1 GHz and 10 GHz is plotted as the substrate width is varied from 1 mm to 30 mm. It is graphically determined that 15 mm provides a sufficiently wide substrate.

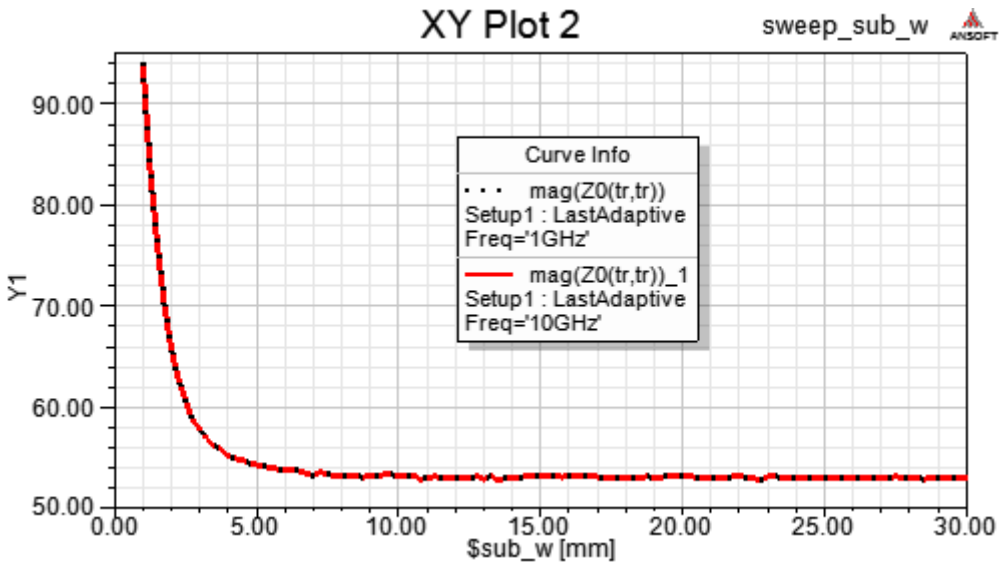

Error in S-parameter data is magnified when the Nicholson-Ross-Weir method is used to solve for characteristic impedance. Longer transmission lines reduce this error as shown in the following data sets. HFSS is used to model lines 10 mm, 50 mm, and 100 mm long and the NRW method is used to solve for the characteristic impedance. It can be clearly seen that the 100 mm line exhibits the least error.

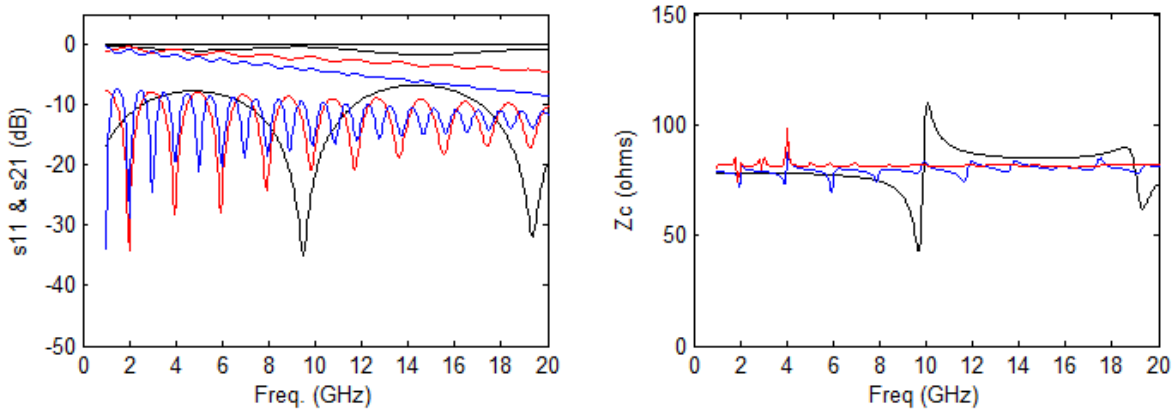

Figure 135 Microstrip length variations

Additional length sweeps are conducted on suspended microstrip. Improved agreement between methods is achieved when the length of the structure is increased. Table 36 shows data extracted from S-parameters generated by HFSS and processed using custom MATLAB functions which determine characteristic impedance, effective permittivity, and loss. The data are compared between methods amongst different model lengths.

Table 36 Loss modeling

Method	**Length**	**Alpha (Np/m) @ 30 GHz**	**Alpha (dB/m) @ 30 GHz**
Q2D port solver	2D	10.83 Np/m	94.21 dB/m
Q2D s2p extract	50 mm	10.83 Np/m	94.07 dB/m
Q2D s2p extract	100 mm	10.83 Np/m	94.07 dB/m
HFSS port solver	10 mm	13.88 Np/m	120.56 dB/m
HFSS s2p extract	10 mm	16.30 Np/m	141.60 dB/m
HFSS port solver	50 mm	13.88 Np/m	120.56 dB/m
HFSS s2p extract	50 mm	13.99 Np/m	121.51 dB/m
HFSS port solver	100 mm	13.85 Np/m	120.30 dB/m
HFSS s2p extract	100 mm	13.85 Np/m	120.30 dB/m

Appendix Q Modeling Parameters

Figure 136 shows a conceptual view of the mathematic models which are implemented using MATLAB for this work. Ovals represents a way of representing transmission line data. The text near the directional connecting arrows show the type of conversion which must be used to convert from one data representation to another.

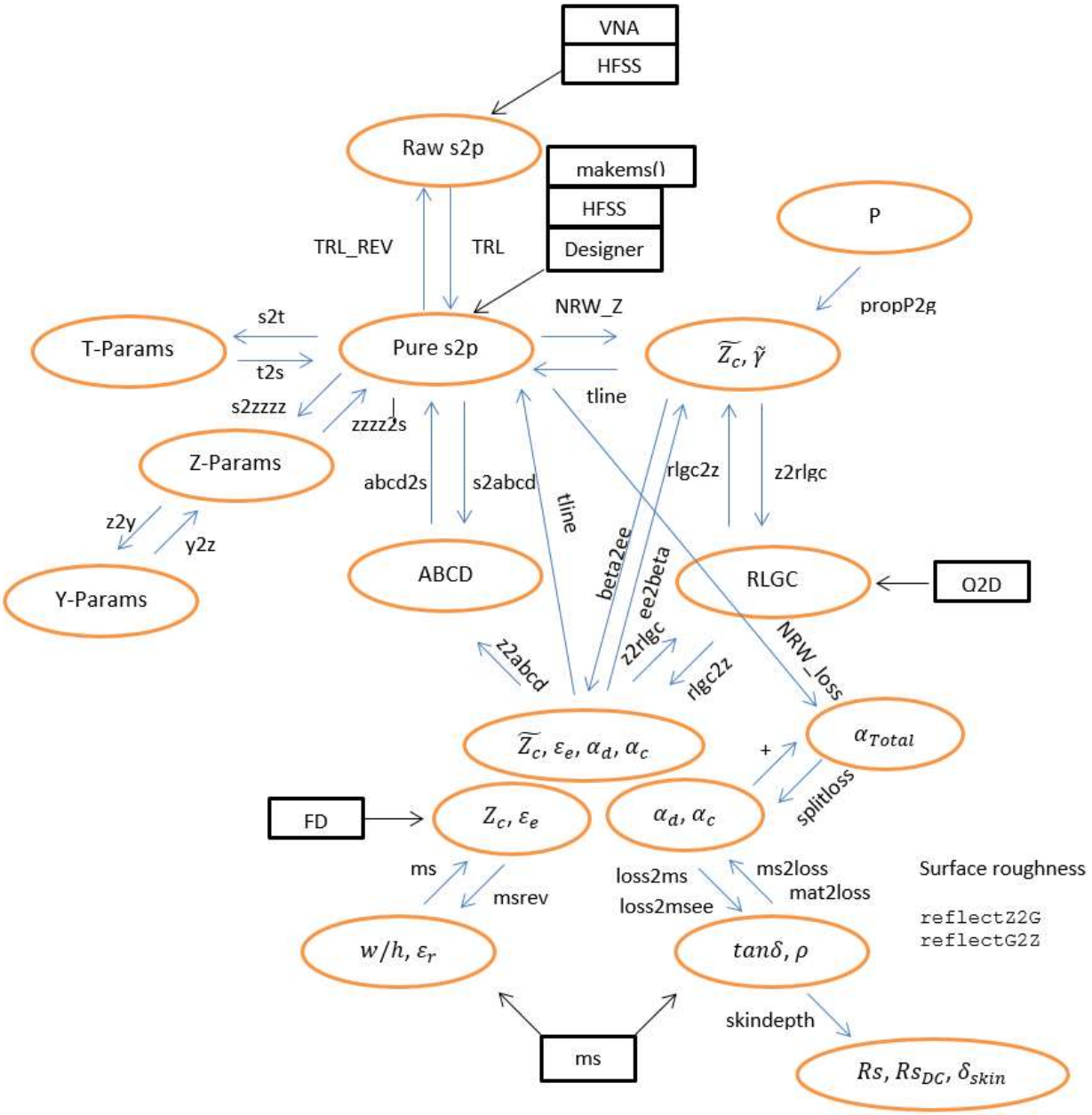

Figure 136 MATLAB modeling overview

HFSS is used in several situations in this work to model transmission lines and antennas. The typical modeling parameters which are used are shown here.

Table 37 HFSS Settings

Parameter	*Value*
Solution Type	Driven Modal
Solution Type	Network Analysis
Port	Wave Port
Port Renormalization	Renormalize All Modes
Solution Frequency	Max frequency
Maximum Number of Passes	25
Maximum Delta S	0.02
Do Lambda Refinement	Yes
Lambda Target	0.3333
Use Default Value	Yes
Maximum Refinement Per Pass	20 %
Minimum Number of Passes	5
Minimum Converged Passes	3
Order of Basis Functions	First Order
Max Refinement	1,000,000
Enable Iterative Solver	Yes, 0.001
Enable Use of Solver Domains	No
Maximum Delta Zo:	2 %
Sweep Type	Interpolating
Max Solutions	250
Error Tolerance	0.5 %

Appendix R Printing Parameters

A short study is conducted on the relation between printing parameters such as tip size and number of passes and the actual line dimensions. This is important for printing many types of transmission lines where the conductor width affects the characteristic impedance and must be well controlled. Excess material at the start of lines is to be minimized so as to avoid shorting or impedance discontinuities. Table 38 shows the printing parameters which are used throughout this study. Parameters are adjusted for reliable printing.

Table 38 Printing parameters

Parameter	Tip 75/125 (ID/OD)	Tip 125/175 (ID/OD)
Resulting width	215 µm	340 µm
Slump amount	90 µm	170 µm
Start size	500 µm	830 µm
Required gap	30-75 µm	50-200 µm
Speed	20 mm/s	20 mm/s
Pressure	10 psi	4 psi
Opening	0.4 mm @ 5 mm/s	0.4 mm @ 5 mm/s
Trig wait	0.08 s	0.08 s
Comments	Narrower lines allows higher resolution on smooth/level surfaces.	Broader gap requirement allows printing on more surfaces.

Figure 137 and Figure 138 show a selection of the printed lines. Table 39 compares repeatability for each tip size. Each line is identified by its sample identification number (SID) and its width averaged over three measurements and a mean is computed for the set. When using a 75/125 tip the printed line is 90 µm wider than the outer diameter (OD) of the tip. When using a 125/175 tip the printed line is 170 µm wider than the tip OD.

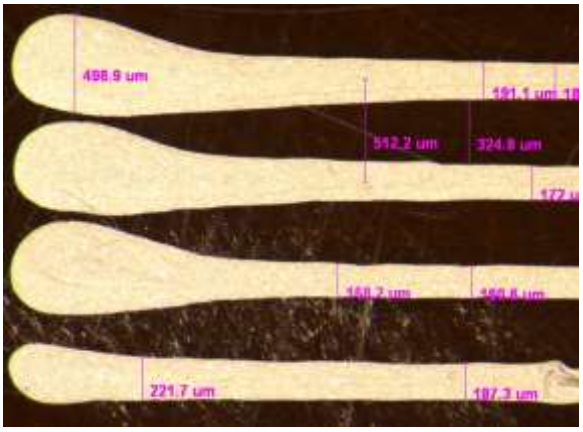

Figure 137 75/125 tip size

Table 39 Line width

SID	Line width (um) with 75/125	Line width (um) with 125/175
1	192.9	362.8
2	205.0	341.5
3	207.2	325.9
4	358.9	337.7
5	273.9	345.4
6	201.8	333.9
7	191.1	
8	172.0	
9	160.6	
10	187.3	
MEAN	215.1	

Minimum line spacing is determined from the size of the beginning of the line which is simply called the “start” and is shown in Figure 138. Start timing can be adjusted; however, adjusting it too tightly diminishes the reliability since minor variations in the valve mechanism can cause the start to be delayed. Start parameters are adjusted conservatively and the size of the start is measured and a mean is computed for each tip size.

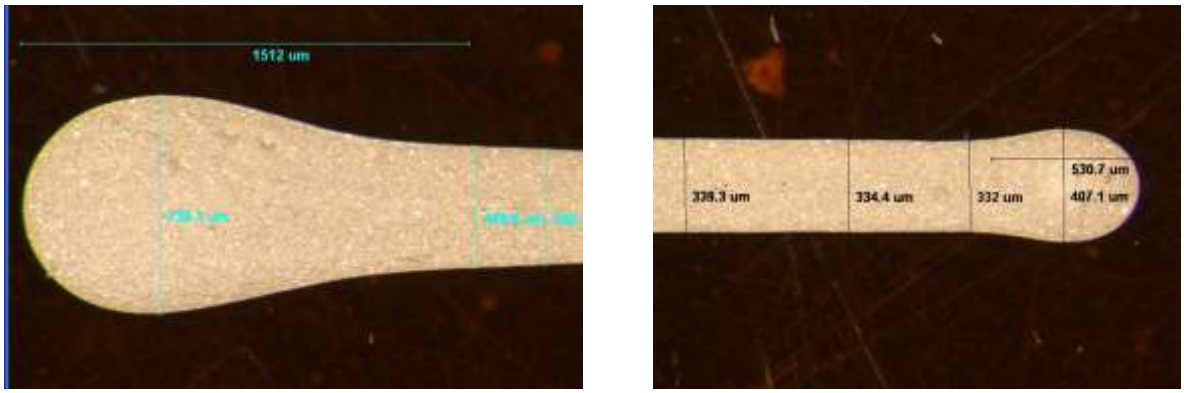

Figure 138 125/175 tip size

Table 40 Start size for 75/125 tip

Tip Size	SID	Start Size
75/125	1	458.7
75/125	2	492.2
75/125	3	493.3
75/125	4	585.0
75/125	5	493.1
75/125	6	485.5
75/125	7	496.9
	MEAN	500.7

Table 41 Start size for 125/175 tip

Tip Size	SID	Start Size
125/175	16	704.3
125/175	17	789.9
125/175	18	747.0
125/175	19	747.3
125/175	27	560.4
125/175	28	606.4
125/175	29	729.2
	MEAN	832.9

Making additional passes improves the error in the start size since start size is fixed as shown in Figure 139. Table 42 and Table 43 show the measurement of the start error. Printing 4 to 6 passes produces lines 10% wider than the 200 um pitch would predict. Starts of lines are

64% wider than line width for single lines. Starts of lines are 23-42% wider than line width for 2-6 passes.

Figure 139 Improvement in start error with more passes

Table 42 Line width vs. number of passes

Tip Size (ID/OD µm)	SID	Pitch (µm)	Passes	Theoretical Width (µm)	Width (µm)	Spillage (µm)	Error
125/175	11	200	1	200	350	150	75 %
125/175	12	200	2	400	666	266	67 %
125/175	13	200	4	800	867	67	8 %
125/175	14	200	6	1200	1328	128	11 %

Table 43 Start width vs. number of passes

Tip Size (ID/OD µm)	SID	Pitch (µm)	Passes	Actual Width (µm)	Start Width (µm)	Spillage (µm)	Error
125/175	11	200	1	350	575	225	64 %
125/175	12	200	2	666	843	177	27 %
125/175	13	200	4	867	1228	360	42 %
125/175	14	200	6	1328	1630	302	23 %

Vita

Paul I. Deffenbaugh is from Palm Bay, Florida, USA. He received the Bachelor of Science in Electrical Engineering, from Florida Institute of Technology in Melbourne, Florida, USA in 2010 and the Master of Science in Electrical Engineering from The University of Texas at El Paso (UTEP), El Paso, Texas, USA, 2011. He worked at Rockwell Collins, Inc. as an intern in the Reliability Group and in new product development during the summers of 2008 and 2009. During the summer of 2010 he worked with nScrypt, Inc. in Orlando, Florida where he met Dr. Kenneth Church, CEO of nScrypt, Inc. and Ph.D. adviser. For one year from 2010–2011, he studied 3D printing and direct-print technologies at nScrypt, Inc. in Orlando, Florida while attending masters' classes remotely from UTEP before eventually moving to El Paso, Texas to study and research full time for two years in the W.M. Keck Center for 3D Innovation. For one year from 2013–2014 he collaborated with Dr. Thomas Weller and the students at the University of South Florida in the Wireless and Microwave Applications (WAMI) research group and labs and was given the opportunity to use state of the art microwave and RF measurement equipment as well as SEM, XRD, micro probe stations, and other high precision measurement tools. His research interests are RF and microwave electromagnetics and the improvements which can be made in the field by 3D printing. At the time of this publication he works with Sciperio, Inc., in Orlando, Florida.

Email: pdeffenbaugh@miners.utep.edu